National Library of Canada
Canadian Theses Service
Ottawa, Canada
K1A 0N4

Bibliothèque nationale du Canada
Service des thèses canadiennes

## NOTICE

The quality of this microform is heavily dependent upon the quality of the original thesis submitted for microfilming. Every effort has been made to ensure the highest quality of reproduction possible.

If pages are missing, contact the university which granted the degree.

Some pages may have indistinct print especially if the original pages were typed with a poor typewriter ribbon or if the university sent us an inferior photocopy.

Reproduction in full or in part of this microform is governed by the Canadian Copyright Act, R.S.C. 1970, c. C-30, and subsequent amendments.

## AVIS

La qualité de cette microforme dépend grandement de la qualité de la thèse soumise au microfilmage. Nous avons tout fait pour assurer une qualité supérieure de reproduction.

S'il manque des pages, veuillez communiquer avec l'université qui a conféré le grade.

La qualité d'impression de certaines pages peut laisser à désirer, surtout si les pages originales ont été dactylographiées à l'aide d'un ruban usé ou si l'université nous a fait parvenir une photocopie de qualité inférieure.

La reproduction, même partielle, de cette microforme est soumise à la Loi canadienne sur le droit d'auteur, SRC 1970, c. C-30, et ses amendements subséquents

NL-339 (r. 88/04) c

Canada

THE UNIVERSITY OF ALBERTA

# SOME MECHANISMS OF WATER PROTON NMR RELAXATION IN MODEL TISSUE SYSTEMS

BY

RAVI SHANKAR MENON

A THESIS

SUBMITTED TO THE FACULTY OF GRADUATE STUDIES AND RESEARCH

IN PARTIAL FULFILLMENT OF THE REQUIREMENTS FOR THE DEGREE

OF DOCTOR OF PHILOSOPHY

IN

MEDICAL SCIENCES (APPLIED SCIENCES IN MEDICINE).

EDMONTON, ALBERTA

FALL 1990

National Library of Canada | Bibliothèque nationale du Canada

Canadian Theses Service | Service des thèses canadiennes

Ottawa, Canada
K1A 0N4

The author has granted an irrevocable non-exclusive licence allowing the National Library of Canada to reproduce, loan, distribute or sell copies of his/her thesis by any means and in any form or format, making this thesis available to interested persons.

L'auteur a accordé une licence irrévocable et non exclusive permettant à la Bibliothèque nationale du Canada de reproduire, prêter, distribuer ou vendre des copies de sa thèse de quelque manière et sous quelque forme que ce soit pour mettre des exemplaires de cette thèse à la disposition des personnes intéressées.

The author retains ownership of the copyright in his/her thesis. Neither the thesis nor substantial extracts from it may be printed or otherwise reproduced without his/her permission.

L'auteur conserve la propriété du droit d'auteur qui protège sa thèse. Ni la thèse ni des extraits substantiels de celle-ci ne doivent être imprimés ou autrement reproduits sans son autorisation.

ISBN 0-315-54778-7

Canada

**BIOPHYSICAL JOURNAL**

PUBLISHED FOR THE BIOPHYSICAL SOCIETY

BY THE ROCKEFELLER UNIVERSITY PRESS

*Edited in cooperation with the Division of Biological Physics of The American Physical Society*

T. E. THOMPSON, EDITOR
*Box 401*
*University of Virginia Medical Center*
*Charlottesville, VA 22908*

*(804) 924-2138*

*biophysva.virginia.bitnet*

March 27, 1990

Mr. Ravi Menon
In-vivo NMR Group
Department of Applied Sciences in Medicine
10-102 Clinical Sciences Building
University of Alberta
Edmonton, AB
CANADA T6G 2G3

Dear Mr. Menon:

This letter is to inform you that your copyright permission is granted to include the manuscript "Solvent Proton Relaxation of Aqueous Solutions of the Serum Proteins 2-Macroglobulin, Fibrinogen, and Albumin," by yourself and Dr. Allen, as a chapter in your Ph.D. thesis and for microfilming purposes.

Sincerely,

Thomas E. Thompson/vs

Thomas E. Thompson, Ph.D.
Editor

TET/vs

UNVERSITY OF ALBERTA

RELEASE FORM

NAME OF AUTHOR: RAVI SHANKAR MENON

TITLE OF THESIS: SOME MECHANISMS OF WATER PROTON NMR RELAXATION IN MODEL TISSUE SYSTEMS

DEGREE: DOCTOR OF PHILOSOPHY

YEAR THIS DEGREE GRANTED: 1990

Permission is hereby granted to THE UNIVERSITY OF ALBERTA LIBRARY to reproduce single copies of this thesis and to lend or sell such copies for private, scholarly or scientific research purposes only.

The author reserves other publication rights, and neither the thesis nor extensive extracts from it may be printed or otherwise reproduced without the author's written permission.

4331 Staulo Crescent,
Vancouver, B.C.
V6N 3S3

Date: 7th August 1990

*montani semper liberi*

THE UNIVERSITY OF ALBERTA

FACULTY OF GRADUATE STUDIES AND RESEARCH

The undersigned certify that they have read, and recommend, a thesis entitled SOME MECHANISMS OF WATER PROTON NMR RELAXATION IN MODEL TISSUE SYSTEMS submitted by RAVI SHANKAR MENON in partial fulfilment of the requirements for the degree of DOCTOR OF PHILOSOPHY in MEDICAL SCIENCES.

P.S. Allen
Dr. P.S. Allen (Supervisor)

D.G. Hughes
Dr. D.G. Hughes

S.F.P. Man
Dr. S.F.P. Man

Dr. R.E. Snyder

Brian D. Sykes
Dr. B.D. Sykes

Dr. J.D.R. Miller

Dr. M.J. Bronskill

Date: 15 Aug 90

To my family, for all their love and support.

## ABSTRACT

Biological systems exhibit heterogeneity at many levels, giving rise to the observation of multiple relaxation time components for water protons as measured by nuclear magnetic resonance. The longitudinal, transverse and spin-locked rotating frame relaxation rates have been measured for water protons at 100 MHz in a variety of model tissue systems, in order to unravel the contributions of the major tissue constituents to the generation of contrast in images using the magnetic resonance technique. This has the potential to improve the specificity and diagnostic potential of magnetic resonance imaging, especially in edematous brain tissue.

In aqueous solutions of human serum proteins albumin, fibrinogen and $\alpha_2$-macroglobulin, the linear concentration dependence of the three relaxation rates has been explained in terms of a model that invokes two motions that contribute to the complete averaging of the dipolar interaction between water protons in the hydration shells of the proteins.

In order to evaluate hypotheses concerning the possible sources of multiple exponential components in tissue, relaxation measurements were performed on model cellular systems composed of human red blood cell ghosts. The data show that although trans-membrane exchange is too fast to give rise to multiexponential relaxation, multiple components can arise from compartmentalization at the level of cellular organization. In addition, the data clearly demonstrate the importance of protein adsorption to cellular membranes as a determinant of freely mobile solute protein molecules in tissue fluids.

We have also investigated the ability of one particular linear inverse theory technique to reproduce known relaxation time distributions in controllable model systems. Application of this technique to *in-vitro* relaxation time measurements on excised cat brain tissue gives rise to multiple transverse relaxation components in

grey and white matter, but only single exponential decays for the longitudinal magnetization. Similar studies on excised crayfish abdominal nerve cords have demonstrated four components for the transverse magnetization. The major transverse magnetization component in white matter and crayfish nerves is assigned to the axonal water which is in slow exchange with the other tissue water due to myelination. Characteristic changes in the relaxation rates have been observed during nerve degeneration.

## ACKNOWLEDGEMENTS

I must thank my supervisor, Dr. Peter S. Allen, for giving me the opportunity to do research in his laboratory. I have learned a great deal from working with him as well as all the other members of my supervisory committee.

I am eternally grateful to Marg Rusinko for the dual role she has played in my life. As a technologist, she proved extremely resourceful in "procuring" material and her patience and skill in sample preparation, dissection and chess at unGodly hours were uncanny. In her alter ego as my dear friend and sidekick, she helped preserve my mental health through all the barren times. Without her guidance and trusted companionship, this thesis would not have come to fruition.

The contributions of "Damji Enjuneering", "Doran Industries" and "Ellinger Research" kept both myself and the machines up and running. Ivy Ho and Commander Dan ensured that I could always communicate with the mysterious grey boxes we call "computers". Chris (Professor) Hanstock and Lair Alexander Trimble served as great sounding boards for my ideas, as well as educating me in the "Bruker Way". I thank you all for your technical expertise, patience and friendship.

Mrs. Margot Szalay and Mrs. Halyna Marusyk found time in their hectic schedules to do the beautiful electron microscopy studies found in this thesis. Generous laboratory facilities were provided by Dr. T. Allen of Pharmacology and Maxine Farr-Jones in Surgery. Max's help and advice on many other fronts was invaluable. Drs. Tatton and Martin of Toronto Western Hospital not only showed us a good time, but saved us months of effort by teaching MSR the intricacies of crayfish dissection. The Canadian Red Cross provided us with a seemingly endless supply of human blood and we were only too glad to return the favor. The Alberta Heritage Foundation for Medical Research Studentship I held for the past four years helped make my life in Edmonton quite comfortable.

Much of my schooling in NMR and data analysis I owe to Drs. MacKay, Whittal and Bloom, of UBC's infamous Room 100, especially Myer, who sparked my early interest in NMR when I was an undergraduate.

Finally, I must remember the supportive friends, too numerous to mention, here and elsewhere who made my time in Alberta a memorable experience. George and Ann Sexsmith and "Mother" Ingham, who took me into their home; Sharon, Ernie, Kent and Edith who were all just a phonecall away.

I suppose if a thesis is meant to guide those who follow, then this volume is meant for a very special girl... quiet, talented Frances...who follows in my footsteps. *Good luck!*

## TABLE OF CONTENTS


| Chapter | | | Page |
|---|---|---|---|
| 1 | Introduction | | |
| | 1.0 Introduction to the thesis | | 25 |
| | 1.1 Water homeostasis in brain | | 29 |
| | 1.2 Neuronal structure | | 31 |
| | 1.2.1 Membrane structure | | 33 |
| | | 1.2.1.1 Membrane lipids | 33 |
| | | 1.2.1.2 Membrane proteins | 35 |
| | | 1.2.1.3 Water transport across the membrane | 37 |
| | | 1.2.1.4 Volume regulation in cells | 39 |
| | 1.2.2 Myelin membranes | | 41 |
| | 1.2.3 Protein structures in neural cells | | 43 |
| | 1.2.4 Glial structures | | 45 |
| | 1.2.5 Neuron-glial cell relationships | | 46 |
| | | 1.2.5.1 The blood-brain barrier | 47 |
| | | 1.2.5.2 Extracellular space in brain | 50 |
| | 1.3 Introduction to NMR studies of water in biological systems | | 50 |
| | 1.3.1 The macroscopic magnetization | | 53 |
| | 1.3.2 Relaxation in a two-spin system | | 55 |
| | | 1.3.2.1 Form of the hamiltonian | 55 |
| | | 1.3.2.2 Eigenvectors and eigenvalues of a two-spin system | 56 |
| | | 1.3.2.3 Equations of motion for a two-spin system | 57 |

1.3.2.4 The dipole-dipole interaction 58
1.3.2.5 Spin-lattice relaxation in the rotating frame 61
1.3.2.6 Forms of the spectral densities 62
1.3.3 Exchange between phases 64
1.3.4 Effect of constrained motions on relaxation 68
1.4 Intoduction to proton NMR imaging 71
1.5 The problem of cerebral edema 73
1.5.1 Studies of edema using proton NMR 74
1.6 References and selected bibliography 85
2 Relaxation studies of the serum proteins fibrinogen, $\alpha_2$-macroglobulin and albumin in aqueous solution
2.1 Introduction 96
2.2 Experimental 98
2.2.1 Materials 98
2.2.2 Relaxation measurements 99
2.3 Results 100
2.4 Analysis and discussion 101
2.5 Conclusions 109
2.6 References 116
3 Multiexponential water proton relaxation in a model tissue system
3.1 Introduction 120
3.2 Experimental 122
3.2.1 RBC ghost preparation by hemolysis 122
3.2.2 Sample configuration for NMR experiments 122

3.2.3 NMR measurements 124
3.2.4 Data processing 125
3.3 Results 126
3.4 Analysis and discussion 127
3.4.1 Mixed samples 127
3.4.2 Layered samples 132
3.5 Conclusions 138
3.6 Appendix of calculations 139
3.7 References 155

4 Application of continuous relaxation time distributions to the fitting of data from model systems and excised tissue
4.1 Introduction 160
4.2 Theory 162
4.3 Experimental 164
4.3.1 Layered model samples 164
4.3.2 Excised cat brain 165
4.3.3 Relaxation measurements 165
4.3.4 Imaging methods 166
4.4 Results 167
4.4.1 Layered model samples 167
4.4.2 Cat brain samples 168
4.5 Analysis and discussion 168
4.5.1 Layered model samples 169
4.5.2 Cat brain samples 171
4.6 Conclusions 173
4.7 References 186

5 NMR relaxation studies of water compartmentalization in a model neurological system: the crayfish nerve cord

5.1 Introduction 191

5.2 Morphology of the crayfish nerve cord 192

5.2.1 Gross anatomy 192

5.2.2 The ganglia 193

5.2.3 The connectives 193

5.2.4 The sheath 194

5.2.5 The blood capillary system 195

5.2.6 Water compartments in the nerve cord 195

5.3 Experimental 197

5.3.1 Removal of the nerve cord 197

5.3.2 NMR relaxation measurements 198

5.3.3 NMR microscopic imaging experiments 199

5.3.4 Invasive procedures 200

5.4 Data Analysis 201

5.5 Results 202

5.6 Analysis and discussion 203

5.6.1 Longitudinal relaxation in fresh nerve cords 203

5.6.2 Transverse relaxation in fresh and manipulated nerve cords 204

5.6.3 Time-dependent measurements 207

5.6.4 Microscopic imaging 211

5.7 Conclusions 213

5.8 References 242

6 General discussion and conclusions

6.1 Towards quantifying cerebral edema 246

6.2 Conclusions 251

6.3 References 263

Appendix A $T_2$ pulse programs and processing software 264

Appendix B $T_1$ pulse programs and processing software 268

Appendix C $T_{1\rho}$ pulse programs and processing software 271

Appendix D Microscopic imaging pulse program 272

Appendix E Design of a gradient coil set for microscopic imaging 273

## LIST OF TABLES


| Table | | Page |
|---|---|---|
| 2.1 | Physical parameters of the human serum proteins | 111 |
| 2.2 | Molar sensitivities of $R_1$, $R_2$ and $R_{1\rho}$ to proteins in aqueous solution | 111 |
| 2.3 | Calculated parameters derived from molar sensitivities | 111 |
| 4.1 | A comparison between different techniques for fitting relaxation data | 175 |
| 4.2 | An evaluation of the longitudinal relaxation data from excised cat brain using the continuous NNLS method of analysis | 176 |
| 4.3 | An evaluation of the transverse relaxation data from excised cat brain using the continuous NNLS method of analysis | 177 |
| 5.1 | Calculation of volume fractions of different regions in the crayfish nerve cord | 214 |
| 5.2 | Summary of populations and relaxation times in freshly excised nerve cords | 215 |

## LIST OF FIGURES


| Figure | | Page |
|---|---|---|
| 1.1 | Major structural features of a neuron | 76 |
| 1.2 | Fluid mosaic model of the membrane | 77 |
| 1.3 | Typical schematic of cell volume regulation in an RBC | 78 |
| 1.4 | Summary of glial cell types | 79 |
| 1.5 | Examples of compartmentation in biological systems | |
| | (A) cells in dilute suspension | 80 |
| | (B) packed cells with supernatant | 80 |
| | (C) nerve cord | 80 |
| 1.6 | Eigenstates relevant to longitudinal relaxation in a two-spin system | 81 |
| 1.7 | Eigenstates relevant to transverse relaxation in a two-spin system | 82 |
| 1.8 | Interpretation of rotational correlation times | 83 |
| 1.9 | Simple 1-D imaging experiment | 84 |
| 2.1 | A comparison of the concentration dependence for the $^1H$ longitudinal relaxation rates obtained for the serum proteins albumin, fibrinogen and $\alpha_2$-macroglobulin in aqueous solution | 112 |
| 2.2 | A comparison of the concentration dependence for the $^1H$ transverse relaxation rates obtained for the serum proteins albumin, fibrinogen and $\alpha_2$-macroglobulin in aqueous solution | 113 |
| 2.3 | A comparison of the concentration dependence for the $^1H$ longitudinal relaxation rates in the rotating frame, observed at 3.07 Gauss for the serum proteins albumin, fibrinogen and $\alpha_2$-macroglobulin in aqueous solution | 114 |
| 2.4 | The $^1H$ longitudinal relaxation rate in the rotating frame as a function of the spin-locking field. | 115 |

| | | |
|---|---|---|
| 3.1 | (A) CPMG decay of a layered sample | 144 |
| | (B) residual of biexponential fit | 144 |
| | (C) $T_2$ spectrum of a layered sample | 145 |
| 3.2 | (A) mixed solution data at $c_{pb} = 0$ g/l | 146 |
| | (B) mixed solution data at $c_{pb} = 25$ g/l | 147 |
| | (C) mixed solution data at $c_{pb} = 75$ g/l | 148 |
| 3.3 | (A) data for a layered preparation with $c_{pb} = 0$ g/l | 149 |
| | (B) data for a layered preparation with $c_{pb} = 25$ g/l | 150 |
| | (C) data for a layered preparation with $c_{pb} = 75$ g/l | 151 |
| 3.4 | Correspondence between the amount of layered buffer added to a layered sample and the amount measured by NMR | 152 |
| 3.5 | Electron micrograph of a red blood cell ghost | 153 |
| 3.6 | Phase contrast micrograph of a ghost preparation | 154 |
| 4.1 | $T_2$ measurements made as a function of displacement from the top of samples in the layered model systems | 178 |
| 4.2 | Normalized CPMG echo amplitude measured from the 120 µl volumes of samples A, B and C | 179 |
| 4.3 | Semi-logarithmic plots of magnetization measured in excised cat grey and white matter | |
| | (A) Inversion Recovery | 180 |
| | (B) CPMG | 180 |
| 4.4 | $T_2$ distributions of samples A, B and C | 181 |
| 4.5 | Comparison of integrals of calculated and imaged $T_2$ distributions | 183 |
| 4.6 | Continuous NNLS Solutions for the magnetization measured in excised cat grey and white matter | |
| | (A) from Inversion Recovery data | 185 |
| | (B) from CPMG data | 185 |
| 5.1 | (A) layout of the crayfish central nerve cord | 216 |
| | (B) a 35-mm photograph of an abdominal segment of the crayfish nerve cord | 217 |

| | | |
|---|---|---|
| 5.2 | (A) light microscopy of a cross-section through the 4th abdominal ganglion | 218 |
| | (B) light microscopy of a longitudinal section through the 4th abdominal ganglion | 219 |
| | (C) light microscopy of a cross-section through the 3-4 connective | 220 |
| 5.3 | (A) EM of neuropil area in the ganglion | 221 |
| | (B) EM of axon field in the ganglion | 222 |
| | (C) EM of extracellular collagen in the ganglion | 223 |
| | (D) EM of large axons in the 3-4 connective | 224 |
| | (E) EM of small axons in the 3-4 Connective | 225 |
| | (F) EM of the ventral sheath of the 3-4 connective | 226 |
| | (G) EM of the dorsal sheath of the 3-4 connective | 227 |
| | (H) EM of the connective tissue sheath between two axons | 228 |
| 5.4 | Transverse and longitudianal proton magnetization decay for the nerve cord in Van Harreveld's bathing solution | 229 |
| 5.5 | Transverse and longitudinal relaxation time distributions | 230 |
| 5.6 | Transverse relaxation time distribution before and after subperineural injection of the nerve cord with Van Harreveld's solution | 231 |
| 5.7 | Transverse relaxation time distribution of the whole and dissected nerve cord | 232 |
| 5.8 | Effects of paramagnetic doping of the bathing solution on the transverse relaxation time of the nerve cord | 233 |
| 5.9 | (A) Change in the transverse relaxation time as a function of time after excision with a linear abscissa | 234 |
| | (B) Change in the transverse relaxation time as a function of time after excision with a logarithmic abscissa | 235 |
| | (C) Behavior of the component populations over time after excision | 236 |
| | (D) Behavior of the component transverse relaxation times as a function of time after excision | 237 |

5.10 (A) behavior of the component populations over time after excision and storage at 4° C for 3.75 hours 238
(B) behavior of the component transverse relaxation times over time after excision and storage at 4° C for 3.75 hours 239

5.11 Image projections through the 3-4 connective of the crayfish nerve cord as a function of spin-echo time 240

5.12 Transverse proton microsccpic NMR imaging of the 3-4 connective 241

6.1 $R_2$ vs. $R_1$ of three serum proteins in aqueous solution. 259

6.2 $R_2$ vs. $R_1$ for a model of edematous grey matter. 260

6.3 $R_2$ vs. $R_1$ for a model of edematous white matter using different edema fluids. 261

6.4 Induction of edema in Shioya's model of pulmonary edema. 262

## LIST OF SYMBOLS AND ABBREVIATIONS

| | |
|---|---|
| AQ | NMR signal acquisition time in a pulse sequence |
| $A_{(k)}$ | Functions of spin operators |
| $A_s$ | Surface area |
| ATP | Adenosine triPhosphate |
| BBB | Blood-Brain Barrier |
| $\mathbf{B}_1, \mathbf{B}_{rf}$ | Amplitude of RF pulse in magnetic field units (G) |
| c | concentration |
| CNS | Central Nervous System |
| CSF | Cerebrospinal Fluid |
| $C_e, C_i$ | Extra-, intracellular ion concentrations |
| $D_r$ | Rotational diffusion constant |
| ECF | Extracellular Fluid |
| F | Faraday constant |
| FID | Free induction decay |
| $F_{(k)}$ | Functions of spatial coordinates |
| FT | Fourier transform |
| $g_i$ | Molar sensitivity gradient of relaxation rate $R_i$ to solute |
| G | Gauss |
| $G_i$ | Sensitivity gradient of relaxation rate $R_i$ to solute concentration |
| $G_{(k)}$ | Correlation functions |
| $G_z$ | Magnetic field gradient in z direction |
| h | number of water molecules associated with a macromolecule |
| $H$ | Hamiltonian |
| H | Magnetic field |

| | |
|---|---|
| $H'$ | Perturbation Hamiltonian |
| $H_D$ | Dipolar Hamiltonian |
| $H_o$ | Static magnetic field |
| $H_{rf}$ | Radio frequency magnetic field |
| I | Spin quantum number |
| **I** | Spin angular momentum operator |
| id | Inner diameter |
| $I_x$, Iy, Iz | Spin operators |
| $J_{(k)}$ | Spectral density functions |
| k | Boltzman's constant |
| kD | kiloDalton |
| $L_p$ | Specific hydraulic conductance |
| **M** | Net magnetization vector |
| M | protein molecular weight, arbitrary magnetization, molarity |
| MW | Molecular Weight |
| $M_o$ | Equilibrium magnetization |
| $M_x$, $M_y$ | Transverse magnetization components |
| $M_z$ | Longitudinal magnetization |
| N | Number of spins |
| NMR | Nuclear Magnetic Resonance |
| NMRI | Nuclear Magnetic Resonance Imaging |
| NNLS | Non-negative least-squares |
| $N_{++}$, $N_{-+}$, | |
| $N_{+-}$, $N_{--}$ | Occupancies of energy eigenstates |
| $N_{aa}$, $N_{ab}$, | |

| | |
|---|---|
| $N_{ba}$, $N_{bb}$ | Occupancies of eigenstates |
| od | Outer diameter |
| $\langle p \rangle$ | Order parameter |
| P | Hydrostatic pressure |
| p-CMBS | p-chloromercuribenzene sulphonate |
| $p_i$ | population of compartment i |
| $p_{a,b,k}$ | True populations in the Zimmerman and Brittin model |
| $\dot{Q}$ | Net water flow |
| R | Rydberg constant |
| r,a | Radius |
| RBC | Red Blood Cell |
| RF | Radio Frequency |
| $R_i$ | Relaxation rate i = 1, 2, 1ρ |
| $R_1$ | Longitudinal relaxation rate |
| $R_{1\rho}$ | Longitudinal relaxation rate in the rotating frame |
| $R_2$ | Transverse relaxation rate |
| $R^2$ | Correlation coefficient |
| $S_{pm}$,$S_{ar}$ | Dipolar interaction strengths |
| T | Absolute temperature, Tesla |
| TR | Pulse sequence repetition time |
| $T_i$ | Relaxation time i = 1, 2, 1ρ |
| $T_1$ | Longitudinal relaxation time |
| $T_{1\rho}$ | Longitudinal relaxation time in the rotating frame |
| $T_2$ | Transverse relaxation time |

| | |
|---|---|
| $T_2^*$ | Time constant characterising decay of FID in an inhomogeneous static magnetic field |
| $u_i$ | Transition probabilies between eigenstates |
| $V$, $\Delta E_c$ | Membrane potential |
| $V_i$ | Volume of compartment i |
| $w_i$ | Transition probabilies between energy eigenstates |
| $Z$ | Ion valence |
| $\sigma$ | Protein reflection coefficient |
| $\sigma^2$ | Rigid lattice constant |
| $\tau(\text{lock})_\phi$ | Spin-locking pulse of duration $\tau$ and phase $\phi = \pm x$ or $\pm y$ |
| $\tau_c$, $\tau_{ar}$, $\tau_{pm}$ | Correlation times |
| $\gamma$ | Gyromagnetic ratio |
| $\phi$ | interstitial volume in ghost preparations |
| $\psi$, $P(\Omega)$ | Probability functions |
| $\mu$ | Magnetic moment |
| $\omega$ | angular frequency |
| $\omega_1$ | angular frequency of precession about the RF field. $\omega_1 = \gamma B_1$ |
| $\pi$ | Colloidal oncotic pressure |
| $\Pi$ | Fraction of buffer added in model tissue system |
| $\lambda^{\pm}$ | Observed populations in Zimmerman and Brittin model |
| $\chi$ | Order parameter |
| $\chi^2$ | Chi-squared statistic |
| $\chi_o$ | Static magnetic susceptibility |
| $\zeta$ | Sum of Debye spectral densities |
| $\xi$ | Fraction of buffer trapped during layering process |

| | |
|---|---|
| $\Omega$ | Orientation of a water molecule |
| $\Delta G$ | Change in Gibbs Free Energy |
| $\Delta z$ | slice thickness |
| $\Phi_i$, $R_i^{\pm}$ | Observed relaxation rates in Zimmerman and Brittin model |
| $\hbar$ | Planck's constant divided by $2\pi$ |
| $\eta$ | Viscosity |
| 2DFT | Two-dimensional Fourier Transform |
| $90_{\phi}$ | 90 degree pulse along ø axis, where ø is one of $\pm x$, $\pm y$ or $\pm z$ |
| $180_{\phi}$ | 180 degree pulse along ø axis, where ø is one of $\pm x$, $\pm y$ or $\pm z$ |

# CHAPTER 1

## Introduction

### 1.0 Introduction to the thesis

The nuclear magnetic resonance (NMR) properties of water in biological systems have been a problem of longstanding interest and debate (1-30) since the first applications of NMR to biology (31, 32). Important findings include the first suggestion that NMR relaxation times could be used to differentiate between normal and pathological tissue *in vitro* (33). More recently, the emergence of proton NMR imaging (NMRI) as a quantitatively specific in-vivo diagnostic modality has been hampered by the fact that the mechanisms governing proton relaxation in tissue are not well understood despite 35 years of intensive study. In particular, there is little ability to exploit the often observed multiple proton relaxation components in tissue for diagnostic purposes since the mechanism of the changes in the relaxation rates due to pathology are uncertain (17).

It is the overall aim of this study to increase our understanding of the mechanisms that give rise to water proton relaxation in tissue by analyzing the individual contributions of the various cellular and tissue structures. In heterogeneous systems such as tissue, which are composed of many cellular and macromolecular building blocks, the measured NMR observables (such as relaxation times) depend on the relative proportions of bulk water and water molecules associated with or adsorbed on macromolecular surfaces (34). Furthermore the relaxation rates are sensitive to the mobility of the macromolecular surfaces and the rate of water exchange between different tissue environments (1, 3, 4). By

understanding the individual contributions of the tissue architecture to proton relaxation, one can establish which NMR observables are most sensitive to (i) differences between tissue and (ii) pathological changes in tissue.

Attempts to further the understanding of the NMR properties of tissue have often consisted of *in-vitro* measurements of relaxation rates in aqueous protein solutions (1-8), in cell systems (9-13), in excised tissue (14-32) and occasionally *in vivo* (35). We have chosen to adopt a somewhat different approach to understanding tissue-water relaxation. By reasoning that tissue is made up of different components, all of which affect the NMR relaxation times, our strategy has been to understand the contributions of each individual component of the tissue architecture (e.g. protein or membranes) to the water-proton relaxation times. Once this was accomplished, we integrated the individual tissue components into simple model tissue systems. This "building-block approach" is extremely powerful since it allows one to increase the complexity of a model system in incremental stages so that the affect on the NMR observables due to each incremental change can be individually isolated and understood.

In order to quantify the motions of the macromolecular surfaces it was decided to do measurements of three different relaxation rates on the model systems, namely (i) the transverse relaxation rate, sensitive to very slow motions, (ii) the spin-lattice relaxation rate in the rotating frame, sensitive to motions in the range 10 to 100 kHz, and (iii) the spin-lattice relaxation rate, sensitive to motions around a Larmor frequency of 100 MHz. By applying relatively standard measurements with great care and using modern (36, 37) techniques for multiexponential signal

decomposition, one can extract significant information about the state of water in biological systems from the measured relaxation times.

Although the choice of models in this thesis is of general applicability to all tissue systems, we were motivated in particular to try to understand tissue in the edematous state. Several NMRI projects in this NMR facility are concerned with the delineation and characterization of cerebral and pulmonary edema. Similarly, a significant proportion of routine diagnostic NMRI examinations are concerned with the edematous condition (38). Considerable effort has gone into the development of exogenous contrast agents which, when injected, can aid in clarifying diagnosis in cerebral edema (39). It is our view, however, that this turns NMRI into an invasive technique and that it may be possible to obtain the same diagnostic information from the non-invasively acquired NMR relaxation times. Thus we chose to focus on modelling cerebral tissue and different types of cerebral edema as a potential application for the NMR techniques developed in this study.

The remainder of this chapter serves to identify the role of the various cellular and neuroanatomical structures in water homeostasis in brain in order to justify the choice of models made. As well, a theoretical framework for the relaxation rates is developed to show how one can extract information about the microscopic macromolecular dynamics and water exchange from the measured NMR observables. A little background on NMR applications to cerebral edema in animal models is given to show the difficulties involved in quantifying the condition.

The simplest possible model of a biological tissue or an edematous fluid is that of an aqueous solution of proteins. NMR relaxation measurements on serum proteins of various sizes are reported in Chapter 2. The next stage in building a

model of tissue is to incorporate intact membranes (pseudo-cells) into a protein solution and to investigate the effects on the water proton relaxation rates of (i) the membrane, (ii) the protein-membrane interactions, and (iii) compartmentalization. Such a study is described in Chapter 3, where the relaxation time data are analysed using two different techniques for multiexponential decomposition of the NMR signal to show that the measured trends are not artifacts of the analysis. In Chapter 4 a critical evaluation of the use of continuous relaxation time distributions is made to see if such distributions do indeed reflect the true nature of the relaxation time distribution in model systems. We then further investigate the application of continuous distributions to *in-vitro* relaxation time measurements made on cat grey and white matter that are not easily characterized by conventional techniques. Using the information gathered in Chapters 2 through 4, we proceed to test several hypotheses on a considerably more complex model of brain, namely the excised abdominal segments of the crayfish nerve cord. An attempt was also made to reconcile the transverse relaxation times measured on the bulk nerve cord with the results from an NMR microscopic imaging study on the same cord to demonstrate the potential application of relaxation techniques to clinical NMRI. These studies on the crayfish model are presented in Chapter 5.

It should be pointed out that the present studies are not an exhaustive relaxation study of any one system. Instead, we examine selected aspects of the relaxation in a variety of model tissue systems in an attempt to establish the importance of the contributions of the individual cellular constituents and their motions to proton relaxation *in vivo*. A complete consideration of each system would be a major undertaking on its own, a fact which immediately suggests paths for

future work. These various studies are related to one another in Chapter 6, where the relevance of the individual studies to the goals of the thesis is reviewed.

## 1.1 Water Homeostasis in the Brain

Water is the essential milieu for life as we know it. Current thinking suggests that life began in the primordial soup of the earth's oceans or perhaps even a puddle. Water is the essential component that allows the cellular subsystems in a complex organism such as man to communicate and exchange with one another. In man, total body water makes up 60 % of the lean body weight subdivided into 20 % being extracellular and 40 % being intracellular. Of the extracellular, roughly 4% composes the blood while the remaining 16 % is in the interstitial spaces. These fluid compartments are separated by epithelial cells, whose job it is to maintain fluid and electrolyte balance between compartments. The water regulation properties of the epithelial cells arise from the properties of the membranes from which they are made (40).

In order to separate themselves from the hostile environment, the first unicellular lifeforms are believed to have evolved a plasma membrane, within which they developed mechanisms to control and regulate the intracellular conditions, a concept known as homeostasis. The membrane does not isolate the cell completely from its external environment. Instead, it allows the highly controlled exchange of water, ions and macromolecules across itself. Some molecules may traverse the membrane with or without aid from transporters in the membrane, while others are not allowed to pass at all. This selective sieving property is probably the most important function of the plasma membrane.

Occasionally, cells separating the major fluid compartments may be damaged by disease or trauma. If this happens, homeostasis in a particular organ or region may be lost, often resulting in death to the animal. A particularly dangerous breakdown of fluid regulation occurs in the various types of cerebral edema. Cerebral edema, like many neurological problems, lends itself to qualitative study and diagnosis by proton magnetic resonance imaging, but as with all NMRI studies, the results are difficult to quantify (38).

It is, however, well known that the motion of such macromolecules as proteins and lipids play an important role in proton relaxation of tissue water and that membranes play a large part in controlling water exchange in and out of cells. The main goal of this thesis was to do NMR relaxation measurements on simple biological models of brain tissue in which fluid compartments and membrane barriers could be manipulated in a controlled and straightforward manner. When making an initial foray into modelling a complex biological system such as brain, the obvious path seems to be to try to mimic the structural aspects before attempting to make a functional model. The models produced for this thesis are thus oriented to structurally modelling brain tissue. Section 1.2 presents some of the gross anatomical and functional features of neuronal systems which may affect the development of an NMR model for nervous tissue as well as help in the interpretation of results in Chapters 2 to 5. A rudimentary background on cerebral edema is presented in section 1.5.

## 1.2 Neuronal Structure

The function of a neuron is to generate an electrical impulse in response to a mechanical, chemical or electrical stimulus; then to transmit that electrical impulse through some distance and, finally, to turn that transmitted electrical impulse into a chemical signal. The chemical that is released is called a neurotransmitter; its subsequent action may be local (e.g., by starting another electrical impulse in an adjacent neuron) or distant (e.g., released into the extracellular fluid to interact with receptors at distant target sites). Neurons do not function in the brain on their own. The other major components of nervous tissue, the glial cells, are discussed in section 1.2.4. Most of the application of this section is found in the discussion of the crayfish central nervous system in Chapter 5.

All neurons found in animals have the same three basic functions discussed above. And they all share the same three fundamental structural features that enable them to accomplish their goals (41-46). These are discussed with reference to Figure 1.1. The cell body or perikaryon contains the cytoplasm and includes most of the metabolic machinery of the nerve cell. The cytoplasm contains a large amount of endoplasmic reticulum in addition to a usually spherical nucleus with one or more dense nucleoli. The mitochondria consist of long, threadlike structures which can be seen to undulate in time-lapse photomicrography. Lysosomes are also found in neuronal cytoplasm and probably serve the same digestive and degrading purposes as in other cells. In addition, vacuoles used for endocytosis and pinocytosis can be found in the perikaryon region. For functional information on these structures, the reader is referred to the standard textbooks (44-46). The important feature from the

point of view of this thesis is that the cytoplasmic structures mentioned so far are all composed of membranes that separate their internal contents from the cytoplasm.

The ability of a neuron to generate synaptic and action potentials is a consequence of the special properties of its membrane. Typically, only 5 to 10 % of the surface area of a neuron is made up of the cell body membrane; this is an important consideration in designing models of neural systems. The remainder of the surface area is in the dendrites and axons emanating from the cell body, which provides the maximal area for making synaptic contacts with other cells. It is through these synapses that information is transmitted from one neuron to the next.

The axon emerges from the perikaryon in a structurally distinct pattern, in which the somewhat haphazard arrangement of filamentous cytoplasmic protein structures (neurotubules, neurofilaments and microfilaments; section 1.2.2) changes to an essentially uniform and parallel distribution of protein strands. The specialized membrane of the axon is known as the axolemma and both it and the contents of the axoplasm are relatively uniform in morphology except at the Nodes of Ranvier (in myelinated axons) and the nerve terminals. The dominant membranous objects in the axoplasm are the mitochondria and synaptic vesicles, the latter occurring only in the terminal portion of the axon, known as the presynaptic junction. The electrical impulse that propagates down the axon causes fusing of these vesicles with the synaptic membrane and release of their neurotransmitter contents into the extracellular space or synaptic cleft.

Dendrites rarely contain neurofilaments, which aids in their identification under the electron microscope. They usually exist in a branched structure extending from the perikaryon and in some instances exceed 40 % of the nerve cell's membrane

area. Axon terminals typically abut the synaptic regions of dendrites. The nature of the different types of synapses can be found elsewhere. The dendrites perform an afferent or integrative function, by receiving inputs from many different axons. These inputs can be excitatory or inhibitory; depending upon their spatial-temporal summation, an action potential can be transmitted down the axon to the presynaptic (or efferent) regions.

Perhaps it is worthwhile to note that no cytoplasmic or membrane inclusions truly distinguish a neuron from any other cell. All structures of nerve cell can be found in other cells, which aids in picking a model for them. In fact, much of what is known about other cells was first studied in nerve cells.

### 1.2.1 Membrane Structure

It should be apparent by this point that the single most critical cellular structure is the plasma membrane. Its integrity allows biochemical reactions to proceed in a controlled environment and its disruption results in certain cell death. Furthermore, water exchange across cell membranes is a major factor in trying to understand tissue water proton relaxation mechanisms. The understanding of how water exchange is modified during pathology such as cerebral edema could provide a clue towards exploiting NMRI for quantitative diagnosis.

#### 1.2.1.1 Membrane Lipids

Our concept of the membrane has improved over the past twenty years. It is now viewed as a lipid sea in which hydrophobic proteins diffuse around (47-50). Phospholipids are the major component of most cell membranes. They consist of a polar head group and a nonpolar tail made of two chains of esterified fatty acids. The

head group is typically a negatively charged glycerphosphoryl ester. Short oligosaccharide chains (complex sugar molecule sequences) are often covalently bound to the head group, forming glycolipids. These oligosaccharides play an important role in cell-cell and cell-protein interactions. In water, at physiological pH and ion concentrations, the phospholipids form the bilayer structure of Figure 1.2 in which the hydrophobic tail segments are shielded from the water by the polar headgroups (47, 50). To function as designed, cell membrane bilayers must be in the liquid crystalline state. This allows high mobility of the phospholipids in the bilayer plane although flipping between layers has an exceedingly low probability of occurrence. The lack of such "flip-flop" activity allows the cell membrane to maintain a different lipid composition on either side of the bilayer.

Much of what is known about membrane structure comes from the study of the red blood cell (RBC), due to its high yield and easy availability. The lipid bilayer of the RBC is known to be asymmetric with phosphatidylcholine and sphingomyelin being found only on the outside while phosphatidylethanolomine is usually found on the inside (52, 53). The significance of this is not known, nor is it established that such a difference exists in nerve cells, although there are indications that myelin is arranged there in a similar fashion (42).The fatty acid chains of the membrane phospholipids are typically limited in length and usually have one double bond. The most abundant lipid in animal membranes is cholesterol, a very rigid, planar, hydrophobic structure that tends to absorb fatty acid chains onto its surface. This restricts membrane fluidity. Typically the outer membrane has twice as much cholesterol incorporated in its structure, suggesting that it is more rigid than the inner membrane.

Finally, there is considerable evidence that in the case of integral membrane proteins, there exists an annulus of certain lipids that surround these proteins. Some work suggests that 20 to 90 % of all membrane lipid may be specifically associated in this fashion (54).

### 1.2.1.2 Membrane Proteins

As mentioned above, the RBC membrane has been highly characterized. Hence this discussion will concentrate on the structures of the RBC that could influence tissue water proton relaxation with references to known equivalent structures in the nerve cell (52-55). Most structural features in the RBC have analogues in nerve cells, which makes the RBC useful as a first order structural model of nerve.

A typical plasma membrane contains 50 % protein by weight. Several of these proteins are known in structural detail. From the point of view of NMR relaxation studies of water protons in brain, the important determinants are macromolecular surfaces. The macromolecular surfaces found in tissue are those of membrane and protein. Protein may be found in cellular solution, as part of the intra- and extracellular architecture and as membrane-associated stuctures. Proteins in membrane may associate with the membrane as shown in Figure 1.2 via a direct incorporation in the bilayer or by associating with specific sites on integral proteins. Glycophorin A is one of several glycoproteins that constitute the type 1 integral proteins of the RBC membrane. These proteins function as ion pumps and channels and fully span the membrane. Glycophorin A has 60 % of its molecular weight (MW) in the form of carbohydrate residues that extend outwards from the RBC

membrane. In nerve, well characterized type 1 integral proteins include the acetylcholine receptor, the voltage sensitive sodium channel and the sodium-potassium pump ($Na^+K^+$ ATPase protein). Ionic currents through the sodium channel are responsible for action potentials while the ionic gradient that exists across cell membranes is maintained by the sodium-potassium pump (53).

Peripheral proteins (42, 55) are linked by ionic binding with either surface of the membrane and can easily be removed with salt solutions. As much as 30 % of the RBC membrane proteins may be associated in this manner. Spectrin is a well characterized two-subunit protein (MW 240 kD and 220 kD) which forms a scaffold-like structure on the inside of the RBC membrane. Spectrin attaches to the inner membrane via another peripheral protein, ankyrin, which in turn is bound to the membrane by the so called Band III transmembrane integral protein. This arrangement must be to prevent the diffusion of the Band III protein (which is an ion channel) in the plane of the bilayer. Spectrin and ankyrin analogues are known to exist in nerve cell bodies, where they probably serve the same cytoskeletal function. In axons, the spectrin analogue is fodrin, which constitutes 3 % of the total protein in brain. It is also found in the cell bodies and in both cases probably attaches to an ankyrin-like transmembrane integral protein. Fodrin is transported in axons, and is suspected of playing a role in axon growth.

One last note about integral membrane proteins: it is now ascertained that they may travel as far as 0.05 to 2 μm per second in the bilayer (42). This suggests a dynamic picture of protein movement even when they are incorporated into membranes. Anchored proteins such as the anion channel do not diffuse nearly so fast but the rotation about an axis normal to the bilayer is almost as fast as in free

water. These protein motions have important implications for water proton relaxation in tissue, because large amounts of the macromolecular surface can move in apparently stationary objects such as cells. For example, in Chapter 3 it is shown that albumin can bind to the RBC cell surface, but that its motion is not significantly restricted.

#### 1.2.1.3 Water Transport across the Membrane

For a molecule to enter or exit the cell it must cross the combination lipid-bilayer-protein complex. The lipids are always fluid, in that, while their headgroups may pack tightly together, the fatty acid tails are very flexible. For a molecule to cross a bilayer, it must pass through this hydrophobic region. Any molecule must break all its bonds with the aqueous environment in order to cross a hydrophobic region. Thus a charged group such as an ion, which is usually surrounded by a hydration shell of water, will not be energetically predisposed to cross the barrier. Likewise, larger metabolites which invariably contain associated water molecules on their hydrophillic regions will seldom pass through the bilayer.

Water transport studies can be done by measuring the efflux of radiolabelled or "NMR labelled" water from the cell over time. The decay of the amount of labelled water in the cell is described by a first-order rate constant whose inverse is defined as the average lifetime of the water molecules in the cell. Such tracer and NMR studies show that the average lifetime of a water molecule in a human RBC or RBC ghost is 7 to 20 ms at 25 °C (56 and references therein). This is very short, considering that the water must cross the hydrophilic region of the bilayer. In fact membrane permeability to water appears to be two orders of magnitude greater than

would be expected for a membrane with a simple bimolecular structure. This has led to the postulation of aqueous channels or pores in the membrane.

A membrane protein has been suggested as a primary route for water entrance into the human RBC (56). It has been known for 25 years that water moves across the RBC membrane much faster under an osmotic gradient than by diffusion (52, 53). Osmotic flow through a channel is a forced (hydraulic) movement, which of course would be more efficient at moving water molecules than random diffusion. When human RBC's are treated with p-chloromercuribenzene sulphonate (p-CMBS is a sulphydyl-reactive agent that crosslinks proteins, rendering them unfunctional), osmotic permeability is suppressed, by 90 % and diffusional permeability by 50 %. If the proposed channels are thus closed by p-CMBS the basal water diffusion must be through the bilayer (58). Radiolabelled p-CMBS, under conditions where water permeability is suppressed, has been found bound to band 3 and band 4.5 proteins that could be associated with the water channels. It has been suggested that the channels are formed between 2 subunits of a band 3 dimer or at the center of a tetramer of band 3 monomers (59 to 61). However, the features and identity of the channel are still in much debate. Diffusion through the hydrophobic bilayer may occur by the opening of transient pores or kinks in the continually moving lipids. One odd feature of the RBC membrane is that, under an osmotic force, water efflux is 35 % slower than water influx, a property of the membrane known as rectification (58-62). Details of water transport across neurons is not understood either, but is expected to be similar to the RBC membrane in most instances.

### 1.2.1.4 Volume Regulation in Cells

Cells have developed a large number of mechanisms to preserve internal homeostasis, many of which involve the active transport of ions and small molecules. Although none of the neural models developed in this thesis deal with active (pumps that use metabolic energy) transport of ions from one side of the membrane to another, it is appropriate to describe how cells control the flux of ions across their membranes *in-vivo* because "active" water movement across the cell membrane occurs only in conjuction with ion transport or flux. From the discussion it will be seen that water movement across a cell in steady-state osmotic equilibrium with the extracellular space is by diffusion. That is, under conditions of homeostasis, there is no net coupled water transport.

Cells store potential energy in the form of transmembrane ion gradients. This potential energy is used for adenosine triphosphate (ATP) synthesis, recovery of nutrients and metabolites, regulation of intracellular pH and the generation and propagation of action potentials. The Gibbs free energy $\Delta G$ associated with an electrical potential across a membrane is

$$\Delta G = ZFV \qquad (1.1)$$

where Z is the valence of the ion, F the Faraday constant (98324 J $V^{-1}$ $mol^{-1}$) and V the transmembrane potential difference (42). The free energy associated with a concentration difference of an ion across the membrane is

$$\Delta G = RT \ln ([C_e]/[C_i]) \qquad (1.2)$$

where R = 8.33 J $K^{-1}$, T is the absolute temperature in Kelvin, $[C_e]$ is the extracellular concentration of the ion and $[C_i]$ is its intracellular concentration. The

free energy change from moving one mole of solute across a membrane that has an electrochemical gradient across it is

$$\Delta G = RT \ln ([C_e]/[C_i]) + ZFV. \qquad (1.3)$$

If $\Delta G$ is not equal to zero for a transport process it means that work must be done by something to maintain a steady-state. Protein channels in membranes allow passive diffusion of ions and molecules down the prevailing electrochemical gradients. All known active transport proteins in animals transport cations: $Na^+$, $H^+$, $K^+$ and $Ca^+$. The transport of anions is usually electrochemically coupled to the cations via ion channels and does not directly require energy. The channels or ports are selective on the basis of solute size and charge.

The membrane potential reached in a system with only one permeant ion is called the Nernst potential for that ion. For a semipermeable membrane the ion will diffuse down its concentration gradient generating a membrane potential, $\Delta E_c$, until the free energy change caused by the concentration difference equals the free energy change due to the generation of the membrane potential. This corresponds to $\Delta G = 0$ in Equation 1.3 which can then be rewritten as the Nernst equation for practical use as

$$\Delta E_c = (58 \text{ mV}/Z) \log ([C_e]/[C_i]). \qquad (1.4)$$

The typical plasma membrane is found to be primarily permeable to $K^+$ and $Cl^-$ so that the resting membrane potential is close to the Nernst potential for these ions. However, it is found that, *in vivo* $Na^+$ concentrations are not distributed according to this model because the cell actively extrudes $Na^+$ using the $Na^+K^+$ ATPase ion pump. Since the sodium concentration is not that expected on the basis

of $\Delta G = 0$, the extrusion process must consume energy. As well, since the potassium Nernst potential is somewhat less than the actual cell membrane potential, some $K^+$ tends to leak out down its concentration gradient. The pump helps preserve the membrane potential by pumping 3 $Na^+$ out and 2 $K^+$ in. This serves to hyperpolarize the membrane, but is not the primary cause of the membrane potential: the resting membrane potential is due to the selective permeability of the membrane as discussed above.

Cells have evolved several major mechanisms for maintaining cell volume constant. These are outlined in Figure 1.3. The double-Donnan hypothesis suggests that, to avoid swelling, cells extrude $Na^+$. To see why this may be, consider what would happen if the cell ran out of ATP. Sodium would flow down its electrochemical gradient. Since sodium is positive, $Cl^-$ would leak in too to keep the charge on both sides of the membrane conserved, since this results in the most energetically favorable situation according to Equation 1.3. As ions flow into the cell, water does too, driven by osmotic pressure, and the cell swells and eventually lyses. This is a simple-minded model of what happens in cytotoxic edema caused by deranged cellular metabolism. Utilizing the various pumps and channels, the cell can move ions about (Figure 1.3) in response to hypotonic or hypertonic conditions. Also, net water movement across the membrane occurs not as an active process, but as an osmotically coupled process.

### 1.2.2 Myelin Membranes

While the motion of proteins may be an important determinant of the proton relaxation of water in tissue, membranes, which control the rate of exchange of water molecules between cells and their environment, are also important. It appears that a

normal plasma membrane does not provide much of a barrier to water diffusion. However, the white matter of the nervous system consists of axons wrapped in many layers of a fatty membrane known as myelin (41, 42). The major function of myelin is to insulate the axon electrically so that action potentials can propagate only between nodes ( Figure 1.1). This speeds up the rate of impulse transmission in a nerve considerably. As a consequence of the lamellar structure of the myelin, water diffusion between a myelinated axon and the extracellular space is significantly slowed.

Myelination is accomplished by specialized glial cells in the nervous system, known as oligodendrocytes and Schwann cells. In the central nervous system, oligodendroglia wrap extensions of their membrane about one or more axons. In the peripheral nervous system a similar function is performed by the Schwann cells except that in this case the Schwann cell only myelinates one node of a single axon. Despite this difference between myelination in the central and peripheral nervous systems, the net effect on water transport into or out of an myelinated axon is the same. In the particular model of nervous tissue we have chosen in Chapter 5 (crayfish abdominal nerve segments), the myelination is carried out by Schwann cells. Their cytoplasm is rich in the usual cellular organelles but, the Schwann cell is also rich in filaments and microtubules unlike the oligodendrocytes. In disease, Schwann cells are remarkably good at phagocytosing damaged myelin and replacing it; this does not happen in the central nervous system. The process of myelination is not important for this thesis; only the composition and organization of the membrane are relevant to water diffusion.

The composition of myelin is very different from the membrane of the cell that lays it down. Myelin contains far more lipid than normal membranes and its lipid composition is unique. The myelin membrane seems to be in a liquid crystal state *in vivo*, with its fluidity and permeability controlled by cholesterol. Only 30 % of the dry weight of myelin is protein (the rest being lipid) and almost 80 % of this protein is in either basic protein or proteolipid protein, the latter being very hydrophobic. In contrast, typical plasma membranes have only 50 % lipid by weight. Myelin proteolipid has an MW of 23.5 kD and appears to be a 3.8 nm sphere spanning the membrane. Myelin basic protein appears to be a protein of MW 18.5 kD which forms a dimer with a random coil configuration in the membrane. The protein is highly positively charged and is probably responsible for gluing the multiple layers of myelin together.

The resistive properties of myelin membranes are really not different from those of other membranes. The high insulation property stems from the compaction of the myelin layers, which exclude extracellular fluid very well. In peripheral nerves, glial cell cytoplasmic inclusions in the myelin, known as Schmidt-Lantermann clefts, can occur, which prevent complete packing of the myelin layers. Regardless, multiple myelin layers around an axon must present typically a 50-fold decrease in water permeability into or out of an axon.

### 1.2.3 Protein Structures in Neural Cells

Having discussed the plasma membrane and its associated proteins at some length, it is now necessary to consider the protein structures that exist within the volume bounded by the membrane. This is because it appears that proteins are the

primary determinants of water proton relaxation in tissue and hence must be incorporated in any model of tissue. As is shown in Chapter 2, the water proton relaxation times are sensitive to the size and shape of proteins, so we must investigate the nature of these proteins in nervous tissue. The average protein content in human white matter is 390 mg/g dry weight of tissue, while in gray matter it is 553 mg/g. Roughly 30 % of this protein is considered soluble, the rest is structurally associated in some way. The remainder of the dry tissue mass is made from lipid.

Both glial cells and neural cells have cytoplasmic structures that give mechanical strength to the cells. This support is provided by thin, rod-like strands made of protein, which are found in many cell types (41, 42). The specialized structures are known as neurotubules, neurofilaments and microfilaments (Figure 1.1). Neurotubules are tubular organelles made of 13 filaments each of diameter 5 nm, which line the periphery of a central empty cavity of 14 nm diameter. The filaments run roughly parallel within axons, with occasional short branches. They are made almost exclusively of tubulin (MW 120 kD). In addition to conferring strength, neurotubules have been implicated in axoplasmic transport and in the fluidity of cell membranes, the latter property arising from the neurotubules anchoring certain integral membrane proteins.

Neurofilaments are a fibrous cytoplasmic protein complex about 10 nm in diameter. They are found in all parts of neurons, usually intertwined in rope-like arrangements that run the full length of the axonal process, and are found in greatest densities in large-diameter axons. In brain, the filaments are made from triplets of MW 68 kD, 150 kD and 200 kD. Morphologically similar units are found in glial cells. In neither case is their complete function known.

Another class of fibrous organelles is known as microfilaments, due to their small (5 nm) sizes. They are composed of actin and appear to interact with the headgroup of myosin to produce contractile activity. They are randomly oriented in nerve cells but appear to be concentrated at growing axonal tips, with concentrations as high as 200 g/l.

### 1.2.4 Glial Structures

Glial cells can make up 50 % of the volume in brain and are thus a significant when modelling nervous tissue space (41-46). Glial cells (literally "glue cells") are responsible for numerous functions in nervous tissue; current ideas include: (i) trophic support of neurons, (ii) production of the myelin sheath and associated insulating qualities, (iii) rapid inactivation of neurotransmitters released by neurons, (iv) repair of brain tissue after trauma, (v) phagocytosis, (vi) formation of the blood-brain barrier and (vii) control of ion levels in the extracellular space. Of these, only items (i), (ii) and (vi) are relevant to the first order to water diffusion in brain, and (vii) to the second order.

Glial cells share just about every structure discussed with reference to the nerve cell or RBC, which suggests that the RBC model discussed in Chapter 3 can be used for glial cells as well. The largest glial cells are the astrocytes, which are star-shaped and typically 10 to 40 μm in diameter. Astrocytes are rich in neurofibrillar structures but are subdivided into two rather misleading categories: protoplasmic astrocytes, which constitute a large fraction of volume in grey matter, and fibrous astrocytes, which are found in white matter. Astrocytes and their foot processes (which swell into structures known as end feet) abut the blood capillaries, leaving

only small gaps (10 to 20 nm) for the diffusion of substances out of the capillaries and into the extracellular space of brain.

A smaller group of glia (5 μm in diameter) are the oligodendrocytes; they contain a large nucleus and most other cellular organelles, but not gliofilaments. In white matter some are responsible for myelination, while in grey matter they are associated with the neuron cell bodies. An oligodendrocyte can easily produce 3000 times its own surface area in myelin.

Microglia are the smallest glial cells. They have small elongated nuclei, very little cytoplasm and are rarely larger than 2 to 3 μm in diameter. Microglia seem to serve the same role as macrophages do in the rest of the body; that is, they respond to inflammation by migrating to the injured area and actively phagocytosing cellular debris.

Schwann cells are the major cell component in peripheral nerve. In addition to laying down myelin and sustaining the myelin sheaths, they form deep furrows in which nonmyelinated axons often lie. In ganglia, layers of satellite glial cells lie between the wall of the ganglion and the synapsing nerve cells. Finally, there are several groups of ependymal cells that line many cavities of the brain and spinal cord (e.g., cerebral ventricles).

A schematic summary of the various glial cells is found in Figure 1.4.

### 1.2.5 Neuron-Glial Cell Relationships

Neurons are continuosly producing toxic waste in the form of ions, neuro-transmitters and especially potassium during extended neural activity. Since the

extracellular space is small, the concentration of these and other metabolic byproducts could easily interfere with neuronal function. The glial network forms a very efficient fluid filter and absorption system that removes these byproducts as well as providing metabolic substrates. The glial system presents a large ratio of glial surface area to extracellular volume, and the glial membranes are capable of absorbing many substances.

### 1.2.5.1 The Blood-Brain Barrier

For a long time it was thought that, because astrocytes envelop 90 % of the blood capillary surface area in brain, this was the site of the blood-brain barrier (BBB). We now know (41-46, 63) that substances that enter brain tissue via the blood capillaries are forced to diffuse through a tortuous route between glial cells, where specific transport mechanisms remove them from the extracellular fluid (ECF) before they get far enough into the tissue to encounter neurons. Thus, substances that are selectively transported into the ECF via the endothelial lining of the blood capillaries are further selected by the glial filter system.

The ependymal cells also allow diffusional entry of molecules at least as large as albumin (MW 69 kD). Large molecules will penetrate into the brain ECF from the cerebrospinal fluid (CSF) in the ventricles, despite the presence of tight junctions between the ependymal cells. These cells are thus not the site of the BBB either and it is well accepted that the cerebral extracellular space communicates freely with the CSF.

The dominant restriction on the entry of ions and molecules into the brain is due to the tightly apposed endothelial cells of the blood vessel walls (Figure 1.4)

which have overlapping tight junctions. In addition, a complete sheath of basement membrane also envelops the blood capillaries. Many substances, such as glucose, that are normally too large to diffuse across the BBB, are transported across it. In general the entry of polar substances is rare while nonpolar substances may cross. Pinocytosis can also account for some protein crossing the BBB.

Volume regulation in the brain is best appreciated by considering Starling's hypothesis of transcapillary water exchange (64). Starling postulated that the driving force for water flow across a cell membrane is given by the net osmotic and hydrostatic pressure across the cell membrane as well as the permeability of the membrane to proteins. This can be stated mathematically as

$$Q = LA_S [ (P_{cap}-P_{is}) - \sigma (\pi_{cap} - \pi_{is}) ] \qquad (1.5)$$

where,

Q = net flow of water across capillary (ml/min mmHg $cm^2$)

L = specific hydraulic conductance (ml/min)

$A_S$ = surface area ($cm^2$)

P = Hydrostatic pressure (mmHg)

$\sigma$ = protein reflection coefficient

$\pi$ = protein generated or colloidal oncotic pressure (mmHg)

and the subscripts "cap" and "is" refer to the capillaries and interstitial space respectively.

Let us see how the individual terms influence water flow to the brain. In normal brain there is very little hydrostatic pressure difference between the capillary and the interstitial space. The actual pressure provided by the heart is counteracted by the extremely high colloidal oncotic pressure driving water back into the capillaries. This arises from the low permeability of the brain capillaries to protein. Thus the low hydraulic conductance of the BBB and the high osmotic activity of the blood solutes are the opposing forces in regulating fluid volume in the normal brain.

In tissue, hydraulic resistance is defined as the impedance offered to the fluid flow by tissue. Tissue compliance is an indication of the "give" of the cellular constituents in brain under hydraulic pressure. In normal brain, hydraulic resistance is very high due to the glial cells and the small extracellular space. The interstitial fluid flows into the cerebral ventricles and Virchow-Robin spaces, where the osmotic and hydraulic pressures are very low and returns to the circulation via the arachnoid villi. This completes the picture of static homeostasis in the brain.

Under dynamic conditions, the impermeability of the BBB to large molecules and non-electrolytic solutes counteracts changes in the capillary hydrostatic pressure that would normally force fluid out of the vascular space. This works as follows; the solute-poor fluid that is forced out by an increase in capillary hydrostatic pressure further dilutes the interstitial fluid and increases the osmotic force, which then drives the fluid back into the vasculature. Furthermore, the low tissue compliance in brain (more so in grey matter) limits the accumulation of fluid in the extracellular space, due to the marked increases in hydrostatic and osmotic pressures that result from small interstitial volume increases.

### 1.2.5.2 Extracellular Space in Brain

What is the exact nature of the interstitial (extracellular) space in brain ? Two decades of study suggest that 12 to 25 % is the maximum volume of extracellular space in grey or white matter and in many invertebrate nervous systems. This space is not well characterized in white matter. Compared to grey matter, white matter has a lower water content (70 vs 82 % wet weight), a higher lipid content (16.5 vs 6 % wet weight) but a similar protein content (roughly 10 %). If the contribution of the myelin is excluded, grey and white matter are almost identical in composition; the major difference in protein, lipid and water content between grey and white matter would appear to arise from the 25 % volume fraction of myelin in white matter (41-46).

## 1.3 Introduction to NMR Studies of Water in Biological Systems

Independent experiments by the groups of Bloch and of Purcell led to the discovery of NMR in 1946 (65, 66). However, it was not until the middle of the next decade that the technique was first used to study biological systems in detail (31-32). Since those first measurements, NMR measurements of relaxation times in biological systems have concentrated on water because of the relative ease with which it can be studied as well as the historical importance and controversy over the nature of water in biological systems (28, 29). Since diseases that produce cerebral edema involve the redistribution of water, proteins and ions between cellular and tissue compartments, it seems worthwhile to investigate whether NMR can be used to detect and localize these changes *in vivo*.

The power of NMR for studying water in biological systems arises from the strong sensitivity of the NMR relaxation times to the motional dynamics of the water molecules. Biological macromolecules impose a constraint on the water molecules due to the weak water-macromolecule interactions and this constraint is reflected in NMR measured quantities. As a result, all microscopic surfaces in biological systems can support a loosely defined hydration layer in solution. The water behavior in this hydration layer has been the subject of much study using different techniques, including NMR. However, interpretation of the NMR water proton relaxation times requires a model of the molecular dynamics of the macromolecular surface and the hydration water, as well as a knowledge of the exchange characteristics between free and hydration water.

It was twenty years ago when the first careful NMR relaxation time measurements of water in tissue showed that the behavior of the NMR signal deviated from that of pure water (13). The measurements showed that several ensembles of water existed in tissue, each with a different relaxation time. The multicomponent nature of the NMR signal is still not widely observed, acknowledged or carefully analysed, and the mechanisms giving rise to it remain elusive (16, 28, 29, 37, 67). Considerable evidence now exists that multiexponential relaxation decays in tissue may be due to the compartmentalization that exists in heterogeneous tissue (9, 14, 17, 20, 22, 25, 30, 31). Compartmentalization in biological systems has a somewhat vague definition (28, 29), depending very much upon the model that is used to explain the NMR results. Defining compartmentalization in terms of boundaries (e.g. cell membranes) is too restrictive when discussing a technique such as NMR. NMR detects populations of molecules with particular properties (e.g., a

given relaxation time), and evidence for compartmentalization of a water molecule is obtained by showing that it exists in two or more distinct populations which may or may not be in exchange.

Water compartmentalization exists at many different levels in tissue. Hydration water versus free water is one such natural division. Nuclear versus cytoplasmic water is another. The most commonly postulated but rarely demonstrated division used to explain NMR results is that between extracellular and intracellular water (10-14, 17, 20, 22, 23, 26, 28-30). Depending on the rate of water diffusion or exchange between microscopic environments, the dimensions of "NMR detectable" compartments can range from 10 μm to 1000 μm. The scope of this thesis is limited to compartmentalization at the intracellular level, since NMR is sensitive to changes in the cellular milieu and to exchange effects.

Tissue systems can be interpreted in terms of the schematic in Figure 1.5. For example, aqueous suspensions of RBC ghosts can be interpreted in terms of Figure 1.5(A) in which "a" represents intracellular water in an RBC and "f" represents extracellular water. Packed preparations of ghosts can be interpreted in terms of a model such as in Figure 1.5(B). In a schematic of a nerve cord such as Figure 1.5(C), intracellular water from inside the differently sized axons ,"b" and "c", must cross the myelinated axon's barrier, the extracellular space compartment "d" and the endothelial layers of the sheath "e" in order to exchange with the perfusing medium "f". Often, heterogeneity in the spaces "a", "b",..."f" will be ignored to simplify the models. Compartmentalization on a larger level (e.g., delineating grey vs white matter) can be examined using NMRI as outlined in section 1.4.

The remainder of this section (1.3) introduces the physical concepts governing relaxation in heterogeneous systems. It shows how fluctuations in the motion of a water molecule can effect the observed relaxation times and it outlines the derivation of the usual expressions that are used in the interpretation of data in subsequent chapters. The outlining of expressions for the relaxation follows the less-often used, but perhaps more intuitive treatment by Solomon (75). For an introduction to NMR, one is referred to the classic textbooks in the field (68-72).

### 1.3.1 The Macroscopic Magnetization

In a typical pulsed spectrometer, one measures the response of a system of nuclear magnetic dipoles, each characterized by a magnetic moment $\boldsymbol{\mu} = \gamma\hbar\mathbf{I}$ to an externally applied magnetic field $\mathbf{B}(t) = \mathbf{B}_0+\mathbf{B}_{rf}(t)$. $\mathbf{I}$ is known as the spin angular momentum operator or "spin", $\gamma$ is the unique gyromagnetic ratio for a particular nuclear species and $\hbar$ is Planck's constant divided by $2\pi$. The external field is characterized by a uniform static component $\mathbf{B}_0$ defining the z direction of a right - handed Cartesian reference frame, and a component rotating counterclockwise in the xy plane. This rotating magnetic field, $\mathbf{B}_{rf}$, is applied using the magnetic component of a circularly polarized radio frequency field. $\mathbf{B}_{rf}$ (also commonly denoted $\mathbf{B}_1$) is generally much smaller than $\mathbf{B}_0$ and can be considered as a perturbation of the main static (or Zeeman) field. Details of how an NMR spectrometer is set up and run can be found in several books (72, 73).

In the presence of a static magnetic field, there are 2I+1 available Zeeman energy levels for a nucleus of spin I. Thus, for spin 1/2 nuclei, such as protons, there are two possible Zeeman energy levels and the excess of spins in the lower

energy state leads to a net macroscopic magnetization oriented parallel to the static field. This excess arises as follows. From statistical mechanics, it is known that if a given energy E is distributed between N identical spins at temperature T, each with individual energy levels, then the most probable occupancy among the states will be a Boltzmann one. The spectrum of states corresponding to the different motional and vibrational degrees of freedom of the ensemble is also characterized by a Boltzmann distribution and hence a unique temperature. This collection of states is known as the "lattice". For a nuclear spin system of N spins in thermal equilibrium, the net magnetization, $M_o$, is given to first order by

$$M_o = N\gamma^2\hbar^2 I(I+1)H_o / 3kT = \chi_o H_o \qquad (1.6)$$

where $\chi_o$ is called the bulk susceptibility and k is Boltzmann's constant. The proportionality of $\chi_o$ on 1/T is the well known Curie law (78).

If the spin system is perturbed from this thermal equilibrium state by $\mathbf{B}_{rf}$, equilibrium is restored by the interactions of the nuclear spins among themselves and with the lattice. It is the nature of these interactions that are of interest in this thesis. Bloch described the recovery of the magnetization to the equilibrium value, $M_o$, by a set of equations based on phenomenological arguments for liquid-like systems. These equations can be written as

$$d\mathbf{M}/dt = \gamma \mathbf{M}x\mathbf{H} - (iM_x + jM_y)/T_2 - \mathbf{k}(M_z - M_o)/T_1 \qquad (1.7)$$

where $M_{x,y,z}$ are the components of the macroscopic magnetization in the i, j and k directions, i.e. the unit vectors in the x, y and z directions. Essentially, Bloch allowed the transverse magnetization to decay with a time constant $T_2$, while the longitudinal component was allowed to recover with time constant $T_1$. The

longitudinal (or spin-lattice) relaxation time characterizes the exchange of energy between the spin system and the lattice as the spin system re-establishes an internal Boltzmann distribution. The transverse (or spin-spin) relaxation time describes the time taken for the spin system to reach an internal equilibrium by the exchange of energy between the spins themselves. In the simplest liquid systems the return to equilibrium in both cases is described by a simple exponential function. Bloombergen, Purcell and Pound (74) were the first to put forward a theory of nuclear spin relaxation in liquids ("BPP theory"). The object was to extract information from the observed relaxation times about the microscopic parameters relating to the molecular dynamics of the spin system. In this thesis we will be concerned mainly with the dipolar interaction between protons in water.

### 1.3.2 Relaxation in a Two-Spin System

We will treat proton relaxation in biological systems as being very similar to that of relaxation in bulk water. In free water, rapid motions occur which greatly simplify the derivation of expressions for the relaxation rates. The averaging produced by these motions (rotation, relative translations and chemical exchange of protons) greatly reduces the dipolar coupling between nuclear spins. Since the nuclear spin-spin coupling is weak and comparable to the coupling of the spins to the lattice, we may treat groups of spins as separate systems coupled independently to the lattice.

#### 1.3.2.1 Form of the Hamiltonian

Experimentally, relaxation in liquid like systems can be explained well in terms of the sum of many two-spin interactions, assuming the motion of the two

spins is uncorrelated. The two-spin interaction is the building block of all the models developed in this thesis, and will be dealt with at length here. In a static magnetic field, a system of two spins I = 1/2 and I' = 1/2 posseses a Hamiltonian $H = H_o + H'$ where $H_o = -\gamma\hbar B_0(I_z + I_z')$. $H_o$ represents the Zeeman energy of the system, while $H'$ is considered as a small arbitrary interaction between the two spins. $I_z$ and $I_z'$ are the spin angular momentum operator's components in the z direction and are written as such to emphasize that the spins are "like", that is they have the same $\gamma$. The form of the interaction that will be considered later is that of the dipolar Hamiltonian, but in fact the treatment presented here (75, 76) holds for any interaction that can be treated as a perturbation.

### 1.3.2.2 Eigenvectors and Eigenvalues of a Two-Spin System

The advantage of treating $H'$ as a small perturbation lies in the fact that in first order perturbation theory one may use the eigenstates of the unperturbed Hamiltonian for calculation purposes. For the two-spin system, the four eigenstates and eigenvalues of the z component of the spin angular momentum operators I and I' are

$$\begin{aligned} I_z|+\rangle_1 &= 1/2|+\rangle_1 \\ I_z|-\rangle_1 &= -1/2|-\rangle_1 \\ I'_z|+\rangle_2 &= 1/2|+\rangle_2 \\ I'_z|-\rangle_2 &= -1/2|-\rangle_2 \end{aligned} \qquad (1.8)$$

Then the four eigenstates of the pair can be written as $|{+}{+}\rangle$, $|{+}{-}\rangle$, $|{-}{+}\rangle$ and $|{-}{-}\rangle$ with $N_{++}$ spins in the $|{+}{+}\rangle$ eigenstate, $N_{+-}$ spins in the $|{+}{-}\rangle$ eigenstate and so on. Longitudinal relaxation is brought about by transitions between these states as shown

in Figure 1.6. In that figure, the $w_i$ denote the transition probabilities per unit time between the states.

When discussing transverse magnetization, the above eigenstates are not appropriate since they are not eigenstates in the transverse plane. Instead we use the eigenstates of the operators $\mathbf{I}_x$ and $\mathbf{I}'_x$ defined as

$$\begin{aligned} \mathbf{I}_x|a\rangle_1 &= 1/2|a\rangle_1 \\ \mathbf{I}_x|b\rangle_1 &= -1/2|b\rangle_1 \\ \mathbf{I}'_x|a\rangle_2 &= 1/2|a\rangle_2 \\ \mathbf{I}'_x|b\rangle_2 &= -1/2|b\rangle_2 \end{aligned} \qquad (1.9)$$

giving the four eigenstates $|aa\rangle$, $|ab\rangle$, $|ba\rangle$ and $|bb\rangle$, which, however, are not eigenstates of the energy. Since the four states are orthogonal, their occupancies can be defined as $N_{aa}$, $N_{ab}$, etc., and the transition probabilities between states may be diagrammed as in Figure 1.7.

One can always express these states $|a\rangle$ and $|b\rangle$ in terms of the energy eigenstates as $|a\rangle = 1/\sqrt{2}[|+\rangle + |-\rangle]$ and $|b\rangle = 1/\sqrt{2}[|+\rangle - |-\rangle]$ so that perturbation theory may be used to evaluate the $u_i$ using the unperturbed energy eigenstates. Transverse relaxation is brought about by transitions (denoted by the $u_i$ in the Figure 1.7) between the four states and these transitions conserve energy within the spin system.

1.3.2.3 Equations of Motion of a Two-Spin System

Experimentally we observe quantities proportional to the ensemble averages of $I_z$ and $I'_z$ which are in turn proportional to the occupancy of the states, i.e.

$$\langle I_z \rangle \alpha (N_{++}+N_{+-}) - (N_{-+}+N_{--})$$
$$\langle I'_z \rangle \alpha (N_{++}+N_{-+}) - (N_{+-}+N_{--}). \qquad (1.10)$$

Using these equations and the definition of the $w_i$'s and $u_i$'s, the longitudinal and transverse components may be written as

$$d/dt\ (\langle I_z \rangle + \langle I'_z \rangle) = -2\ (w_1+w_2)(\langle I_z \rangle + \langle I'_z \rangle - \langle I_o \rangle + \langle I'_o \rangle)$$
$$d/dt\ (\langle I_+ \rangle + \langle I'_+ \rangle) = -2\ (u_1+u_2)(\langle I_+ \rangle + \langle I'_+ \rangle) \qquad (1.11)$$

where $I_o$ is the equilibrium magnetization associated with the ensemble of spins. We have made use of the fact that $\mathbf{I}_+ = \mathbf{I}_x + i\mathbf{I}_y$ is the observable associated with the transverse magnetization, not $\mathbf{I}_x$ or $\mathbf{I}_y$ as one might expect. This is because the eigenvectors of $\mathbf{I}_x$ and $\mathbf{I}_y$ do not form a basis set for the energy eigenstates of the system. If we associate $(\langle I_z \rangle + \langle I'_z \rangle)$ with the longitudinal magnetization and $(\langle I_+ \rangle + \langle I'_+ \rangle)$ with the transverse magnetization, then comparison of Equation 1.11 with Equation 1.7 yields

$$1/T_1 = 2\ (w_1+w_2)$$
$$1/T_2 = 2\ (u_1+u_2). \qquad (1.12)$$

### 1.3.2.4 The Dipole-Dipole Interaction

We now return to consider the form of the perturbation Hamiltonian $\mathcal{H}'$. For protons in liquids or liquid-like systems, the overwhelming contribution to relaxation comes from the dipolar interaction between spins. The dipolar Hamiltonian can be written as the sum of the scalar product of two terms, $A_{(k)}$ and $F_{(k)}$, where the A terms are functions of the spin operators, whereas the F terms are functions of the spatial coordinates of the spins. For spins that are in motion, these spatial coordinates become functions of time, resulting in a time dependent modulation of the

dipolar interaction capable of inducing transitions between the states of the two-spin system discussed above. The product may be expanded as

$$H' = H_D = \sum_{k=0}^{2} A_{(k)}F_{(k)} = [I_zI'_z - 1/4(I_+I'_- + I_-I'_+)]F_0 + [I_+I'_z + I_zI'_+]F_1 + [I_-I'_z + I_zI'_-]F_1^* + [I_+I'_+]F_2 + [I_-I'_-]F_2^* \quad (1.13)$$

where

$$F_0(t) = K\,[1-3\cos^2\theta(t)]$$

$$F_1(t) = -3/2\ K \sin\theta(t)\cos\theta(t)e^{i\phi(t)}$$

$$F_2(t) = -3/4\ K \sin^2\theta(t)e^{2i\phi(t)}$$

$$K = \hbar^2\gamma^2/a^3(t)$$

$$F_i^*(t) = F_i(t) \quad (1.14)$$

with the understanding that **a** is the internuclear distance between the interacting spins and the orientation of the vector **a** with respect to the external magnetic field is specified by the polar ($\theta$) and azimuthal ($\phi$) angles. The $F_i^*(t)$ stand for the complex conjugates of the $F_i(t)$. The transition probabilities $w_i$ and $u_i$ can then be calculated by the method of Abragam and Pound (76).

We define the spectral densities $J_{(k)}$ as the Fourier transforms of the autocorrelation functions of the $F_k(t)$. That is,

$$J_k(\omega) = \int_{-\infty}^{\infty} \langle F_k(t)\cdot F^*_k(t+\tau)\rangle \exp(-i\omega\tau)\, d\tau \quad (1.15)$$

where $\langle F_k(t)\cdot F^*_k(t+\tau)\rangle$ represents the ensemble average over all the pairs of interacting spins. The $J_k(\omega)$ represent the spectral densities of the magnetic field fluctuations due to fluctuations in the spatial coordinates. Furthermore, we define the correlation functions, $G_k(\tau)$, for a random stationary process involving the $F_k(t)$ as

$$G_k(\tau) = \langle F_k(t) \cdot F^*_k(t+\tau) \rangle = \lim_{T \to \infty} \frac{1}{2T} \int_{-T}^{T} \langle F_k(t) \cdot F^*_k(t+\tau) \rangle dt \qquad (1.16)$$

where we can loosely define a correlation time $\tau_c$ such that $G_k(\tau)$ is very small for $|\tau| >> \tau_c$. Essentially $\tau_c$ represents the time taken for the interaction between the two spins to die away.

Only fluctuations of the magnetic field at certain frequencies can cause transitions between the states represented in Figures 1.6 and 1.7. These transition probabilities are calculated to be (75, 76)

$$\begin{aligned} w_o &= 2C(5/12)\, J_0(0) \\ w_1 &= 2C(15/4)\, J_1(\omega) \\ w_2 &= 2C(15/4)\, J_2(2\omega) \\ u_o &= C\{(15/24)\, J_0(0) + (15/16)\, J_2(2\omega)\} \\ u_1 &= C\{(15/4)\, J_1(\omega) + (15/16)\, J_2(2\omega)\} \\ u_2 &= C\{(15/8)\, J_0(0) + 15\, J_1(\omega) + (15/16)\, J_2(2\omega)\} \end{aligned} \qquad (1.17)$$

where $C = (3/40)\gamma^4\hbar^2$. Utilizing Equations 1.12 and 1.17 we can then write the standard forms for the relaxation rates $R_1$ and $R_2$ as

$$\begin{aligned} R_1 &= 1/T_1 = (9/8)\gamma^4\hbar^2\{J_1(\omega) + J_2(2\omega)\} \\ R_2 &= 1/T_2 = (9/32)\gamma^4\hbar^2\{J_0(0) + 10J_1(\omega) + J_2(2\omega)\} \end{aligned} \qquad (1.18)$$

It is thus seen that both $R_1$ and $R_2$ are sensitive to the spectral density of the microscopic magnetic field fluctuations at $\omega$ and $2\omega$, and that the efficiency of $R_2$ is also determined by fluctuations around zero frequency. If these low frequency fluctuations are due to the motion of the spins, then the motional process causing them must occur on a long timescale (i.e. they are slow motions). It is thus

commonly said that $R_2$ is sensitive to slow motions while $R_1$ is governed by fast motions. A model for relating the motions to the $J_k(\omega)$ will be discussed in section 1.3.2.6.

**1.3.2.5** Spin-Lattice Relaxation in the Rotating Frame

In addition to measurements of $R_1$ and $R_2$ that are commonly used to characterize tissue, it was decided that measurements of the spin lattice relaxation rate in the rotating frame ($R_{1\rho} = 1/T_{1\rho}$) could provide additional insight into tissue relaxation mechanisms. This is because $R_{1\rho}$ is not only sensitive to slow motional processes which give rise to transverse relaxation, but can also be measured over a range of low frequencies.

In the rotating frame, the effective magnetic field seen by the spins on resonance is $\mathbf{B}_1$. $T_{1\rho}$ is the characteristic time associated with the decay of magnetization oriented along $\mathbf{B}_1$. Essentially, the magnetization that was tipped into the transverse plane tries to establish a new Boltzmann distribution in the field $\mathbf{B}_1$, much like that giving rise to the initial magnetization of the sample (with characteristic time $T_1$) when it is placed in the static field $\mathbf{B}_o$.

Since the magnitude of $\mathbf{B}_1$ used in typical spectrometers is less than 100 G, a weak-collision theory (BPP theory) approach may be used to evaluate an expression for $R_{1\rho}$. Starting from the laboratory-frame dipolar Hamiltonian, Jones (79) has derived an expression for $R_{1\rho}$ using the same assumptions as used for $R_1$ and $R_2$. On resonance, his expression for $R_{1\rho}$ reduces to

$$R_{1\rho} = 1/T_{1\rho} = (9/32)\gamma^4\hbar^2\{J_o(\omega_1) + 10J_1(\omega) + J_2(2\omega)\} \qquad (1.19)$$

where $\omega_1 = \gamma B_1$. By measuring $R_{1\rho}$ as a function of $B_1$, one can obtain some information about the low-frequency spectrum of the process giving rise to the relaxation. The frequency range ($\omega_1$) covered by the $T_{1\rho}$ experiments in this thesis is 12 to 80 kHz which corresponds to motional processes occurring on a timescale of $10^{-6}$ to $10^{-5}$ s. These are relatively long timescales at the molecular level. A model to relate the spectral densities, $J_k(\omega)$, to the motional processes is discussed in the next section.

### 1.3.2.6 Forms of the Spectral Densities

A definitive expression for the relaxation times depends on the model chosen to describe the microscopic magnetic field fluctuations, i.e. the form of the $J_k(\omega)$. Examination of Equations 1.14 shows that only changes in $\theta$, $\phi$ or **a** between the two spins can give rise to changes in the magnetic field experienced by each spin. Within a molecule such as water, the variation of the dipolar coupling arises almost solely from the rotation of the molecule as a whole, since the interproton distance in a water molecule does not change at an appropriate frequency to effect NMR relaxation. For interactions between spins on different molecules, both their relative translations (hence changes in **a**) and rotations (hence changes in $\theta$ and $\phi$) must be considered. Abragam has worked out the relative contributions of translational and rotational motions to water proton relaxation and shown that for free water the rotational contribution dominates (68).

For random rotations of a water molecule, fluctuations in the angular coordinates $\theta$ and $\phi$ can induce transitions between the eigenstates of a two-spin system. For smooth, isotropic random rotation of a spherical molecule of radius r,

the diffusion equation can be used to describe the probability, $\psi$, of finding the proton-proton axis in a direction ($\theta$, $\phi$) at time t. This can be written as

$$\partial\psi(\theta,\phi,t)/\partial t = (D_r/r^2)\Delta\psi(\theta,\phi,t) \qquad (1.20)$$

where the coefficient of rotational diffusion, $D_r$, in a medium of viscosity $\eta$, is given by

$$D_r = kT/8\pi r^3\eta. \qquad (1.21)$$

One can expand $\psi(\theta,\phi,t)$ in terms of spherical harmonics in order to obtain the correlation functions

$$G_k(\tau) = (\beta_k/r^6)e^{-|\tau|/\tau_c} \qquad k=0, 1, 2 \qquad (1.22)$$

where $\beta_0 = 4/5$, $\beta_1 = 2/15$, $\beta_2 = 8/15$ and the correlation time is given by

$$\tau_c = 1/6D_r = 4\pi r^3\eta/3kT. \qquad (1.23)$$

We see that the correlation function is an exponentially decaying function of time, which is a consequence of the solution to the diffusion equation (1.20). $\tau_c$ is loosely interpreted as the time taken for the interproton vector to reorient one radian. The resulting spectral densities are obtained by substituting Equation 1.22 in Equation 1.15 to give

$$J_k(\omega) = (\beta_k/r^6)\, 2\tau/(1+\omega^2\tau^2) \qquad (1.24)$$

which when substituted into Equations 1.18 and 1.19 yields the result (68, 74, 79)

$$R_1 = (2/3)\sigma^2\{\tau_c / (1 + \omega^2\tau_c^2) + 4\tau_c / (1 + 4\omega^2\tau_c^2)\}$$

$$R_2 = (1/3)\sigma^2\{3\tau_c + 5\tau_c / (1 + \omega^2\tau_c^2) + 2\tau_c / (1 + 4\omega^2\tau_c^2)\}$$

$$R_{1\rho} = (1/3)\sigma^2[3\tau_c/(1+\omega_1{}^2\tau_c{}^2) + 5\tau_c / (1 + \omega^2\tau_c{}^2) + 2\tau_c / (1 + 4\omega^2\tau_c{}^2)] \quad (1.25)$$

where $\sigma^2 = (9/20)\gamma^4\hbar^2/\mathbf{a}^6$ is called the rigid lattice constant, with a value of $2.1 \times 10^{10}$ $s^{-2}$ for water and the interproton distance, **a**, is 0.152 nm. The Equations 1.25 are the standard expressions obtained using the continuous rotational diffusion model of Debye. They incorporate dispersive Lorentzian terms $\tau_c/(1+\omega^2\tau_c{}^2)$ which confer a frequency dependence on the measured relaxation times.

### 1.3.3 Exchange Between Phases

In a heterogeneous material such as tissue, the motion of the water molecules depends on their immediate surroundings. If the water is associated with a macromolecular surface, there is a partial or total constraint on the normally random motion of the water molecule and the relaxation rate of the hydration water will therefore depend on the nature of the constraint on the water molecule. In general, the water molecules exchange between different environments in tissue by diffusion. To describe relaxation in such a system it is necessary to incorporate some adjustments that take into account the effect of these dynamical constraints on the water molecule.

Towards this end we consider that the heterogeneous tissue is in fact made up of J homogeneous phases. Each homogeneous phase possesses the specific characteristics of a microscopic environment. Let $p_j$ denote the fractional population of spins in phase j and let $R_{1j}$, $R_{2j}$ and $R_{1\rho j}$ denote the appropriate relaxation rate of the spins in phase j. The observed relaxation rates in tissue reflect specific characteristics of each phase and the exchange of molecules between phases. It

should be pointed out that the term "phase" is used in the literature to denote any homogeneous collection of spins having the same intrinsic relaxation parameters. Thus "phase" could refer to an entire physical compartment, such as those shown in Figure 1.5, within which there can be made further natural subdivisions such as hydration-water phases, macromolecular-proton phases and a free-water phase. It is thus important to understand the context in which a particular set of equations is being used.

The exchange between phases may involve chemical exchange or spin-diffusion between neighboring phases. Chemical exchange involves the physical exchange of water molecules or protons from one phase to another by diffusion. Such exchange can be considered to occur between hydration and free water or on a larger scale, between intra- and extracellular spaces. For multiphase systems the form of the relaxation rates can be obtained from the Bloch equations (80) or by the use of the Chapman-Kolmogoroff equations (78). Using the latter technique, Zimmerman and Brittin (34) derived an analytic solution for a two-phase system in which the observed magnetization $\Phi_i$ is described in general by a double-exponential function (81, 82)

$$\Phi_i(t) = \lambda^+ \exp(-R_i^+ t) + \lambda^- \exp(R_i^- t) \qquad (1.26)$$

with

$$\lambda^+ + \lambda^- = 1$$

$$\lambda^{\pm} = \pm\{(R_i^o - R_i^{\pm})/(R_i^+ - R_i^-)\}$$

$$R_i^{\pm} = (1/2)\{(R_{ia}+R_{ib}+k_a+k_b) \pm [(R_{ib}-R_{ia}+k_b-k_a)^2+4k_ak_b]^{1/2}\}$$

$$R_i^o = p_aR_{ia} + p_bR_{ib}$$

$$i = 1, 2 \text{ or } 1\rho \qquad (1.27)$$

where the $\lambda_i^{\pm}$ and $R_i^{\pm}$ are, respectively, the measured fractional populations and the relaxation rates. These will not in general be equal to the actual fractional populations of the spins in the two phases, $p_a$ and $p_b$ ($p_a+p_b = 1$), and the intrinsic relaxation times in the two phases, which are $R_{ia}$ and $R_{ib}$. This complicates the interpretation of measured multiexponential relaxation rates in tissue. The exchange rate $k_a$ is the probability per unit time of a molecule diffusing from phase a to phase b while $k_b$ is the likelihood of the reverse process. The rates are inversely proportional to the lifetime of a water molecule in each phase, that is $k_a = 1/\tau_a$ and $k_b = 1/\tau_b$. Detailed balance dictates that $p_a k_a = p_b k_b$.

There are, however, two cases where the form of the equations simplifies considerably. If the exchange of water molecules between phases is very slow, such that for all phases j = a,b,c... $\tau_j >> T_{ij}$, then the expression for the observed magnetization is

$$\Phi i(t) = \sum_j p_j \exp(-t/T_{ij}). \qquad (1.28)$$

In this so-called slow-exchange limit where $T_{ij}$ is the relaxation time in the $j^{th}$ phase, the observed magnetization decay reflects the sum of the j discrete exponential functions weighted by their fractional populations. Using standard techniques for analyzing time dependent signals, one can in principle decompose the observed NMR signal to extract the intrinsic parameters $p_j$ and $T_{ij}$, which in this case will reflect the true populations and relaxation rates. Equation 1.28 is used extensively to interpret the NMR relaxation measurements on aqueous solutions of red blood cell ghosts in Chapter 3.

At the opposite extreme, the so called fast exchange limit between phases, $\tau_{ij} << T_{ij}$ and the observed magnetization decay is

$$\Phi_i(t) = \exp(-t/T_i) \tag{1.29}$$

with

$$1/T_i = \sum_j p_j(1/T_{ij}). \tag{1.30}$$

In this case the magnetization decay consists of a single exponentially decaying component whose relaxation time is given by the weighted sum of the individual relaxation times. Here, the water molecule samples all the phases over a timescale characterized by the relaxation times $T_i$. This latter condition (Equation 1.29 and 1.30 with j = a or b) describes the two-site rapid-exchange model, often used to explain relaxation in aqueous solutions of macromolecules as in Chapter 2.

For two neighboring phases that do not exchange water molecules, one still has the possibility of the two phases communicating via a process known as spin diffusion. Spin diffusion occurs between phases that have intrinsically different relaxation rates but which are sufficiently close to interact magnetically. The interaction transfers spin energy via a mutual flip-flop of spins in each proton phase leading to cross relaxation between the two phases. This transfer of energy corresponds to the $|+-\rangle \leftrightarrow |-+\rangle$ transitions in Figure 1.6. This suggests that spin diffusion only directly affects the longitudinal relaxation (83, 84).

The solutions of the modified Bloch equations for the magnetization behavior for two-phase cross relaxation can be written almost identically to Equations 1.26 and 1.27, except that now each phase is characterized by the two relaxation times $R_i^{\pm}$ and

there is no simple correspondence between the apparent $\lambda_i$'s and $R_i^{\pm}$'s and the true $p_i$'s and $R_i$'s (15). The $k_i$ can then be interpreted as being proportional to the cross-relaxation rate between phases. Since the magnetic interaction between spins varies as $1/a^6$, cross-relaxation is only effective between phases that are very close. In particular cross-relaxation does not effect the relaxation of compartments which are macroscopic and spatially discrete. Spin-diffusion is thought to play an important role in tissue where the hydration water on the macromolecular surface is postulated to cross relax with the protons of the macromolecule (8, 15, 21, 24, 83, 111).

### 1.3.4 Effect of Constrained Motions on Relaxation

As suggested above, water in biological systems can be considered to exist in distinct phases. Hydration layers of water on macromolecular surfaces can be considered the most important of such phases, this water being "associated" or "bound" in some way with the macromolecular surface via ionic or van der Waal's interactions. The associated water has constraints placed on its thermally driven random motion by the association with the macromolecular surface.

The motional constraints can be put into two broad categories. A partial or total inhibition of the motion of the water molecule at the surface results in a slower motion and hence a longer correlation time compared to free water. Secondly, if the surface itself is moving, as in the case of a protein tumbling in solution, there is a superposition of the Brownian motion of the protein upon the motion of the associated water molecule. In either case, the normally isotropic motion of a free-water molecule becomes anisotropic. This anisotropy may arise from the nature of the association with the surface itself, since proteins in general are not spherical. Although cell membranes in tissue do not rotate, the lipids and proteins in the

membrane do diffuse around on the surface of the membrane and any hydration-water associated with them will move too. Therefore, one should not think of tissue as being completely static with respect to hydration water movement.

Several models have been proposed in the literature to explain anisotropic constraints (86) and in particular bound water relaxation in protein solutions (85, 87). The most general of these is the model of Halle and Wennerstrom (85): other models (86) can usually be reduced to special cases of their model. They (85) allow the orientation of a water molecule to take on the coordinates $\Omega = (\Delta,\Psi,\rho)$ with respect to a reference frame fixed to the macromolecular surface, having at least three fold symmetry about a principal axis described by a probability distribution $P(\Omega)$. Thus, anisotropic motion of the water is incorporated through the use of $P(\Omega)$. The reorientation of the water molecule (characterized by correlation time $\tau_{ar}$) is assumed to be much faster than that of the reorienting support ($\tau_{pm}$). This condition ($\tau_{ar} << \tau_{pm}$) lets one consider the two motions as statistically independent, allowing the definition of two correlation functions. For the dipolar interaction one may define an order parameter $\langle p \rangle$ such that

$$\langle p \rangle = \int P(\Omega)\,((3\cos^2\beta - 1)/2)\,d\Omega = \langle 3\cos^2\beta - 1 \rangle/2 \qquad (1.31)$$

where $\beta$ is the angle between the interproton vector in the water molecule and the axis of rotation of the protein or phospholipid. The order parameter provides an indication of the residual anisotropy of the water molecule motion (88, 89). For example, if the water is assumed to be rigidly bound to the protein surface, $\beta = 0$ and $\langle p \rangle^2 = 1$. This means that the water molecule reorients with the same correlation time as the protein ($\tau_{pm}$). If, however, $\langle p \rangle^2 = 0$ as for free water, then the water proton

relaxation is determined solely by the isotropic rotation of the water molecule. In practice we expect the motional behavior of the hydration water to fall somewhere in between the two extremes. Studies using several different techniques estimate $0.01 < \langle p \rangle < 0.1$; that is, there exists a weak anisotropic constraint on the hydration water. The observed hydration water relaxation rate (Figure 1.8) may be modelled as

$$R_i = \langle p \rangle^2 R_i(\tau_{pm}) + (1-\langle p \rangle^2) R_i(\tau_{ar}) \qquad (1.32)$$

If the motion of the protein itself is anisotropic, the $\tau_{pm}$ should be decomposed into the correlation time for rotation about each of its principal axes. This is difficult to achieve in practice since the rotational diffusion values about different axes are rarely substantially different.

A further modification of Equation 1.26 should be dealt with as well. In the very fast exchange limit, the condition $\tau_{pm} << \tau_a, \tau_b$ may not be met. If the lifetime of a water molecule in the associated phase is less than or comparable to the correlation time of water in that phase then an exchange contribution to relaxation can occur. This is because the exchanging proton travels between an environment where the dipolar Hamiltonian is zero when averaged over all two-spin systems (bulk water) and one where there is a residual dipolar Hamiltonian (associated water). This serves to modulate the dipolar Hamiltonian between zero and some finite value, giving an additional mechanism for relaxation and complicating the interpretation of the $\tau_{pm}$. While this mechanism may not be dominant in protein solutions, it is undoubtedly significant in tissue where much of the macromolecular surface is rigid ($\tau_{pm} \rightarrow \infty$). In this case, it may be appropriate to replace $\tau_{pm}$ by $\delta$, the lifetime of water in the associated phase (88, 89).

## 1.4 Introduction to Proton NMR Imaging

There are two basic reasons for including a brief description of NMR imaging here. Firstly, NMR microscopic imaging played an important role in assigning relaxation components both in preparations of RBC ghosts (Chapter 3) and in excised crayfish nerve cords (Chapter 4). Secondly, it is the hope that the studies presented in this thesis will eventually be useful in the interpretation of NMR images, particularly in the delineation and quantification of cerebral edema.

NMRI arose from the fundamental NMR property that nuclear spins placed in a magnetic field will resonate at a frequency proportional to that field. Lauterbur (90) was among the first to propose the use of a spatially varying magnetic field to encode the position of the spins in a static magnetic field. In current use, one particular form of Lauterbur's original concept is almost ubiquitous. This modification, known as two-dimensional Fourier transform (2DFT) imaging is introduced in many papers, reviews and books (91-93).

In the simplest possible imaging experiment the object to be imaged is placed in a static magnetic field $H_o$, which defines the z direction as usual. If a magnetic field gradient in the z direction ($G_z$) is then superimposed on the static field, as in Figure 1.9, the resonance frequency becomes a function of the spatial coordinate z. The object can then be subjected to a frequency-bandwidth-tailored RF pulse that tips the macroscopic magnetization into the transverse plane. Only spins with Larmor frequencies $\omega = \gamma(H_o+G_z z)$ within the RF pulse frequency bandwidth are affected. The spread of frequencies across an element of thickness $\Delta z$ is $G_z \Delta z$. The resulting NMR signal is composed of a mixture of frequencies, corresponding to the position

of the spins in the field. A mathematical tool known as the Fourier transform (FT) is used to analyze the acquired NMR signal for its frequency components. Since the Larmor frequency is linearly related to the position of the spins in the object, a 1-D projection of the spin density is obtained.

The 2DFT imaging technique (93) utilizes small (relative to the main field) field gradients in $B_0$ in each of the x,y and z directions. These gradients are produced by orthogonal coil sets and each gradient produces a position-dependent offset of the resonance frequency $\omega_0 = \gamma H_0$. In the 2DFT technique, one usually excites a narrow slice of the object (94) with a shaped RF pulse applied in conjunction with a gradient parallel to the normal defining the plane of the slice. The time domain shaping or tailoring of the RF pulse is used to produce the desired slice excitation profile in the sample, usually a rectangular slice. The other two gradients are subsequently used to encode spatially the object in a plane perpendicular to the slice direction. Details of the technique for normal imaging and microscopic imaging can be found elsewhere (91, 92, 95). Suffice it to say that such indices of the NMR parameters as proton density, $T_1$, $T_2$ and $T_{1\rho}$ (96) can be obtained as a function of position from a NMRI image.

Damadian claimed in 1971 (33) that water proton relaxation rates could be used to differentiate between normal and neoplastic tissues. Although his results did not substantiate his claim, his announcement did much to spark the application of NMR to medicine. Images based on the NMR technique were published within the decade by groups in the USA (90) and England (93, 97-99). The latter group (at Nottingham) soon showed that NMRI could detect abnormal pathology in brain (100). Since then, huge strides have been made in the clinical application of the

technique. In particular, NMRI is now the method of choice for neurological investigations, where the contrast between soft tissues is otherwise elusive. Although indices of the NMR parameters $T_1$ and $T_2$ can be spatially mapped, they have not proven to be specific for diagnosis. However, by manipulating the NMR imaging sequence parameters, $T_1$ and $T_2$ differences between tissue can be used to generate contrast between different anatomical structures. Despite that, delineation of a tumor mass from the surrounding peritumoral edema and measuring the extent of the edema remain unresolved without the use of exogenous contrast agents; both could benefit from the studies in this thesis.

## 1.5 The Problem of Cerebral Edema

For the purposes of this thesis, cerebral edema can be considered as an increase in brain tissue water due to the impairment of the mechanisms responsible for cell volume regulation within the cerebral parenchyma. This accumulation of water can occur in the intracellular spaces, the extracellular spaces or both. Klatzo's widely used classification (101) is perhaps the most relevant here. He recognizes vasogenic edema and cytotoxic edema. The more common form is vasogenic edema characterized by an accumulation of proteinaceous exudate in the extracellular cerebral space; this exudate comes from a breakdown of the BBB in which plasma leaks in from the blood vessels. Cyotoxic edema is the accumulation of protein-poor fluid within the cells of the brain. Manz (102) has noted that this classification really describes two ends of a spectrum of cerebral edema and that in clinical practice the type of edema usually falls somewhere in between. A third classification, that of interstitial edema, is also useful (102). This occurs when the protein fluid in the

ventricles is forced back into the extracellular space in brain by reversal of the normal fluid flow pattern, as in blockage of the arachnoid villi.

The mechanisms involved in the formation, spread and resolution of cerebral edema are beyond the scope of this thesis; the reader is referred to a selected bibliography for details (101, 103, 104). The important points for modelling edema are that, due to the high tissue resistance of the grey matter, tissue edema usually forms in the white matter, regardless of the site of the initial damage. Also, in a gradual breakdown of the BBB, smaller proteins, such as albumin, will leak out before larger ones, such as the immunoglobins. This means that the timecourse of the relaxation measurements from NMRI promises opportunity to assess the stage of the edema as well as its clearance.

### 1.5.1 Studies of Brain Edema using Proton NMR

There have been several conflicting NMR studies in the last decade concerning proton relaxation in experimental models of vasogenic and cytotoxic edema. These have been carried out on animal models and in general there is only agreement on one general aspect of the process, namely that $T_1$ and $T_2$ are generally elevated in the edematous tissue.

Bederson et al (105) found for several different types of edema that $T_2$ correlates linearly with water content of the region while $T_1$ does not. However, using the more meaningful relaxation rates, Kanman et al (106) found that $R_1$ and $R_2$ vary linearly with inverse total water fraction somewhat in agreement with Naruse (107) and Go (108).

Part of the discrepancy may lie in the fact that some workers find multiexponential relaxation in tissues while others do not. Backay (109) first observed two $T_2$ components in normal and edematous white matter and ascribed this as being due to intracellular and extracellular water. Go (108) found two components for $T_1$ and $T_2$ in white matter, while Naruse (107) found $R_1$ and $R_2$ monoexponential in normal brain but biexponential in vasogenic and cytotoxic edema. Naruse also noted that the slow component may be due to extracellular water while the fast $R_2$ component arises from intracellular water. This type of behavior is found in a figure in the paper by Kanman et al (106) but is not mentioned in his text.

Work in our laboratory by Castro (110) on a tumor model of vasogenic edema and a tri-ethyl tin model of cytotoxic edema in cats showed results similar to the above work. $T_2$ is found to be biexponential only in pathological white matter where the behavior of the slow component depends on the type of edema.

In none of the studies outlined here are any NMR parameters given. These parameters (number of echos, echo spacing, repetition times) are crucial for the critical evaluation and interpretation of their work and it must be concluded that along with an enormous body of work on tissue systems over the 30 years, most relaxation studies have been far from optimal in elucidating the details of tissue relaxation.

The models described in the following chapters try to show how long-established NMR techniques, applied carefully and analyzed properly, can yield much information on the water in biological systems.

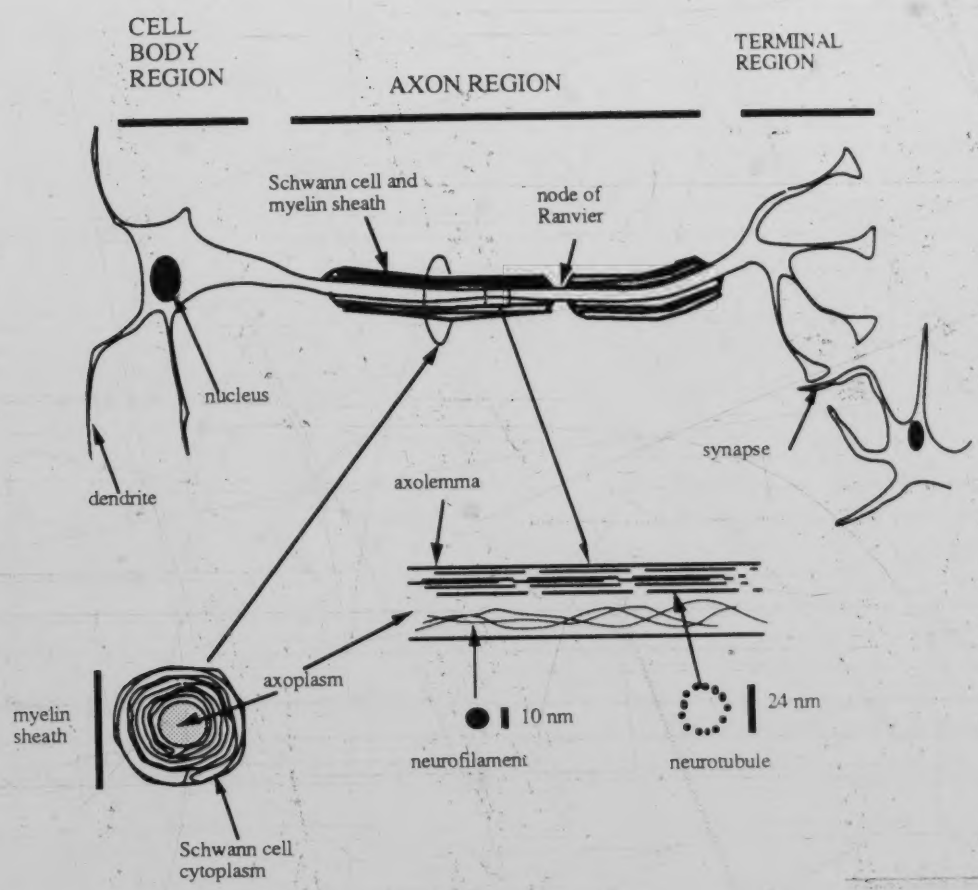


**Figure 1.1** Major structural features of a neuron. The structures shown are relevant to water diffusion across the cell or are capable of affecting water proton relaxation rates to a large extent. The cellular organelles discussed in the text are not drawn here.

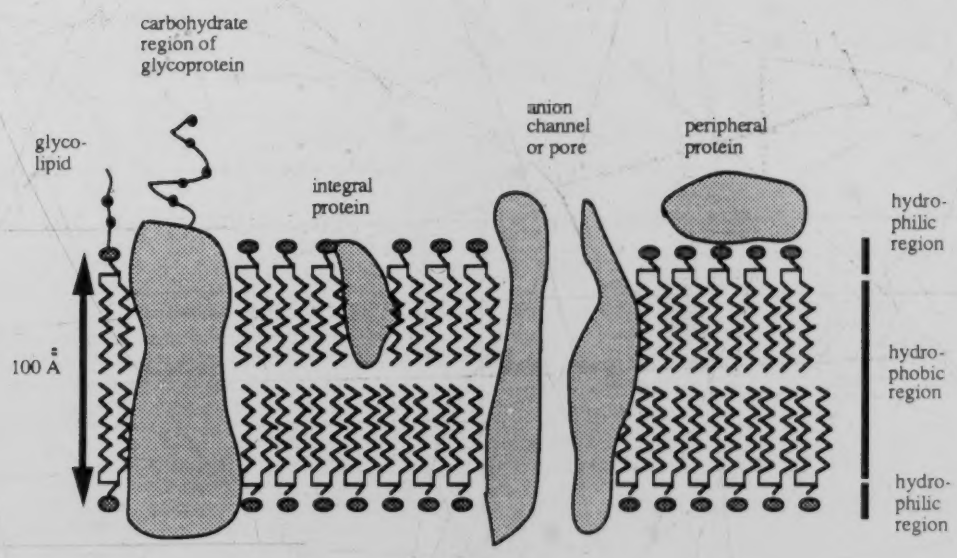


**Figure 1.2** Fluid mosaic model of the membrane. Current views of the membrane suggest a lipid sea in which the proteins float. To be incorporated in the membrane a protein must have hydrophobic regions that match with the hydrophobic regions of the membrane. Water diffusion could occur through a pore, such as the one shown here, or through the lipids themselves as kinks open up in the bilayer.

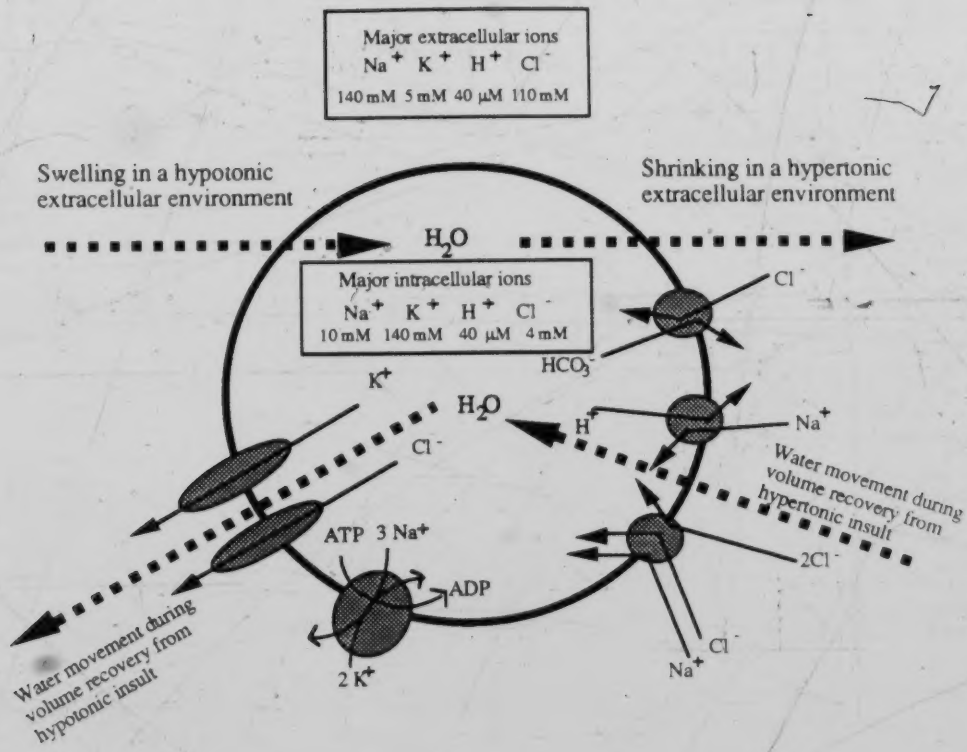


**Figure 1.3** Typical schematic of cell volume regulation in an RBC. The heavy dashed lines indicate water flow into or out of the cell. Water movement is *always* coupled to ion movements; there is no known water pump in cells. The cell volume decreases in response to a hypotonic extracellular environment can occur by outflow of KCl through the ion channels shown, and concomitant coupled outflow of water. In a hypertonic extracellular medium, the volume can be restored by increased NaCl influx through symporters. Note however that there are two possible routes for NaCl to enter the cell and that coupled water transport can occur with both.

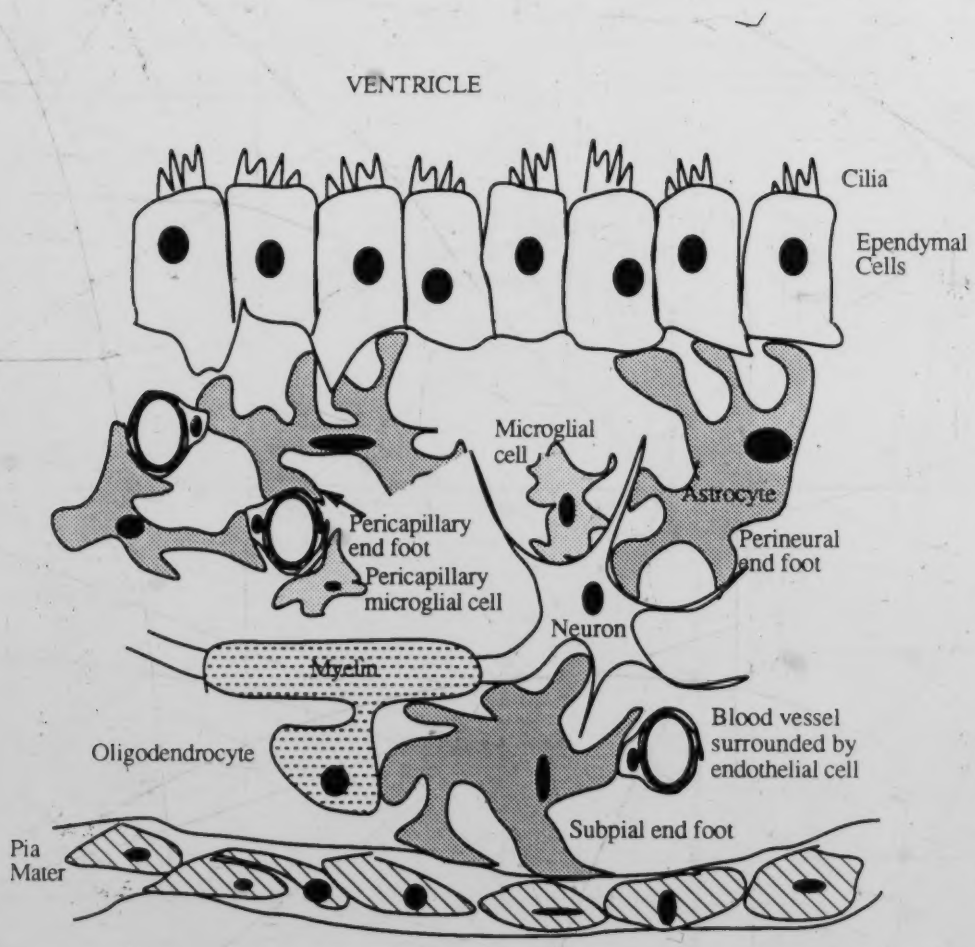


**Figure 1.4** Summary of glial cell types. Shown is a section between the pia mater below the skull and the cerebral ventricles where the CSF is located. The site of the BBB is in the tight junctions between the endothelial cells composing the capillaries. Additional barriers are provided by the glial cells that surround the blood vessels.

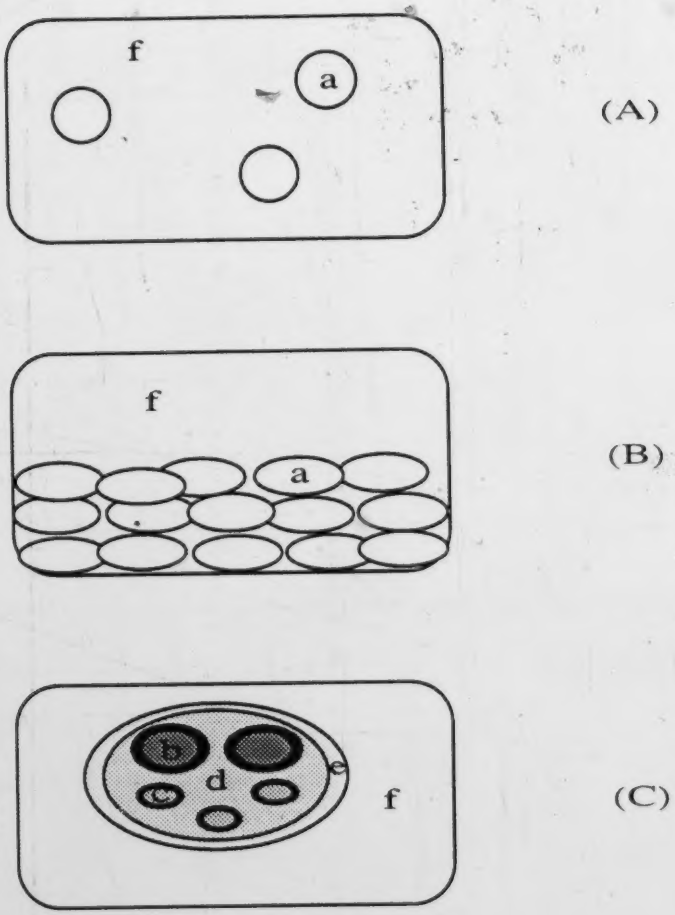


**Figure 1.5** Examples of compartmentation in biological systems. (A) cells in dilute suspension. (B) packed cells with supernatant. (C) nerve cord. Usually, heterogeneity in any given compartment "a", "b", "c", "d" and "e" is ignored unless NMR can distinguish clearly between them. For the models outlined in this thesis, "a" is a red blood cell, "b" and "c" are NMR distinguishable axons in the crayfish nerve cord, "d" is the extraaxonal space in the same nerve cord, "e" is the glial cell sheath of the nerve cord and "f" is the perfusing fluid.

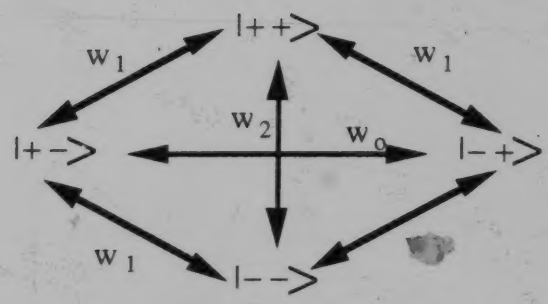


**Figure 1.6** Eigenstates relevant to longitudinal relaxation in a two-spin system. The arrows indicate the possible transitions between states. Since these states commute with $I_z$, they are in fact energy eigenstates of the Zeeman system.

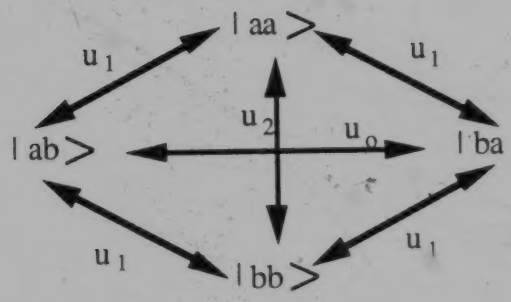


**Figure 1.7** Eigenstates relevant to transverse relaxation in a two-spin system. The arrows indicate the possible transitions between states. These states do not commute with $I_z$ hence are not energy eigenstates. To do the perturbation-theory calculation which involves energy eigenstates, one must first express these states in terms of the energy eigenstates as discussed in the text.

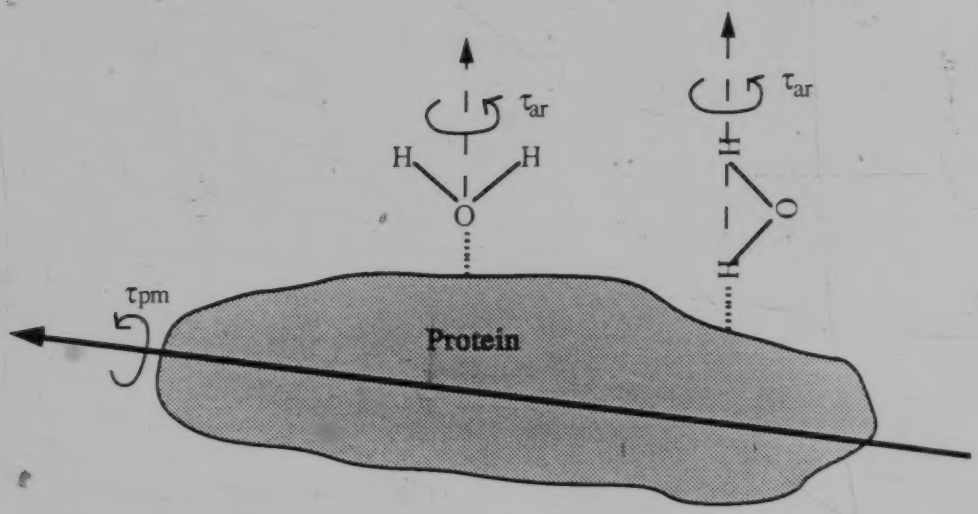


**Figure 1.8** Interpretation of the rotational correlation times. The tumbling of the protein is characterized by the time ($\tau_{pm}$) it takes to rotate 1 radian. Similarly $\tau_{ar}$ is the time taken for a hydration-shell water molecule to reorient the same amount. In the limit that the water is rigidly bound, $\tau_{ar} \rightarrow \infty$ and the rotation of the bound water is characterized by $\tau_{pm}$.

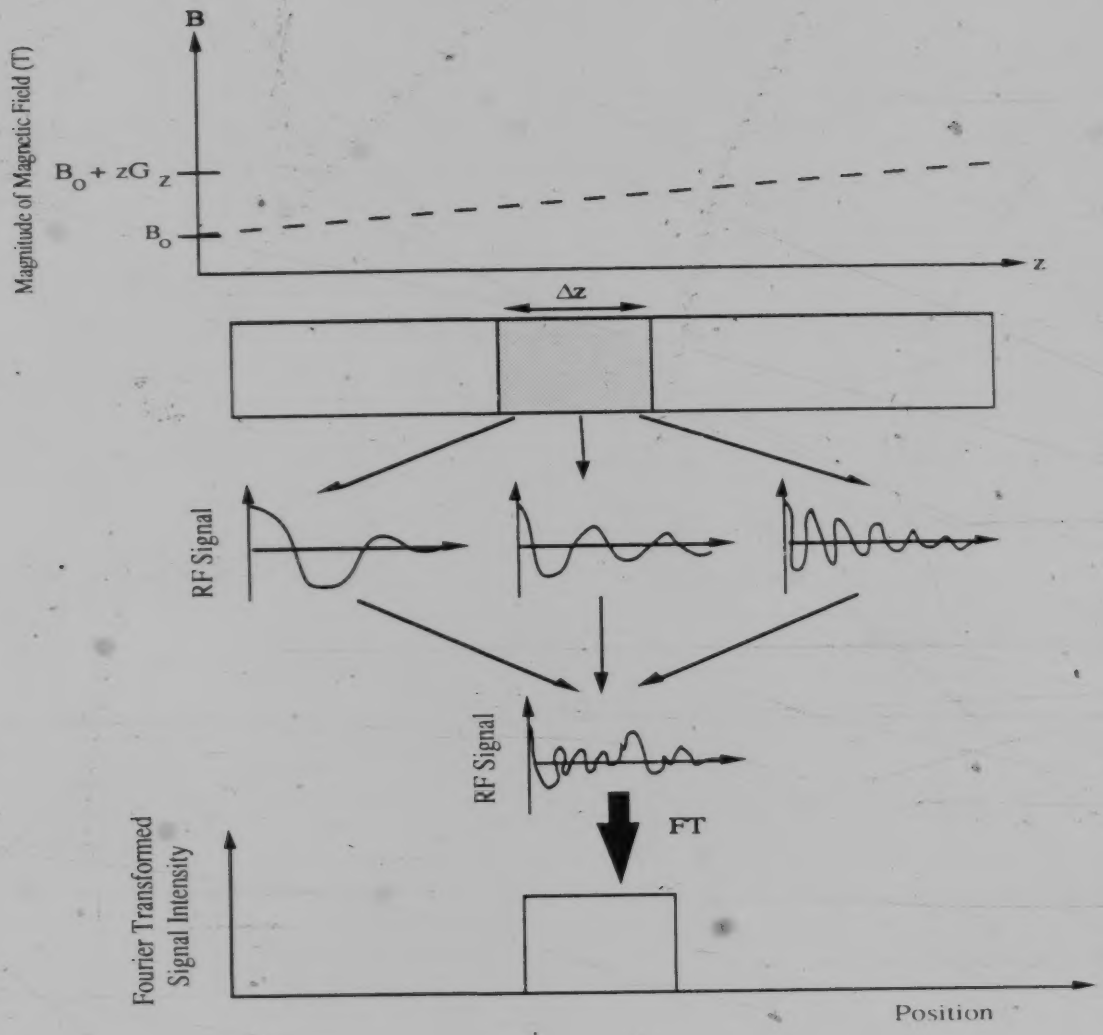


**Figure 1.9** Simple 1-D NMR imaging experiment. It is assumed that only a narrow slice of thickness $\Delta z$ is excited to begin with. The NMR,signal is then composed of many frequencies which can be separated by means of the Fourier transform, to yield the proton density of the object as a function of position.

**1.6** References and Selected Bibliography

1. S. Conti, Proton magnetic relaxation dispersion in aqueous biopolymer systems I. Fibrinogen solutions, *Mol. Phys.* **59**, 449 (1986).

2. P.S. Allen, M.E. Castro, E.O. Treiber, J.A. Lunt and D.P.J. Boisvert, A proton NMR relaxation evaluation of a model of brain edema fluid, *Phys. Med. Biol.* **31**, 699 (1986).

3. R.S. Menon, and P.S. Allen, Solvent proton relaxation of aqueous solutions of the serum proteins $\alpha_2$-macroglobulin, fibrinogen and albumin, *Biophys. J.* **57**, 384 (1990).

4. S.H. Koenig, The dynamics of water-protein interactions, *in* "Water in Polymers" (S.P. Rowland, Ed.), **127**, 157, ACS Symposium Series, Amer. Chem. Soc., Washington, D.C. 1980.

5. S.H. Koenig, R.G. Bryant, K. Hallenga and G.S. Jacob, Magnetic cross-relaxation among protons in protein solutions, *Biochemistry* **17**, 4349 (1978).

6. L. Grösch and F. Noack, NMR relaxation investigation of water mobility in aqueous bovine serum albumin solutions, *Biochim. Biophys. Acta* **453**, 218 (1976).

7. J. Oakes, Protein hydration nuclear magnetic relaxation studies of the state of water in native bovine serum albumin solutions, *J. Chem. Soc. Farad. Trans.* I **72**, 216 (1976).

8. R. Kimmich and F. Noack, Zur deutung der kernmagnetischen relaxation in proteinlsösungen, *Z. Naturforsch.* **25a**, 1680 (1970).

9. D.C. Chang and C.F. Hazlewood, Nuclear magnetic resonance study of squid giant axon, *Biochim. Biophys. Acta* **630**, 131 (1980).

10. P.T. Beal, C.F. Hazlewood and P.N. Rao, Nuclear magnetic resonance patterns of intracellular water as a function of HeLa cell cycle, *Science* **192**, 904 (1976).

11. G.P. Raaphorst, J. Kruuv and M.M. Pintar, Nuclear magnetic resonance study of mammalian cell water, *Biophys. J.* **15**, 391 (1975).

12. D.C. Chang, C.F. Hazlewood, B.L. Nichols and H.E. Rorschach, Spin echo studies of cellular water, *Nature* **235**, 170 (1972).

13. T.J. Swift and O.G. Fritz, Jr., Proton spin-echo study of the state of water in frog sciatic nerve, *Biophys. J.* **9**, 54 (1969).

14. A. Francois, L. Van Gerven, G. Atassi, H. Eisendrath, M. Geilen and R. Willem, Analysis by the Carr-Purcell-Meiboom-Gill sequence of the influence of P388 leukemia and cis-diamminedichloroplatinum (II) nephrotoxicity on water compartmentalization in kidneys and spleens of mice, *Magn. Reson. Med.* **7**, 449 (1988).

15. W.T. Sobol, I.G. Cameron, W.R. Inch and M.M. Pintar, Modeling of proton spin relaxation in muscle tissue using nuclear magnetic resonance spin grouping and exchange analysis, *Biophys. J.* **50**, 181 (1986).

16. S.H. Koenig and R.D. Brown III, Determinants of proton relaxation rates in tissue, *Magn. Reson. Med.* **1**, 437 (1984).

17. C.J.G. Bakker and J. Vriend, Multiexponential water proton spin-lattice relaxation in biological tissues and its implications for quantitative NMR imaging, *Phys. Med. Biol.* **29**, 509 (1984).

18. J.M. Escanye, D. Canet and J. Robert, Frequency dependence of water proton longitudinal NMR relaxation times in mouse tissue at 20 °C, *Biochim. Biophys. Acta* **721**, 305 (1982).

19. G.D. Fullerton, J.L. Potter and N.C. Dornbluth, NMR relaxation of proteins in tissue and other macromolecular water solutions, *Magn. Reson. Imaging* **1**, 209 (1982).

20. E.E. Burnell, M.E. Clark, J.A.M. Hinke and N.R. Chapman, Water in barnacle muscle III. NMR studies of fresh fibres and membrane damaged fibres equilibrated with selected solutes, *Biophys. J.* **33**, 1 (1981).

21. J.G. Diegel and M.M. Pintar, Origin of non-exponentiality of the water proton spin relaxations, *Biophys. J.* **15**, 855 (1975).

22. B.M. Fung and T.W. McGaughy, The state of water in muscle as studied by pulsed NMR, *Biochim. Biophys. Acta* **343**, 663 (1974).

23. E.D. Finch and L.D. Homer, Proton nuclear magnetic resonance relaxation measurements in frog muscle, *Biophys. J.* **14**, 907 (1974).

24. R.R. Knispel, R.T. Thompson and M.M. Pintar, Dispersion of proton spin lattice relaxation in tissues, *J. Magn. Reson.* **14**, 44 (1974).

25. P.S. Belton, K.J. Packer and T.C. Sellwood, Pulsed NMR studies of water in striated muscle, *Biochim. Biophys. Acta* **304**, 56 (1973).

26. R.K. Outhred and E.P. George, Water and ions in muscles and model systems, *Biophys. J.* **13**, 97 (1973).

27. C.F. Hazlewood, B.F. Nichols and N.F. Chamberlain, Evidence for the existence of a minimum of two phases of ordered water in skeletal muscle, *Nature* **222**, 747 (1969).

28. P.S. Belton and R.G. Ratcliffe, NMR and compartmentalization in biological tissue, *Prog. NMR Spectrosc.* **17**, 241 (1985).

29. R. Mathur-De Vre, The NMR studies of water, *Prog. Biophys. Molec. Biol.* **35**, 103 (1979).

30. R. Cooke and I.D. Kuntz, The properties of water in biological systems, *Ann. Rev. Biophys. Bioeng.* **3**, 95 (1974).

31. T.M. Shaw and R.H. Elsken, Investigation of proton magnetic resonance linewidth of sorbed water, *J. Chem. Phys.* **21**, 565 (1953).

32. B.Jacobsen, W.A. Anderson and J.T. Arnold, A proton magnetic resonance study of the hydration of Deoxyribonucleic acid, *Nature* **173**, 772 (1954).

33. R. Damadian, Tumor detection by nuclear magnetic resonance, Science 171, 1151 (1971).

34. J.R. Zimmerman and W.E. Brittin, Nuclear magnetic resonance studies in multiple phase systems: Lifetime of a water molecule in an adsorbing phase on silica gel, *J.Chem. Phys.* **61**, 1328 (1957).

35. R.M. Kroeker, E.R. McVeigh, P.Hardy, M.J. Bronskill and R.M. Henkelman, In-vivo measurement of NMR relaxation times, *Magn. Reson. Med.* **2**, 1 (1985).

36. K.P. Whittal and A.L. Mackay, Quantitative interpretation of NMR relaxation data, *J.Magn. Reson.* **84**, 134 (1989).

37. D.W. Marquardt, An algorithm for least-squares estimation of nonlinear parameters, *J. Soc. Indust. Appl. Math.* **11**, 431 (1963).

38. M. Brant-Zawadzki and D. Norman (Eds.), "Magnetic Resonance Imaging of the Central Nervous System", Raven Press, New York , 1987.

39. R.C. Brasch, D.E. Nitecki, M. Brant-Zawadzki et al. Brain nuclear magnetic resonance imaging enhanced by paramagnetic contrast agent: a preliminary report. *Am. J Neuro. Radiol.* **4**, 1035 (1983).

40. A.J. Vander, J.H. Sherman and D.S. Luciano, "Human Physiology, The Mechanisms of Body Function", McGraw-Hill , New York, 1980.

41. H.F. Bradford, "Clinical Neurobiology, An Introduction to Neurochemistry", W.H. Freeman, New York, 1986.

42. G.J. Sieger, B.W. Aranoff, R.W. Albers and P.B. Molinoff (Eds.), "Basic Neurochemistry", Raven Press, New York , 1989.

43. H.D Patton, J.W. Sundsten, W.E. Crill and P.D. Swanson, "Introduction to Basic Neurology" W.B. Saunders, Philadelphia, 1976.

44. G.H. Bourne (Ed.), "The Structure and Function of Nervous Tissue.", Vol. I Academic Press, New York, 1968.

45. W.E. Watson, "Cell biology of the Brain", John Wiley and Sons, New York, 1976.

46. D. Jensen, "The Human Nervous System", Appleton-Century-Croft, New York, 1980.

47. S.J. Singer and G.L. Nicolson, The fluid mosaic model of the structure of cell membranes, *Science* **175**, 720 (1972).

48. G. Weissman and R. Clairborne (Eds.) "Cell Membranes: Biochemistry, Cell Biology and Pathology", Hospital Practice, New York, 1975.

49. M.S. Bretsher and M.C. Raff, Mammalian plasma membranes, *Nature* **258**, 43 (1975).

50. R. Harrison and G.G. Lunt, "Biological membranes", Blackie and Sons, Glasgow, 1980.

51. D.E. Vance and J.E. Vance (Eds.), "Biochemistry of Lipids and Membranes," Benjamin/Cummings, Menlo Park, 1985.

52. D.M. Surgenor (Ed.), "The Red Blood Cell," Vol. II, Academic Press, New York, 1975.

53. J.C. Ellory and V.L. Lew (Eds.), "Membrane Transport in Red Cells", Academic Press, New York, 1977.

54. F. Sjostrand and L. Barajas, A new model for mitochondrial membranes based on structural and biochemical information, *J. Ultrastruct. Res.* **32**, 293 (1970).

55. T.L. Steck, The organization of proteins in the human red blood cell membrane. *J. Cell Biol.* **62**, 1 (1974).

56. T. Colon and R. Outhred, The temperature dependence of erythrocyte water diffusion permeability, *Biochim. Biophys. Acta* **511**, 408 (1978).

57. A.K. Solomon, B. Chasan, J.A. Dix, M.F. Lukacovic, M.R. Toon and A.S. Verkman, the aqueous pore in the red cell membrane, *Annals New York Acad. Sci.* **414**, 97 (1983).

58. R. Macey, Transport of water and urea in red blood cells, *Am. J. Physiol.* **246**, c195 (1984).

59. G. Benga, Water permeability in human erythrocytes: identification of membrane proteins involved in water transport, *Eur. J. Cell Biol.* **41**, 252, (1986).

60. G. Benga, p-CMBS binding by membrane proteins and the inhibition of water transport in human erythrocytes, *Biochem.* **25**, 1535 (1986).

61. R. Benz, Formation and properties of tetrameters of band 3 protein from human erythrocyte membrane in planar lipid bilayers, *Biochim. Biophys. Acta* **775**, 347 (1984).

62. W.D. Stein, "Transport and Diffusion across Cell Membranes", Academic Press, Orlando, 1986.

63. M. Bradbury, "The Concept of a Blood-Brain Barrier," John Wiley and Sons, New York, 1979.

64. E. Starling, On the absorption of fluids from the connective tissue spaces, *J. Physiol.* **19**, 312 (1986).

65. F. Bloch, W.W. Hansen and M. Packard, The nuclear induction experiment, *Phys. Rev.* **69**, 127 (1946).

66. E.M. Purcell, H.C. Torrey and R.V. Pound, Resonance absorption by nuclear magnetic moments in a solid, *Phys. Rev.* **69**, 37 (1946).

67. A.E. English, "Multi-component relaxation measurements in muscle", M.Sc. Thesis: University of Toronto (1989).

68. A. Abragam, "The Principles of Nuclear Magnetism", Oxford University Press, Oxford, 1961.

69. C.P. Slichter, "Principles of Magnetic Resonance", 2nd Ed., Springer-Verlag , 1980.

70. E.R. Andrew, "Nuclear Magnetic Resonance", Cambridge University Press, Cambridge, 1955.

71. M. Goldman, "Spin Temperature and Nuclear Magnetic Resonance in Solids", Clarendon Press, Oxford, 1970.

72. T.C. Farrar and E.D. Becker, "Pulse and Fourier Transform NMR", Academic Press, New York, 1971.

73. E. Fukushima and S.B.W. Roeder, "Experimental Pulse NMR: A Nuts and Bolts Approach", Addison-Wesley, Reading, 1981.

74. N. Bloembergen, E.M. Purcell and R.V. Pound, Relaxation effects in NMR absorption, *Phys. Rev.* **73**, 679 (1948).

75. I. Solomon, Relaxation process in a system of two spins, *Phys. Rev.* **99**, 579 (1955).

76. A. Abragam and R.V. Pound, Influence of electric and magnetic fields on angular correlations, *Phys. Rev.* **92**, 943 (1953).

77. M.C. Wang and G.E. Uhlenbeck, Reference unavailable,*Rev. Mod. Phys.* **17**, 323 (1945).

78. L.E. Reichl, "A Modern Course in Statistical Physics", University of Texas Press, Austin, 1980.

79. G.P. Jones, Spin-lattice relaxation in the rotating frame: weak-collision case, *Phys. Rev.* **148**, 332 (1966).

80. H.M. McConnell, Reaction rates by NMR, *J.Chem. Phys.* **28**, 430 (1958).

81. D.E. Woessner, Nuclear transfer effects in NMR pulse experiments, *J. Chem. Phys.* **35**, 41, (1961).

82. D.E. Woessner and J.R. Zimmerman, Reference unavailable, *J. Phys. Chem.* **67,** 1590 (1963).

83. H.T. Edzes and E.T. Samulski, The measurement of cross-relaxation effects in the proton NMR spin-lattice relaxation of water in biological systems: hydrated collagen and muscle, *J. Magn. Reson.* **31**, 207 (1978).

84. M. Eisenstadt and M.E. Fabry, NMR relaxation of the hemoglobin-water proton spin system in reb blood cells, *J. Magn. Reson.* **29**, 591 (1978).

85. B. Halle and H. Wennerstrom, Interpretation of magnetic resonance data from water nuclei in heterogeneous systems, *J. Chem. Phys.* **75**, 1928 (1981).

86. P.S. Allen, On nuclear spin-lattice relaxation due to hindered molecular reorientation. *J. Phys.* C. **6**, 3174 (1973).

87. D.E. Woessner, Spin relaxation processes in a two-proton system under anisotropic rotation, *J. Chem. Phys.* **36**, 1 (1962).

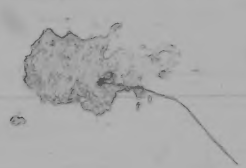

88. S.H. Koenig and W.E. Schillinger, NMR dispersion in protein solutions, *J. Biol. Chem.* **244**, 3283 (1969).

89. R.H. Walmsley and M. Shporer, Surface induced NMR line splittings and augmented relaxation rates in water, *J. Chem. Phys.* **68**, 2584 (1978).

90. P.G. Lauterbur, Image formation by induced local interactions: examples employing nuclear magnetic resonance, *Nature* **242**, 190 (1973).

91. K.F. King and P.R. Moran, A unified description of NMR imaging, data-collection strategies and reconstruction, *Med. Phys.* **11**, 1 (1984).

92. P. Mansfield and P.G. Morris, "NMR Imaging in Biomedicine", Academic Press, London, 1982.

93. A. Kumar, D. Welti and R.R. Ernst, NMR Fourier zeugmatography, *J. Magn. Reson.* **18**, 69 (1975).

94. P.R. Locher, Computer simulation of selective excitation in nmr imaging, *Phil. Trans. R. Soc. Lond.* B **289**, 537 (1980).

95. P.T. Callaghan and C.D. Eccles, Diffusion-limited resolution nuclear magnetic resonance microscopy, *J. Magn. Reson.* **78**, 1 (1988).

96. G.E. Santyr, R.M. Henkleman and M.J. Bronskill, Spin-locking for magnetic resonance imaging with application to human breast, *Magn. Reson. Med.* **12**, 25 (1989).

97. W. Hinshaw, E.R. Andrew, P.A. Bottomley, G.N. Holland, W.S. Moore and B.S. Worthington. Display of cross sectional anatomy by nuclear magnetic resonance imaging, *Brit. J. Radiol.* **51**, 273 (1978).

98. W.S. Hinshaw, P.A. Bottomley and G.N. Holland, Radiographic thin-section image of the human wrist by nuclear magnetic resonance, *Nature* **270**, 722 (1977).

99. P Mansfield, I.L. Pykett, P.G. Morris and R.E. Coupland, Human whole body line-scan imaging by NMR, *Brit. J. Radiol.* **51**, 921 (1978).

100. R.C. Hawkes, G.N. Holland and W.S. Moore, Nuclear magnetic resonance (NMR) tomography of the brain: a preliminary clinical assessment with demonstration of pathology, *J. Comput. Assist. Tomogr.* **4**, 577 (1980).

101. I. Klatzo and F. Seitelberger (Eds.), "Brain Edema", Springer-Verlag, New York, 1967.

102. H.J. Manz, The pathology of cerebral edema, *Human Pathol.* **5**, 291 (1974).

103. M. de Vlieger, S. A. de Lange and J.W.F. Beks, "Brain Edema", John Wiley and Sons, New York, 1974.

104. L. Backay and J.C. Lee, "Cerebral Edema", Charles C. Thomas, Springfield , 1965.

105. J.B. Bederson, H.M. Bartkowski, K. Moon, M. Halks-Miller, M.C. Nishimura, M. Brant-Zawadzki and L.H. Pitts, Nuclear magnetic resonance imaging and spectroscopy in experimental brain edema in a rat model, *J. Neurosurg.* **64**, 795 (1986).

106. L. Kanman, K.G. Go, W. Brouwer and H.J. Berendsen, Nuclear magnetic resonance relaxation in experimental brain edema: effects of water concentration, protein concentration and temperature, *Magn. Reson. in Med.* **6**, 265 (1988).

107. S. Naruse, Y. Horikawa, T. Chuzo, K. Hirakawa, H. Nishikawa and K. Yoshizakai, Proton nuclear magnetic resonance studies on brain edema, *J. Neurosurg.* **56**, 747 (1982).

108. K.G. Go and H.T. Edzes, Water in brain edema, *Arch. Neurol.* **32**, 462 (1975).

109. L. Backay, R.J. Kurland, R.G. Parish, J.C. Lee, R.J. Peng and H.M. Bartkowski, Nuclear magnetic resonance studies in normal and edematous brain tissue, water in brain edema, *Exp. Brain Res.* **23**, 241 (1975).

110. M.E. Castro, "Experimental brain edema studied with proton NMR", Ph.D. Thesis: University of Alberta (1986).

111. J. Zhong, J.C. Gore and I.M. Armitage, Relative contributions of chemical exchange and other relaxation mechanisms in protein solutions and tissues, *Magn. Reson. in Med.* **11**, 295 (1989).

# CHAPTER 2[1]

## Solvent proton relaxation in aqueous solutions of the serum proteins $\alpha_2$-macroglobulin, fibrinogen and albumin

### 2.1 Introduction

The modification of water proton relaxation rates by soluble proteins in both model systems and tissue has been a problem of longstanding interest and debate (reviews 1-3 and references therein). It is a problem that is very relevant to the development of proton nuclear magnetic resonance imaging (NMRI) as a quantitatively specific diagnostic modality. The development of specificity has been hindered by at least two factors, namely by an insufficient understanding of the mechanisms governing proton relaxation in tissues, of which protein solutions (4-11) are often used as the simplest of models, and by a self-imposed limitation of the imaging technique to the laboratory frame longitudinal ($R_1$) and transverse ($R_2$) relaxation rates. The inclusion of rotating frame relaxation measurements ($R_{1\rho}$) offers an additional means of interrogating the changes in water motion that take place during pathological change in tissue (12). This, together with a more complete body of understanding of the sensitivity characteristics of the various proton relaxation mechanisms to the concentration of individual serum proteins and their mixtures in aqueous solution, could improve our current understanding of water proton relaxation in tissue.

---

[1] A version of this chapter has been published. R.S. Menon and P.S. Allen, Solvent proton relaxation in aqueous solutions of the serum proteins $\alpha_2$-macroglobulin, fibrinogen and albumin, *Biophys. J.* 57, 384 (1990).

For both the aqueous protein solution model and for tissue, it is usually accepted that the two-site rapid exchange of water molecules, between aqueous solvent and the surface region of protein macromolecules, is an important determinant of the observed water proton relaxation rates. In the aqueous solvent compartment of either system, motional averaging is always taken to be complete. However, the relaxation mechanisms operating at the sites of water molecules 'associated' with protein surfaces have been interpreted differently. For macromolecular solutions, where the majority of data has come from measurements of the field dependence of the longitudinal relaxation rate, (4, 9, 10), two successive motional processes have been invoked to explain the experimental results. At the higher frequencies of the motional power spectrum, anisotropic reorientation of the 'associated' water molecules has been proposed (13) as an active relaxation mechanism but this motion acts as only a partial averager of the local fields at the water proton sites. Protein motion through the solvent has been proposed (14) as the slower motion that completes the averaging of these local fields prior to two-site exchange. In tissue experiments on the other hand (15, 16), the lower frequency motion that completes the averaging started by anisotropic reorientation is assumed to be the two-site exchange process itself. If this difference in mechanism is indeed the case, even for the largest of serum proteins, then it limits the potential usefulness of protein solutions as a model of tissue in the experimental regime of transverse and rotating frame relaxation.

By taking an approach that is somewhat different from the $R_1$ dispersion method, namely the study of several proteins spanning a very wide range of size by means of relaxation measurements that are readily accessible for *in-vivo* NMR

purposes, it has been possible to demonstrate that even for the two very large proteins fibrinogen and $\alpha_2$-macroglobulin, protein motion and not two-site exchange completes the averaging of the local fields at 'associated' water sites. Moreover, changes in the molar sensitivity between the different relaxation parameters are sufficiently different, from those that would be expected from a simple single motion model, to enable us to establish a quantitative consistency between the data presented here and the two-motion model that has emerged from a substantial amount of previous $R_1$ dispersion work on aqueous macromolecular solutions. A preliminary report of this chapter was presented at the VI$^{th}$ Annual Meeting of the Society of Magnetic Resonance in Medicine (17).

## 2.2 Experimental

### 2.2.1 Materials

Solutions of human $\alpha_2$-macroglobulin, human fibrinogen and human serum albumin were made using isotonic saline buffers that consisted of doubly distilled, deionized water, which have been made isotonic with human serum by dissolving reagent grade NaCl in appropriate amounts. In order to keep the pH of the protein solution physiological, and to facilitate dissolving large amounts of protein, Tris-HCl was used to bring the solution pH between 7.2 and 8. Previous studies (4, 9, 10) suggest that there is little pH dependence of the relaxation rates $R_1$ and $R_2$ in this physiological pH range. The protein concentrations were also chosen to represent the range of physiologically expected values. Human fibrinogen (lyophilized, Sigma Chemical Co., St. Louis, MO) and human serum albumin (supplied as 100 g/l in 0.9 % NaCl, Sigma Chemical Co.) were studied in the range 0 g/l to 50 g/l (0 to 147 μM and 0 to 725 μM, respectively). Human $\alpha_2$-macroglobulin (lyophilized,

Sigma Chemical Co.), on the other hand, was studied only in the range 0 g/l to 16.67 g/l (0 to 23 μM) because of its poor solubility. The relevant properties of these proteins are shown in Table 2.1. All samples were stored at 4 °C and used within 72 hr of preparation, although repeatable results could be obtained over periods of as long as 3 weeks.

### 2.2.2 Relaxation Measurements

The proton relaxation rates were measured at 100 MHz with a Bruker CXP spectrometer. The line width obtained for a 100 μl sample in the 40 cm bore magnet was typically 5 Hz. During the experiment, sample temperatures were kept at 37 ± 2 °C by warm airflow. The coil and receiver electronics had a combined dead time of 40 μs; this precluded accurate measurement of the "solid" signal originating from protons bound firmly in the protein structure. The transverse relaxation of the solvent was measured using a Carr-Purcell-Meiboom-Gill (CPMG) add/subtract sequence (20, 21), with an inter-echo spacing of 400 μs. This choice of echo time was made to minimize the effects of diffusion on $R_2$. The add/subtract sequence was repeated 32 times and the resulting signal was averaged. The longitudinal magnetization was measured using the Freeman-Hill (22) modification of the inversion recovery sequence

$$[180_y - \tau - 90_x - AQ - TR / 0 - \tau - 90_{-x} - AQ - TR] \qquad (2.1)$$

where TR is a fixed magnetization recovery interval. The τ values, ranging from 10 μs to 7.9 s, were arranged to provide 10 data points in each decade of time. The advantage of using this particular sequence lay in the fact that the magnetization recovery curve is always positive, dropping from $2M_0$ to zero, with the initial

magnetization $M_o$ being measured as often as the partly relaxed magnetization. Eight acquisitions of each add/subtract pair were averaged. The magnetization decay in the rotating frame was measured using the phase alternated sequence

$$[90_x\text{ -- }\tau(\text{lock})_y\text{ -- AQ -- TR / }90_{-x}\text{ -- }\tau(\text{lock})_{-y}\text{ -- AQ -- TR}] \qquad (2.2)$$

in which the free induction decay was collected after each spin-locking pulse. The length of the spin-locking pulse was varied over the same sixty $\tau$ values used for the inversion recovery experiment and the signal averaging was also equivalent to that of the inversion recovery experiment. Four different amplitudes, $B_1$, of the spin-locking pulse were employed, namely, 0.3, 0.6, 0.9 and 1.8 mT. $B_1$ was calculated from the length of a 90° pulse in a special pulse program and was known to ± 5 %.

All relaxation rates were obtained with a recovery interval (TR) of 30s and a 90° pulse length of 7.5 μs. $R_1$, $R_2$, and $R_{1\rho}$ were obtained by means of a non-linear least-squares fitting program capable of fitting up to four exponentially decaying components to a curve. The repeatability of a particular relaxation rate measurement on the same samples over a period of several weeks was ± 0.4 % for $R_2$, ± 3 % for $R_1$, and ± 5 % for $R_{1\rho}$. These uncertainties do not include all sources of random error, such as that in concentration for example, that contribute to the scatter in later figures.

## 2.3 Results

The concentration dependence of $R_1$ and $R_2$ of the protein solutions are shown in Figures 2.1 and 2.2. The concentration dependence of $R_{1\rho}$ for the same solutions is shown in Figure 2.3 at a spin-locking field of 0.3 mT. The buffer intercepts for albumin are different from those of fibrinogen and $\alpha_2$-macroglobulin

because of the influence of the supplier's buffer in which the parent sample of albumin was dissolved. A crucial point in all three cases is that the magnetization recovery, or decay, was mono-exponential over a change in amplitude of several decades. This is consistent with the results of other workers on the laboratory frame relaxation in dilute solutions of fibrinogen (4) and albumin (10, 23, 24). The spin-locking field dependence of $R_{1\rho}$ is shown for selected concentrations in Figure 2.4.

Of primary interest is the relative molar sensitivity of the relaxation rates $R_i$ ($R_1$, $R_2$, or $R_{1\rho}$) to protein solute. These sensitivities, namely the gradients $g_i$ ($g_1$, $g_2$, or $g_{1\rho}$), of the $R_i$ versus molarity are detailed in Table 2.2. For comparative purposes, the range of sensitivities $g_1$ and $g_2$ derived from the work of various other workers is also shown. It should be borne in mind however, that in addition to differences in frequency and temperature, these other workers employed different buffers, and in many cases, did not divulge their inter-echo spacing. That this is an important omission for protein solutions that exhibit substantial diffusion is exemplified by the fact that, with our magnet inhomogeneity and at 37 °C, the apparent $R_2$ can be increased by a factor of two if one increases the inter-echo interval from 0.4 to 40 ms.

## 2.4 Analysis and Discussion

From the data presented in the results section, it is clear that, in common with several other workers on protein solutions (4, 23, 24), we find that each of the relaxation rates displays a linear concentration dependence over the concentration range to 50 g/l. Such behaviour is consistent with a two-site rapid-exchange model of relaxation (27), and even though this model is not universally accepted (11), it has been invoked (4, 9, 14, 23, 24-26, 29, 30) to explain the observed relaxation of

solvent nuclei in many dilute macromolecular solutions. We therefore choose to analyse our results according to this model. Workers using macromolecular concentrations much higher than those found physiologically have suggested an extension of this model to three or more exchanging fractions (3, 10, 30-33). These extra fractions, generally thought to consist of very tightly bound water, are only expected to be discernable when the overall proportion of water is very low and not at physiological concentrations.

For a two-site rapid-exchange model in which the motion at each site completely averages the local magnetic fields, the observed solvent relaxation rate, $R_i$, is given by

$$R_i = p_a R_{ia} + p_b R_{ib} \qquad (2.3)$$

where $R_{ia}$ is the relaxation rate of the 'associated' water protons, $R_{ib}$ is that of the bulk water protons, and $p_a$ and $p_b$ represent their relative fractions, i.e., $p_a + p_b = 1$. The relaxation efficiency at each site, namely, $R_{ia}$ and $R_{ib}$, is then dependent upon the magnitude of the local field being averaged and on the rate at which it is being modulated. Rewriting the relative fractions of the water species, in terms of the protein concentration, c, $R_i$ becomes,

$$R_i = R_{ib} + c\,[0.018\, h_a\, (R_{ia} - R_{ib})/M] \qquad (2.4)$$

where $h_a$ is the average number of water molecules 'associated' with each protein macromolecule and M is the protein molecular weight (9). The linear dependence of $R_i$ on c shown in Figures 2.1 to 2.3 reflects the form of Equation 2.4 and is consistent with a concentration independence of $h_a$ and $R_{ia}$ at the low physiological concentrations studied. These two variables define a molar sensitivity, $g_i$, where

$$g_i = 0.018\, h_a\, (R_{ia} - R_{ib}) \qquad (2.5)$$

that is tabulated in Table 2.2. It will be noticed that, although the gradients of Figures 2.1 to 2.3 do not increase monotonically with increasing solute molecular size, the molar sensitivities do.

The dependence of $g_i$ on protein solute could arise through either $h_a$ or $R_{ia}$ or both. Assuming that $h_a$ is proportional to the surface area, $A_S$, of the model molecular shapes whose dimensions are given in Table 2.1, any remaining dependence on protein solute that might arise through $R_{ia}$ can be detected from the variation of $g_i/A_S$, listed in Table 2.3. For the transverse and rotating frame relaxation, $g_i/A_S$ retain a strong dependence on protein solute. In fact they are in a very similar ratio, 1:5:8, to that for the solute molecular mass, namely, 1:5:10, suggesting that the mechanisms governing $R_{2a}$ and $R_{1\rho a}$ depend on protein motion within the solvent. In contrast, $g_1/A_S$ shows much less solute dependence, being essentially unchanged between the ellipsoidal molecules albumin and fibrinogen. One might therefore speculate that for albumin and fibrinogen at least, and to a lesser extent for $\alpha_2$-macroglobulin, the longitudinal relaxation rate $R_{1a}$ is governed by a mechanism that is not too sensitive to overall molecular size but more to the local environment of the 'associated' water molecules. The protein dependence of the molar sensitivities, is therefore suggestive of the same model as that derived from $R_1$ dispersion measurements on a variety of protein solutes (4, 10, 11), namely that the lower frequency motional spectral densities that determine transverse and rotating frame relaxation efficiencies arise primarily from overall solute motion, whereas local motion on the surface of the macromolecule is apparently much more important in determining the high frequency motional spectral densities that govern the

longitudinal relaxation efficiency at 100 MHz. One mechanism previously suggested for this local motion is the anisotropic reorientation of the water molecules associated with the protein surface (13). Although such reorientation is an effective relaxation agent, it is not capable of fully averaging the local dipolar fields and therefore it leaves the opportunity for the slower protein motion to complete the averaging, prior to two-site exchange becoming effective at averaging the local fields at 'associated' sites of water molecules.

This view is not however consistent with the interpretation of results from tissue, a system that one might wish to model using protein solutions. Burnell et al (15) as well as Diegel and Pintar (16) have explained the marked dispersion of their $R_{1\rho}$ data from tissue by using the two-site exchange process itself as the mechanism that completes the averaging of local dipolar fields. The $R_{1\rho}$ data presented here on the other hand, display a much smaller frequency dependence than that observed in tissue, even for large molecules such as fibrinogen and $\alpha_2$-macroglobulin, and moreover, $g_{1\rho}/A_s$ is strongly solute dependent. We therefore assume protein motion to be the ultimate averager of the local fields at the sites of water molecules 'associated' with these protein surfaces, prior to two-site exchange with bulk water molecules, and write

$$R_{ia} = R_{iar} + R_{ipm} \qquad (2.6)$$

where $R_{iar}$ and $R_{ipm}$ correspond respectively to the contributions to the relaxation efficiency of the 'associated' water molecules from their anisotropic re-orientation and from protein motion. The tissue data can be reconciled with this if one supposes that in tissue the majority of the macromolecular surface results from the non-mobile cellular architecture and not from mobile proteins

Having made this assumption, the consistency between the solute and concentration dependence data presented here and that of earlier workers using $R_1$ dispersion methods can be carried further, because the relative magnitudes of the different $g_i$ for a single protein solute are indicative of the relative strengths and the frequency ranges of influence of these two relaxation mechanisms. For example, in very simple circumstances where all three relaxation processes are governed by the same single motion, it is possible, by taking the ratios $g_i/g_j$, to relate all three sensitivities in terms of a single variable, the correlation time of that motion $\tau_c$. Such relationships are arrived at by making the standard assumptions about dipolar relaxation (34, 35); by taking the ratio of the sensitivities one is able to eliminate the unknown parameter, $h_a$. Solution of the ratio equations in this simplest of cases will then give consistent values for $\tau_c$, irrespective of which ratio of experimental sensitivities is chosen. For our data on albumin and fibrinogen, $g_2/g_{1\rho}$ and $g_2/g_1$ predict values of $\tau_c$ that are different by 2 to 3 orders of magnitude, differences that are well beyond the uncertainties carried through from the measurement error. The assumption embodied in Equation 2.6 enables us to reconcile these differences and at the same time demonstrate the agreement between the two experimental methods.

The ratios of the molar sensitivities, $g_i$, for a single protein species give rise to an expression in $R_{iar}$ and $R_{ipm}$ alone, i.e., one that eliminates the need to estimate the unknown parameter $h_a$, namely,

$$g_i/g_j = \{(R_{iar} + R_{ipm})/(R_{jar} + R_{jpm})\} \cdot \{1 - R_{ib}/(R_{iar} + R_{ipm}) + R_{jb}/(R_{jar} + R_{jpm})\} \qquad (2.7)$$

where the terms in $R_{ib}$ and $R_{jb}$ are small and can usually be neglected. For instance, from the data presented in the results section, it is clear that terms containing $R_{ib}$ and $R_{jb}$ are of the order of $5 \times 10^{-3}$ for $R_2$ and $R_{1\rho}$, and $5 \times 10^{-2}$ for $R_1$. We have therefore neglected them in what follows.

If the motions that govern $R_{iar}$ and $R_{ipm}$ can be characterized by correlation times $\tau_{ar}$ and $\tau_{pm}$ respectively, and if the corresponding dipolar interaction strength factors can be represented by $S_{ar}$ and $S_{pm}$, Equation 2.7 can be rewritten

$$g_i/g_j \cong \{S_{ar}\,\zeta_i(\tau_{ar}) + S_{pm}\,\zeta_i(\tau_{pm})\} / \{S_{ar}\,\zeta_j(\tau_{ar}) + S_{pm}\,\zeta_j(\tau_{pm})\} \qquad (2.8)$$

where $\zeta_i$ is the sum of Debye spectral density functions governing the relaxation rate $R_i$ (34, 35).

Parenthetically, it should be noted at this point that the dipolar interaction that is modulated by anisotropic reorientation, and which leads to $R_{iar}$, also facilitates the exchange of spin energy between protein protons and 'associated' water protons (36). The consequence of the spin energy exchange will be a reduction of the effective $R_{iar}$, because this pathway to the thermal bath will now also be used to transfer Zeeman energy from the protein protons to that bath (37). Estimates of the number of 'associated' water molecules from hydration fractions (3), suggests that in a 20 g/l solution the protein protons and the 'associated' water protons have similar thermal capacities. As a result, spin energy exchange could have a significant effect on the strength $S_{ar}$ of $R_{iar}$.

If we assume that $R_2$ and $R_{1\rho}$ are both dominated by the slower motion characterized by $\tau_{pm}$, Equation 2.8 for the case of these two relaxation rates reduces to

$$g_2/g_{1\rho} \cong \zeta_2(\tau_{pm}) / \zeta_{1\rho}(\tau_{pm}) \cong \tau_{pm}/\zeta_{1\rho}(\tau_{pm}) \qquad (2.9)$$

from which an estimate of $\tau_{pm}$ can be obtained. This low frequency motion hypothesis is supported by the observation of a weak RF field dependence in the $R_{1\rho}$ measurements and gives rise to the estimates for $\tau_{pm}$ given in Table 2.3 that are consistent with $R_1$ dispersion data at low fields from several different macromolecules (4, 10, 11). $R_1$, on the other hand, depends only upon spectral densities at $\omega_o$ and $2\omega_o$ (where $\omega_o/2\pi$ = 100 MHz) and will therefore be influenced more by the faster of the two motions. For $R_2$ and $R_1$, Equation 2.8 will approximate to

$$g_2/g_1 \cong S_{pm}\, \zeta_2(\tau_{pm}) / S_{ar}\, \zeta_1(\tau_{ar}). \qquad (2.10)$$

Using the $\tau_{pm}$ from Table 2.3 enables us to obtain estimates for the product $S_{pm}/S_{ar}$ $\zeta_1(\tau_{ar})$.

In order to relate $S_{ar}$ and $S_{pm}$, earlier workers (4, 15) took advantage of the fact that both of the motions under discussion were modulating the local field at the same proton site. By writing the static value of this local field as S, the strengths $S_{ar}$ and $S_{pm}$ can be related (15) in terms of an order parameter $\chi$, such that

$$S_{ar} = (1-\chi^2)\, S, \text{ and } S_{pm} = \chi^2 S. \qquad (2.11)$$

$g_2/g_1$ therefore gives rise to a value for the quantity $\chi^2/(1 - \chi^2) \cdot \zeta_1(\tau_{ar})$. To separate $\chi$ from $\tau_{ar}$ in this quantity, it is necessary to invoke additional information. For example, an upper limit for $\chi^2/(1 - \chi^2)$ may be obtained by utilizing in Equation 2.10 the maximum value of $\zeta_1(\tau_{ar})$. At a Larmor frequency of 100 MHz, this maximum is $2.268 \times 10^{-9}$ and it occurs when $\omega_0\tau_{ar} = 0.62$ at the so-called BPP maximum in $R_1$. The values of $\chi^2/(1-\chi^2)$ in this limiting case are given in Table 2.3. For fibrinogen the limit is consistent with the value obtained from $R_1$ dispersion measurements (4), suggesting that $\tau_{ar} \equiv 10^{-9}$ s (also consistent with the results of references 4 and 11). For albumin the lower limit for $\chi^2/(1-\chi^2)$ is an order of magnitude smaller (consistent with $R_1$ dispersion measurements of reference 10). It should be noted that the quantity $\chi^2/(1 - \chi^2)$ is analogous to the ratio $A\tau_{ar}/D\tau_{pm}$ (where A and D are defined in reference 4) introduced by workers using the modified Cole-Cole expression to explain $R_1$ dispersion measurements (4, 6, 7, 10, 11). The values of $\chi^2/(1 - \chi^2)$ obtained here are very similar to their values of $A\tau_{ar}/D\tau_{pm}$.

In the analysis presented here, we have interpreted the data in terms of two motional processes, each having a unique correlation time. The unique correlation time is likely to be an oversimplification of reality, particularly for the motion of anisotropic molecules such as fibrinogen. However, it is our view that the nature of the data presented does not justify the inclusion of other adjustable parameters in its interpretation, and we have therefore limited ourselves to the simplest of models (with three adjustable parameters $\tau_{pm}$, $\tau_{ar}$ and $\chi$) that is capable of establishing the consistency of our data with that from a variety of aqueous and macromolecular solutions using $R_1$ dispersion techniques.

## 2.5 Conclusions

We have investigated aqueous solutions of two very large serum proteins, namely fibrinogen (340 kD and markedly anisotropic) and $\alpha_2$-macroglobulin (725 kD and isotropic), in conjunction with measurements on solutions of albumin (69 kD and anisotropic). We have, moreover, employed a physiological range of concentrations of these proteins together with proton relaxation measurements that are readily accessible for in-vivo NMR purposes namely, $R_1$, $R_2$ and $R_{1\rho}$, in order to obtain the molar sensitivities of each of these relaxation processes for each protein solute.

The solute dependence of the molar sensitivities of both transverse and rotating frame relaxation shows that the low frequency motional power spectrum which governs the dipolar relaxation of water protons, is dependent on protein mass in a way which suggests that protein motion through the solvent, and not two-site exchange, is responsible for completion of the averaging of the local fields at the water sites 'associated' with macromolecular surfaces. This conclusion is reinforced by the weak RF field and strong solute dependence of $R_{1\rho}$. Even with very large proteins, therefore, protein solutions are not an appropriate model for $R_2$ and $R_{1\rho}$ in tissue. The longitudinal relaxation rate at 100 MHz does not exhibit the same behaviour.

In extracting our conclusions, we have used only three parameters, namely, $\tau_{pm}$, $\tau_{ar}$ and $\chi$, in addition to the assumptions of the conventional models of dipolar relaxation. We have estimated a value for one, $\tau_{pm}$, from our data, assumed a range for another, $\tau_{ar}$, from previously published $R_1$ dispersion information, and estimated a limiting value for a third, $\chi$. The models used to interpret $R_1$ dispersion data are

often more complex, typically using four fitting parameters to interpret the data in terms of two different motions of the protons at the water sites associated with the macromolecule, namely, anisotropic motion on the macromolecular surface and overall macromolecular motion. Nevertheless, the relative magnitudes of $g_1$, $g_2$ and $g_{1\rho}$ for a single protein are consistent not only with the correlation times derived from $R_1$ dispersion data, but also with the relative strengths, previously reported, for the two interactions that are modulated by these motions.

Table 2.1*

Physical parameters of the human serum proteins

| Protein | Molecular Weight (kD) | Molecular Radii† (A) | Diffusion Constant§ ($\times 10^{-7}$ cm$^2$s$^{-1}$) | Plasma Concentration (g/l) |
|---|---|---|---|---|
| Albumin | 69 | 70 x 25 x 25 | 6.7 | 40.0 - 50.0 |
| Fibrinogen | 340 | 450 x 15 x 15 | 1.9 | 2.0 - 5.0 |
| $\alpha_2$-Macroglobulin// | 725 | 100 x 100 x 100 | 2.3 | 2.2 - 3.8 |

*Reference 18 and references therein
†Shapes modelled as prolate ellipsoids with symmetric semi-minor axis.
§$D_{20,w}$
//Reference 19

Table 2.2

Molar sensitivities of $R_1$, $R_2$, and $R_{1\rho}$ to proteins in aqueous solution

| PROTEIN | $g_1$ ($\times 10^3 s^{-1}M^{-1}$) | $R_{1b}$ ($s^{-1}$) | $g_2$ ($\times 10^3 s^{-1}M^{-1}$) | $R_{2b}$ ($s^{-1}$) | $g_{1\rho}$ (@3G) ($\times 10^3 s^{-1}M^{-1}$) | $g_{1\rho}$ (@18G) ($\times 10^3 s^{-1}M^{-1}$) | $R_{1\rho b}$ ($s^{-1}$) |
|---|---|---|---|---|---|---|---|
| Albumin | 0.21 | 0.27 | 0.8 | 0.35 | 0.7 | 0.6 (@9G) | 0.27 |
| Fibrinogen | 0.63 | 0.24 | 15 | 0.30 | 14 | 11 | 0.26 |
| α-Macro-globulin | 5.0 | 0.24 | 46 | 0.30 | 46 | 44 | 0.26 |
| Albumin (9,23,25,26) | 0.1-0.75 | | 1.0-2.5 | | | | |
| Fibrinogen (4) | 0.85 | | | | | | |

Uncertainty in $g_i \leq \pm 10\%$
Uncertainty in $R_i \leq \pm 5\%$

Table 2.3

Calculated prameters derived from molar sensitivities

| PROTEIN | $g_1/A_s$ ($s^{-1}M^{-1}Å^{-2}$) | $g_2/A_s$ ($s^{-1}M^{-1}Å^{-2}$) | $g_{1\rho}/A_s$ ($s^{-1}M^{-1}Å^{-2}$) | $\tau_{pm}$ ($s^{-1}$) | $\frac{S_{pm}}{S_{ar}\zeta_1(\tau_{ar})}$ | $\left(\frac{\chi^2}{1-\chi^2}\right)_{min}$ |
|---|---|---|---|---|---|---|
| Albumin | 0.012 (@9G) | 0.045 | 0.034 | $(2.3\pm0.7) \times 10^{-6}$ | $1 \times 10^6$ | 0.003 |
| Fibrinogen | 0.009 (@18G) | 0.23 | 0.16 | $(1.6\pm1.4) \times 10^{-6}$ | $1 \times 10^7$ | 0.02 |
| $\alpha_2$-Macroglobulin | 0.040 (@18G) | 0.37 | 0.35 | $(1\pm1) \times 10^{-6}$ | $5 \times 10^6$ | 0.01 |

The uncertainties in $g_i/A_s$ are at least 10% due to the uncertainty in $g_i$.
The uncertainty in estimates $S_{pm}/S_{ar}\,\zeta_1(\tau_{ar})$ are of the order of 100%
$\left(\frac{\chi^2}{1-\chi^2}\right)_{min}$ is a lower limit

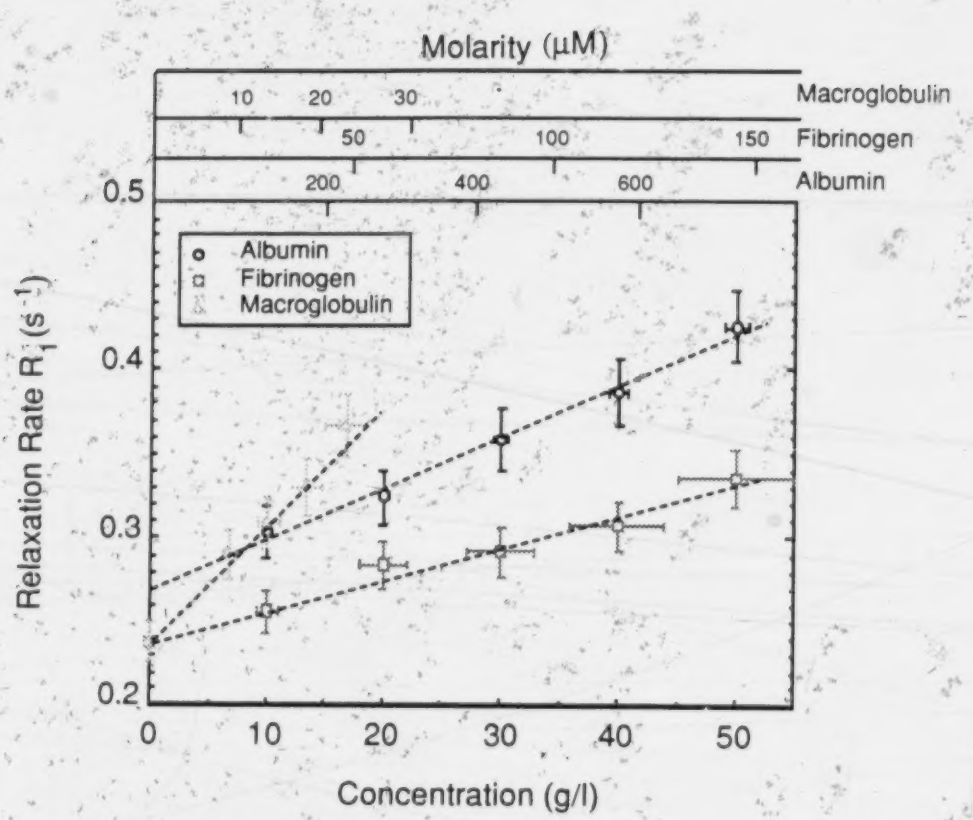


**Figure 2.1**. A comparison of the concentration dependence for the $^1H$ longitudinal relaxation rates obtained for the serum proteins albumin (o), fibrinogen (□), and $\alpha_2$-macroglobulin (Δ) in aqueous solution. The error bars represent the standard deviations derived from measurements on four repeated occasions when a solution of the same concentration was manufactured. The fitted lines were calculated from a linear least squares procedure. The slopes and intercepts thus calculated are shown in Table 2.2.

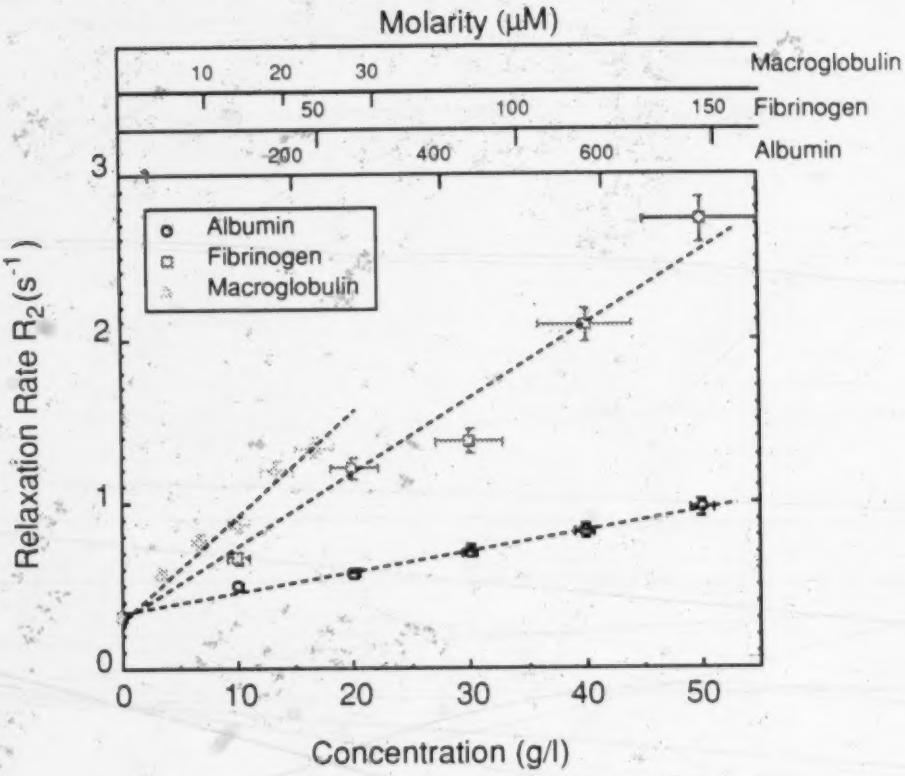


**Figure 2.2**. A comparison of the $^1H$ transverse relaxation rate concentration dependence for the serum proteins albumin (o), fibrinogen (□), and $\alpha_2$-macroglobulin (Δ) in aqueous solution. The error bars represent the standard deviations derived from measurements on four repeated occasions when a solution of the same concentration was manufactured. The best-fit lines were derived from a linear least squares procedure. The slopes and intercepts are shown in Table 2.2

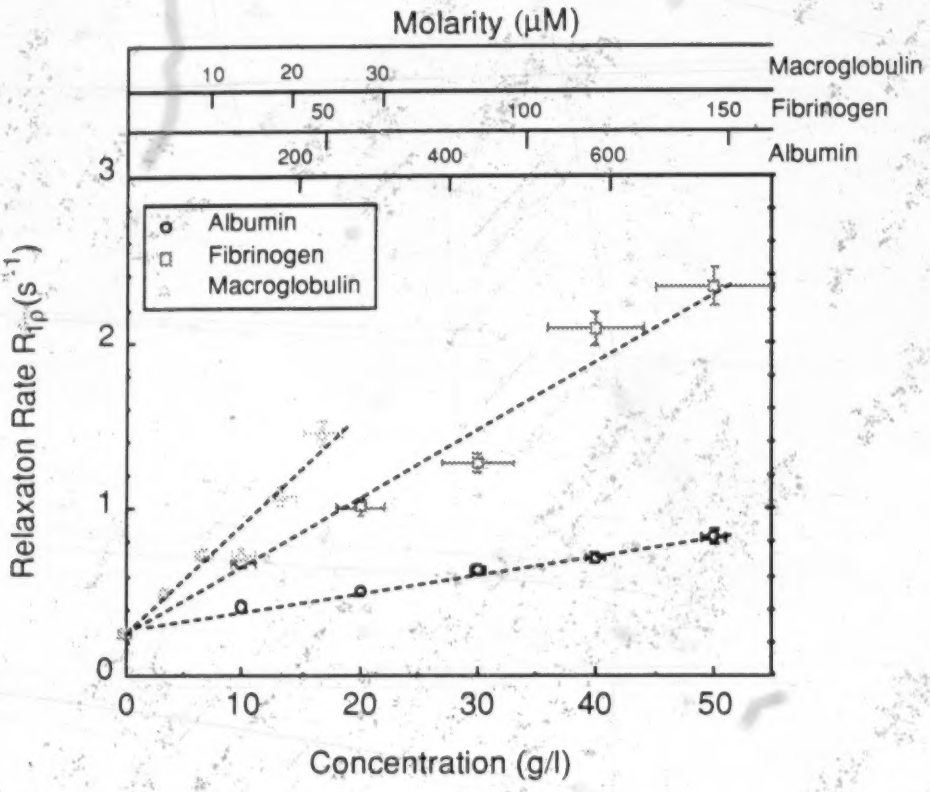


**Figure 2.3**. A comparison of the $^1H$ longitudinal relaxation rates in the rotating frame, observed at a spin-locking field of 3.07 G for the serum proteins albumin (o), fibrinogen (▫), and $\alpha_2$-macroglobulin (Δ) in aqueous solution. The error bars represent the standard deviations derived from measurements on four repeated occasions when a solution of the same concentration was manufactured. The lines were derived from a linear least squares fit to the data and the slopes and intercepts are shown in Table 2.2. The relaxation rates observed at higher spin-locking fields are qualitatively similar to those shown in this figure.

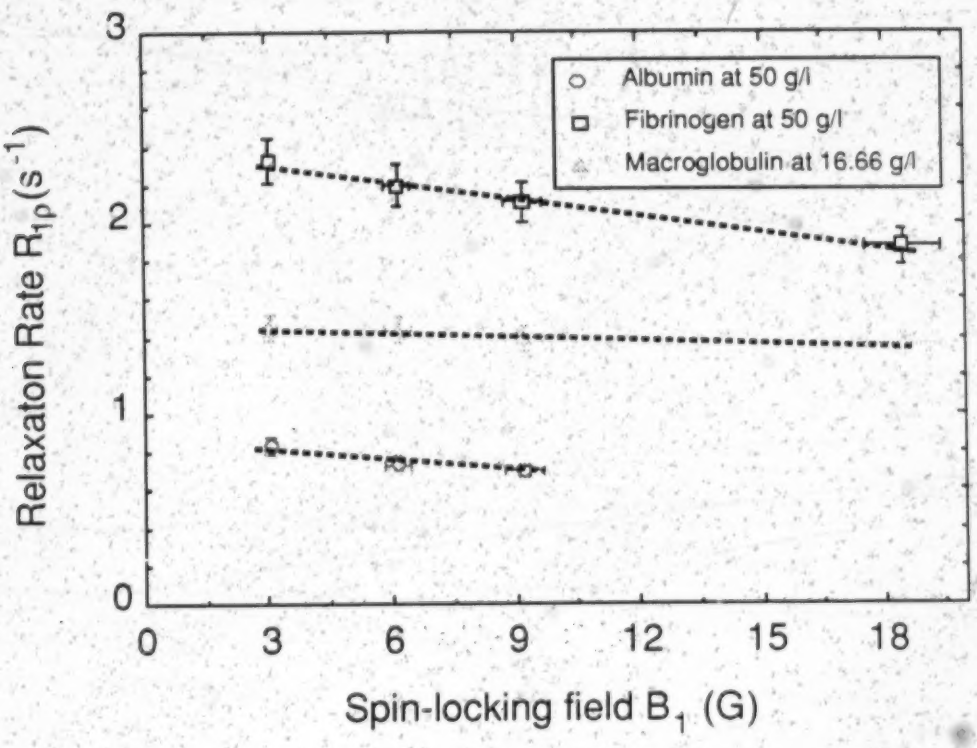


**Figure 2.4.** The $^1H$ longitudinal relaxation rate in the rotating frame as a function of the spin-locking field. Data are shown for the concentration of each protein indicated in the figure. The best-fit lines were obtained from a linear least squares fitting routine.

## 2.6 References


1. P.S.Belton and R.G. Ratcliffe, NMR and compartmentation in biological tissues, *Progress in NMR Spectroscopy* **17**, 241 (1985).
2. R. Mathur-De Vre, The NMR studies of water, *Prog. Biophys. Molec. Biol.* **35**, 103 (1979).
3. G.D. Fullerton, J.L. Potter and N.C. Dornbluth, NMR relaxation of proteins in tissue and other macromolecular water solutions, *Magn. Reson. Imaging* **1**, 209 (1982).
4. S. Conti, Proton magnetic relaxation dispersion in aqueous biopolymer systems I. Fibrinogen solutions, *Mol. Phys.* **59**, 449 (1986).
5. R.G. Bryant and W.M. Shirley, Dynamical deductions from nuclear magnetic resonance relaxation measurements at the water-protein interface, *Biophys. J.* **32**, 3 (1980).
6. S.H. Koenig, R.G. Bryant, K. Hallenga and G.S. Jacob, Magnetic cross-relaxation among protons in protein solutions, *Biochemistry* **17**, 4349 (1978).
7. S.H. Koenig and R.D. Brown III, Determinants of proton relaxation rates in tissue, *Magn. Reson. Med.* **1**, 437 (1984).
8. B.M. Fung and T.W. McGaughy, The state of water in muscle as studied by pulsed NMR, *Biochim. Biophys. Acta* **343**, 663 (1974).
9. P.S. Allen, M.E. Castro, E.O. Treiber, J.A. Lunt and D.P.J. Boisvert, A proton NMR relaxation evaluation of a model of brain edema fluid, *Phys. Med. Biol.* **31**, 699 (1986).

10. L. Grösch and F. Noack, NMR relaxation investigation of water mobility in aqueous bovine serum albumin solutions, *Biochim. et Biophys. Acta* **453**, 218 (1976).

11. S.H. Koenig, The dynamics of water-protein interactions, *in* "Water in Polymers", (S.P. Rowland Ed.), American Chemical Society Symposium Series, **127**, 157 (1980).

12. R.E. Sepponen, R.E., J.A. Pohjonen, J.T. Sepponen, J.I. Tanttu, A method for $T_{1\rho}$ imaging, *J. Comput. Asst. Tomogr.* **9**, 1007 (1985).

13. S.H.Koenig and W.E. Schillinger, Nuclear Magnetic Relaxation Dispersion in Protein Solutions. *J. Biol. Chem.* **244**, 3283 (1969).

14. O.K. Daskiezicz, J.W. Hennel, B. Lubas, and T. Szczepkowski, Proton magnetic relaxation and protein hydration. *Nature* **200**, 1006 (1963)

15. E.E. Burnell, M.E. Clark, J.A.M. Hinke and N.R. Chapman, Water in barnacle muscle III. NMR studies of fresh fibres and membrane damaged fibres equilibrated with selected solutes, *Biophys. J.* **33**, 1 (1981).

16. J.G. Diegel and M.M. Pintar, Origin of non-exponentiality of the water proton spin relaxations, *Biophys. J.* **15**, 855 (1975).

17. R.S. Menon and P.S. Allen, Proton relaxation in aqueous solutions of fibrinogen and $\alpha_2$-macroglobulin, *in* "Proc. of the VIth Annual Meeting, Society of Magnetic Resonance in Medicine", New York, 436, 1986.

18. T.E. Creighton, "Protein Structures and Molecular Properties." W.H. Freeman, New York, 184, 1983.

19. F. Van Leuven, Human $\alpha_2$-macroglobulin: structure and function. *Trends Biochem. Sci.* **7**, 185 (1982).

10. L. Grösch and F. Noack, NMR relaxation investigation of water mobility in aqueous bovine serum albumin solutions, *Biochim. et Biophys. Acta* **453**, 218 (1976).

11. S.H. Koenig, The dynamics of water-protein interactions, *in* "Water in Polymers", (S.P. Rowland Ed.), American Chemical Society Symposium Series, **127**, 157 (1980).

12. R.E. Sepponen, R.E., J.A. Pohjonen, J.T. Sepponen, J.I. Tanttu, A method for $T_{1\rho}$ imaging, *J. Comput. Asst. Tomogr.* **9**, 1007 (1985).

13. S.H.Koenig and W.E. Schillinger, Nuclear Magnetic Relaxation Dispersion in Protein Solutions. *J. Biol. Chem.* **244**, 3283 (1969).

14. O.K. Daskiezicz, J.W. Hennel, B. Lubas, and T. Szczepkowski, Proton magnetic relaxation and protein hydration. *Nature* **200**, 1006 (1963)

15. E.E. Burnell, M.E. Clark, J.A.M. Hinke and N.R. Chapman, Water in barnacle muscle III. NMR studies of fresh fibres and membrane damaged fibres equilibrated with selected solutes, *Biophys. J.* **33**, 1 (1981).

16. J.G. Diegel and M.M. Pintar, Origin of non-exponentiality of the water proton spin relaxations, *Biophys. J.* **15**, 855 (1975).

17. R.S. Menon and P.S. Allen, Proton relaxation in aqueous solutions of fibrinogen and $\alpha_2$-macroglobulin, *in* "Proc. of the VIth Annual Meeting, Society of Magnetic Resonance in Medicine", New York, 436, 1986.

18. T.E. Creighton, "Protein Structures and Molecular Properties." W.H. Freeman, New York, 184, 1983.

19. F. Van Leuven, Human $\alpha_2$-macroglobulin: structure and function. *Trends Biochem. Sci.* **7**, 185 (1982).

20. H.Y.Carr and E.M. Purcell, Effects of diffusion on free precession in nuclear magnetic resonance experiments, *Phys. Rev.* **94**, 630 (1954).

21. S. Meiboom and D. Gill, Modified spin-echo method for measuring nuclear relaxation times. *Rev. Sci. Instrum.* **29**, 688 (1958).

22. R. Freeman and H.D. Hill, Fourier transform study of NMR spin-spin relaxation, *J. Chem. Phys.* **55**, 1985 (1971).

23. J.Oakes, Protein hydration - nuclear magnetic resonance relaxation studies of the state of water in native bovine serum albumin solutions. *J. Chem. Soc.* Faraday Trans. I. **72**, 216 (1976).

24. Y.S. Kang, J.C. Gore, and I.M. Armitage, Studies of factors affecting the design of NMR contrast agents: manganese in blood as a model system, *Magn. Reson. Med.* **1**, 396 (1984).

25. J.L. Brown, E. van Sonnenberg, K.H. Gerber, G. Stritch, G.R. Wittich and R.A. Slutsky, Magnetic resonance relaxation times of percutaneously obtained normal and abnormal body fluids. *Radiology* **154**, 727 (1985).

26. M.E. Clark, E.E. Burnell, N.R. Chapman and J.A.M. Hinke, Water in barnacle muscle IV. Factors contributing to reduced self-diffusion, *Biophys. J.* **39**, 289 (1982).

27. J.R. Zimmerman and W.E. Britfin, Nuclear magnetic resonance studies in multiple phase systems: Lifetime of a water molecule in an adsorbing phase on silica gel, *J.Chem. Phys.* **61**, 1328 (1957).

28. J. Clifford, B.A. Pethica, and E.G. Smith, *in* "Membrane Models and the Formation of Membranes", (L. Bolis and B.A. Pethica, Eds.) North Holland, Amsterdam, 19, 1968.

29. W.R. Inch, J.A. McCredie, C. Geiger, and Y. Boctor, Spin-lattice relaxation times for mixtures of water and gelatin or cotton, compared with normal and malignant tissue. *J. Natl. Canc. Inst.* **53**, 689 (1974).

30. G.D. Fullerton, I.L. Cameron, and V.A. Ord, Frequency dependence of magnetic resonance spin-lattice relaxation of protons in biological materials, *Radiology*. **151**, 135 (1984).

31. P. Belton and K. Packer, Pulsed NMR studies of water in striated muscle III. The effects of water content. *Biochim. Biophys. Acta.* 354, 305 (1974).

32. R. Cooke and I. Kuntz, The properties of water in biological systems. *Ann. Rev. Biophys. Bioeng.* **3**, 95 (1974)..

33. C. Hazelwood, D. Chang, L. Buford, B. Nichols, and D. Woessner, Nuclear magnetic resonance transverse relaxation times of water protons in skeletal muscle, *Biophys. J.* **14**, 583 (1974)..

34. A. Abragam, "The Principles of Nuclear Magnetism", Oxford University Press, Oxford (1961).

35. G.P. Jones, Spin-lattice relaxation in the rotating frame: weak-collision case, *Phys. Rev.* **148**, 332 (1966).

36. H.T. Edzes and E.T. Samulski, The measurement of cross-relaxation effects in the proton NMR spin-lattice relaxation of water in biological systems: hydrated collagen and muscle, *J. Magn. Reson.* **31**, 207 (1978).

37. R.G.Bryant and W.M. Shirley, Water-protein interactions, *in* "Water in Polymers" (S.P. Rowland, Ed.), American Chemical Society Symposium Series **127**, 147 (1980).

# CHAPTER 3[1]

## Multiexponential proton relaxation in a model tissue system

### 3.1 Introduction

The various relaxation rates of water protons in heterogeneous tissue provide a very sensitive means of manipulating tissue contrast in an NMR image. The changes in these rates that occur as a result of pathology enable NMR images to provide valuable diagnostic information. Unfortunately, the absolute magnitudes of the global averages of the relaxation rates that are determined in imaging procedures, have, so far, not fulfilled their early promise to provide information that is specific. In particular, the ability to exploit for diagnostic purposes the multiple proton relaxation components that are sometimes observed in tissue has been hampered by a lack of understanding of the mechanisms that give rise to the multiexponential behaviour. However, as our understanding of the mechanisms of tissue relaxation improves, it is expected that not only will the demand for more incisive measurement techniques increase, but that the degree of specificity of quantitative relaxation measurements will also increase.

Attempts to further this understanding have often consisted of careful *in-vitro* measurements of relaxation rates in aqueous protein solutions (1-8), in cellular systems (9-13) and in excised tissue (14-30). This chapter reports work on a system that is intermediate between aqueous protein solutions and true cellular systems, namely, preparations of red blood cell (RBC) ghosts. Intact RBC ghosts have been used to increase the level of complexity from that of aqueous protein solutions by the

---

[1] A version of this chapter has been accepted for publication. R.S. Menon, M.S. Rusinko and P.S. Allen, Multiexponential proton relaxation in a model tissue system, *Magn. Reson. Med.* (1990).

incorporation of a membrane to form the simplest of quasi-cellular structures. By increasing the complexity of a series of model systems in an incremental fashion, one may hope to retain control over the cellular constituents in the sample, so that their respective effects on the water proton relaxation rates can be isolated. Preparations of RBC ghosts have allowed us to evaluate the effects of intracellular to extracellular water exchange, the effects of serum albumin in the extracellular space (as one might encounter in vasogenic brain edema) and the effects of compartmentalization. In order to retain sensitivity to changes in the motional power spectrum of the water molecules in these systems, the evaluations conformed to the methods of our earlier work on aqueous protein solutions (3) by employing the rotating frame relaxation rate, $R_{1\rho}$, in addition to the more conventional longitudinal and transverse relaxation rates, $R_1$ and $R_2$ respectively.

Our findings show that macroscopic compartmentalization of the RBC ghosts and the "extracellular fluid" leads to biexponential relaxation curves for the transverse and rotating frame relaxation processes, but that water exchange between the two compartments is fast enough to render the longitudinal relaxation monoexponential. They also show, that to explain the consequences of introducing albumin into the "extracellular fluid", one needs to take account of the dynamic equilibrium of protein molecules between adsorption sites on the "cellular membrane" and the freely mobile state of the protein in solution. This latter finding points to a limitation of the *in-vivo* usefulness of relaxation studies in aqueous protein solutions.

A preliminary report on this work has been presented at the VII$^{th}$ Annual Meeting of the Society of Magnetic Resonance in Medicine (31).

## 3.2 Experimental

### 3.2.1 Red Blood Cell Ghost Preparation by Hemolysis

RBC Ghosts were prepared using several modifications of the method of Steck and Kant (32) from outdated packed O+ blood obtained from the Canadian Red Cross. The ghosts were washed and resuspended in Phosphate Buffered Saline (PBS, Sigma Chemical Co.) which was slightly hypotonic in relation to the intracellular fluid of the ghosts in order to maximize the inside volume of the ghosts. All solutions were prepared with ultrapure distilled and deionized water (18.2 MΩ).

### 3.2.2 Sample configuration for NMR experiments

Relaxation experiments were carried out on two distinct configurations of RBC ghost preparations. In the first configuration, the ghosts were allowed to remain as a stable layer separated from the particular buffer. In the second configuration, the ghosts were prepared as uniformly mixed suspensions in the various buffers. In both of these configurations it is possible to identify both intracellular and extracellular compartments of the overall samples. To facilitate the examination of the relaxation characteristics in these compartments of the RBC ghost samples, the volume of the various buffer solutions added to the packed ghosts was varied, with respect to the ghost volume, across six percentages (0, 20, 40, 60, 80, and 100 %), with 0 % being a sample of packed ghosts and 100 % being the buffer alone. In all samples except those of packed ghosts, NMR relaxation measurements were made with three different concentrations of albumin (0, 25, 75 g/l) in the added buffer. The overall volume of each NMR sample was 100 µl. Although this choice of overall volume provides a convenient percentage measure for the amount of buffer

added to the packed ghosts, it must also be borne in mind that the total amount of extracellular fluid must also include the interstitial fluid present between the ghosts in the initial packed ghost preparations. The particular behavior of the ghost samples - that they form a stable sediment when layered carefully with added buffer, but also form stable suspensions in the same buffer when mixed - permitted us to compare cases of macro (layered) and micro (mixed) compartmentalization in the same sample. Layered samples were allowed at least 6 hours after preparation to enable the ghosts to equilibrate osmotically with the buffer, even though the largest amounts of protein used represent only a 1 mM contribution to the 13.27 mM PBS solution used as a buffer inside the ghosts. A visual check assured us that the layering persisted throughout the experiments.

To observe the effect of the membranes alone, NMR measurements were made on unresealed ghosts (i.e. washed RBC membranes) with 50 g/l albumin in all of the previously described range of added buffer volumes (0 - 100 %). In addition, NMR measurements of mixed and layered configurations were made when the movement of water molecules across the membrane was first reduced by a factor of 3 by the addition of pCMBS (p-chloromercuribenzene sulfonate) to the final wash in the ghost preparation procedure, and secondly using the tissue fixative gluteraldehyde (3 % in the added buffer).

The cleanliness of the intra and extracellular spaces of the ghost preparations was confirmed by electron micrographs of freeze fractures and sectioned pellets of ghosts. Phase contrast micrographs were utilized to ensure that the ghosts were intact, to visualize ghost shape and size, and to estimate the concentration of ghosts in the samples for NMR.

### 3.2.3 NMR measurements

The proton relaxation rates were measured with a Bruker CXP spectrometer at 100 MHz. The line width obtained for the 100 µl samples in the 40 cm bore magnet was better than 5 Hz. The measurements were made at a room temperature of $22 \pm 2$ °C. This temperature combined with the sample pH ensures that the RBC ghost membrane is in a region where permeability does not change much with temperature.

The transverse relaxation was measured using a 16384 echo Carr-Purcell-Meiboom-Gill (CPMG) add/subtract sequence (33,34), with an inter-echo spacing, $\tau$, of 400 µs. The CPMG sequence was phase cycled as suggested by (35) in order to eliminate baseline errors generated by both receiver dc offsets and residual magnetization generated by phase errors in the 180° pulses. The choice of the echo time was made to minimize the effects of diffusion on $R_2$. The add/subtract sequence was repeated 8 times and the resulting signal was averaged.

The longitudinal relaxation was measured using the Freeman-Hill modification (36) of the inversion recovery sequence [$180_y$--$\tau$--$90_x$--AQ--TR/0--$\tau$--$90_{-x}$--AQ--TR], where TR is the sequence repetition interval. The $\tau$ values, ranging from 1 ms to 7.9 s, provided 10 points, equally spaced logarithmically, in each decade of time. The advantage of using this sequence is that the magnetization recovery curve is always positive, dropping from $2M_O$ to zero, with the initial magnetization, $M_O$ being measured as often as the partly relaxed magnetization. Four acquisitions of each add/subtract pair were averaged.

The magnetization decay in the rotating frame (37) was measured using the phase alternated sequence [$90_x$--$\tau$(lock)$_y$--AQ--TR / $90_{-x}$--$\tau$(lock)$_{-y}$--AQ--TR], in which the free induction decay was collected after each spin locking pulse, denoted $\tau$(lock). The length of the spin locking pulse was varied over the same forty $\tau$ values used for the inversion recovery experiment and the same signal averaging scheme was also used. Three different amplitudes, $B_1$, of the spin locking pulse were employed, namely 0.3 , 0.6, and 0.9 mT. $B_1$ was calculated using a simple pulse program and was known to ± 5 %. The relaxation rates were all obtained with a 90° pulse length of 7.5 μs. All data were acquired using the Bruker 12 bit digitizer alternately sampling between real and imaginary data points every 4 μs.

### 3.2.4 Data Processing

A total of 153 echos were selected from the complete $R_2$ data set so that they logarithmically spanned the time interval between 400 μs and 6.55 s. This nonlinearly sampled data set, as well as the complete $R_1$ and $R_{1\rho}$ data sets, were fitted by two completely different methods to ensure that the trends observed in the data were in fact real. The first and more conventional method involved a non-linear least-squares program (38) capable of fitting up to four unique exponentially decaying components to a data curve. The second and more sophisticated method, fits the data to a continuous distribution of relaxation times using a linear non-negative least-squares technique (39) with no *a priori* assumptions as to the number of exponentially decaying components in the data. Figure 3.1 demonstrates the application of both techniques to a logarithmically sampled CPMG echo train obtained from a sample which had 80 μl of supernatant layered on 20 μl of packed ghosts. The relaxation times calculated using both methods agreed to ± 1 % for

monoexponential fits and ± 3 % for biexponential fits. Moreover, from the known variance of the data points, the error in the fitted parameters can be calculated to be better than ± 1 % for monoexponential fits and ± 3 % for biexponential fits. However, for any given sample, fitting successive NMR measurements yielded a repeatability of the relaxation times and amplitudes of ± 5 %. Hence, the error bars in our figures (± 5 %) are determined primarily by the repeatability of the NMR experiments and not by the errors in our fitting procedures.

## 3.3 Results

In data sets acquired from samples containing a high proportion of ghosts, it was possible to detect the presence of a small component of the magnetization (< 2 % of the total observable signal at most) that was characterized by much shorter relaxation times ($T_1 \equiv 230$ ms and $T_2^* \equiv 430$ μs) than those displayed by the rest of the observable magnetization. We attribute this small component of magnetization to the partially mobile protons in the membranes and it has been neglected in the following data analysis, which concentrates only on the long relaxation time signals from the very mobile protons in free and exchanging water molecules. For the samples of the uniformly mixed configuration, all very mobile water proton relaxation processes were monoexponential in character. Figure 3.2 shows, for the mixed samples, the dependence of the relaxation rates $R_1$ , $R_2$ and $R_{1\rho}$ on the fraction of protein buffer added ($\Pi$), on the albumin concentration of the added buffer, and for $R_{1\rho}$, on the spin locking pulse amplitude.

When the sample was layered rather than mixed uniformly, biexponential transverse and rotating frame relaxation were observed. However the longitudinal relaxation was still monoexponential (ignoring the partially mobile proton signal)

and equal to its value in the mixed sample case. In those cases where the relaxation was biexponential, the fast relaxing component was identified with the water in the ghost layer, whereas the slowly relaxing compartment was identified as the water in the protein buffer layer. The behavior of the two $R_2$ components and the single $R_1$ component for the layered configuration is shown in Figure 3.3 as a function of the fraction, $\Pi$, of buffer added and of the protein concentration in the added buffer. The behavior of $R_1$ in the layered case correlates well with the $R_1$ in the mixed case ($R^2 = 0.967$). Also shown in the figure are the two components of $R_{1\rho}$ at spin locking fields of 0.33 and 0.9 mG. The data at 0.6 mT are intermediate between those shown but have been omitted for clarity. As the fraction of protein containing buffer is increased it is interesting to the see the slope of the $R_{1\rho}$ dispersion change sign. This observation will be discussed below. Figure 3.4 shows how the NMR measured proportion of the total signal corresponding to the protein buffer compartment correlates with the actual percentage corresponding to the protein buffer layered onto the ghosts. The deviation from a line of unit slope was used in calculations to estimate interstitial volumes.

## 3.4 Analysis and Discussion

### 3.4.1 Mixed Samples

In uniformly mixed solutions of intact ghosts and protein buffer, all three relaxation processes were found to be monoexponential in character. This is consistent with the results of other workers (40-42) who report the exchange rate, $k_a$, of a water molecule out of an intact ghost to be 50 to 150 $s^{-1}$. This rate is much higher than the intrinsic relaxation rate in either the added buffer or the ghosts (between 0.4 $s^{-1}$ and 2 $s^{-1}$), resulting in a fast exchange regime within which the

measured relaxation rates reflect the weighted average of the rates in each compartment (43). If we assign one compartment to the water inside the ghosts and the other compartment to the water in the 'extracellular fluid' (ECF), then the observed relaxation rates, $R_i$, may be written in terms of a two-site rapid-exchange model as,

$$R_i = p_{ecf}R_{iecf} + p_gR_{ig} \qquad (3.1)$$
$$= R_{ig} - p_{ecf}(R_{ig} - R_{iecf}),$$

where i = 1, 2 or 1ρ. $R_{iecf}$ and $R_{ig}$ represent respectively the relaxation rates measured in isolated bulk samples of ECF and of ghosts, while $p_{ecf}$ and $p_g$ correspond to the relative populations of water protons in each of the two compartments.

At first sight, one might expect that the experimental data can be compared with the model represented by Equation 3.1, if $p_{ecf}$ is replaced by Π, the experimentally measured proportion of protein buffer added, and if $R_{iecf}$ is written in terms of a second exchange process between water in a protein free bulk water environment and water attached to the adsorbtion sites on the surface of the buffer protein molecules. In terms of this second exchange process, $R_{iecf} = R_{ib} + G_ic_{ecf}$, where $R_{ib}$ is the relaxation rate in a protein free buffer, $c_{ecf}$ is the protein concentation in the protein buffer and $G_i$ is a proportionality constant that can be obtained from relaxation studies in aqueous protein solutions (2, 3). In fact, this expectation would be an oversimplification. The method of preparation of the packed ghosts always gave rise to some residual phosphate-buffered saline remaining in the interstitial spaces between ghosts, leading to a dilution of the protein buffer (volume, $V_{pb}$) added to the packed ghosts. We shall assume that this interstitial volume is

always a fixed fraction $\phi$ of the ghost volume $V_g$. From considerations of packing as well as from light microscopy, this interstitial fraction is normally less than 10 % and data presented later show that in our case it is typically 3 %. As a result of the dilution,

$$p_{ecf} = (\Pi+\phi) / (1+\phi) \qquad (3.2)$$

and

$$\Pi = V_{pb} / \{V_{pb} + V_g (1+\phi)\} \qquad (3.3)$$

This dilution process will also reduce the protein concentation in the ECF, namely $c_{ecf}$, from that of the protein buffer added ($c_{pb}$). However, a second process, namely the affinity of the protein molecules for the RBC membranes (44-47), will also reduce this concentration. As shown in section 3.6, the combination of these two effects gives rise to a resultant concentration, $c_{ecf}'$, given by,

$$c_{ecf}' = c_{pb} \frac{\Pi(1+\phi)}{(\Pi+\phi)} \{1-\lambda\} \qquad (3.4)$$

where $\lambda$ is the proportion of protein molecules lost to the RBC membranes. In calculating the observed relaxation rate, one must also take account of the possibility that albumin molecules adhering to the RBC membranes are still net contributors of adsorption sites for water exchange. If one assumes, following the work on mixtures of proteins in solution (2), that the contributions of both types of albumin to the relaxation efficiency are additive, $R_{iecf}$ becomes,

$$R_{iecf} = R_{ib} + G_i c_{ecf}' + G_{iads} c_{ads}, \qquad (3.5)$$

where $G_{iads}$ is the relaxation sensitivity per unit concentration of bound albumin molecules and $c_{ads}$ is their concentration in the ECF. Combining Equation 3.1 to 3.5, Equation 3.1 can be rewritten as

$$R_i = \frac{1}{(1+\phi)}[R_{ig} + \phi R_{ib}] - \Pi\left(\frac{1}{(1+\phi)}[R_{ig} - R_{ib}] - c_{pb}[G_i(1-\lambda) + G_{iads}\lambda]\right) \tag{3.6}$$

Equation 3.6 summarizes the dependence of the observed $R_i$ on the proportion of protein buffer added, $\Pi$, that is predicted by the simple model outlined above. The effects of interstitial-buffer dilution alone, i.e., $\lambda = 0$, give rise to the prediction of a linear dependence of $R_i$ on $\Pi$, albeit with a modified $\Pi = 0$ intercept and gradient from those expected if $\phi = 0$. The incorporation of protein adhesion to the RBC membranes will affect this linearity to a degree that depends on $\lambda$ and on $G_{iads}$, the greatest deviation from linearity occurring around $\Pi = 0.2$. One can estimate a magnitude for $\lambda$ from the functionality derived in section 3.6 and from the independent quantitative work on protein affinity for RBC membranes (44-47). For example, $0.45 > \lambda > 0.03$ over the range $0.2 < \Pi < 0.8$ when $c_{pb} = 25$ g/l. Using such numbers, one would not expect the deviation from linearity of even the most sensitive relaxation process, namely, transverse, to be more than $\approx 2$ % at $c_{pb} = 75$ g/l for the range $0 < G_{iads}/G_i < 2$. Only an order of magnitude difference in $G_i$ and $G_{iads}$ is likely to be measurable in the transverse relaxation of mixed samples. The data shown in Figure 3.2 for mixed ghost solutions cannot be distiguished from a linear dependence on $\Pi$. For example, the regression line drawn through the $R_2$ values in Figure 3.2 has an $R^2$ of 0.999 for $c_{pb} = 0$ g/l, 0.972 for $c_{pb} = 25$ g/l and 0.922 for $c_{pb} = 75$ g/l. Similar results were obtained for $R_1$ and $R_{1\rho}$. We conclude

from this that albumin molecules that adhere to RBC membranes do not become markedly more efficient at promoting water proton transverse relaxation, even though they are motionally more hindered. In support of this, it is worth noting that Oakes (7) found that increases in the efficiency of transverse relaxation by factors of two or three, could only be brought about by drastically reducing the motional freedom of albumin in aqueous solution through increases in concentration up to 700 g/l .

The $c_{pb}$ = 0 g/l data shown in Figure 3.2a, highlights differences between the relaxational efficiency of the water inside the ghosts and that in free buffer. $R_1(\Pi = 0)$ is essentially unchanged from its free buffer value, whereas $R_{1\rho}(\Pi = 0)$ and $R_2(\Pi = 0)$ are significantly enhanced over their free buffer values. We attribute the difference between $R_i(\Pi = 0)$ and $R_{ib}$ observed for transverse and rotating frame relaxation to a second, faster exchange process occurring within the ghosts. In this second process water molecules exchange between the 'free' water inside the ghosts and a "hydration layer" associated with the membrane and with the residual microfilamentary intracellular structure that remains after repeated aspiration, washing and resealing. EM evaluation of our ghost preparation revealed a residual amount of long filaments, whose length was comparable to the ghost dimensions. The immobility of this cytoskeleton increases the transverse and rotating frame relaxation efficiency of the water in the "hydration layer" by increasing the intensity of the motional power spectrum in the region of $\omega = 0$. The same immobility will add nothing to the longitudinal relaxation efficiency of hydration water. This interpretation is supported by the RF field dependence of $R_{1\rho}$ , which is shown in Figure 3.2a to increase at greater ghost concentrations ($\Pi \rightarrow 0$). This increase in $R_{1\rho}$ dispersion reflects a motional power spectrum for water molecules that has an increasing slope, as the extent of the ghost architecture increases. The presence of

proteins in the ECF also increases $R_{1\rho}$ dispersion (see Figures 3.2b and 3.2c). This effect of solute protein has previously been observed in aqueous solutions (3). However, its magnitude is somewhat less than the dispersion resulting from the presence of ghosts in solution. On a practical note, we ascribe most of the variation that is observed in transverse or rotating frame relaxation rates at $\Pi = 0$ to the variations in the amount of cytoskeleton remaining inside the different batches of ghosts after preparation.

### 3.4.2 Layered Samples

In marked contrast to the data from uniformly mixed preparations of ghosts, the $R_2$ and $R_{1\rho}$ data from the layered ghost/protein-buffer preparations exhibit a distinct biexponential character. The longitudinal relaxation is, however, still monoexponential and will not be discussed in detail.

The appearance of biexponential relaxation only when the ghosts are packed adjacent to the protein solution is strongly suggestive that when biexponentiality is observed in tissue, it reflects physiologically separate compartments (28, 29) and not the slow exchange of water between two distinct water environments within a single compartment. The decomposition of a typical transverse decay is illustrated in Figure 3.1, which clearly shows the marked separation of the two component relaxation rates. The confirmation of this separation by imaging studies has been published elsewhere (48) and is discussed in Chapter 4. The processed data for the layered ghost preparations, summarized in Figure 3.3, establish that the component relaxation rates are not independent of the relative fractions of each component and thus the naive model of two totally independently relaxing compartments is untenable.

To account for the two component nature of the transverse and rotating frame relaxation, we postulate a ghost compartment that relaxes quickly and a protein-buffer compartment that relaxes slowly. The ghost compartment is assumed to arise from the fast exchange of water molecules between intraghost water ($V_g$) and water in the interstitial volume, $V_i$, between the packed ghosts, that, in the layered samples, can no longer be combined with water in the protein buffer layer to form a single 'extracellular' fluid compartment. The interstitial volume is assumed to arise from a combination of the interstitial buffer, $\phi V_g$, present in the undisturbed packed ghosts, and a volume of protein-containing buffer, $\varepsilon V_{pb}$, which is trapped during layering. The introduction of a trapped volume (that is roughly proportional to $V_{pb}$) is necessary to explain the decrease in the fast $R_i$ component with increasing $\Pi$, when $c_{pb} = 0$. It is clear from Figure 3.3a that, when the proportion of ghosts is small ($\Pi \simeq 0.8$), the layering of larger quantities of buffer can disturb the integrity of the packed ghosts if great care is not taken. Water exchange between the slowly relaxing protein-buffer compartment and the ghost compartment is assumed to be slow on the time scale of transverse relaxation but fast on that of the longitudinal relaxation, in view of the monoexponential nature of the inversion recovery data. Finally, in experiments where protein is present in the protein buffer layer, we assume that the protein molecules can diffuse into the interstitial space and equilibrate between this space and that of the protein buffer. This equilibration includes the adhesion of albumin molecules to the ghost membranes.

On the basis of this model, we derive (using symbols defined in section 3.6) the following expressions for the relaxation rates $R_{is}$ and $R_{if}$ of the slow and the fast relaxing components respectively,

$$R_{is} = R_{ib} + G_i\, c_{pb} \frac{\Pi(1+\phi)}{(\Pi+\phi)} (1-\lambda) g\eta \qquad (3.7)$$

$$R_{if} = \frac{1}{(1+\phi)} [R_{ig} + \phi R_{ib}] - \frac{1}{(1+\phi)} \frac{\Pi\varepsilon}{[1-\Pi(1-\varepsilon)]} [R_{ig} - R_{ib}] + c_{pb} \frac{\Pi}{(\Pi+\phi)} \left( \phi + \frac{\Pi\varepsilon}{[1-\Pi(1-\varepsilon)]} \right) [G_i(1-\lambda) + G_{iads}\lambda]\eta \qquad (3.8)$$

where in the expression for $R_{if}$, the first term represents the effect of dilution by the interstitial buffer, $\phi V_g$, alone when $c_{pb} = 0$, the second term reflects the effect of trapping when $c_{pb} = 0$, and the final term includes successively the effects of dilution, trapping, membrane affinity for albumin and a protein concentration gradient, g, between the two compartments, when $c_{pb}$ is finite.

In Figure 3.3a, where $c_{pb} = 0$ , the increasing volume of the interstitial space ($\phi V_g + \varepsilon V_{pb}$) as $\Pi$ explains the dependence of $R_{if}$ on $\Pi$. This dependence, together with the NMR measurements of the relative weights of the fast and slow components, gives rise to estimates of 0.03 and 0.07 for typical values of $\phi$ and $\varepsilon$ respectively. The slow component is not expected to be affected by changes in $\Pi$ and as shown by Figure 3.3a does not deviate beyond the ± 5 % scatter of the data points.

When $c_{pb}$ is finite, the dilution of the protein buffer by the interstitial buffer volume, $\phi V_g$ , results in small changes of the right sign but never greater than a few percent, in both $R_{is}$ and $R_{if}$ over the whole range $0.2 < \Pi < 0.8$. These changes are well within the scatter of the data points and cannot account for the large changes observed when $c_{pb} = 75$ g/l. The inclusion of a trapped volume, $\varepsilon V_{pb}$ , during layering will have no effect on $R_{is}$ , but will introduce two terms into $R_{if}$ that respectively decrease and increase $R_{if}$ as $\Pi$ increases. If $c_{pb} = 25$ g/l, the negative

term is the greater and leads to the prediction of a decrease in $R_{if}$ as $\Pi$ increases. If $c_{pb}$ = 75 g/l , these two terms tend to balance. It is clear, therefore, that when taken together, the effects of dilution and trapping cannot account for the observations shown in Figures 3.3b and 3.3c on either $R_{is}$ or $R_{if}$, when $c_{pb}$ is either 25 g/l or 75 g/l.

To explain the data of Figure 3.3 when $c_{pb}$ is finite, particularly the increasing values of both $R_{is}$ and $R_{if}$ as $\Pi$ increases at $c_{pb}$ = 75 g/l , it is necessary to invoke the adhesion of albumin molecules to the ghost membranes (44-47), as well as a protien concentration gradient between the two layers. These mechanisms cause the protein concentration in the protein buffer to become much more dependent on $\Pi$, as the different concentrations of ghosts draw correspondingly different amounts of albumin into the ghost compartment. To estimate the degree to which the protein concentration is affected, one needs to make some assumptions about the equilibrium state of the albumin adsorption and about the possible presence of an albumin concentration gradient between the interstitial volume and the residual protein buffer layer. In the interests of simplicity we explored the effects of the two processes independently in an appendix (section 3.6), during the derivation of Equations 3.7 and 3.8. First, we assumed that the adsorbed and solute albumin were in dynamic equilibrium but also that the solute concentration was uniform throughout the interstitial and protein-buffer spaces. In the second place,we considered primarily the effects of a concentration gradient without reanalyzing the modified adsorption equilibrium in the interstitial space. In the first of these cases, we used the numerical values given in references (44, 45), to provide estimates of the association constant, 1/K, ($\cong 5\times10^{-21}$ l) and the ghost-volume density of albumin adsorption sites, $\sigma$, ($\cong 5.4\times10^{19}$ $l^{-1}$). These quantities enable the fractional concentration difference, $\lambda$,

and hence the concentration of albumin in the residual protein buffer to be estimated. Equation 3.7 was then used to predict a change of + 0.3 $s^{-1}$ in $R_{2s}$ between $\Pi = 0.2$ and $\Pi = 0.8$, when $c_{pb} = 75$ g/l. This positive change, which is of the same order as the experimental value of 0.55 $s^{-1}$, seems to support the inclusion of membrane adsorption of protein in the models of these systems. The corresponding predicted change in $R_{2s}$ at $c_{pb} = 25$ g/l, is however + 0.2 $s^{-1}$, sustantially greater than the experimental value of 0.05 $s^{-1}$. By adjusting the constants K and $\sigma$ one might arrange for better agreement with experiment at either 75 g/l or 25 g/l, but not at both. A greater difference between the changes in $R_{2s}$ at the two values of $c_{pb}$ follows from the second avenue explored in section 3.6, namely that of a concentration gradient. If the means for producing the concentration gradient are neglected, a $\Pi$ independent $\dot{g} = 0.5$ doubles the differential between the $c_{pb} = 25$ g/l and the $c_{pb} =$ 75 g/l situations predicted by the factor $(1-\lambda)$ alone. At this point it must be emphasised that these two processes cannot be treated independently but must arise naturally out of the analysis of a two way dynamic equilibrium for albumin molecules that has not been attempted here. Treating these processes independently offers only a guide that we are on the right track.

Turning to the fast-relaxing component, Equation 3.8 shows that the reduction in $R_{if}$ with increasing $\Pi$ caused by the trapped fluid volume ($2^{nd}$ term), can be offset if the albumin molecules within that volume provide sufficient enhancement of the water proton relaxation ($3^{rd}$ term). Such an enhancement depends first upon the values used for $G_i$ and $G_{iads}$, coupled to the estimate of $\lambda$ derived from the assumed adsorption equilibrium, and secondly on the concentration gradient factor $\eta$. Because $\lambda \rightarrow 0$ as $\Pi \rightarrow 1$, the factor that represents the protein adsorption, namely, $[G_i(1-\lambda) + G_{iads}\lambda]$, is unable, under uniform concentration

conditions, to affect the ultimate balance between the second and third terms in Equation 3.8, as $\Pi$ approaches unity. A concentration gradient ($\Pi$ independent in our very simplified model) can on the other hand provide a factor that increases as $\Pi$ increases, i.e. $\eta > 1$. This factor can affect the the balance between the second and third terms of Equation 3.8; for example, a concentration gradient of 5 gives rise to a factor $\eta = 3$, which would make the predictions of Equation 3.8 for $R_2$ in the cases of $c_{pb}$ = 25 g/l and 75 g/l agree with experiment.

Finally, one must draw attention to the intriguing dispersion behaviour of $R_{1\rho}$ when both albumin and ghosts are present in a layered preparation. For all values of $c_{pb}$ at $\Pi = 1$, the slow component results are in agreement with previous work (3) on aqueous albumin solutions which showed that increasing concentrations not only increased $R_{1\rho}$ at a given $B_1$ field, but also increased the weak $B_1$ dispersion of the rotating frame relaxation efficiency. At $c_{pb} = 0$, the fast component shows that the presence of ghosts also produces dispersion in $R_{1\rho}$ and in this case (see Figure 3.3a) it seems largely independent of $\Pi$. At $c_{pb}$ = 25 g/l or 75 g/l, when both albumin and ghosts are present, a significant dispersion now manifests itself in the slow component of $R_{1\rho}$ as well as in the fast component. The dispersion of these two components exhibits two striking features. First, it is $\Pi$ dependent and changes sign at some intermediate value of $\Pi$. Secondly, the fast and slow components have dispersions of opposite signs at their $\Pi$ extremes. Although the general $\Pi$ dependence of the components of $R_{1\rho}$ can be explained in similar terms to those used for $R_2$, the characteristic behaviour of the dispersion is not well understood and is the subject of further investigation.

## 3.5 Conclusions

Using RBC ghosts to establish a membrane barrier around individual volumes of protein free saline buffer, it has been possible to manufacture a pseudo-cellular system with which to test hypotheses concerning the origin of multi-exponential behavior in the water proton relaxation from tissue. The data obtained from these ghost preparations has been interpreted in terms of the fast or slow exchange of water molecules between sites of different relaxational efficiency.

When a preparation of RBC ghosts is uniformly mixed with "extracellular" fluid in the form of an aqueous protein solution, it is clear that fast exchange of water molecules takes place not only within the ghosts and within the extracellular fluid, using respectively the residual cytoskeleton and the protein molecules as the absorbing surfaces of low mobility, but also across the membrane, thus rendering $R_1$, $R_2$ and $R_{1\rho}$ monoexponential. In order to produce compartments, between which exchange was slow enough to render transverse and rotating frame relaxation biexponential, it was necessary to layer the ghosts and the protein containing buffer, giving rise to two distinct regions within the sample. These findings suggest to us that multiple components in the relaxation profile of water protons in tissue can originate in compartmentalization at the level of the cellular organization. Trans-membrane exchange is too fast to generate multiple components on a finer scale and it is necessary to expand the macroscopic scale of say, grey-white matter tissue types, before multiple components can be observed.

The behavior of the two relaxation components, derived from the layered samples as both the proportion of the added protein buffer and its protein

concentration are varied, shows that the influence of the protein molecules, even in this simple model system, is more complex than might have been anticipated. It appears that the affinity of protein molecules for the membrane surface is instrumental in governing the free solute concentrations in proximity to the membranes, while protein diffusion between compartments determines their relative protein concentrations. As a result of this finding, it seems unlikely that studies of relaxation rates in aqueous solutions of proteins will provide a quantitative yardstick that one can use in conjunction with *in-vivo* relaxation measurements, as a measure of protein infiltration into the extracellular spaces of tissue.

## 3.6 Appendix of calculations

In the slowly relaxing, residual protein buffer of the layered ghost preparations, the observed relaxation rate, $R_{is}$, is determined by the same rapid exchange of water molecules that characterizes aqueous protein solutions (1-8). At protein concentrations ≤ 100 g/l, this gives rise to a linear dependence on the protein concentration. In the residual protein buffer of protein concentration, $c_{res}$, this can be written as,

$$R_{is} = R_{ib} + G_i c_{res} \qquad (A1)$$

where $R_{ib}$ is the relaxation rate in the protein-free buffer and $G_i$ is the relaxational sensitivity per unit change in solute protein concentration.

In the rapidly relaxing ghost compartment of the layered preparations, several exchange processes are active. First, water molecules exchange between intraghost water (relaxation rate, $R_{ig}$) and interstitial water (relaxation rate, $R_{iI}$), giving,

$$R_{if} = R_{ig} + p_I(R_{iI} - R_{ig}) , \qquad (A2)$$

where $p_I$ is the fractional probability of finding a water molecule in the interstitial space. Secondly, $R_{iI}$ is determined by the exchange of water molecules between the bulk-buffer water environment and adsorption sites on albumin, either in solution (concentration, $c_I$) or adsorbed on RBC ghost membranes (concentration, $c_{ads}$), giving,

$$R_{iI} = R_{ib} + G_{ic}c_I + G_{iads}c_{ads}, \qquad (A3)$$

where $G_{iads}$ is the relaxational sensitivity to unit concentration of adsorbed albumin molecules. This additive nature of two exchange mechanisms has been verified for mixtures of proteins in solution (2). Expressions A2 and A3 are analagous to those obtaining in the mixed samples, where the ECF space corresponds to the interstitial space of Equations A2 and A3.

It is now necessary to relate all of the different concentrations to the measured quantities. In terms of the single extracellular fluid compartment that is present in the mixed samples, the protein dilution brought about by the interstitial protein-free buffer that is present in the initial packed ghost preparations, gives,

$$c_{pb}V_{pb} = c_{ecf}(V_{pb} + \phi V_g),$$

or,

$$c_{ecf} = c_{pb}\frac{\Pi(1+\phi)}{(\Pi+\phi)} \qquad (A4)$$

If a protein solution of this concentration is placed in contact with a quantity of RBC ghosts that provides a total concentration of binding sites in the ECF of [B], and of which [AG] are occupied and [G] are unoccupied, then,

$$[B] = [AG] + [G], \qquad (A5)$$

and

$$c_{ecf} = [AG] + c_{ecf}' \qquad (A6)$$

where $c_{ecf}'$ is the concentration of free albumin that exists in dynamic equilibrium with the adsorbed albumin. In the mixed samples, where the equilibrium exists between the ghosts and all of the ECF, one obtains the following expression for [B],

$$[B] = \sigma \frac{(1-\Pi)}{(\Pi+\phi)} \qquad (A7)$$

where $\sigma$ is the ghost-volume density of the binding sites (note that all other concentrations are measured in terms of the ECF volume). In the layered samples, if one assumes that no concentration gradient exists between the resultant interstitial space and the residual protein buffer, then $c_{ecf}' = c_{res} = c_I$ and Equation A7 is still valid. However, if a concentration gradient did exist, then Equation A7 would need to be modified for the layered case because the relevant concentration of binding sites would then need to be with respect to the interstitial volume, $V_I$.

The association constant for the adsorbtion equilibrium may be written as 1/K, where,

$$\frac{[AG]}{c_{ecf}'[G]} = \frac{1}{K} \qquad (A8)$$

From the work of Kikuchi and Koyama (44,45), one can estimate a value for $K^{-1}$ of the order of $5 \times 10^{-21}$ l, and a value of $5.4 \times 10^{19}$ $l^{-1}$ for $\sigma$. From these numerical values and the assumptions of a uniform concentration made above, it is clear that the conditions of our experiments correspond to $c_{ecf} \geq K > [B]$, for which one can obtain the following solution to Equations A5, A6 and A8,

$$c_{ecf}' = c_{ecf} \{1-\lambda\}$$

where,

$$\lambda = [B] / (c_{ecf} + K + [B]) \qquad (A9)$$

In the range $0.2<\Pi<0.8$, we have $0.45 > \lambda > 0.03$ when $c_{ecf} = 25$ g/l and $0.18 > \lambda > 0.01$ when $c_{ecf} = 75$ g/l.

Returning to the expressions for the relaxation rates, we have for the slowly relaxing component from Equations A1, A4 and A9,

$$R_{is} = R_{ib} + G_i c_{pb} \frac{\Pi(1+\phi)}{(\Pi+\phi)} (1-\lambda) \qquad \text{(A10)}$$

For the rapidly relaxing component, when both $\phi V_g$ dilution and $\varepsilon V_{pb}$ trapping are included,

$$pI = \left(1 - \frac{(1-\Pi)}{(1+\phi)[1-\Pi(1-\varepsilon)]}\right) \qquad \text{(A11)}$$

Thus from Equations A2, A3, A4, A9 and A11, we obtain,

$$R_{if} = \frac{1}{(1+\phi)} [R_{ig} + \phi R_{ib}] - \frac{1}{(1+\phi)} \frac{\Pi\varepsilon}{[1-\Pi(1-\varepsilon)]} [R_{ig} - R_{ib}] + c_{pb} \frac{\Pi}{(\Pi+\phi)} \left(\phi + \frac{\Pi\varepsilon}{[1-\Pi(1-\varepsilon)]}\right) [G_i(1-\lambda) + G_{iads}\lambda] \qquad \text{(A12)}$$

If the transport of albumin between the interstitial space and the residual protein buffer space is such that the adsorption equilibrium of albumin to the RBC membranes supports a concentration gradient between the two spaces, then a two way equilibrium equation for albumin should be solved that includes this transport. Because the numerical data available do not justify the sophistication of this approach, we have chosen to explore the fuctionality of the effect on Equations A10 and A12 of an albumin concentration gradient. Retaining the name ECF to describe all fluid external to the ghosts,

$$V_{ecf}\, c_{ecf} = V_I\, c_I + V_{res}\, c_{res}$$

where we no longer assume that $c_I$ and $c_{res}$ are equal, but that a gradient $g$ exists between them such that,

$$c_{res} = g\, c_I \qquad \text{(A13)}$$

Substituting for $V_{ecf}$, $V_I$ and $V_{res}$ in terms of $V_{pb}$, $V_g$, $\phi$ and $\varepsilon$, these two equations can be solved to give,

$$c_I = c_{ecf}\,\eta = c_{ecf}\left(\frac{(\Pi+\phi)}{\left(\phi+\Pi[\varepsilon(1-g)+g]+\Pi\phi[(\varepsilon-1)(g-1)]\right)}\right) \qquad \text{(A14)}$$

Using Equations A13, A14 and A4 to determine the solute concentrations of albumin, Equations A10 and A12 can be rewritten,

$$R_{is} = R_{ib} + G_i\, c_{pb}\,\frac{\Pi(1+\phi)}{(\Pi+\phi)}\,(1-\lambda)g\eta \qquad \text{(A15)}$$

and

$$R_{if} = \frac{1}{(1+\phi)}[R_{ig} + \phi R_{ib}] - \frac{1}{(1+\phi)}\frac{\Pi\varepsilon}{[1-\Pi(1-\varepsilon)]}[R_{ig} - R_{ib}] + c_{pb}\,\frac{\Pi}{(\Pi+\phi)}\left(\phi+\frac{\Pi\varepsilon}{[1-\Pi(1-\varepsilon)]}\right)[G_i(1-\lambda) + G_{iads}\lambda]\eta \qquad \text{(A16)}$$

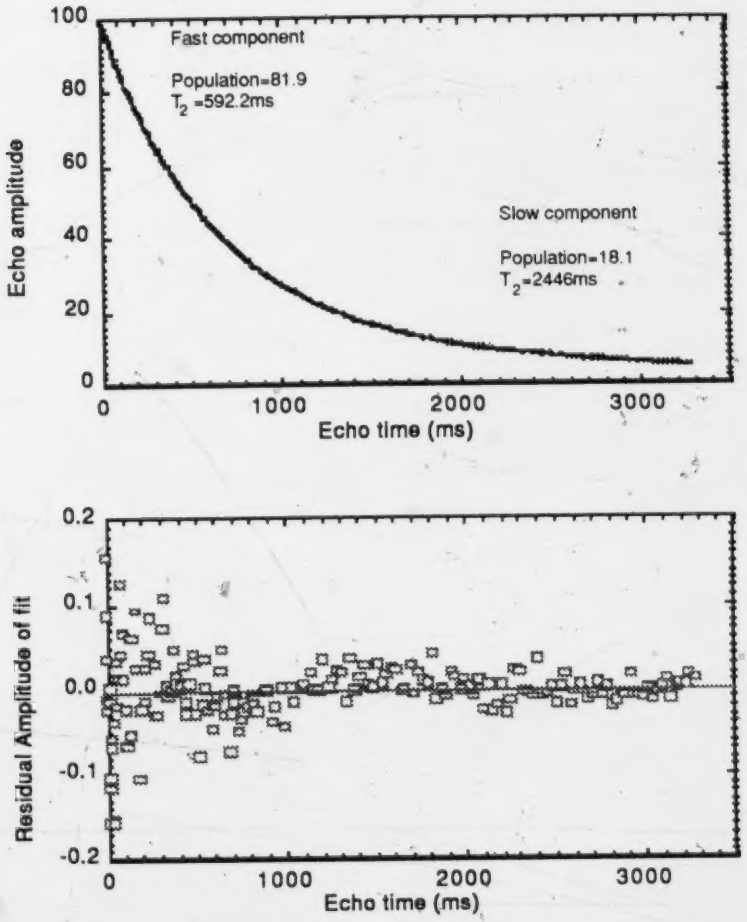


**Figure 3.1** (a) CPMG decay of a layered sample. An illustration of how the two different curve fitting techniques were used to extract the populations and relaxation rates from the log sampled CPMG data shown here.(b) Residual of biexponential fit. Since the fitted curve using the linear-least-squares method would be hidden by the data points in (a), we show the difference between the actual data and the fitted curve here. The rms deviation of the residuals was 0.044, which is the same as the measured noise in the data, so there is no justification for adding another component to the fit. As well, the sum of the residuals is zero, showing that there is no DC offset in the acquired CPMG data.

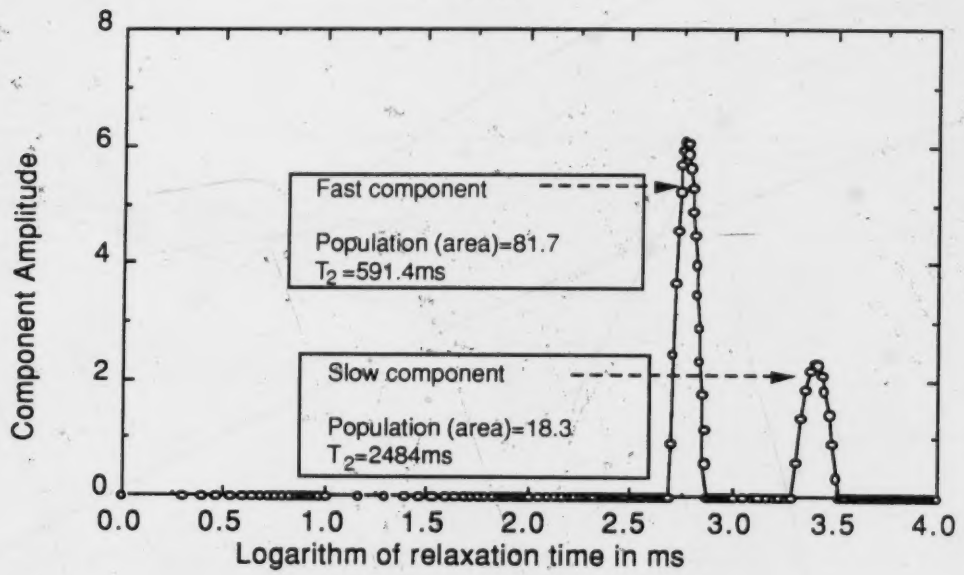


**Figure 3.1(c).** $T_2$ spectrum of a layered sample. Shown is a "$T_2$ spectrum" is shown, in which the area of a peak corresponds to the population of the $T_2$ component and the location of the centroid of the peak gives its relaxation time. Many distribution widths are possible; the one shown optimizes the $\chi^2$ to be the same as the number of data points.

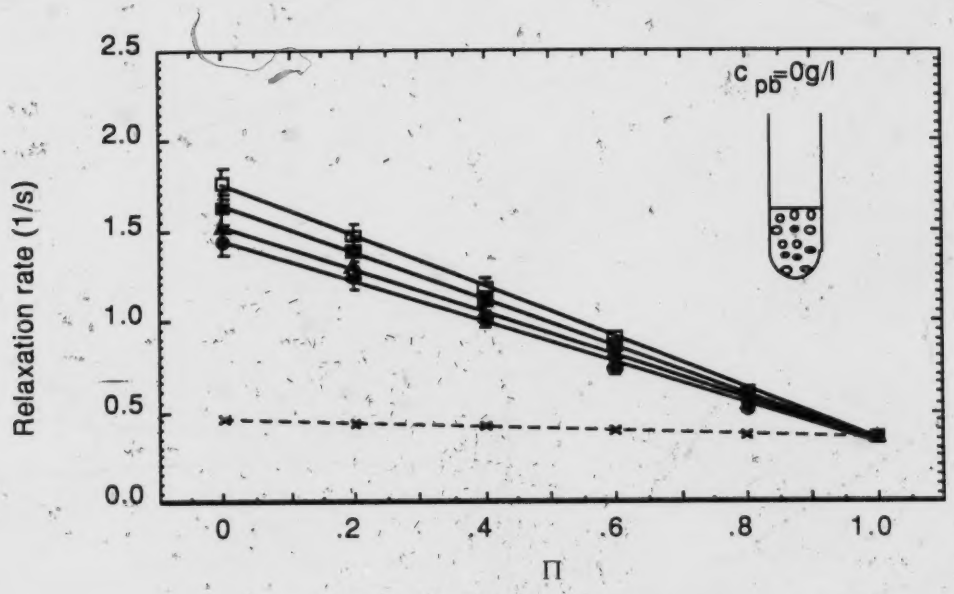


**Figure 3.2(a).** Mixed solution data at $c_{pb}$ = 0 g/l: dependence of the relaxation rates measured in uniformly mixed samples on the fraction of buffer used in the samples. Only one component is measured for each of the relaxation rates $R_2$(□),$R_1$(x) and $R_{1\rho}$ at 0.3 mT(■), 0.6 mT(▲) and 0.9 mT(●). The ordinate Π = 0 corresponds to a packed sample of ghosts while Π = 1 corresponds to a sample containing only buffer. The fitted lines are calculated from a linear regresssion through the points corresponding to each relaxation rate.

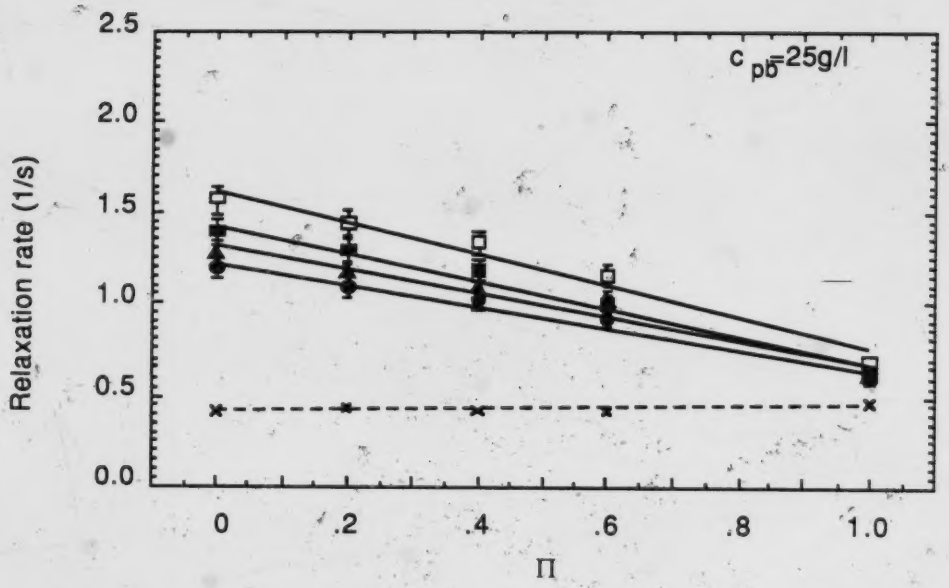


**Figure 3.2(b)**. Mixed solution data at $c_{pb}$ = 25 g/l; deependence of the relaxation rates measured in uniformly mixed samples on the fraction of buffer used in the samples. Only one component is measured for each of the relaxation rates $R_2$(□),$R_1$(x) and $R_{1\rho}$ at 0.3 mT(■), 0.6 mT(▲) and 0.9 mT(●). The ordinate $\Pi = 0$ corresponds to a packed sample of ghosts while $\Pi = 1$ corresponds to a sample containing only buffer. The fitted lines are calculated from a linear regresssion through the points corresponding to each relaxation rate.

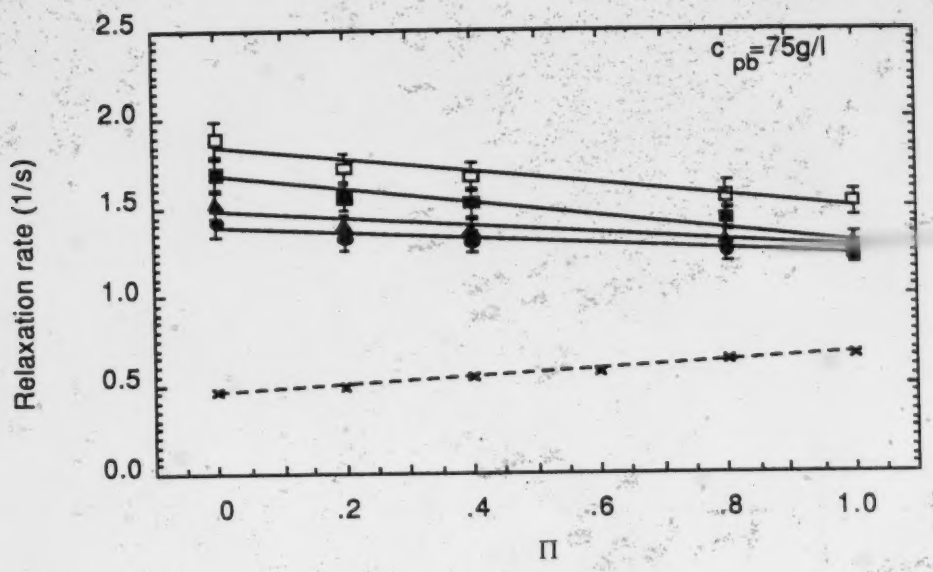


**Figure 3.2(c).** Mixed solution data at $c_{pb}$ = 75 g/l; dependence of the relaxation rates measured in uniformly mixed samples on the fraction of buffer used in the samples. Only one component is measured for each of the relaxation rates $R_2$(□),$R_1$(x) and $R_{1\rho}$ at 0.3 mT(■), 0.6 mT(▲) and 0.9 mT(●). The ordinate $\Pi = 0$ corresponds to a packed sample of ghosts while $\Pi = 1$ corresponds to a sample containing only buffer. The fitted lines are calculated from a linear regresssion through the points corresponding to each relaxation rate.

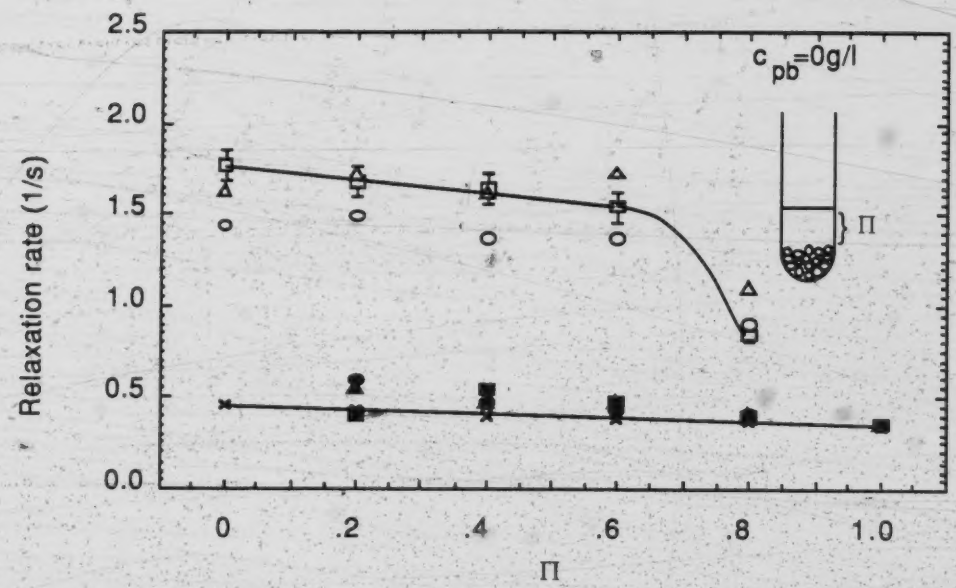


**Figure 3.3(a).** Data for layered preparations with $c_{pb}$ = 0 g/l. Behavior of the two components of $R_2$ and $R_{1\rho}$ as the fraction of buffer in a layered preparation is changed. $R_1$ remains monoexponential and equal to its value in mixed solutions. To improve the clarity, error bars are shown only for the $R_2$ data, and the $R_{1\rho}$ data at 0.6 mT have been omitted. The points at $\Pi = 0$ (packed ghosts) and $\Pi = 1$ (buffer) are duplicated from the corresponding points on the mixed sample graphs. Including them provides unambiguous assignment of the fast relaxing component to the ghost compartment and the slowly relaxing component with the layered buffer compartment. The symbols are defined as follows: In the ghost compartment, $R_2$(□), $R_{1\rho}$ at 0.3 mT(▲) and 0.9 mT(○); in the layered buffer compartment, $R_2$(■), $R_{1\rho}$ at 0.3 mT(▲) and 0.9 mT(●); for the entire sample, $R_1$(x). All lines are calculated using a linear regression except the curve for $R_2$(□).

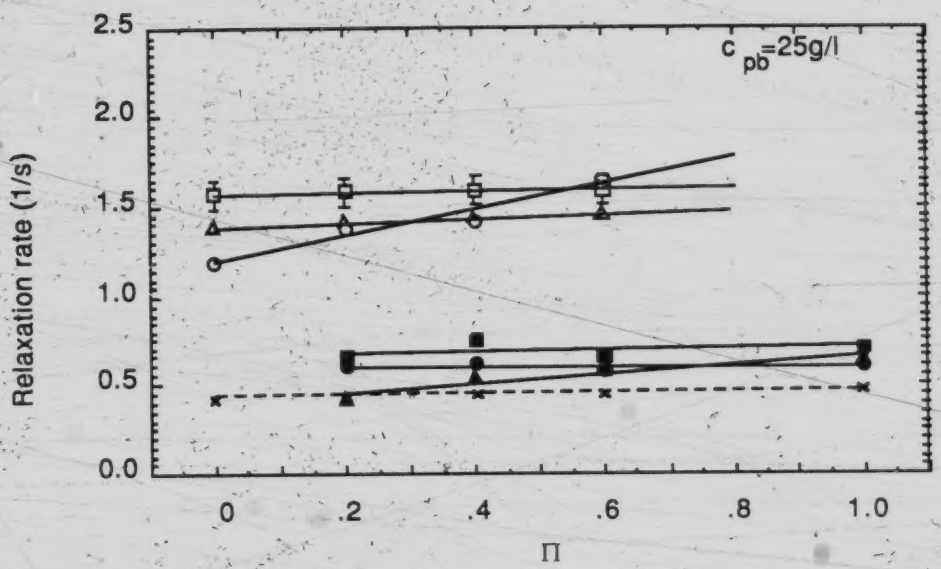


**Figure 3.3(b).** Data for layered preparations with $c_{pb}$ = 25 g/l. Behavior of the two components of $R_2$ and $R_{1\rho}$ as the fraction of buffer in a layered preparation is changed. $R_1$ remains monoexponential and equal to its value in mixed solutions. To improve the clarity, error bars are shown only for the $R_2$ data, and the $R_{1\rho}$ data at 0.6 mT have been omitted. The points at $\Pi = 0$ (packed ghosts) and $\Pi = 1$ (buffer) are duplicated from the corresponding points on the mixed sample graphs. Including them provides unambiguous assignment of the fast relaxing component to the ghost compartment and the slowly relaxing component with the layered buffer compartment. The symbols are defined as follows: In the ghost compartment, $R_2$(□), $R_{1\rho}$ at 0.3 mT(▲) and 0.9 mT(○); in the layered buffer compartment, $R_2$(■), $R_{1\rho}$ at 0.3 mT(▲) and 0.9 mT(●); for the entire sample, $R_1$(x). All lines are calculated using a linear regression.

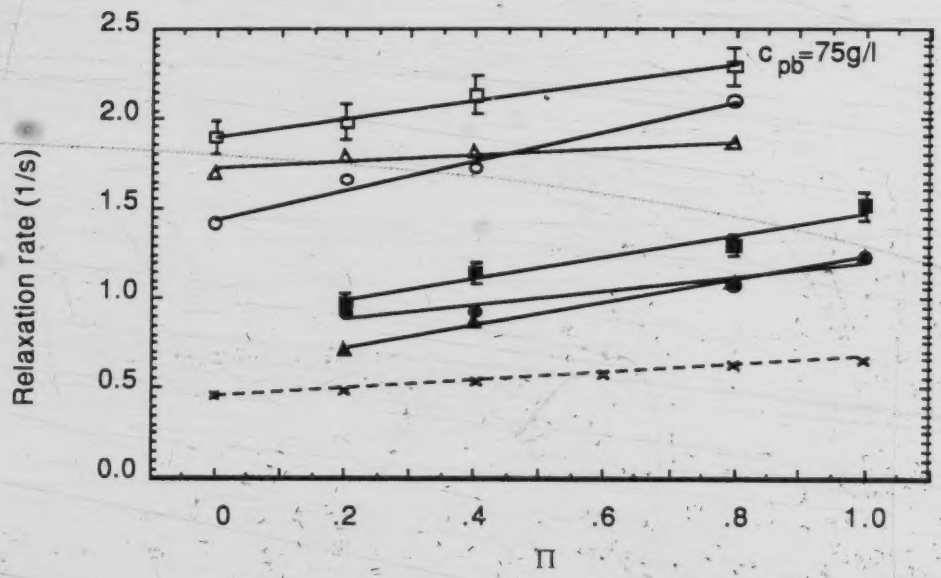


**Figure 3.3(c)**. Data for layered preparations with $c_{pb}$ = 75 g/l. Behavior of the two components of $R_2$ and $R_{1\rho}$ as the fraction of buffer in a layered preparation is changed. $R_1$ remains monoexponential and equal to its value in mixed solutions. To improve the clarity, error bars are shown only for the $R_2$ data, and the $R_{1\rho}$ data at 0.6 mT have been omitted. The points at $\Pi = 0$ (packed ghosts) and $\Pi = 1$ (buffer) are duplicated from the corresponding points on the mixed sample graphs. Including them provides unambiguous assignment of the fast relaxing component to the ghost compartment and the slowly relaxing component with the layered buffer compartment. The symbols are defined as follows: In the ghost compartment, $R_2$(□), $R_{1\rho}$ at 0.3 mT(▲) and 0.9 mT(○); in the layered buffer compartment, $R_2$(■), $R_{1\rho}$ at 0.3 mT(▲) and 0.9 mT(●); for the entire sample, $R_1$(x). All lines are calculated using a linear regression.

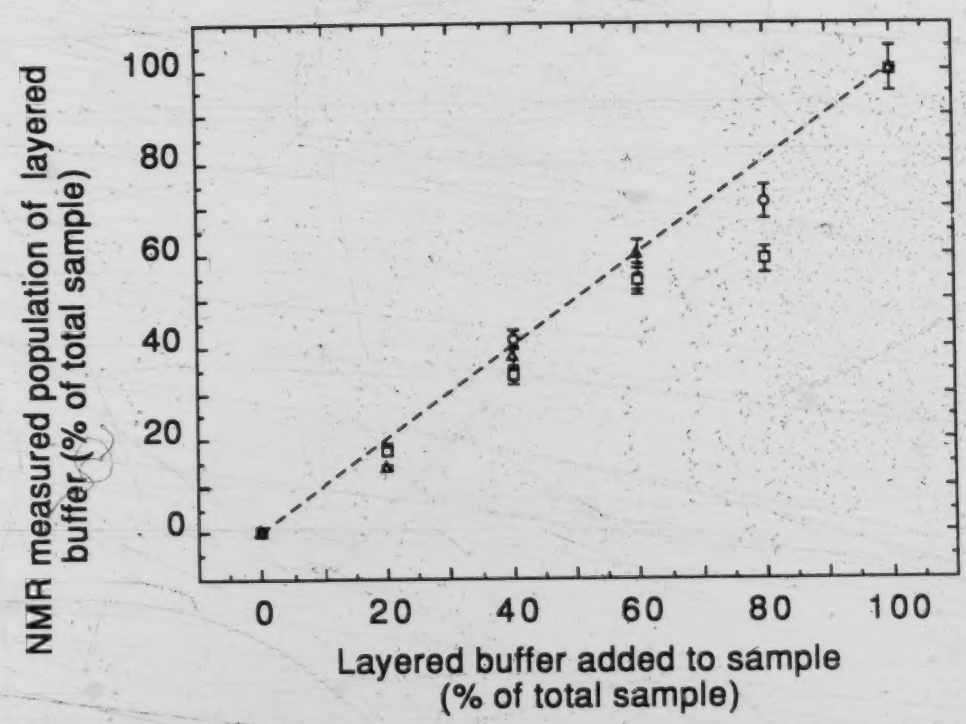


**Figure 3.4.** Correspondence between the amount of layered buffer added to a layered sample and the amount measured by NMR. The symbols indicate layered buffers containing no albumin(□), 25 g/l albumin(▲) and 75 g/l albumin(○). Points falling on the dashed line would indicate a one-to-one correspondence between the two quantities.

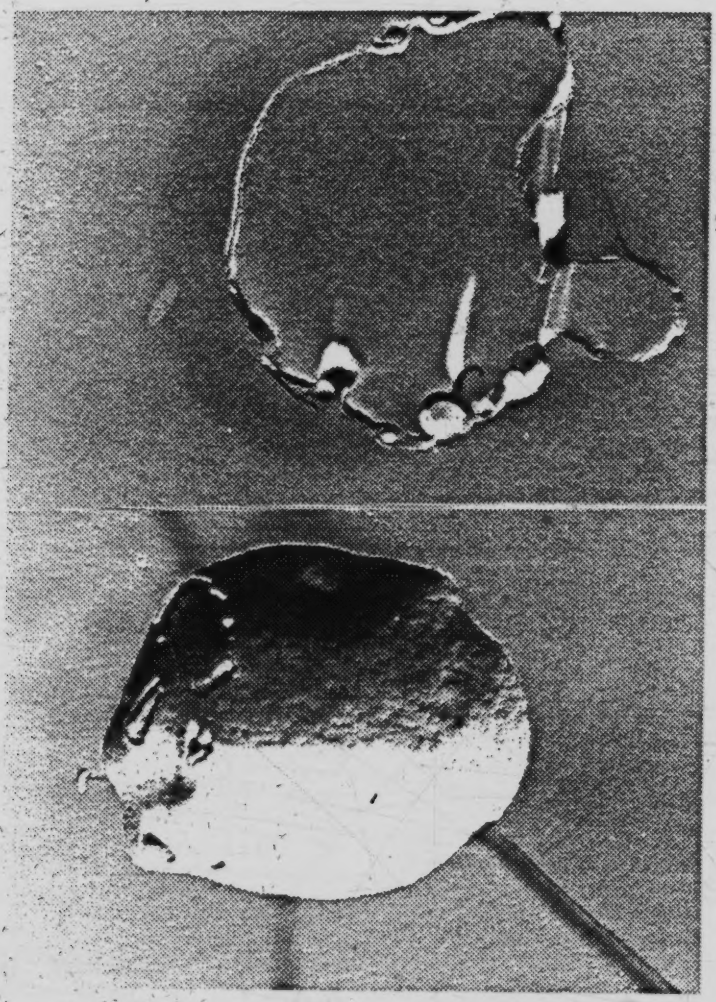

**Figure 3.5.** Electron micrograph of a red blood cell ghost. This is a freeze-fracture of a ghost (x 18,000). In addition to illustrating the cell membrane and internal characteristics, freeze-fractures revealed the amorphous and pliable nature of the erythrocyte ghosts. This micrograph shows that the preparation is clear of debris inside and out. Higher magnifications show the cellular cytoskeleton still in place.

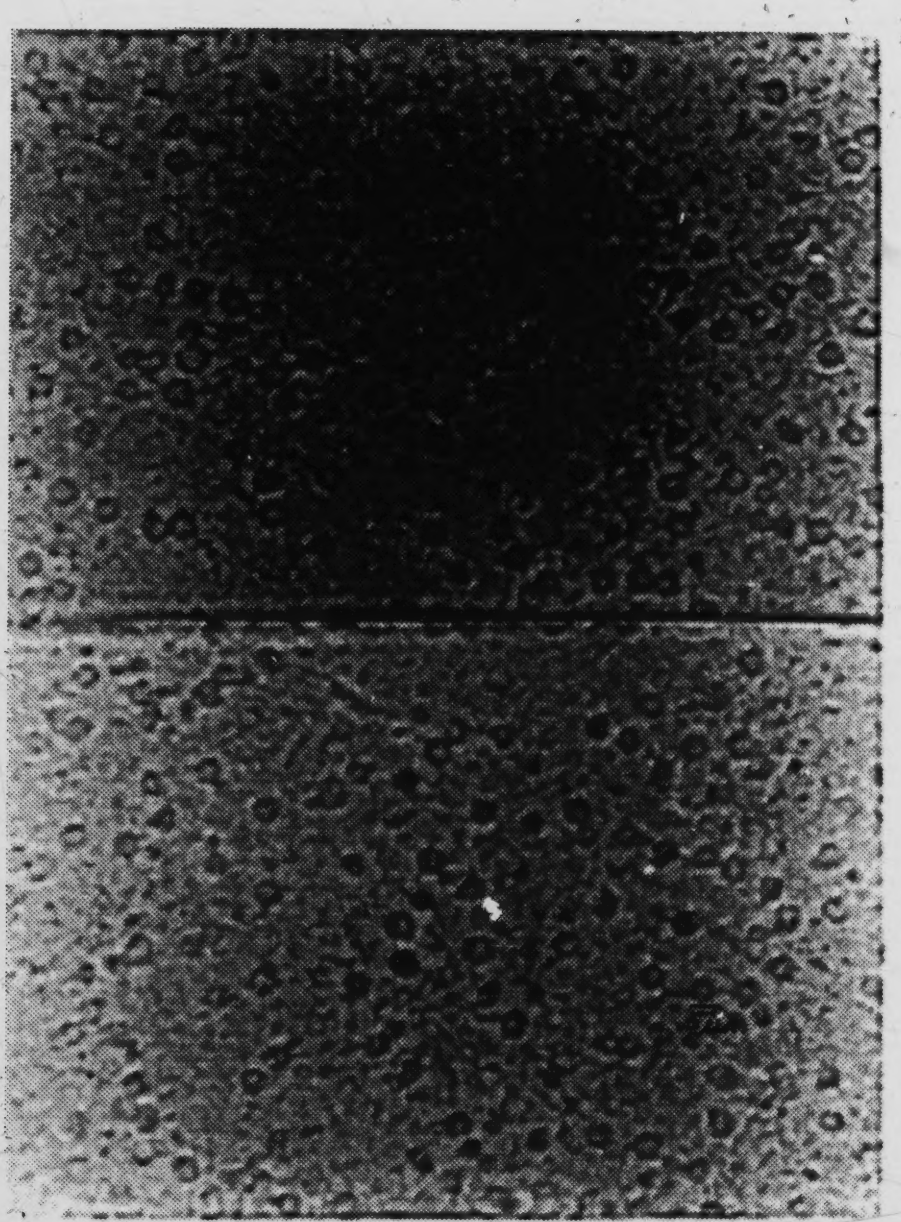

**Figure 3.6**. Phase contrast micrograph of a ghost preparation. The sample contains 66% extracellular buffer and gives an accurate idea of size at the expense of magnification. The small, fainter dots in the background are from ghosts above and below the focal plane of the microscope.

## 3.7 References


1. S. Conti, Proton magnetic relaxation dispersion in aqueous biopolymer systems I. Fibrinogen solutions, *Mol. Phys.* **59**, 449 (1986).
2. P.S. Allen, M.E. Castro, E.O. Treiber, J.A. Lunt and D.P.J. Boisvert, A proton NMR relaxation evaluation of a model of brain edema fluid, *Phys. Med. Biol.* **31**, 699 (1986).
3. R.S. Menon, and P.S. Allen, Solvent proton relaxation of aqueous solutions of the serum proteins $\alpha_2$-macroglobulin, fibrinogen and albumin, *Biophys. J.* **57**, 389 (1990).
4. S.H. Koenig, The dynamics of water-protein interactions, *in* "Water in Polymers" (S.P. Rowland, Ed.), p. 157, ACS Symposium Series, No. 127, Amer. Chem. Soc., Washington, D.C. 1980.
5. S.H. Koenig, R.G. Bryant, K. Hallenga and G.S. Jacob, Magnetic cross-relaxation among protons in protein solutions, *Biochemistry* **17**, 4349 (1978).
6. L. Grösch and F. Noack, NMR relaxation investigation of water mobility in aqueous bovine serum albumin solutions, *Biochim. et Biophys. Acta* **453**, 218 (1976).
7. J. Oakes, Protein hydration nuclear magnetic relaxation studies of the state of water in native bovine serum albumin solutions, *J. Chem. Soc. Farad. Trans.* I **72**, 216 (1976).
8. R. Kimmich and F. Noack, Zur deutung der kernmagnetischen relaxation in proteinlsösungen, *Z. Naturforsch.* **25a**, 1680 (1970).
9. D.C. Chang and C.F. Hazlewood, Nuclear magnetic resonance study of squid giant axon, *Biochim. et Biophys. Acta* **630**, 131 (1980).

10. P.T. Beal, C.F. Hazlewood and P.N. Rao, Nuclear magnetic resonance patterns of intracellular water as a function of HeLa cell cycle, *Science* **192**, 904 (1976).

11. G.P. Raaphorst, J. Kruuv and M.M. Pintar, Nuclear magnetic resonance study of mammalian cell water, *Biophys. J.* **15**, 391 (1975).

12. D.C. Chang, C.F. Hazlewood, B.L. Nichols and H.E. Rorschach, Spin echo studies of cellular water, *Nature* **235**, 170 (1972).

13. T.J. Swift and O.G. Fritz, Jr., Proton spin-echo study of the sate of water in frog sciatic nerve, *Biophys. J.* **9**, 54 (1969).

14. A. Francois, L. Van Gerven, G. Atassi, H. Eisendrath, M. Geilen and R. Willem, Analysis by the Carr-Purcell-Meiboom-Gill sequence of the influence of P388 leukemia and cis-diamminedichloroplatinum (II) nephrotoxicity on water compartmentalization in kidneys and spleens of mice, *Magn. Reson. Med.* **7**, 449 (1988).

15. W.T. Sobol, I.G. Cameron, W.R. Inch and M.M. Pintar, Modeling of proton spin relaxation in muscle tissue using nuclear magnetic resonance spin grouping and exchange analysis, *Biophys. J.* **50**, 181 (1986).

16. S.H. Koenig and R.D. Brown III, Determinants of proton relaxation rates in tissue, *Magn. Reson. Med.* 1, 437 (1984).

17. C.J.G. Bakker and J. Vriend, Multiexponential water proton spin-lattice relaxation in biological tissues and its implications for quantitative NMR imaging, *Phys. Med. Biol.* **29**, 509 (1984).

18. J.M. Escanye, D. Canet and J. Robert, Frequency dependence of water proton longitudinal NMR relaxation times in mouse tissue at 20 °C, *Biochim. et Biophys. Acta* **721** (1982).

19. G.D. Fullerton, J.L. Potter and N.C. Dornbluth, NMR relaxation of proteins in tissue and other macromolecular water solutions, *Magn. Reson. Imaging* **1**, 209 (1982).

20. E.E. Burnell, M.E. Clark, J.A.M. Hinke and N.R. Chapman, Water in barnacle muscle III. NMR studies of fresh fibres and membrane damaged fibres equilibrated with selected solutes, *Biophys. J.* **33**, 1 (1981).

21. J.G. Diegel and M.M. Pintar, Origin of non-exponentiality of the water proton spin relaxations, *Biophys. J.* **15**, 855 (1975).

22. B.M. Fung and T.W. McGaughy, The state of water in muscle as studied by pulsed NMR, *Biochim. et Biophys. Acta* **343**, 663 (1974).

23. E.D. Finch and L.D. Homer, Proton nuclear magnetic resonance relaxation measurements in frog muscle, *Biophys. J.* **14**, 907 (1974).

24. R.R. Knispel, R.T. Thompson and M.M. Pintar, Dispersion of proton spin lattice relaxation in tissues, *J. Magn. Reson.* **14**, 44 (1974).

25. P.S. Belton, K.J. Packer and T.C. Sellwood, Pulsed NMR studies of water in striated muscle, *Biochim. et Biophys. Acta* **304**, 56 (1973).

26. R.K. Outhred and E.P. George, Water and ions in muscles and model systems, *Biophys. J.* **13**, 97 (1973).

27. C.F. Hazlewood, B.F. Nichols and N.F. Chamberlain, Evidence for the existence of a minimum of two phases of ordered water in skeletal muscle, *Nature* **222**, 747 (1969).

28. P.S. Belton and R.G. Ratcliffe, NMR and compartmentation in biological tissue, *Prog. NMR Spectrosc.* **17**, 241 (1985).

29. R. Mathur-De Vre, The NMR studies of water, *Prog. Biophys. Molec. Biol.* **35**, 103 (1979).

30. R. Cooke and I.D. Kuntz, The properties of water in biological systems, *Ann. Rev. Biophys. Bioeng.* **3**, 95 (1974).

31. R.S. Menon, M.S. Rusinko and P.S. Allen, *in* "Proc. VII$^{th}$ Annual Meeting of the Society of Magnetic Resonance in Medicine", p. 228 (1988).

32. T.L. Steck and J.A. Kant, Preparation of impermeable ghosts and inside-out vessicles from human erythrocyte membranes, *Methods Enzymol.* **3**, 172 (1974).

33. H.Y. Carr and E.M. Purcell, Effects of diffusion on free precession in nuclear magnetic resonance experiments, *Phys. Rev.* **94**,630 (1954).

34. S. Meiboom and D. Gill, Modified spin-echo method for measuring nuclear relaxation times, *Rev. Sci. Instrum.* **29**, 688 (1958).

35. D.G. Hughes and L. Lindblom, Baseline-drift in the Carr-Purcell-Meiboom-Gill pulsed NMR experiment, *J. Magn. Reson.* **26**, 469 (1977).

36. R. Freeman and D. Hill, Fourier transform study of NMR spin-spin relaxation, *J. Chem. Phys.* **55**, 1985 (1971).

37. S.R. Hartman and E.L. Hahn, Nuclear double resonance in the rotating frame, *Phys. Rev.* **128**, 2042 (1962).

38. D.W. Marquardt, An algorithm for least-squares estimation of non-linear parameters, *J. Soc. Ind. Appl. Math.* **11**, 431 (1963).

39. K.P. Whittal and A.L. MacKay, Quantitative interpretation of NMR relaxation data, *J. Magn. Reson.* **84**, 134 (1989).

40. J.A. Dix and A.K. Solomon, Role of membrane protein and lipid in water diffusion across red cell membranes, *Biochim. et Biophys. Acta* **773**, 219 (1984).

41. J. Brahm, Diffusional water permeability of human erythrocytes and their ghosts, *J. Gen. Physiol.* **79**,, 791 (1982).

42. T. Conlon and R. Outhred, The temperature dependence of erythrocyte water diffusional permeability, *Biochim. et Biophys. Acta* **511**, 408 (1978).

43. J.R. Zimmerman and W.E. Brittin, Nuclear magnetic resonance studies in multiple phase systems: lifetime of a water molecule in an absorbing phase on silica gel, *J. Phys. Chem.* **61**, 1328 (1957).

44. Y. Kikuchi and T. Koyama, Red blood cell deformability and protein absorption on the red blood cell surface, *Am. J. Physiol.* **247**, H739 (1984).

45. Y. Kikuchi and T. Koyama, Effects of $Na^+$ and $K^+$ on protein adsorption on the red blood cell surface, *Am. J. Physiol.* **247**, H748 (1984).

46. S.L. Law, W.Y. Lo, S.H. Pai, G.W. Teh and F.Y. Kou, The adsorption of bovine serum albumin by liposomes, *Int. J. Pharmaceutics* **32**, 237 (1986).

47. E. Ponder, "Hemolysis and Related Phenomena", Grune and Stratton, New York, 1971.

48. R.S. Menon and P.S. Allen, Application of continuous relaxation time distributions to the fitting of data from model systems and excised tissue, accepted in *Magn. Reson. in Med.* (1990).

# CHAPTER 4[1]

## Application of continuous relaxation time distributions to the fitting of data from model systems and excised tissue

### 4.1 Introduction

Heterogeneous systems such as water in biological tissues often give rise to multiple proton relaxation times (1-18). If the diagnostic potential of these relaxation times is to be exploited, an understanding of the mechanisms that give rise to multicomponent relaxation in tissue is needed. However, the assessment of water proton relaxation models in tissue requires a method of accurately characterizing the observed magnetization decay or recovery, in order to detect changes over time or differences between tissues.

In a biological system, the water molecules exist in a variety of different environments, with some degree of exchange occurring between some of them. Since biological systems exhibit heterogeneity (even within supposedly homogeneous tissue) one realistically expects a distribution of relaxation times. Any method of fitting relaxation data to an *a priori* number of discrete exponentially decaying components must necessarily bias the results. In tissue it has, in the past, been assumed that there are two (6), three (19), four (20) or five (21) distinguishable environments or states of water and that these must govern the choice of the number of discrete components to be fitted. Such a framework for the analysis of water proton relaxation in tissue is somewhat restricted, because it forces an interpretation

---

[1] A version of this chapter has been accepted for publication. R.S. Menon and P.S. Allen, Application of continuous relaxation time distributions to the fitting of data from model systems and excised tissue, *Magn. Reson. Med.* (1990).

of the data prior to its analysis. If, instead, the measured data can be modelled by a technique which requires no *a priori* guess as to the nature of the relaxation processes, such restrictions can be lifted (22, 23, 24). Such methods exist, for example, in the form of linear inverse theory techniques (25, 26), which can be used to characterize the time dependence of the magnetization in terms of discrete or continuous distributions of relaxation times. Previous validations of continuous distributions in NMR (22, 23) have involved fitting numerically synthesized relaxation data where the noise is assumed to be uncorrelated and Gaussian. However, it has not been demonstrated that continuous distributions can accurately characterize the true relaxation time distributions in tissue, since, of course, independent assessment of this relaxation time distribution is not normally available. Furthermore, the effects of measurement errors that are not random have not been dealt with either.

In this chapter, we investigated the application of continuous distributions first to a model system of red blood cell (RBC) ghosts. We also obtain an independent measurement of the relaxation time distributions in this model system using a one-dimensional imaging technique to measure relaxation times as a function of position in the axially symmetric samples. Following the establishment of guidelines for picking a particular distribution we then proceed to demonstrate the application of the algorithm to *in-vitro* relaxation time measurements on excised brain samples, where traditional fitting techniques yield unstable and not always consistent results (22, 27).

## 4.2 Theory

A general description of the magnetization decay M(t) in a relaxation time experiment on tissue water is given by a Fredholm integral equation of the first kind, namely

$$M(t)=\int_0^\infty S(T)\exp(-t/T)\,dT \qquad T = T_1,T_2,T_{1\rho} \tag{4.1}$$

where S(T) is the unknown fractional amplitude of the measured magnetization relaxing with the time constant T and for which the solution is sought. A detailed implementation of a solution of Equation (4.1) for NMR experiments is discussed by Whittall and Mackay (23) utilizing the non-negative least-squares (NNLS) algorithm of Lawson and Hanson (28) and by Kroeker and Henkelman (22) using the methods of Provencher (29, 30).

NNLS has been used to generate a solution set $S(T_j)$ when Equation (4.1) is adapted for N discrete data points (23). The data $M(t_i)$ is then represented by

$$M(t_i) = \sum_{j=1}^{D} A_{ij}S(T_j) \qquad i = 1,2,\ldots,N \tag{4.2}$$

where $A_{ij}$ is a matrix with elements $\exp(-t_i/T_j)$. The solution space is parametrized by D possible relaxation time delta-functions at times $T_j$, chosen to span the range of expected relaxation times. We have chosen D = 200 points with 1 ms $\leq T_j \leq$ 100 s. The limits of 1 ms and 100 s were chosen because on one hand, our choice of inversion and echo times preclude accurate measurements of $T_1$ and $T_2$ below 1 ms, and on the other hand, one does not expect water proton relaxation rates in excess of

a few seconds in tissue. Using NNLS, a solution set $S(T_j)$ can be found which contains a usually small number of components (values of $T_j$ for which $S(T_j) \neq 0$) needed to fit the data in a least-squares sense, i.e. by minimizing the least-squares function

$$\sum_{i=1}^{N} \left| \sum_{j=1}^{D} A_{ij} S(T_j) - M(t_i) \right|^2 \qquad (4.3)$$

In order to accommodate the noise that inevitably contaminates $M(t_i)$, the preferred technique is to find a solution $S(T_j)$ which produces a chi-squared misfit ($\chi^2$) of roughly N (23). However, solutions utilizing Equation (4.3) as the minimization function are found to exhibit $\chi^2 < N$, implying that some of the structure in the solution can be attributed to fitting the noise. It has been shown (23) that NNLS can be modified to increase the $\chi^2$ to a more realistic level by producing a pseudo-continuous distribution of the $S(T_j)$ by minimizing a function such as

$$\sum_{i=1}^{N} \left| \sum_{j=1}^{D} A_{ij} S(T_j) - M(t_i) \right|^2 + \mu \sum_{j=1}^{D} S(T_j)^2 \quad , \qquad (4.4)$$

where $\mu$ is a parameter sometimes called the trade-off parameter or regularizor (22, 23). By means of $\mu$, the $\chi^2$ can be increased to a more optimumal value by forcing the algorithm to minimize the "energy" in the spectrum $\{S(T_j)^2\}$ at the expense of smearing out the delta-function solution.

To utilize NNLS rigorously, one needs an estimate of the noise contaminating the magnetization decay. We have found from careful analysis of the residuals from the delta-function fit, as well as from repeated measurements on the same sample, that the usual technique of measuring the noise at times long compared to the

relaxation times seriously underestimates the noise in the data. This results in some of the structure in the solution being due to noise. Our measurements show that the noise for both the $T_1$ and $T_2$ experiments (i) does not have zero mean over short (< 5 s) intervals, (ii) is serially correlated, (iii) is larger at short times and (iv) is roughly Gaussian distributed in amplitude over short (< 0.5 s) intervals. We have chosen to estimate our noise for each point in the magnetization decay from the value of the residuals around that point when using the delta-function fit (31). Each data point is then divided by its estimated noise before fitting, resulting in a weighted least-squares solution. Such a noise estimate gives $\chi^2 << N$ for the delta-function fit and one can then proceed to adjust $\chi^2$ to the desired level using $\mu$ as described above.

## 4.3 Experimental

### 4.3.1 Layered Model Samples

RBC ghosts were prepared using a modification of the method of Steck and Kant (32,33). Three different samples were used. The first sample (Sample A) consisted of 120 µl of packed RBC ghosts in a 5 mm (OD) NMR tube. The second sample (Sample B) consisted of 60 µl of packed RBC ghosts carefully layered onto 60 µl of saline containing 100 g/l of serum albumin in an NMR tube. Similarly, the third sample (Sample C) was made up of 60 µl of saline layered onto 60 µl of packed RBC ghosts. For both Sample B and C, the lighter fraction was layered onto the denser one. Using such samples, the effect of water exchange between compartments with different relaxation times was studied (32).

### 4.3.2 Excised Cat Brain

Six mature cats (random source) were sacrificed, each prior to its immediate use, with an injection of Euthanol IV into the radial artery . The skull cap of each cat was removed and the brain carefully dissected out of the skull. Well demarcated 100 to 200 µl samples of grey and white matter were dissected from the brain and sealed in 10 mm (OD) NMR tubes, within 20 minutes of the animal's death. NMR measurements were then made immediately and, on the same samples from three cats, repeated 10 hours later after storage at 4 °C in order to assess any changes which may have occurred over time.

### 4.3.3 Relaxation measurements

The proton relaxation rates were measured with a Bruker CXP spectrometer at 100 MHz. The water proton line width obtained for these samples in the 40 cm bore magnet was better than 20 Hz. The measurements were made at a room temperature of 22 ± 2 °C. The magnetization decays were all obtained with a 90° pulse length of 7.5 µs.

The longitudinal relaxation was measured using the Freeman-Hill modification (34) of the inversion recovery sequence ($180_y$--$\tau$--$90_x$--AQ--TR/0--$\tau$--$90_{-x}$--AQ--TR), where TR is the sequence repetition interval. The advantage of using this sequence is that the magnetization recovery curve is always positive, dropping from $2M_o$ to zero, with the initial magnetization, $M_o$, being measured as often as the partly relaxed magnetization. The $\tau$ values, ranging from 1 ms to 7.9 s for the ghost samples and 10 ms to 7.9 s for the cat brain samples, provided 10 points, arranged

logarithmically, in each decade of time. Four acquisitions of each add/subtract pair were averaged. The complete data set was used for curve fitting.

The transverse relaxation was measured using a 16384 echo Carr-Purcell-Meiboom-Gill (CPMG) add/subtract sequence (35,36), with an inter-echo spacing, $\tau$, of 400 μs. The CPMG sequence was phase cycled (37) in order to eliminate baseline errors generated by both receiver dc offsets and residual magnetization generated by phase errors in the 180° pulses. The choice of the echo time was made to minimize the effects of diffusion on $T_2$. The add/subtract sequence was repeated 8 times and the resulting signal was averaged. From the complete $T_2$ data set, 153 echos were selected for fitting so that they logarithmically spanned the time interval between 400 μs and 6.55 s.

### 4.3.4 Imaging methods

In order to acquire measurements of the spatial distribution of the relaxation times through a ghost preparation, the usual CPMG sequence was used with a linear field gradient ($10^4$ Hz/cm) oriented parallel to the axis of the NMR tube (38). By stepwise incrementation of the number of echos between 1 and 16384, magnetization profiles of the sample could be obtained corresponding to any given echo of the CPMG sequence. Using typically twenty such well spaced (in echo number) profiles, measurements of $T_2$ as a function of position in the samples were obtained. Based on successive NMR measurements on the same samples, the standard deviation in $T_2$ calculated from the spatial profiles is estimated at less than 7 %.

## 4.4 Results

### 4.4.1 Layered model samples

The inversion recovery data for all three of the samples A, B and C show monoexponential behavior over the range of inversion times used (linear regression coefficient > 0.99) . This is consistent with the work of others on model systems (32) and tissues (1-21) and suggests that in general, the underlying exchange processes between layers in these RBC ghost preparations must be much faster than the rate of longitudinal relaxation.

The transverse relaxation times in the layered samples were determined in two very distinct ways. First, they were calculated using a linear regression on the logarithm of the profile amplitudes at nine different locations along the axis of the sample. At each of the locations chosen for analysis, the decay curves were found to be monoexponential (linear regression coefficient > 0.99). The spatial distribution of $T_2$ values thus measured is illustrated in Figure 4.1, which shows uniform transverse relaxation of the water protons in Sample A, but more complex behavior in samples B and C. The second, and more usual method of characterizing the transverse relaxation in such samples is to perform a CPMG experiment on the whole sample and to analyze the time dependence of the magnetization in terms of a multi-exponential fitting routine (39). The echo trains for samples A, B and C are shown in Figure 4.2 and the $T_2$ values for the whole sample, as computed from three different fitting techniques, are given in Table 4.1.

### 4.4.2 Cat brain samples

The analysis of the inversion recovery data in cat brain (Figure 4.3a) is not clear. The addition of a second component improves the nonlinear fit somewhat, but the $T_1$ values thus measured are sufficiently close to each other (factor of 2) to be considered inseparable using conventional techniques on only 40 points (27). Typical CPMG curves for grey and white matter from cat brain are shown in Figure 4.3b. Because the number of exponential components that should be used to characterize these data is not apparent, either from these plots or from other work (40-46), NNLS was used to characterize these curves. This use is summarized in Table 4.2 for the inversion recovery data and Table 4.3 for the CPMG data.

## 4.5 Analysis and Discussion

The interpretation of the time dependence of the magnetization in an NMR experiment is usually carried out in terms of a physical model. In order to do this in a quantitative manner, one needs accurate information about the nature of the distribution of relaxation times in the sample. One also needs to be able to discriminate between, (i) the situation where the width of the distribution is due to measurement uncertainties and (ii) the situation where the shape of the distribution is a consequence of the underlying physical mechanisms that generate relaxation. The experiments on layered model systems presented here allow one to show that continuous NNLS techniques provide an appropriate way to characterize the relaxation properties of the samples by providing a measure of distribution widths that result from these techniques. These results then give confidence in our

interpretation of features found when the continuous NNLS algorithm is applied to relaxation time measurements on tissue.

### 4.5.1 Layered model samples

Visual examination of Figure 4.2 might suggest that the CPMG curves for samples A and C could be adequately fitted with one exponentially decaying term, while sample B would likely require at least two terms. However, *a priori* knowledge about the sample configurations would lead to a choice of two exponentially decaying terms to describe the relaxation of sample C as well as that of B. Even with such simple models, one is already faced with uncertainty and a potential bias in interpreting the results using either one or two components.

We have analysed the CPMG curves from these three samples using three alternative techniques, the results of which are summarized in Table 4.1. The first technique was the more usual nonlinear least-squares technique (39). The second and third involved the application of NNLS methods, which are also demonstrated graphically in Figures 4.4 and 4.5. When either the nonlinear least-squares or delta-function NNLS solution was sought, we obtained the intuitively expected number of components, based on the number of layers in the samples as can be seen from the populations and relaxation times reported in Table 4.1. While the nonlinear least-squares and delta-function NNLS solutions for sample A and B may be considered adequate from a goodness of fit point of view, because of their discrete nature, neither one provides an indication of the true distribution of relaxation times that must exist in these samples. In principle, this shortcoming should be overcome by the continuous NNLS models shown in Figure 4.4, which, maintain some of the character of the NNLS delta-function solution for samples A and B.

The different curves shown in Figure 4.4 correspond to different confidence levels based on the $\chi^2$ misfit of the solution. For solutions within a reasonable statistical expectation (i.e. having $\chi^2 \geq N$), we notice that there is little change in the shape of the calculated distribution; in other words, solutions with confidence levels of greater than 75 % are an acceptable reflection of the $T_2$ distribution and are not artifactual due to the fitting of noise. Support for this conclusion can be found in previous work (22), using simulated data containing a unimodal Gaussian distribution of relaxation times, that suggests that for signal-to-noise ratios (SNR) exceeding 1000, the width of the calculated distribution approaches that of the true distribution. Our data readily meet this nominal condition on SNR. Further evidence in support of the continuous NNLS solution is provided by Figure 4.5, in which the proton-density-weighted integral of the transverse relaxation measurements from the image profiles are superimposed on the integral of the continuous NNLS solution at 99.99 % confidence. For sample B, the growth of the integrated intensity, as the sample is traversed, shows a distinct step between two individual components that correspond quite closely to the integral of the continuous NNLS solution.

Sample C provides an example that is somewhat more demanding than either A or B. The two discrete methods of solution can each be made to predict two components, though there is little consistency between their estimates of component fractions (see Table 4.1), neither of which agrees with that of the actual sample prepared. At first sight the continuous NNLS technique appears to fail on sample C, because it is unable to separate two components. However, the two components that make up sample C have $T_2$ values that are less than a factor of two apart, a factor considered to be the minimum necessary for reliable separation (27). Moreover,

Figure 4.5c shows that a single broad asymmetric hump is likely to be the more representative picture, because the integrated $T_2$ intensity derived from the image profiles does not show two distinct steps in sample C as the sample is traversed along its axis, as it did for sample B. To account for the lack of discrimination in sample C, we postulate that a stirring up of the ghosts may have occurred during the layering process and this postulate is supported by the fact that the $T_2$ values measured in the buffer layer are less than those measured for the bulk isolated buffer. Such a stirring may also explain why the $T_2$ distribution peaks for sample B are wider and more asymmetric than one would expect for two well delineated layers.

As a result of this experience with the various samples of the two layer RBC ghost system, we believe that continuous NNLS provides a preferable and workable alternative to the discrete techniques that are commonly used for the unbiased analysis of relaxation time distributions

### 4.5.2 Cat brain samples

Having determined that a continuous NNLS technique of analysis is the preferred method in model systems, some justification exists for applying it to the characterization of complex tissues such as brain. The application of continuous NNLS fitting to the data for the excised cat brains is summarized in Table 4.2 for the longitudinal magnetization and Table 4.3 for the transverse magnetization and the relaxation time distributions are shown in Figure 4.6. Confidence in the number and shape of the peaks in Figure 4.6 is derived from the fact that the solution is stable and no additional peaks appear when the confidence level of the NNLS solution is reduced to 75 %.

The measured mean values of $T_1$ and $T_2$ quoted in Table 4.2 for the major components in each of grey and white matter are consistent with previous measurements (40-46). The distribution of $T_1$ for grey and for white matter each contain only one component and the widths of these components are roughly equal. In contrast, the decay of the transverse magnetization can be reliably separated into more compartments by continuous NNLS than has previously been reported, largely because of the extensive raw data set and high SNR. The transverse relaxation time distributions of grey and white matter exhibit two major differences. Firstly, the continuous model NNLS algorithm consistently requires four components to fit the CPMG curve for white matter, while only two components are needed for grey matter. Secondly, the major peak in the white matter $T_2$ distribution is two to three times broader than that for grey matter.

The shortest $T_2$ component ($\cong$ 1 ms) in both grey and white matter is most likely due to the phospholipid protons in the tissue. Our results are consistent with the fact that white matter has roughly twice the phospholipid content of grey matter on a wet weight basis and that the $T_2$ of these protons is expected to be around 1 ms (4.7). The 6.8 % component in white matter has the right fractional population and the right $T_2$ (12.7 ms) to account for the hydration water in the myelin layers. The myelin bound fraction should be in slow exchange with the cellular water due to the appreciable diffusion barrier presented by the myelin layers. The major component (86 %) is undoubted water in fast exchange between the bulk cellular water and hydration sites on both the soluble proteins and the cellular cytoskeleton. The assignment of the small but long $T_2$ fraction in white matter is not obvious and is open to speculation.

In Tables 4.2 and 4.3, we have reported the effects of storage at 4° C on the relaxation times in grey and white matter. No differences were observed between freshly excised tissue (20 minutes post mortem) and refrigerator stored samples (up to 10 hours) for either tissue type. If, as has often been argued (5,6,46), the relaxation characteristics of excised tissue are different from those *in-vivo*, due to shifts in water balance occurring upon the death of the animal it would appear that such changes must take place in the first 20 minutes between death and our first NMR measurements. The purpose of this check in our work was not so much to investigate possible changes in water balance but to establish the stability of the observed relaxation components in our samples over a substantial period of time.

## 4.6 Conclusions

We have used the model system of RBC ghosts to enable an assessment to be made of three alternative methods of analysing relaxation time distributions, namely, the traditional, discrete component, non-linear least-squares technique (39) and both the discrete and continuous form of a non-negative least-squares algorithm (23,28). By means of independent measurements obtained using NMR imaging techniques (38), it was possible to demonstrate that the continuous NNLS solution to the relaxation time distribution question reflected the true distribution more faithfully than either of the discrete-solution methods. Furthermore, this method of solution required no *a priori* assumptions about the number of components.

In order that the width of the NNLS calculated continuous distribution unambiguously reflects the true relaxation time distribution, one requires time domain data with SNR better than $10^3$. It is also necessary to use as many time domain data

as possible ($\geq$ 100) and to follow the signal well down into the noise, in order to best constrain the fit. The use of $\chi^2$ to determine the confidence level of a solution requires an accurate measurement or model of the systematic and random errors in the measurement process. This detailed investigation of the spectrometer noise is necessary in order to to extract the best resolving power from the algorithm and to place a meaningful confidence level on the chosen solution. For complicated multiexponential data, the continuous NNLS method is also more stable than traditional fitting techniques and in the case of *in-vitro* relaxation measurements on excised tissue, can allow us to delineate consistently multiple peaks in the relaxation time distribution. The width of these peaks can provide insight into the mechanisms giving rise to the relaxation.

Table 4.1

A comparison between different techniques for fitting relaxation data.[a]

| | Sample A[b] | Sample B[c] | Sample C[c] |
|---|---|---|---|
| $T_2$ of ghost compartment (ms) | | | |
| using nonlinear least-squares | 1495 (1.0) | 1074 (0.384) | 1602 (0.259) |
| using discreet NNLS[d] | 1491 (1.0) | 1114 (0.545) | 1919 (0.758) |
| using continuous NNLS[d] | 1493 (1.0) | 1103 (0.559) | 2100 (1.0) |
| $T_2$ of buffer compartment (ms) | | | |
| using nonlinear least-squares | | 505 (0.616) | 2300 (0.747) |
| using discreet NNLS[d] | | 557 (0.455) | 2768 (0.242) |
| using continuous NNLS[d] | | 554 (0.441) | not resolved |
| Sample constituents[e] | | | |
| ghost compartment $T_2$ (ms) | 1495 (1.0) | 1495 (0.5) | 1495 (0.5) |
| buffer compartment $T_2$ (ms) | | 519 (0.5) | 2786 (0.5) |

[a] Fractional populations are shown in parenthesis by the respective $T_2$ values.

[b] The average standard deviation is ± 0.5 % for relaxation times.

[c] The average standard deviation is ± 2 % for relaxation times and ± 5 % for populations.

[d] Non-negative least-squares

[e] measured in isolation

Table 4.2

An evaluation of the longitudinal relaxation data from excised cat brain using the continuous NNLS[a] method of analysis.

| | $T_1$ (ms) |
|---|---|
| Grey matter | |
| Freshly excised[b] | 1152 ± 66 (100) |
| Stored 10 hours[c] | 1116 ± 55 (100) |
| All samples | 1140 ± 62 (100) |
| White matter | |
| Freshly excised[b] | 882 ± 62 (99 ± 1) |
| Stored 10 hours[c] | 859 ± 63 (99 ± 1) |
| All samples | 874 ± 58 (99 ± 1) |

[a] Fractional populations are shown in parenthesis by the corresponding $T_1$ values.

[b] Based on 6 cats.

[c] Based on 3 cats.

Table 4.3

An evaluation of the transverse relaxation data from excised cat brain using the continuous NNLS[a] method of analysis.

| | $T_2$ (ms) | $T_2$ (ms) | $T_2$ (ms) | $T_2$ (ms) |
|---|---|---|---|---|
| Grey matter | | | | |
| Freshly excised[b] | 103 ± 3 (0.98 ± 0.03) | 1.0 (0.02 ± 0.01) | | |
| Stored 10 hours[c] | 105 ± 1 (0.98 ± 0.03) | 1.0 (0.02 ± 0.01) | | |
| All samples | 103 ± 4 (0.98 ± 0.03) | 1.0 (0.02 ± 0.01) | | |
| White matter | | | | |
| Freshly excised[b] | 306 ± 59 (0.029 ± 0.001) | 89 ± 3 (0.86 ± 1) | 13.1 ± 1.1 (0.069 ± 0.008) | 1.0 (0.04 ± 0.01) |
| Stored 10 hours[c] | 379 ± 60 (0.017 ± 0.005) | 89 ± 3 (0.87 ± 2) | 12.4 ± 1.3 (0.068 ± 0.009) | 1.0 (0.05 ± 0.01) |
| All samples | 337 ± 52 (0.023 ± 0.009) | 89 ± 3 (0.86 ± 2) | 12.7 ± 1.1 (0.068 ± 0.008) | 1.0 (0.045 ± 0.01) |

[a] Fractional populations are shown in parenthesis by the corresponding $T_2$ values.

[b] Based on 6 cats.

[c] Based on 3 cats.

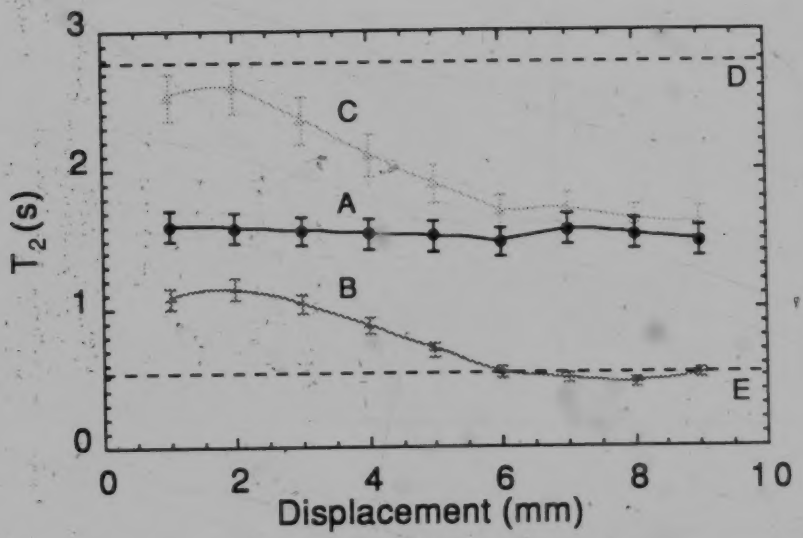


**Figure 4.1**. Transverse relaxation time measurements made from magnetization profile amplitudes that reflect the variation in magnetization as a function of displacement from the top of the sample in the model layered systems, A (packed RBC ghosts), B (packed RBC ghosts layered onto 100 g/l aqueous albumin solution) and C (saline buffer layered onto packed RBC ghosts). The dashed line, D, denotes the bulk $T_2$ of the saline buffer, while the dashed line E denotes the bulk $T_2$ of the 100 g/l albumin buffer.

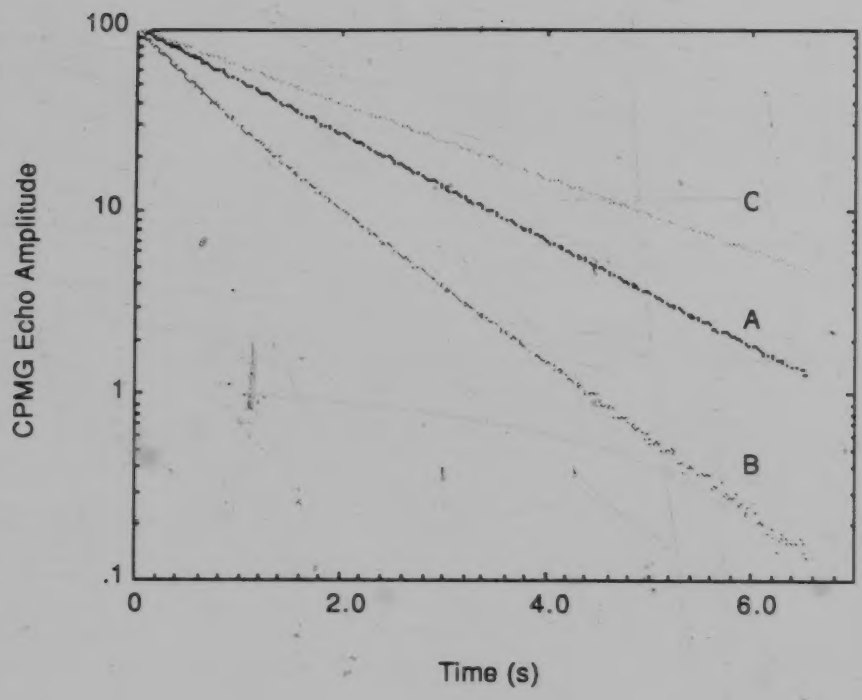


**Figure 4.2**. Normalized CPMG echo amplitude measured from the 120 µl volumes of samples A, B and C. Note that the noise level is almost four orders of magnitude lower than the initial signal intensity.

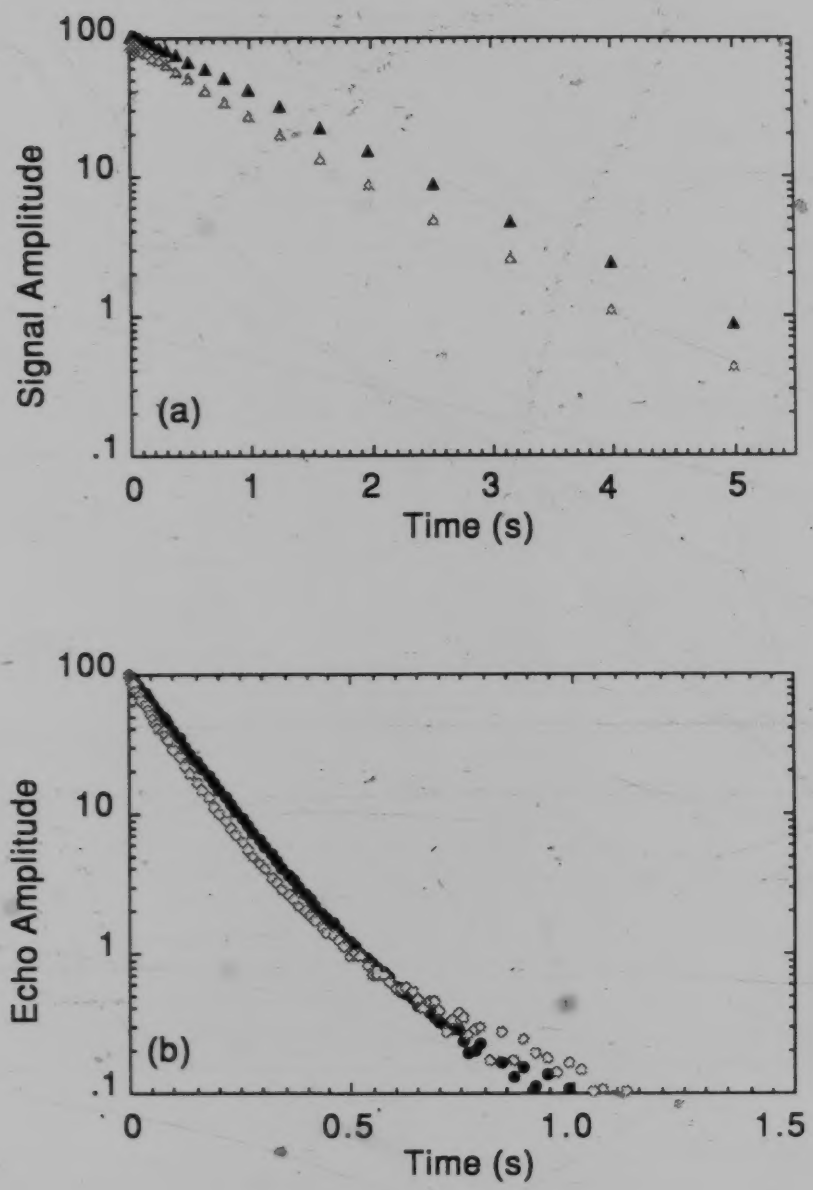


**Figure 4.3**. Semi-logarithmic plots of the inversion-recovery (a) and CPMG (b) measurements made on excised cat brain grey (▲, ●) and white matter (△, ○). The signal intensity was followed over three to four orders of intensity magnitude.

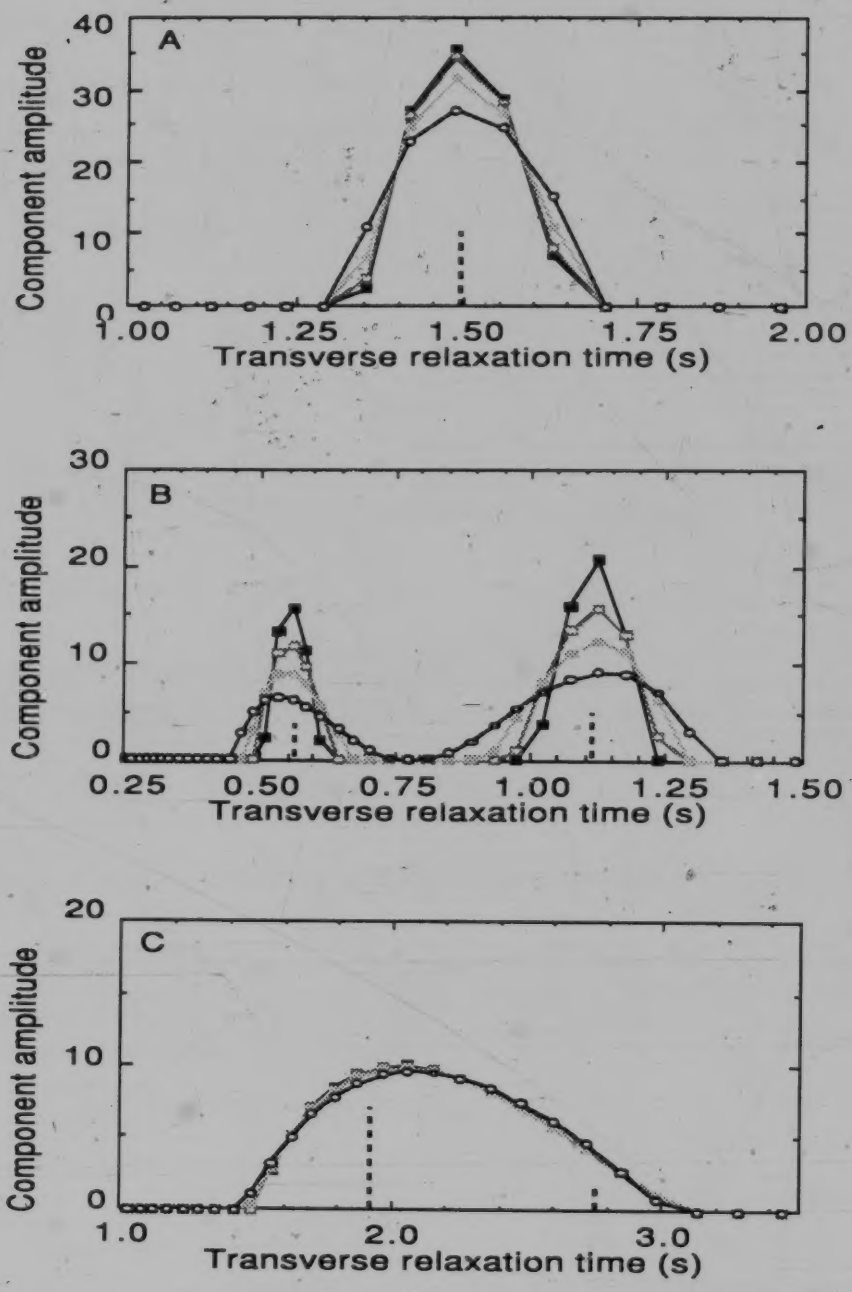


**Figure 4.4**. $T_2$ distributions of samples A, B and C. The solid lines are the calculated $T_2$ distributions using continuous NNLS on samples A, B and C, using the

data from Figure 4.2. The dashed lines come from a delta-function NNLS fit to the same CPMG data and have been divided by 10 to fit within the plot frames. The total integral of each curve represents the total magnetization in the sample and is normalized to 100. The confidence level of each solution (75 % ■, 85 % ◘, 95 % ▫, 99.99 % ○) is based on the noise in the data of Figure 4.2 and the $\chi^2$ misfit. Higher $\chi^2$ misfits allow a larger degree of confidence to be placed on the features of the solution.

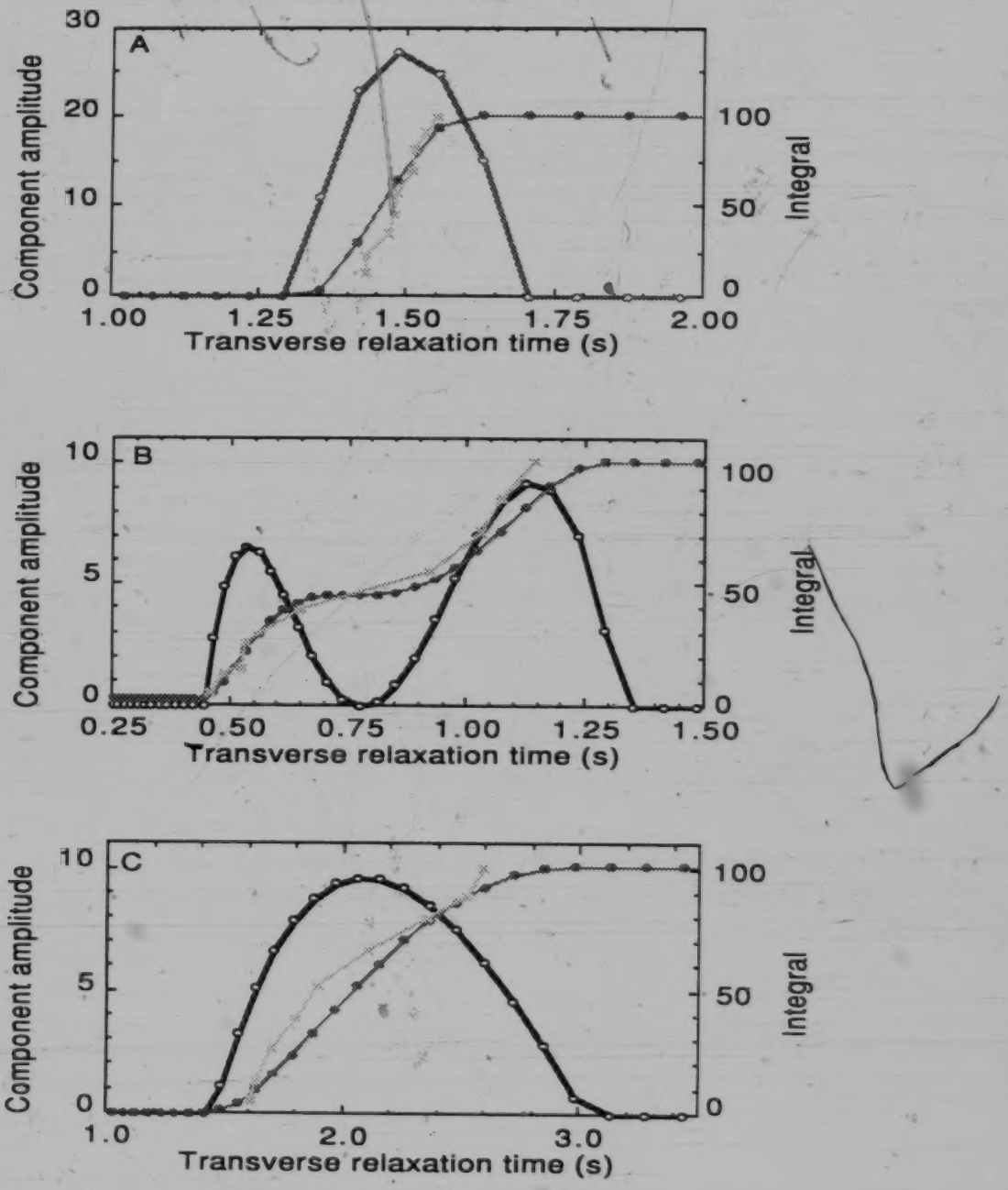


**Figure 4.5**. Comparison of integrals of calculated and imaged $T_2$ distributions. The bold curves (o) are the 99.99 % confidence level solutions from Figure 4.4. Also

shown is the integral for each solution ( • ) which represents the total magnetization in the samples A, B and C. This is compared with the integral of the magnetization (x) for each sample derived from the image profiles as described in the text, taking into account the axially varying proton density due to the shape of the NMR tube.

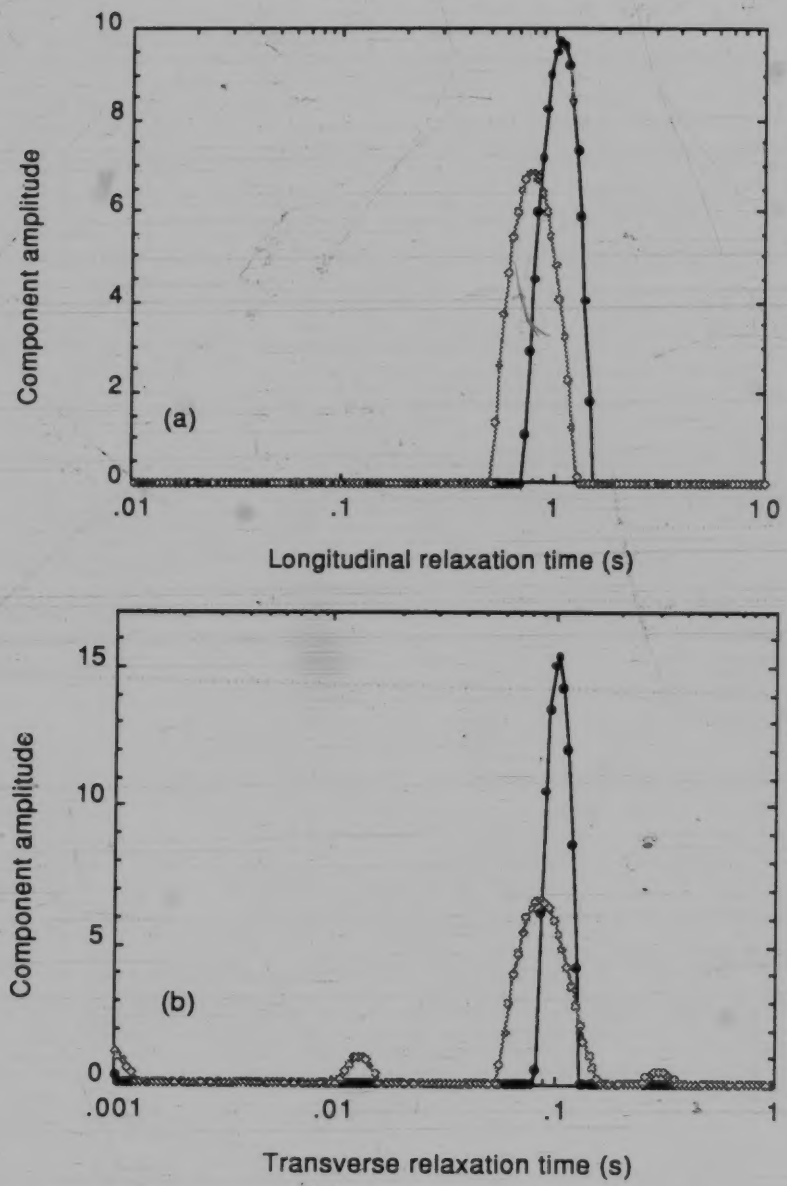


**Figure 4.6**. Continuous NNLS solutions of the *in-vitro* inversion-recovery (a) and CPMG (b) data collected from excised cat grey ( • ) and white ( ○ ) matter. Since the relaxation time scale is logarithmic, the visual areas of the peaks are not directly comparable. The curves are calculated for the 99.99 % confidence limit.

## 4.7 References

1. A. Francois, L. Van Gerven, G. Atassi, H. Eisendrath, M. Geilen and R. Willem, Analysis by the Carr-Purcell-Meiboom-Gill sequence of the influence of P388 leukemia and cis-diamminedichloroplatinum (II) nephrotoxicity on water compartmentalization in kidneys and spleens of mice, *Magn. Reson. Med.* **7**, 449 (1988).

2. W.T. Sobol, I.G. Cameron, W.R. Inch and M.M. Pintar, Modeling of proton spin relaxation in muscle tissue using nuclear magnetic resonance spin grouping and exchange analysis, *Biophys. J.* **50**, 181 (1986).

3. K.R. Sridharan, L.J. Shreiner, D.W. Kydon and M.M. Pintar, Characterization of normal and malignant mouse tissue by NMR lineshape-relaxation correlations in the rotating frame, *Magn. Reson. Med.* **2**, 73 (1985).

5. S.H. Koenig and R.D. Brown III, Determinants of proton relaxation rates in tissue, *Magn. Reson. Med.* **1**, 437 (1984).

6. C.J.G. Bakker and J. Vriend, Multiexponential water proton spin-lattice relaxation in biological tissues and its implications for quantitative NMR imaging, *Phys. Med. Biol.* **29**, 509 (1984).

7. G.D. Fullerton, J.L. Potter and N.C. Dornbluth, NMR relaxation of proteins in tissue and other macromolecular water solutions, *Magn. Reson. Imaging* **1**, 209 (1982).

8. E.E. Burnell, M.E. Clark, J.A.M. Hinke and N.R. Chapman, Water in barnacle muscle III. NMR studies of fresh fibres and membrane damaged fibres equilibrated with selected solutes, *Biophys. J.* **33**, 1 (1981).

9. J.G. Diegel and M.M. Pintar, Origin of non-exponentiality of the water proton spin relaxations, *Biophys. J.* **15**, 855 (1975).

10. M.C. Neville, C.A. Patterson, J.L. Rae and D.E. Woessner, Nuclear magnetic resonance studies and water "ordering" in the crystalline lens, *Science* **184**, 1072 (1974).

11. E.D. Finch and L.D. Homer, Proton nuclear magnetic resonance relaxation measurements in frog muscle, *Biophys. J.* **14**, 907 (1974).

12. R.R. Knispel, R.T. Thompson and M.M. Pintar, Dispersion of proton spin lattice relaxation in tissues, *J. Magn. Reson.* **14**, 44 (1974).

13. P.S. Belton and R.G. Ratcliffe, NMR and compartmentalization in biological tissue, *Prog. NMR Spectrosc.* **17**, 241 (1985).

14. R. Mathur-De Vre, The NMR studies of water, *Prog. Biophys. Molec. Biol.* **35**, 103 (1979).

15. R. Cooke and I.D. Kuntz, The properties of water in biological systems, *Ann. Rev. Biophys. Bioeng.* **3**, 95 (1974).

16. R.S. Menon, and P.S. Allen, Solvent proton relaxation of aqueous solutions of the serum proteins $\alpha_2$-macroglobulin, fibrinogen and albumin, *Biophys. J.* **57**, 389 (1990).

17. T.J. Swift and O.G. Fritz, Jr., Proton spin-echo study of the sate of water in frog sciatic nerve, *Biophys. J.* **9**, 54 (1969).

18. V. Vasilescu, E. Katona, V. Simplaceanu and D. Demko, Water compartments in the myelinated nerve. III. Pulsed NMR results, *Experientia* **34**, 1444 (1978).

19. K.F. Foster, H.A. Resing and A.N. Garroway, Bounds on "bound water", transverse NMR relaxation in barnacle muscle, *Science* **194**, 324 (1976).

20. H. Peemoeler and M.M. Pintar, NMR multiwindow analysis of proton local fields and magnetization distribution in natural and deuterated mouse muscle, *Biophys. J.* **28**, 339 (1979).

21. H. Peemoeler, M.M. Pintar and D.W. Kydon, NMR analysis of water in natural and deuterated mouse muscle above and below freezing, *Biophys. J.* **29**, 427 (1980).

22. R.M. Kroeker and R.M. Henkelman, Analysis of biological NMR relaxation data with continuous distributions of relaxation times, *J. Magn. Reson.* **69**, 218 (1986).

23. K.P. Whittal and A.L. Mackay, Quantitative interpretation of NMR relaxation data, *J.Magn. Reson.* **84**, 134 (1989).

24. R.M. Kroeker, C.A. Stewart, M.J. Bronskill and R.M. Henkelman, Continuous distributions of NMR relaxation times applied to tumors before and after therapy with x-rays and cyclophosphamide, *Magn. Reson. Med.* **6**, 24 (1988).

25. D.W. Oldenberg, An introduction to linear inverse theory, *IEEE Trans Geosci. Remote Sens.*, **GE-22**, 664 (1984).

26. R.L. Parker, Understanding inverse theory, *Ann. Rev. Earth Planet. Sci.* **5**, 35 (1977).

27. R.J.S. Brown, Information available and unavailable from multiexponential relaxation data, *J. Magn. Reson.* **82**, 539 (1989).

28. C.L. Lawson and R.J. Hanson, Solving Least Squares Problems, Prentice-Hall, Englewood Cliffs N.J., 1974.

29. S.W. Provencher, A constrained regularization method for inverting data represented by linear algebraic or integral equations,*Comput. Phys. Commun.* **27**, 213 (1982).

30. S.W. Provencher, CONTIN, a general purpose constrained regularization program for inverting noisy linear algebraic or integral equations,*Comput. Phys. Commun.* **27**, 229 (1982).

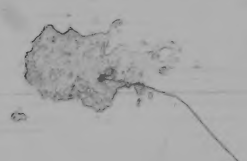

31. N. Draper and H. Smith, Applied Regression Analysis, Second Edition, Wiley-Interscience, New York, 1981.

32. R.S. Menon, M.S. Rusinko and P.S. Allen, *in* "Proc. VII$^{th}$ Annual Meeting of the Society of Magnetic Resonance in Medicine", p. 228, 1988.

33. T.L. Steck and J.A. Kant, Preparation of impermeable ghosts and inside-out vessicles from human erythrocyte membranes, *Methods Enzymol.* **3**, 172 (1974).

34. R. Freeman and D. Hill, Fourier transform study of NMR spin-spin relaxation, *J. Chem. Phys.* **55**, 1985 (1971).

35. H.Y. Carr and E.M. Purcell, Effects of diffusion on free precession in nuclear magnetic resonance experiments,*Phys. Rev.* **94**,630 (1954).

36. S. Meiboom and D. Gill, Modified spin-echo method for measuring nuclear relaxation times, *Rev. Sci. Instrum.* **29**, 688 (1958).

37. D.G. Hughes and L. Lindblom, Baseline drift in the Carr-Purcell-Meiboom-Gill pulsed NMR experiment, *J. Magn. Reson.* **26**, 469 (1977).

38. R.S. Menon, A.L. MacKay, S. Flibotte and J.R.T. Hailey, Quantitative separation of NMR images of water in wood on the basis of $T_2$, *J. Magn. Reson.* **82**, 205 (1989).

39. D.W. Marquardt, An algorithm for least squares estimation of nonlinear parameters, J. *Soc. Ind. Appl. Math.* **11**, 431 (1963).

40. J.B. Bederson, H.M. Bartkowski, K. Moon, M. Halks-Miller, M.C. Nishimura, M. Brant-Zawadzki and L.H. Pitts, Nuclear magnetic resonance imaging and spectroscopy in experimental brain edema in a rat model, *J. Neurosurg.* **64**, 795 (1986).

41. L. Kanman, K.G. Go, W. Brouwer and H.J. Berendsen, Nuclear magnetic resonance relaxation in experimental brain edema: effects of water concentration, protein concentration and temperature, *Magn. Reson. in Med.* **6**, 265 (1988).

42. S. Naruse, Y. Horikawa, T. Chuzo, K. Hirakawa, H. Nishikawa and K. Yoshizakai, Proton nuclear magnetic resonance studies on brain edema, *J. Neurosurg.* **56**, 747 (1982).

43. K.G. Go and H.T. Edzes, Water in brain edema, *Arch. Neurol.* **32**, 462 (1975).

44. L. Backay, R.J. Kurland, R.G. Parish, J.C. Lee, R.J. Peng and H.M. Bartkowski, Nuclear magnetic resonance studies in normal and edematous brain tissue, Water in brain edema, *Exp. Brain Res.* **23**, 241 (1975).

45. M.E. Castro, Experimental brain edema studied with proton NMR, Ph.D. Thesis: University of Alberta (1986).

46. H.W. Fischer, Y. Van Haverbeke, R.A. Rinck, I Schmitz-Feuerhake and R.N. Muller, The effect of aging and storage conditions on excised tissues as monitored by longitudinal relaxation dispersion profiles, *Magn. Reson. Med.* **9**, 315 (1989).

47. A.J. Deese, E.A. Dratz, L. Hymel and S. Fleischer, Proton NMR $T_1$, $T_2$ and $T_{1\rho}$ relaxation studies of natice and reconstituted sarcoplasmic reticulum and phospholipid vesicles. *Biophys. J.* **37**, 207 (1982).

# CHAPTER 5[1]

## NMR relaxation time studies of water compartmentalization in a model neurological system: the crayfish nerve cord

### 5.1 Introduction

A large portion of routine diagnostic NMRI examinations are concerned with the delineation and characterization of cerebral edema. The principal aim of the work described in this thesis has been to improve the quantitative understanding of water proton relaxation in edematous tissue through the use of a series of increasingly complex model systems in conjunction with new methods for multiexponential relaxation time decomposition. Such analysis techniques (Chapter 4) have shown, for example, that the decay of the transverse magnetization from cat brain white matter, as measured *in vitro*, is not a simple single exponential but a combination of four. It is possible that changes in characteristic details such as these can be of diagnostic value. In order to understand the tissue properties that could give rise to such behavior, we have chosen to investigate water proton relaxation in a model system of brain, namely the crayfish central nerve cord.

Historically, studies of the central nervous system (CNS) of the crayfish have played an important role in our understanding of nerve structure and function (1, 2). Comparative studies on this invertebrate have also yielded a better understanding of mammalian systems such as the blood-brain barrier (BBB) and blood-nerve barrier (BNB). Since many of the structural features found in the crayfish CNS are similar

---

[1]A version of this chapter has been submitted for publication. R.S. Menon, M.S. Rusinko and P.S. Allen, NMR relaxation time studies of water compartmentalization in a model neurological system: The crayfish nerve cord, *Magn. Reson. Med.* (1990).

to human nervous tissue, the crayfish nerve cord forms an ideal, well characterized model system which is open to study and manipulation.

In this chapter, we have investigated transverse ($T_2$) and longitudinal ($T_1$) water proton relaxation times in the abdominal nerve cord segment of the crayfish using a continuous relaxation time distribution approach for analysing the magnetization decays (3, 4, 5). The transverse magnetization is found to be distinctly multiexponential in nature, while the longitudinal magnetization is predominantly a single exponentially decaying process. We have attempted to correlate these measured water proton relaxation times with the anatomical compartments seen in light, electron (EM) and proton NMR microscopy. Such correlations allow us to observe directly the role of different elements of the cellular and tissue architecture in affecting water proton relaxation, and should lead to the increased quantitative ability and specificity of NMRI.

## 5.2 Morphology of the crayfish nerve cord

### 5.2.1 Gross anatomy

The CNS of decapod crustaceans is a ladderlike structure (1) as illustrated in Figure 5.1a. It runs from the head to the tail on the ventral side of the crayfish, immediately underneath the ribs. The thoracic and abdominal ganglia are longitudinally separated from one another by paired, bilaterally symmetric connectives within which the axons run. Of particular interest are four large, easily identifiable motor axons that run along the dorsal side of the cord (6). At each ganglion, nerve roots enter from sensory receptors and exit for motor control. The whole CNS is enclosed within a fibrous sheath which is infiltrated by an extensive

blood capillary system (7). The dissected abdominal segment of the nerve cord, consisting of five abdominal ganglia and their connectives as is pictured in Figure 5.1b, was typical of those used for all our experiments and we shall refer to it simply as the nerve cord for brevity.

### 5.2.2 The ganglia

The brain of the crayfish is simply a collection of fused ganglia and thus, in general, the ganglia can be considered the functional equivalent of grey matter in humans. All axons originate or terminate in areas of the ganglia known as neuropils. The incoming sensory signals are collected here, integrated and then reissued as appropriate sensory or motor commands (8). Viewed through the light (Figures 5.2a,b) or electron microscope (Figures 5.3a-c), much of the ganglion consists of a tangled mass of synapses, axonal cell bodies, axons, glial cells and blood vessels. In our preparations, the volume of the ganglia was typically 1.3 to 1.6 times that of the connectives.

### 5.2.3 The connectives

The connectives that run between the ganglia contain bundles of generally parallel axons. In the connective between the second and third abdominal ganglia (similar to Figure 5.2c), there are 8744 axons (2), which can be grouped into twenty broad fields. Most of the axons are ensheathed by two types of glial cells. Schwann cells are found immediately around many axons and are tightly apposed, forming a concentric, isolated, fluid filled cleft ($\equiv$ 15 nm across) about each axon (Figures 5.3d,h). Another family of glial cells, found beyond the Schwann cells are less tightly organized and have much extracellular material between them including closely

packed collagen fibrils (Figure 5.3c). This material forms a basal lamina-like layer about the glial processes. A single Schwann cell can wrap several times around a group of small axons or around a single larger one and in either case may form an extensive extracellular space such as illustrated in Figures 5.3d,e. The multiple lamellae from a Schwann cell about an axon form a rudimentary form of myelin and are expected to constitute an appreciable barrier to the diffusional motion of water (Figure 5.3h).

### 5.2.4 The Sheath

The sheath surrounding the CNS is extremely difficult to preserve via fixation for microscopy but sections of it are shown in Figures 5.3f,g. It consists of an acellular connective tissue layer made from collagen and mucopolysaccharides (the neural lamella) immediately below which lies a perineurium, composed of loose, overlapping glial cells (7). It has been observed that some perineural glial cells secrete collagen when the sheath is traumatized. The spaces between perineural cells are filled with collagenous material as well. The cytoplasm of these perineural cells is either electron dense or quite clear and the cells are associated with one another by gap junctions and occasionally form foot like processes into the underlying glia. The presence of tight junctions, such as those found in human brain, is very rare. A maximum path length of 500 μm has been estimated (7) for the diffusion path of a molecule between the neural lamella and the nearest giant axon due to the tortuous extracellular space (Figure 5.3g).

### 5.2.5 The blood capillary system

Branches from the main arteries enter the ganglia and the connectives, but penetrate only a short distance before opening into glia-lined blood channels which are bound by basement membrane but have no endothelium. The basement membrane is similar to the neural lamella and the perivascular glial cells strongly resemble the perineural glial cells. This has given rise to the consensus that the perivascular glia and the perineurium together constitute the cellular layer of the blood-brain interface in the crayfish. In fact, the blood vessels are considered specialized invaginations of the outer sheath (7, 9). While the sheath does not exclude many small ions, it does provide a significant diffusion barrier to them (10, 11). Thus by placing the nerve cord in a bathing solution of one's choice, one can study the effects of solvent or solute exchange in this model of the BBB found in higher animals (10).

To first order, most nervous systems comprise the same basic elements and differ only in their complexity of organization and number of elements. It should be apparent that the features discussed in this section are similar to those discussed in Section 1.2 for humans. Bearing these similarities in mind, the crayfish CNS can be used as a simple model for more complex neurological tissue such as that found in mammals.

### 5.2.6 Water compartments in the nerve cord

If we make certain basic assumptions about the state of water in the nerve cords we can obtain an idea about the number of relaxation components that might be detectable using NMR. From the optical microscopy shown in Figure 5.2 and the

EM shown in Figure 5.3, certain regions of uniform transparency (electron density in the sample) can be discerned. The most obvious one is the apparently clear space occupied by the axons in Figure 5.2. The EM studies (Figure 5.3e,b,d,e,f) indicate that these spaces are not empty, but are filled with more or less uniform distributions of neurotubules, neurofilaments and microfilaments (see Section 1.2.2) and that the structure of the axoplasm appears to be similar for most axons. These observations suggest that the water molecules in all axons will behave in a quantitatively similar manner, regardless of size. It has also been shown that the contribution of the axonal membrane to water proton relaxation is very much smaller than that due to the proteinaceous structures in the axons (20), reinforcing the belief that the relaxation of water in the axons should be independent of axon size. The relaxation rate of water in an axon is likely to be a fast exchange average between "bulk" water in the cell and the "hydration" layer associated with the intracellular structures. In addition, the diffusion of this exchange-averaged water into the extraaxonal space is expected to be slow due to the diffusion barrier presented by the connective tissue sheaths, with perhaps most of the water exchange occuring at the unsheathed nodes (9, 25). It would seem reasonable then, to assume that the axons taken as a group, should have similar relaxation properties.

While the Schwann cell lamellae form a natural barrier for isolating the axons as a compartment, the extraaxonal space is somewhat more complex. This space consists of collagen like material interspersed with glial cells. While the optical and electron transparency (and hence protein content) of the cells and extracellular space is different (the glia are less dense when viewed in Figure 5.3e), it is known (26-31) that water exchange across plasma membranes of small cells is sufficiently fast to average the relaxation rates inside and outside the cells, making the two regions

indistinguishable. Work on uniform suspensions of RBC's and RBC ghosts (33, 34), which are roughly the same size as glia, suggests that the half life for a water molecule in these cells is less than 17 ms. This is shorter than the expected water proton relaxation times in either the intraglial or the extraaxonal spaces, resulting in the exchange averaging of both compartments and making them indistinguishable using $T_2$. We should therefore not necessarily expect to be able to differentiate between the extracellular space and the glia and we refer to them collectively as the extraaxonal space. The volume of the extracellular space has been estimated at 10-25 % in similar nerves (32). Water also occupies spaces within the connective tissue sheaths of the axons. It is not clear if this water is in exchange with the water in the axons or the extracellular space or both. If it is an isolated compartment, we expect its transverse relaxation time to be short due to the large amount of protein in these sheaths (Figure 5.3h). Our estimates for the relative volume fractions of these compartments are shown in Table 5.1. The cross-sectional areas were measured from Figures 5.2 and 5.3 and then corrected for the volume fraction of solids in each compartment.

## 5.3 Experimental

### 5.3.1 Removal of the cord

The crayfish (*Procambarus bandingi acutus or Procambarus clarkii* depending on the season, obtained from Atchafalaya Biological Supply Company Inc., of Raceland,Louisiana) was anesthetized by immersing it in a ice slurry of Van Harreveld's solution (12) for at least 30 minutes. The abdominal section was cut away and then the head was severed to kill the animal. This tail section was scrubbed with a small brush and pinned out in a dissection tray filled with cold isotonic Van

Harreveld's solution. The ventral integument was dissected carefully away from the underlying muscle, one segment at a time, to reveal the ventral nerve cord. The cord was tied off at both ends before the nerve rootlets were cut, enabling the removal of four to five segments (2 cm) of the nerve cord as shown in Figure 5.1b. Even with the cord tied off and cut from the rest of the CNS, the tail-flip reflex could be elicited by prodding the isolated segment, suggesting that at this time the nerves were still viable. The first water proton relaxation measurements were usually made within 20 minutes of this point in the dissection. For such relaxation measurements the nerve cord (typically 30 μl in volume) was placed in a 5 mm diameter NMR tube and completely bathed with about 50 μl of Van Harreveld's buffer. For NMR microscopic imaging experiments, the cord was pulled into a 2 mm (i.d.), 2 cm long, thin walled teflon tube which was then sealed with plasticine.

### 5.3.2 NMR relaxation measurements

The water proton relaxation times were measured with a modified Bruker CXP spectrometer at 100 MHz. The proton line width obtained for the < 100 μl samples in the 40 cm bore magnet was better than 10 Hz. The measurements were made at a room temperature of 22 ± 2 °C.

The transverse relaxation was measured using a 4096 echo Carr-Purcell-Meiboom-Gill (CPMG) add/subtract sequence (13, 14), with an inter-echo spacing, $\tau$, of 1.6 ms. The CPMG sequence was phase cycled in order to eliminate baseline errors (15) generated by both receiver dc offsets and residual magnetization caused by phase errors in the 180° pulses. The choice of the echo time was made to minimize the effects of diffusion on $R_2$. The add/subtract sequence was repeated 8 times and the resulting signal was averaged.

The longitudinal relaxation was measured using the Freeman-Hill modification (16) of the inversion recovery sequence [$180_y$--$\tau$--$90_x$--AQ--TR/0--$\tau$--$90_{-x}$--AQ--TR], where TR is the sequence repetition interval. The $\tau$ values, ranging from 1 ms to 7.9 s, provided 10 points, arranged logarithmically, in each decade of time. The advantage of using this sequence is that the magnetization recovery curve is always positive, dropping from $2M_o$ to zero, with the initial magnetization, $M_o$, being measured as often as the partly relaxed magnetization. Eight acquisitions of each add/subtract pair were averaged.

The relaxation times were all obtained with a 90° pulse length of 7.5 μs. All data were acquired using the Bruker 12 bit digitizer alternately sampling between real and imaginary data points every 4 μs.

### 5.3.3 NMR microscopic imaging experiments

In order to produce NMR images of the crayfish nerve cord with sufficiently high resolution to resolve at least the giant axons, it was necessary to construct a gradient coil system capable of producing magnetic field gradients of the order of 2.5 mT/cm (Appendix E). The abdominal nerve cord segment in its teflon tube was placed along the long axis of an eight turn, 5 mm diameter RF solenoidal coil. NMR images were made corresponding to a transverse section (oriented as in Figure 5.2c) through the connective between the third and fourth abdominal ganglion. The $T_2$ weighting was controlled by varying the echo time in a single echo imaging sequence utilizing a spin-locking pulse for slice selection to give 150 μm thick slices (Appendix D). Typical acquisition times with a sequence repetition time of 5 s were 2 hours per image. This yielded a typical signal-to-noise ratio of 40 at short echo

times. The in-plane resolution was roughly 20 μm in the read (frequency encoding) direction and 40 μm in the phase encoding direction and was limited more by sample vibration than by the acquisition parameters. The acquisition matrix consisting of 256 complex points in the frequency encoding direction and 64 phase encoding steps was transferred from the Aspect 3000 to a VAX 11/750 (Digital Equipment Corporation, Maynard, MA), where it was zero padded to 256 phase steps before performing a 2DFT implemented on an Analogic AP500 array processor. A Ramtek Corporation RM9645 graphics display system connected to the VAX was used for some image analysis using software developed in-house. A Macintosh IIci interfaced to the VAX and a Hewlett- Packard ScanJet Plus image digitizer were also used for image production and enhancement.

### 5.3.4 Invasive procedures

The assignment of the measured relaxation times in nerve (or tissue in general) to particular compartments has always been subject to uncertainty and debate (17-22). In order to make the identification less ambiguous, we have performed several experiments designed to alter either the relaxation rate or population of a particular known compartment. The first set of experiments was designed to increase the volume of the extracellular compartment by injecting Van Harreveld's saline under the perineurium of a nerve cord bathed in the same solution, using a finely honed 30 gauge needle attached via a polyethylene tube to a remote syringe. An arrangement such as this enabled the needle to be inserted into one end of the cord under a dissecting microscope and held stationary while the syringe plunger was gently depressed. Due to the positive osmotic pressure in the the extracellular space

and the limited compliance of the sheath , the nerve cord had to be carefully tied to prevent the injected fluid from leaking back out.

The second set of experiments involved careful microdissection of the ganglia from the nerve cord, to form separate samples of ganglia and connectives. No effort was made to prevent leakage of the bathing solution into, or extracellular fluid out of, the samples. In another series of experiments copper sulphate was used to dope the bathing solution in order to study the alteration of the relaxation rates by the paramagnetic copper ions. Finally, the relaxation time behavior of the bathed nerve cord was followed over periods up to 15 hours, to observe the changes that might take place as the cell bodies died and the axons underwent Wallerian degeneration. By using such techniques, we hoped to associate the measured relaxation times with particular populations of water protons.

## 5.4 Data analysis

The measured time dependent magnetization from a typical $T_1$ or $T_2$ experiment is shown in Figure 5.4. Such curves were obtained on sample volumes of about 80 µl of which the bathing solution typically constituted about one half. It was not apparent from either manual curve peeling procedures nor from our usual non-linear least-squares algorithm (5) as to how many discrete exponentially decaying components were necessary to characterize these curves. Since the nerve cord contains distributions of axons and other cells, one intuitively expects a distribution of relaxation times in the sample. Our experiences with linear inverse theory techniques (4, 5, Chapter 4) led us to analyse our data using a continuous relaxation time distribution approach involving the non-negative least-squares (NNLS) algorithm of Lawson and Hanson (23), as modified by Whittall and Mackay

(4). This method has the advantages of (i) requiring no *a priori* guess as to the number of components, (ii) producing a fit to the data that is stable and not dependent on initial guesses of the component times and fractions, and (iii) producing a more realistic description of the relaxation times in the sample. The application of this continuous distribution technique to the data in Figure 5.4 is demonstrated in Figure 5.5 for a sample in which the bathing solution initially comprised 14 % of the total signal intensity. The algorithm clearly resolves five components in the transverse magnetization decay, but only two in the longitudinal relaxation time distribution. The confidence level of these solutions ($p < 0.01$ or $99^+$ % confidence level) is related to the noise in the data as investigated previously (5). For a given sample, the repeatability for successive NMR measurements of both the relaxation rates and populations was better than ± 5 % for the large peaks and about ± 20 % for peaks whose populations are less than 5 % of the initial signal intensity.

## 5.5 Results

The application of the continuous distribution algorithm to 18 freshly excised nerve cords is summarized in Table 5.2. The averages for each NMR parameter indicate that while there is considerable biological variability between samples, the same well defined features are common to all $T_1$ or $T_2$ distributions. We have calculated the continuous distributions at the 99 % confidence level. The signal-to-noise ratio of our data was high enough (5, Chapter 4) to allow us to claim that the $T_1$ or $T_2$ distributions calculated closely reflect the actual relaxation time distribution in the samples. The $T_1$ of the nerve cord has been calculated from the $T_1$ of the cord in the buffer, assuming fast exchange between the buffer (whose $T_1$ is 3 s) and the

nerve cord. The volume fraction of the buffer needed for this calculation is deduced from the $T_2$ results as discussed further below.

Figure 5.6 demonstrates the effect of injecting fluid subperineurally, on the $T_2$ distribution of the nerve cord. Figure 5.7 compares the $T_2$ distribution of the intact nerve cord with the distributions found for the connectives and ganglia of the same cord measured in isolation. The effect of paramagnetic doping on the water proton relaxation times in the cord is shown in Figure 5.8. In Figure 5.9a and 5.9b we demonstrate by means of stacked plots, the way in which the $T_2$ distribution of a nerve cord and its bathing solution vary over time. The behavior of the individual relaxation populations and times is shown in Figure 5.9c and 5.9d for this sample. Figure 5.10a and 5.10b summarize the populations and relaxation times over time for a nerve cord which was stored at 4 $^{o}$ C for almost 4 hours before use.

NMR microscopy projections (Figure 5.11) and images (Figure 5.12) were made for a transverse section through a connective. These can be compared with the light microscopy section in Figure 5.2c. Because of the low contrast-to-noise ratio, the original images have been subject to some postprocessing to enhance the features of interest.

## 5.6 Discussion

### 5.6.1 Longitudinal relaxation in fresh nerve cords

The longitudinal relaxation in all cases is found to be essentially monoexponential except for a small (< 5 %), difficult to quantify component, which has a $T_1$ around 1 ms. The $T_1$ of the nerve cord is on average 1.8 times longer than the longest $T_2$ compartment and 6 times longer than the $T_2$ of the largest measured

water fraction, implying a significant degree of motional restriction for much of the water. Most of the water in the nerve cord appears to be within 0.5 μm of proteins or membrane surfaces, making the process of cross-relaxation a possible contributor to the longitudinal relaxation mechanism. On average, water exchange across the perineural sheath and within the nerve cord appears to occur on a timescale faster than $T_1$. This is consistent with our results on model sytems involving multiple membrane barriers to diffusion (26). Thus the $T_1$ distribution does not directly give us information about any underlying compartmentalization in this system although its large width suggests a range of unresolved environments.

**5.6.2** Transverse relaxation in fresh and manipulated nerve cords

Considerably more complex, the $T_2$ distribution shows five distinct components, labelled (i)-(v) in Figures 5.5-5.10, which we shall attempt to identify. From the considerations in section 5.2.6, we expect that it might be possible to delineate at least axonal water from other water fractions in the nerve cord.

The longest $T_2$ component ((v) in Figure 5.5) is easily associated with the bathing solution. This can be verified by changing the amount of bathing solution and observing the same fractional change in the area of this peak relative to the others. Since this solution is (initially) free of macromolecules, it should have a relaxation time closest to that for free water. The ability to separate this compartment from the rest of the nerve cord results from the slow diffusion of water across the neural lamella and perineural glia cell layers. There is essentially no correlation between the $T_2$ of the bathing solution and the $T_2$'s of the rest of the components, (i)-(iv), which must be associated with water in the nerve cord. This fact reinforces the belief that water exchange across the perineurium is very slow. From Figure

5.3g we can measure a typical thickness of the perineurium to be 100 microns, giving a minimum transit time for a water molecule via unimpeded diffusion of 1 s. Because of the multiple membrane and protein barriers to water diffusion, this time could well be closer to 10 s. Since this is the order of $T_1$, it perhaps suggests that the width of the $T_1$ distribution arises from incomplete exchange averaging of all the different water environments.

Table 5.2 indicates that the component corresponding to peak (iv) comprises roughly 32 % of the CPMG measured signal intensity from the nerve cord. Comparison of this with Table 5.1 suggests that water in the glia and some of the extracellular space could account for this. When buffer is injected into the extracellular space, Figure 5.6 indicates that peak (iv) increases in relative area compared with the other peaks. This suggests that the compartments labelled (i)-(iii) are not directly accessible to the injected fluid while the compartment associated with peak (iv) is. The fact that there is some change in the other peaks hints that the water in these components may be exchanging to some degree with the water injected into the extracellular space. The data in Figure 5.7 show that the relative fraction of peak (iv) is considerably higher in the ganglia than in the connectives. Perusal of Table 5.1 shows that the extraaxonal compartment in the ganglia is also much larger than in the connectives. It was hoped that introduction of a paramagnetic ion in the bathing solution, would result in the ion diffusing first into the extracellular space and the the glia and axons. But the paramagnetic doping experiments shown for example in Figure 5.8 proved somewhat inconclusive. Although the relaxation measurements were done within 15 minutes of doping it appears that the copper ion was able to diffused rapidly into all compartments from the bathing solution, since all the relaxation times are similarly shortened. Alternatively, the ion could have diffuse into

cells along the periphery of the cord before it was able to penetrate the extracellular spaces deeper within the cord. There does appear to be a large fraction (34 %) of water that we associate with the extraaxonal space peak (iv) that appears to be inaccessible to the paramagnetic ion at least over times up to one hour. This is most likely the fluid filled clefts between the intersections of Schwann cell wrapped axons such as in Figure 5.3d, since there exists a considerable diffusion barrier between the bathing solution and these spaces.

Examination of the light microscope sections in Figure 5.2 as well as the data in Table 5.1, shows that the largest volume fraction of water should be associated with the axons. In freshly excised nerve cord, the largest volume fraction of water (59 % from Table 5.2) is associated with peak (iii) and corresponds very well with the 58 % volume fraction of axons calculated in Table 5.1. We have seen that this component is not substantially perturbed by injection of Van Harreveld's solution into the extracellular space (Figure 5.6), which suggests it is isolated by some sort of structural barrier from the extracellular space. The connective tissue sheaths around the axons are the site of this diffusion barrier. These sheaths are similar to the structure of the perineural sheath, but are typically only a few microns thick (Figure 5.3h). Furthermore, Table 5.1 tells us that the volume fraction of axons in the connectives is higher than in the ganglia. In microdissected pieces of connective and ganglia, we find that the fraction of water signal associated with peak (iii) in connectives (66 %) is higher than in the ganglia ( 51 %). It would appear therefore, that the water in the axons as a group, seems to relax with a well defined range of relaxation times, on the order of 200 ms. This time is similar to the other observations of $T_2$ in nerves (18-22). This is also borne out by the microscopic imaging studies presented in section 5.6.4.

The remaining two peaks are difficult to assign to anatomical compartments, mainly because of the large error in determining the volume fraction of such small regions from micrographs. The NMR data for these small compartments is also not as precise. We thus turn to other methods in order to try assign the two peaks, (i) and (ii).

### 5.6.3 Time dependent measurements

The experiments described in the previous two sections were done mostly on freshly excised nerve cords to avoid complications due to shifting electrolyte balances and Wallerian degeneration. It was thought, however, that the changes that occurred in populations and relaxation rates during cell death might provide a clue about the origin of the multiexponential transverse magnetization behavior. Furthermore, by following the changes that accompany nerve death, we can evaluate the promise of NMRI techniques to provide quantitative information about healthy and diseased neurological tissue and ways to differentiate the two.

Figure 5.9a demonstrates in a pictorial but quantitative way the behavior of the $T_2$ distribution for a nerve cord in bathing medium over a period of approximately 15 hours after removal from the crayfish. Figure 5.9b shows data from the same experiment but with the information presented using a logarithmic scale with the peak due to the bathing solution removed. The most marked change in Figure 5.9a appears to be the shift by a factor of 1.5 that occurs in the bathing solution peak as the relaxation time drops over the course of the experiment. The other significant feature is the coalescence of the peaks identified with the intra and extraaxonal water with the apparent relative increase of the extraaxonal water component. These and

other changes are quantified in Figure 5.9c and 5.9d as well as in Figure 5.10 for the cord which was stored for 3.75 hours prior to the NMR experiments.

The observed increase in the relaxation time of the bathing solution in both Figure 5.9 and 5.10 could be due to three possible processes. We expect that debris from degeneration of the neural lamella and the perineural sheath could decrease the relaxation time of the bathing solution by increasing the concentration of macromolecules in it. Moreover, it is also known that the perineural cells secrete collagen when traumatized, which will also escape into the bathing solution and shorten its relaxation time. It is not clear if the perineural cells can remain viable long enough to produce collagen in our bathing medium. After a period of 15 hours, the protein concentration in the bathing medium can be estimated at about 40 g/l by assuming that the collagen debris modifies the relaxation times of water in a similar manner to fibrinogen (34). There may be smaller proteins in the bathing medium as well, but they would affect the relaxation times to a lesser extent. Thirdly, we expect that increasing bacterial contamination in the bathing solution could also give rise to shorter relaxation times.

It is interesting that graphs of the relaxation rate of the buffer show a linear change with time. This does not imply a constant rate of production of debris, since the volume of the compartment also increases. This rise in the amount of water in the bathing solution compartment is obviously brought about by a shift in water from the nerve cord to the buffer. Furthermore, analysis of the populations depicted in Figure 5.9c and 5.10a, shows that this water shifts out from the components labelled (i)-(iii). This would imply that the water associated with these three peaks is in compartments that can exchange with the extracellular space and hence the bathing

medium. Perhaps the increase of ions or protein in the bathing solution produce an osmotic gradient which draws water out from the nerve cord.

Figure 5.9d shows that there is a biphasic response of the relaxation rates (and possibly the populations) of the axonal and extraaxonal water fractions. This response is not seen in the stored sample, where the change in the relaxation times appears monotonic in time. It would seem that these two compartments are stable up to 200 minutes post excision and then rapidly change with time, signalling the loss of cellular homeostasis and the onset of cell death.Within the nerve cord, we expect to observe changes consistent with the development of endoneurial edema caused by Wallerian degeneration (36). These include cellular debris in the extracellular space and a shift of water from the axons to the extraaxonal space as was observed in frog sciatic nerve during irreversible depolarization of the nerves(22). This occurs because the extracellular fluid in healthy nerve is hypertonic relative to plasma or plasma analogues such as Van Harreveld's solution (37, 38). Upon cell death, this space is made even more hypertonic due to degranulation of mast cells and the accumulation of cellular debris. Thus the extracellular space should also exhibit a shortening of its relaxation time as well as an increase in its relative water fraction, as is observed. We can verify that the extracellular space is under positive pressure by piercing the sheath while the nerve is immersed in fresh Van Harreveld's medium. A milky substance is expelled from the hole when observed under the dissecting microscope both in freshly excised or stored nerve cords.

The changes in the remaining compartments are less dramatic. The axons do not appear to swell as might be expected from a shutdown of the Na-K ATPase perhaps because the axolemma becomes leaky and is not capable of sustaining

osmotic gradients (25). From both Figure 5.9c and 5.10a, it is apparent that the increase in population of the extraaxonal compartment is matched by an almost equivalent decrease in the axonal compartment. In fact the axonal compartment appears to lose about 10 % more fluid than the extracellular space gains, and this fluid is postulated to enter the bathing solution. Either the axons and their connective tissue sheaths shrivel up over time (36-38) or their membranes gradually become more permeable, eventually allowing fast exchange with the extraaxonal space.This latter possibility could also explain the gradual coalescence of the intra and extraaxonal $T_2$ peaks if the water exchange through the membrane becomes more rapid. In such a scenario, the shortening of the relaxation times of the extracellular space would be brought about in part by increased exchange averaging with the shorter $T_2$ axonal compartment.

Changes in the remaining two compartments (i,ii) are more difficult to discern due to the scatter in the points. Both Figure 5.9c and 5.10a indicate that the population of peak (ii) drops radically over time, although it is not clear whether the relaxation rate increases (Figure 5.9d) or decreases (Figure 5.10b). It is difficult to identify an anatomical compartment that constitutes at most 4 % of the signal intensity. One possibility is the water within the spaces of the connective tissue sheaths which appear to occupy less than 20 % of the area in the electron micrographs and about 12 % of the volume fraction in the whole cord. If pressure develops in the interstitial space, these sheaths and their associated clefts would be compressed. However, the very small ( $\cong$ 1 %) of rapidly relaxing spins ($T_2 \cong 7$ ms) does not appear to drop significantly in population and the transverse relaxation rate appears to either increase (Figure 5.9d) or decrease (Figure 5.10b). Water in the hydration shells of macromolecules has a much shorter $T_2$ than this but membrane

associated water is thought to have a $T_2$ on the order of 10 ms (39) and could account for this fraction.

We have seen from the experiments discussed in the last two sections that the identification of three major compartments from our $T_2$ data is fairly straightforward. The bathing solution is easily distinguished from the water in the nerve cord due to the slow exchange of water between the two. We have shown that the volume of the extracellular space can be perturbed, resulting in an increase in an NMR identifiable water fraction (peak (iv)). Differences in the volume fraction of axons in ganglia and connectives can be discerned from the light and EM microscopy and these differences can also be related to an NMR identifiable water fraction (peak (iii)). However, although there are small volume fractions of water associated with peaks (ii) and (i), we cannot clearly identify them or selectively manipulate such small anatomical compartments.

### 5.6.4 Microscopic imaging

If the hypothesis that axonal (peak (iii)) and extraaxonal spaces (peak (iv)) give rise to different relaxation components is correct, it should be possible to differentiate between these spaces by $T_2$ weighted microscopic NMR images if sufficient spatial resolution can be obtained. Image projections made with the slice selection gradient turned on, but the phase encoding gradients off, are shown in Figure 5.11 as a function of the spin-echo time. These were done in order to unambiguously scale the images made at echo times of 20, 178 and 258 ms which are shown in Figures 5.12a-c. Because of the effects of water diffusion and sample vibration in the presence of such strong gradients, we do not expect to be able to measure accurate relaxation times from these images. Furthermore the spin-locking

used for the slice selection undoubtably produces some yet unascertained contrast in the images. However, useful contrast is generated by relative differences in $T_2$ values which in turn allows us to distinguish microscopic structures.

Compared to the initial signal intensity of the FID from the slice, the projections (and hence images) made at spin-echo times of 20, 178 and 258 ms have respectively, 80, 13 and 6 % of the initial water proton signal remaining. Thus if our assignment of the relaxation times is correct, the image in Figure 5.12a (20 ms echo time) should show evidence of water proton relaxation in the axons postulated to contribute to peak (iii) in the continuous $T_2$ distributions.. Comparison of this image with the transverse section of the cord in Figure 5.12c shows that the pixel intensity in the region of the giant axons and axonal fields is in fact diminished. The dark regions in the contrast enhanced version of this image occupy 50 - 70 % of the cross-sectional area of the connective, in good agreement with the predicted volume fraction from peak (iii) of 59 ± 12 % derived in Table 5.2 and the 58 % volume fraction of axonal water calculated from Table 5.1. The images made at longer echo times presumably reflect the water in the extraaxonal space (peak (iii)) since the axonal water should have completely relaxed by these longer times. Furthermore, the water left in these images constitutes less than 13 % of the initial signal intensity. The signal is distributed over most of the nerve cord cross-section as would be expected for extraaxonal water, but the proton density appears higher in certain regions between the axon fields. While these images do not yield any quantitative information, they do confirm and emphasise that the origin of the multiexponential transverse magnetization decay is due to water in different homogeneous microanatomical compartments and that these compartments relax at different rates, generating $T_2$ contrast.

## 5 7 Conclusions

In this chapter we have investigated the origin of multiexponential magnetization decays in the abdominal segement of the crayfish nerve cord. Components of the transverse magnetization decay have been associated with particular anatomical compartments in the nerve cord based on deductions from a series of experiments designed to manipulate only particular compartments. These compartments are made up of homogeneous collections of microscopically identifiable anatomical sites, such as groups of axons. Another NMR detected compartment is the extraaxonal water fraction which is assumed to be a fast exchange average of water in the glia and the extracellular spaces.The identification of these compartments by NMR relaxation studies is contingent upon there being slow exchange between them. NMR microscopic imaging results lend credence to the postulate that water in the axons relaxes differently and distinctly from water in the extraaxonal space. Finally, the time course of the relaxation times can be used to provide information about the viability of the nerves in this preparation, which should have applications to *in-vivo* imaging studies. The changes observed upon cell death can be used to interpret differences in NMR image intensity between normal brain and diseased tissue.

Table 5.1

Calculation of volume fractions of different regions in the crayfish nerve cord.

| Cross-sectional area[a] (% total area) | | Volume fraction of solids[b] | Corrected fraction of water (% total water) |
|---|---|---|---|
| CONNECTIVES | | | |
| axons | 67 | 0.25 | 70 |
| glia | 7 | 0.15 | 8 |
| connective tissue[c] | 20 | 0.50 | 14 |
| extracellular space[d] | 6 | 0.0 | 8 |
| GANGLIA | | | |
| axons | 50 | 0.25 | 50 |
| glia | 30 | 0.15 | 34 |
| connective tissue[c] | 15 | 0.50 | 10 |
| extracellular space[d] | 5 | 0.0 | 6 |
| WHOLE CORD[e] | | | |
| axons | | | 58 |
| glia | | | 24 |
| connective tissue[c] | | | 12 |
| extracellular space[d] | | | 6 |

[a] Measured from digitized cross-sections.
[b] Estimated from the neuroanatomy references in Chapter 1.
[c] Includes connective tissue sheaths around axons and between other cells.
[d] These are the clear regions found for example at the bottom of Figure 5.3d.
[e] Assumes the ganglionic volume is 60 % ot the tc.al cord (From Figure 5.1b)

Table 5.2

Summary of populations and relaxation times in freshly excised nerve cords.

| Component[d] | Population[a,b] (iv) | $T_2$[b] (iv) | Population[a,b] (iii) | $T_2$[b] (iii) | Population[a,c] (ii) | $T_2$[c] (ii) | Population[a,c] (i) | $T_2$[c] (i) | $T_1$[b] (all) |
|---|---|---|---|---|---|---|---|---|---|
| Crayfish number | | (s) | | (s) | | (s) | | (s) | (s) |
| 1 | 31.9 | 0.537 | 57.0 | 0.184 | 9.1 | 0.059 | 2.0 | 0.010 | 1.23 |
| 2 | 30.3 | 0.523 | 59.9 | 0.185 | 9.3 | 0.057 | 1.5 | 0.011 | 1.04 |
| 3 | 39.5 | 0.753 | 51.7 | 0.204 | 5.3 | 0.034 | 3.5 | 0.006 | 1.34 |
| 4 | 39.3 | 0.717 | 49.1 | 0.209 | 6.6 | 0.050 | 5.0 | 0.010 | 1.30 |
| 5 | 35.5 | 0.876 | 61.4 | 0.216 | 2.8 | 0.022 | 0.3 | 0.003 | 1.42 |
| 6 | 33.9 | 0.870 | 62.5 | 0.222 | 2.9 | 0.025 | 0.8 | 0.004 | 1.38 |
| 7 | 38.6 | 0.572 | 48.5 | 0.207 | 12.9 | 0.095 | | | 1.20 |
| 8 | 47.5 | 0.487 | 47.8 | 0.198 | 4.7 | 0.089 | | | 0.90 |
| 9 | 17.4 | 0.594 | 75.9 | 0.223 | 5.0 | 0.041 | 1.8 | 0.006 | 0.90 |
| 10 | 14.4 | 0.593 | 77.9 | 0.193 | 6.1 | 0.045 | 1.6 | 0.004 | 1.33 |
| 11 | 20.9 | 0.652 | 73.3 | 0.207 | 3.8 | 0.046 | 2.0 | 0.004 | 1.28 |
| 12 | 24.8 | 1.067 | 66.5 | 0.235 | 7.6 | 0.050 | 1.1 | 0.006 | 1.70 |
| 13 | 61.1 | 0.340 | 37.9 | 0.114 | | | 0.9 | 0.006 | 0.86 |
| 14 | 45.3 | 0.300 | 50.0 | 0.135 | 3.1 | 0.030 | 1.6 | 0.004 | 0.78 |
| 15 | 36.3 | 0.423 | 48.4 | 0.183 | 14.7 | 0.053 | 0.6 | 0.010 | 0.93 |
| 16 | 30.7 | 0.825 | 65.2 | 0.208 | 4.1 | 0.030 | | | 1.36 |
| 17 | 22.4 | 0.680 | 76.6 | 0.197 | 1.1 | 0.015 | | | 1.14 |
| 18 | 27.9 | 0.692 | 57.6 | 0.217 | 13.1 | 0.081 | 1.5 | 0.015 | 1.07 |
| Mean[e] | 31.6 | 0.639 | 59.3 | 0.197 | 6.6 | 0.049 | 2.4 | 0.007 | 1.18 |
| | ±9.4 | ±0.197 | ±11.6 | ±0.030 | ±4.0 | ±0.023 | ±2.0 | ±0.004 | ±0.24 |

[a] Normalized to 100
[b] ± 5 %
[c] ± 20 %
[d] As defined in the text and figures. Only one major $T_1$ component is separable with any certainty.
[e] Variability given as the standard deviation of the 18 measurements.
[f] The absence of a number in a column means that the component was not detected.

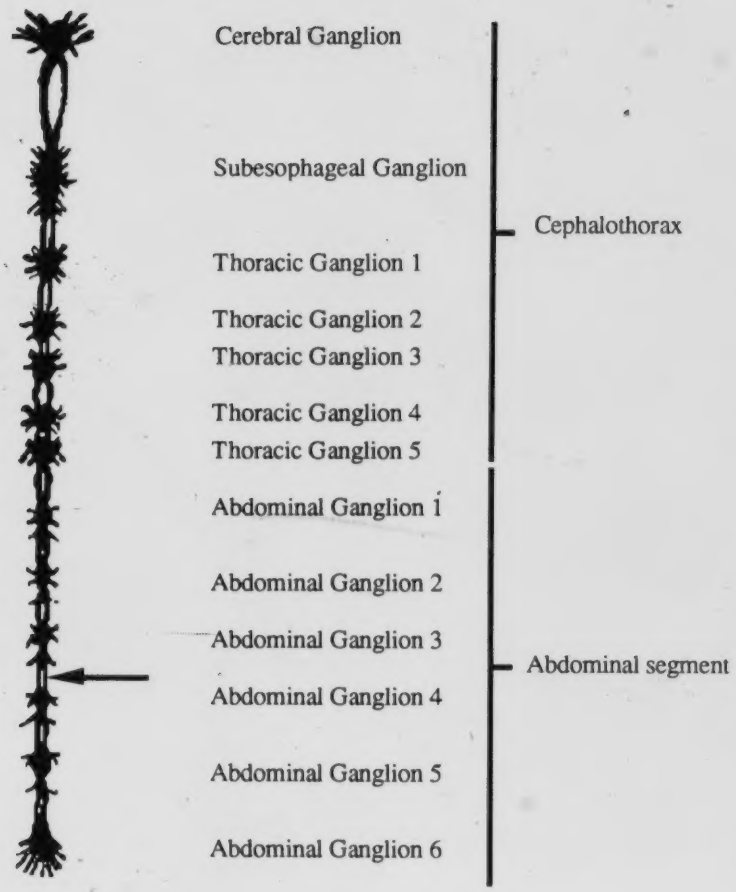


**Figure 5.1a** Layout of the crayfish central nerve cord. The arrow marks the region between the 3rd and 4th abdominal ganglia where NMR microscopy was done (Figure 5.12) and sections were cut for optical microscopy (Figure 5.2) and EM (Figure 5.3). The 4th abdominal ganglion was used to obtain the sections shown in Figure 5.2a and 5.2b. The bar demarcting the abdominal segment represents 2 cm.

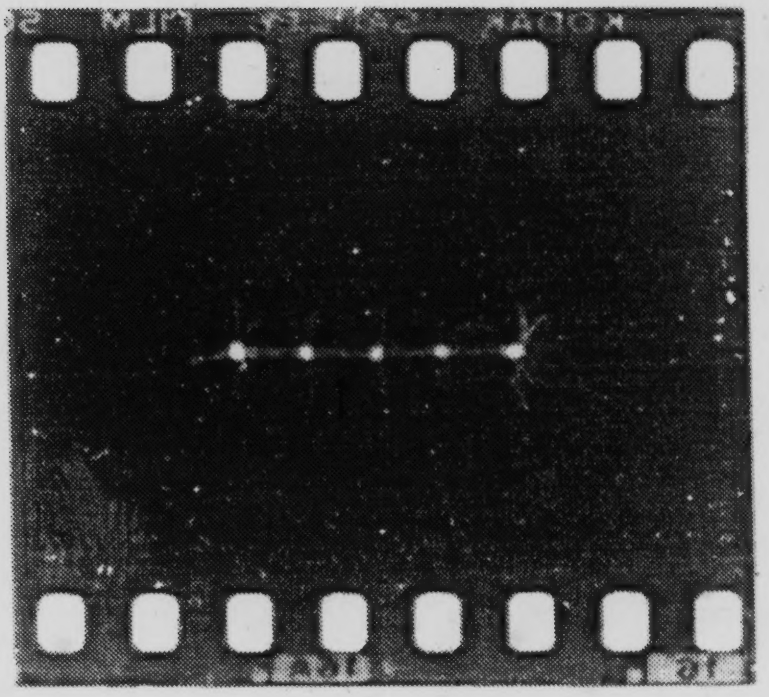

**Figure 5.1b** A 35 mm photograph of an abdominal segment of the crayfish nerve cord. This dissection shows the 2nd through 6th abdominal ganglia from left to right. The arrow marks the 3-4 connective.

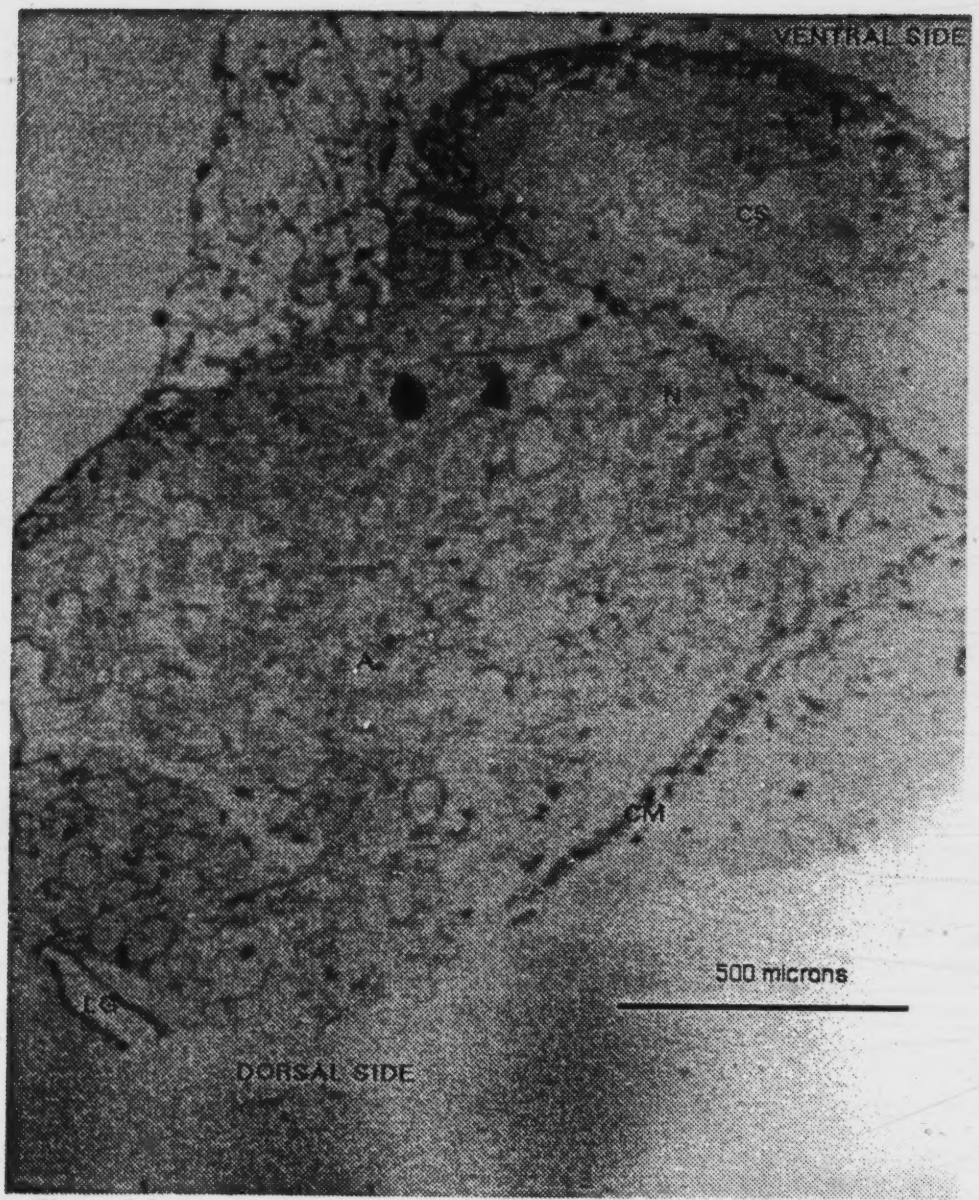


**Figure 5.2a** Light microscopy of a cross-section through the 4th abdominal ganglion. The symbols mark the cell somata (CS), the neuropil areas (N), the axon fields (A), the apparently collapsed lateral giant axon (LG) and the sheath (S). A collagenous membrane (CM) appears to divide the left and right sides of the ganglion. The EM pictures in Figure 5.3 were done on the same sections shown here and in Figure 5.2b and 5.2c.

**Figure 5.2b** Light microscopy of a longitudinal section through the 4th abdominal ganglion. The symbols are as for Figure 5.2a.

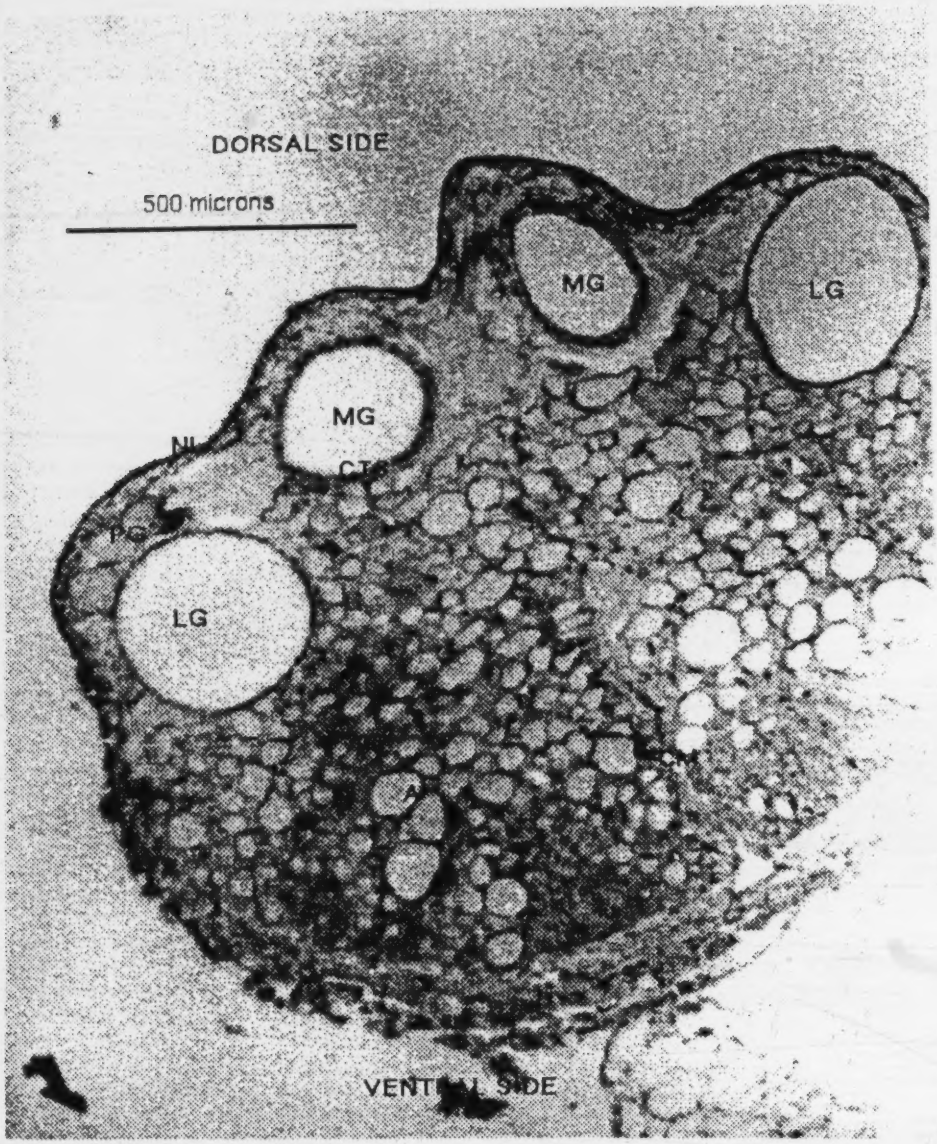


**Figure 5.2c** Light microscopy of a cross-section through the 3-4 connective. The symbols indicate the medial giant axons (MG), the lateral giant axons (LG), the axon fields (A), the sheath around the cord (S) which in turn is made up of the perineural glial cells (PG) encased by the neural lamella (NL). A connective tissue sheath (CTS) typically surrounds the axons and a collagenous membrane (CM) divides the connective bilaterally. The sheath appears to shrivel up on the dorsal side of the cord, becoming tightly apposed to the giant axons.

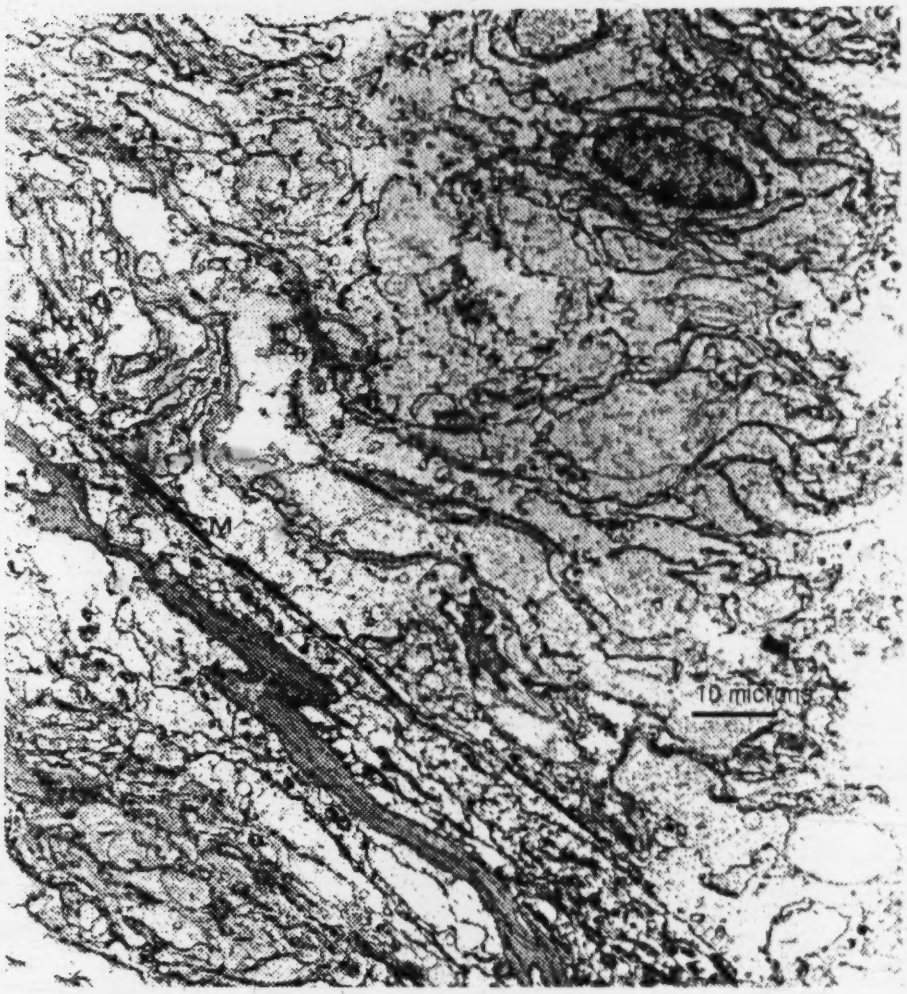


**Figure 5.3a** Neuropil area in the ganglion. This EM picture of the slide in Figure 5.2a shows the tangle of unsheathed axons, dendrites and glia. Collagen fibrils run throughout the extracellular space including the collagenous membrane (CM) that divides the ganglion bilaterally.

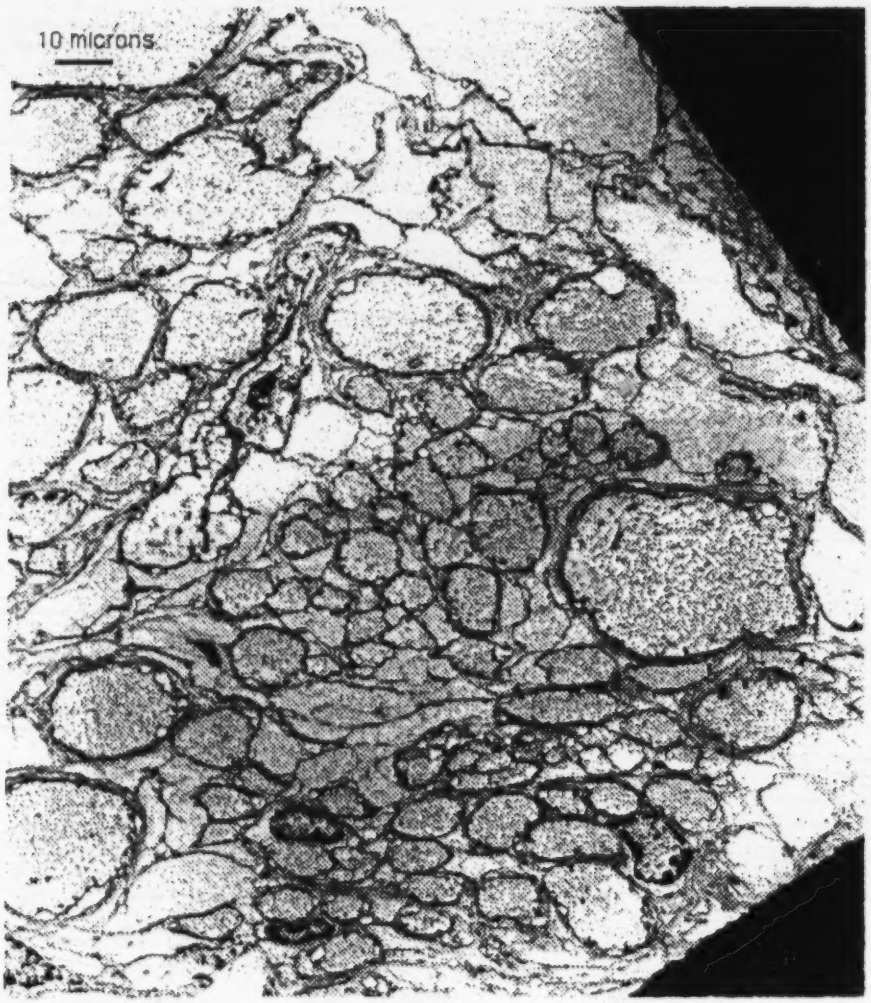


**Figure 5.3b** EM of Axon field in the ganglion. Much of the cross-section of the ganglion is made up of axons complete with connective tissue sheaths that pass through the ganglion without making synapses.

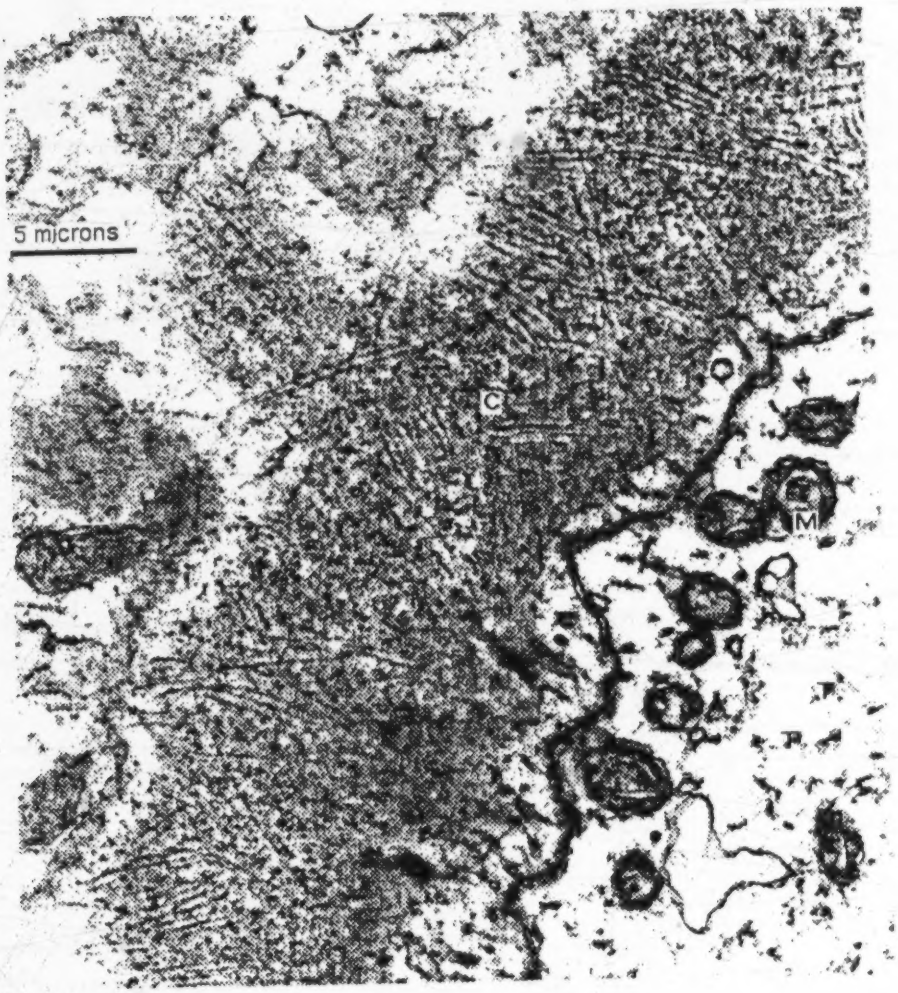


**Figure 5.3c** Extracellular collagen in the ganglion. This EM picture shows the striated layers of collagen (C) that can be found in the extraaxonal space. On the lower right, mitochondria (M) can be seen in the neurotubule, neurofilament and microtubule (T) filled axoplasm. At this magnification, the different types of tubules cannot be distinguished.

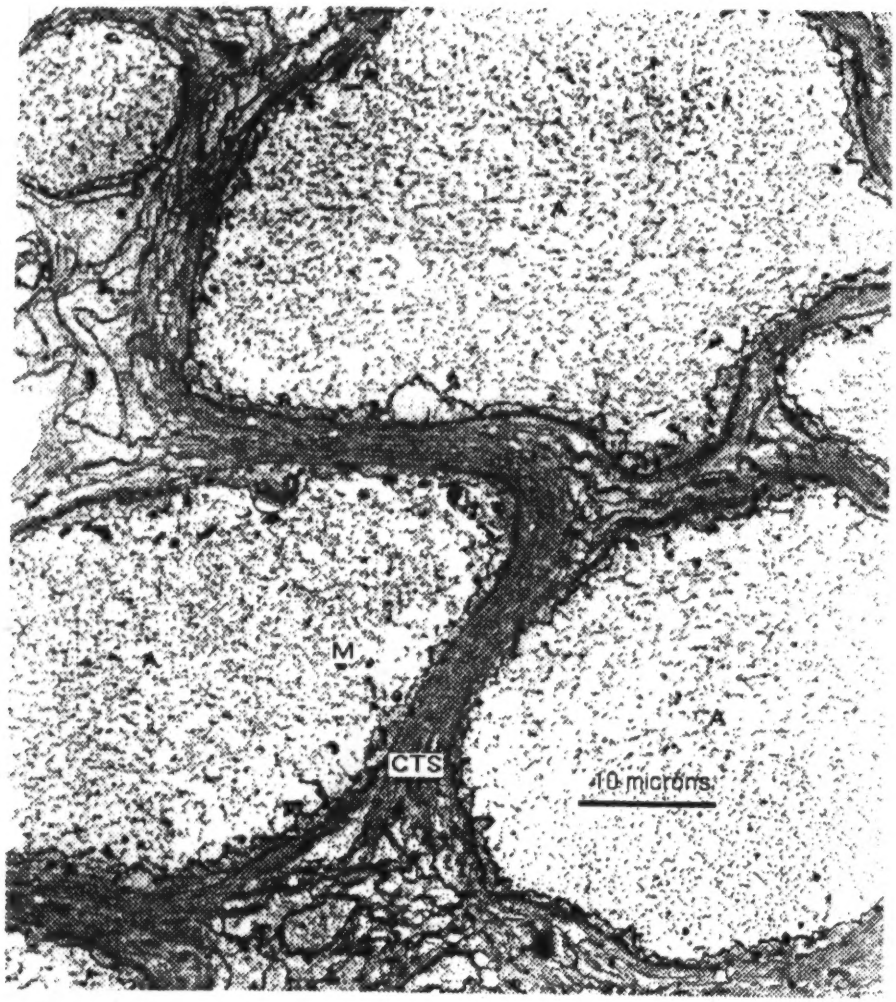


**Figure 5.3d** EM of large axons (A) in the 3-4 connective (these are not the giant axons). The extensive connective tissue sheaths (CTS) around the axons in this EM picture have large clefts between them where fluid can accumulate. The axons show the presence of neurotubules, neurofilaments and microfilaments as well as mitochondria (M). Note the uniform appearance of the axoplasm in the different axons.

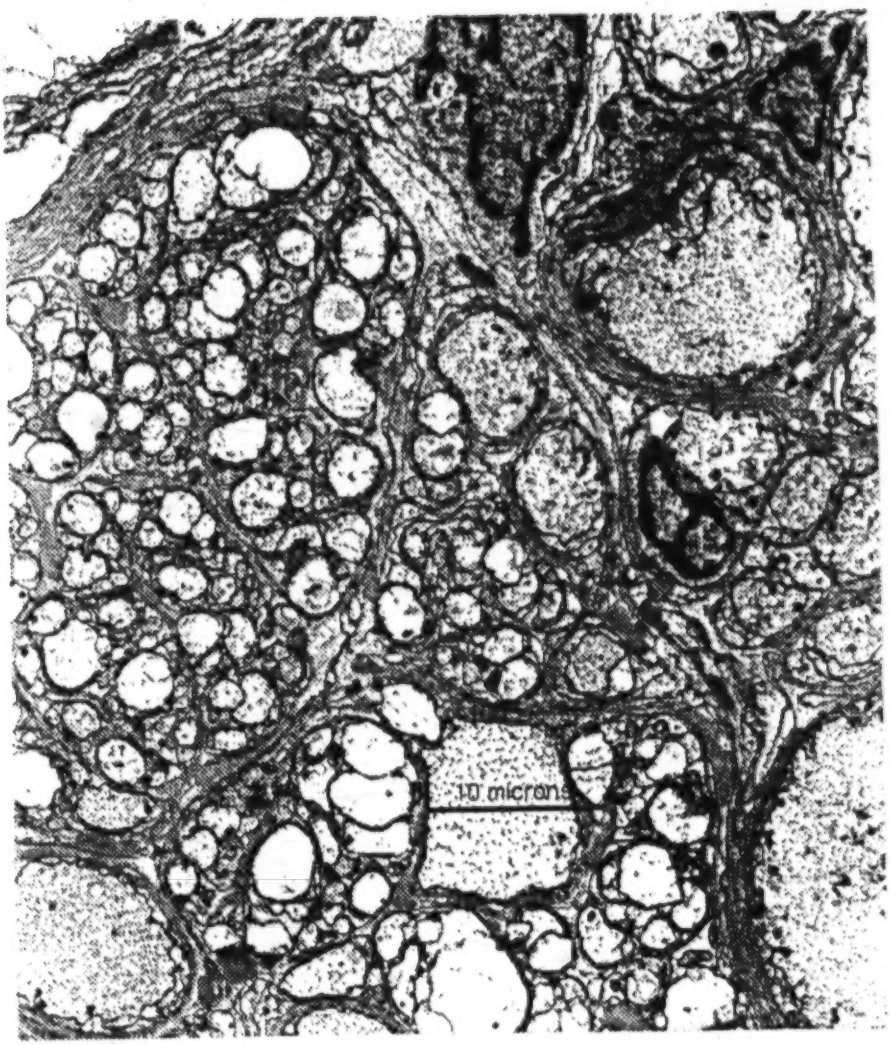


**Figure 5.3e** EM of small axons in the 3-4 connective. Even if the axons are too small to have individual connective tissue sheaths, they can form axon bundles which are extensively wrapped and supported by Schwann cells and collagen derivatives. Note the uniformity of the axoplasm in the different size axons.

**Figure 5.3f** EM of ventral sheath of the 3-4 connective. The EM shows that the collagenous neural lamella is riddled with fluid filled clefts (CL). Immediately below the neural lamella lie the perineural glial cells (PG) which also have space between them and further into the nerve cord one encounters the sheathed axons (A).

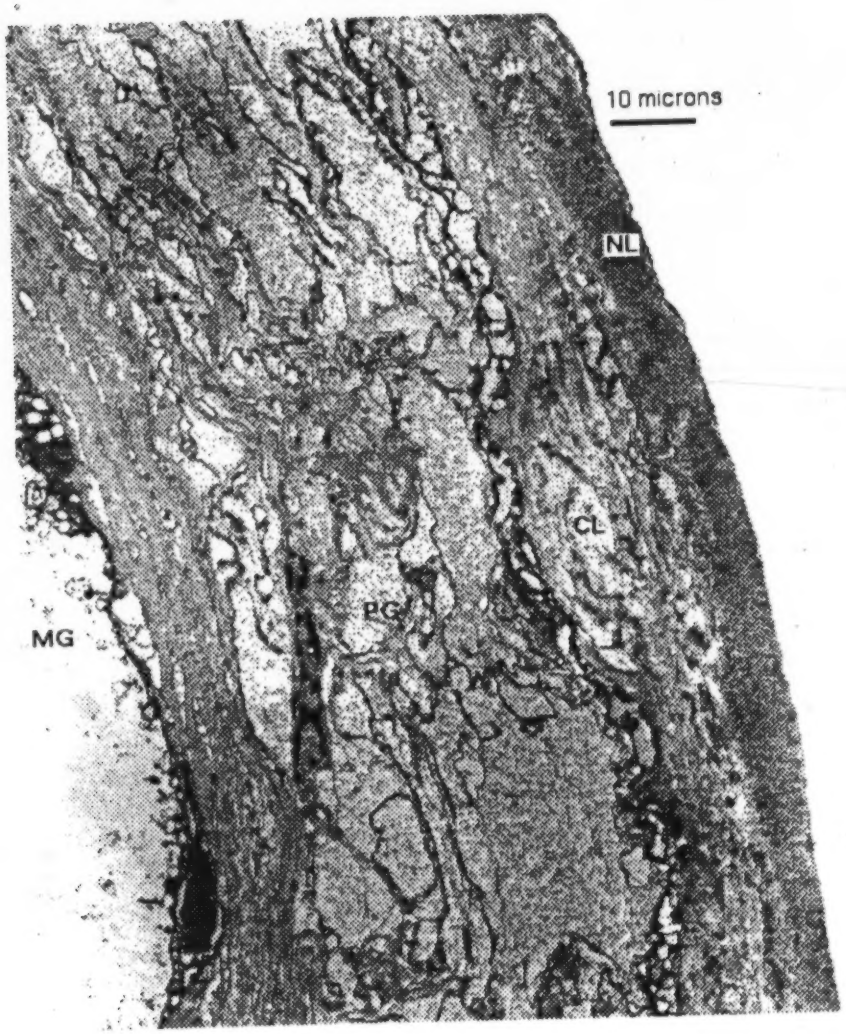


**Figure 5.3g** EM of dorsal sheath of the 3-4 connective. Here the neural lamella (NL) is tightly stretched with fewer clefts (CL). The extensive perineural glial cell layer (PG) separates a medial giant axon (MG) from the neural lamella and any bathing solution. In addition the MG axon has multiple lamellae around it formed by a Schwann cell.

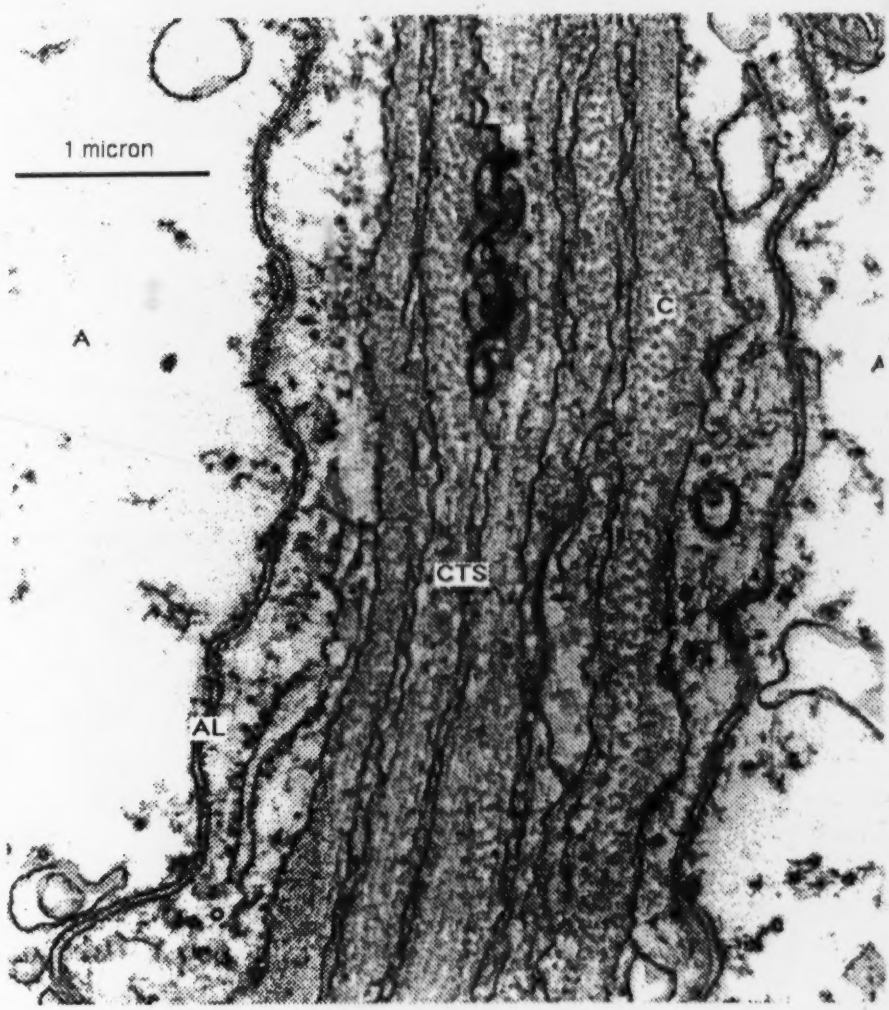


**Figure 5.3h** EM of connective tissue sheath between two axons. The space between the two axons (A) is filled by a connective tissue sheath (CTS) formed by Schwann cells and a collagen filled (C) extracellular space. The axolemma (AL) is well demarcated in this picture.

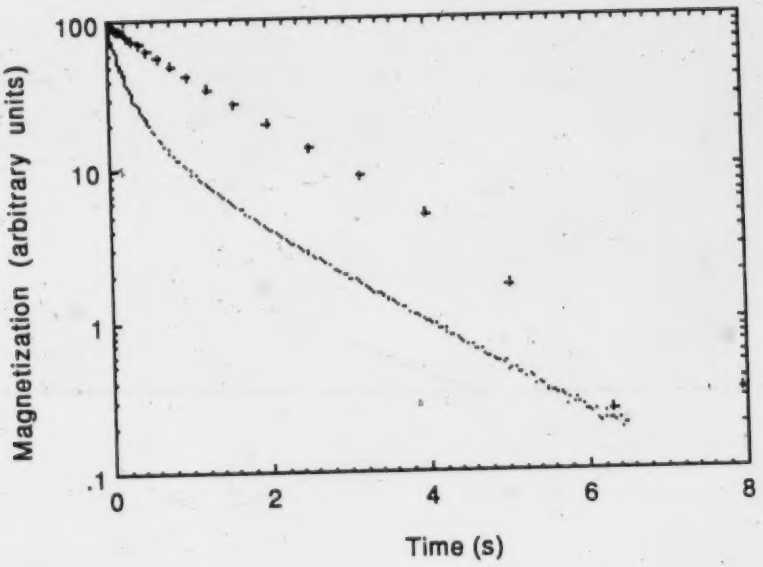


**Figure 5.4** Transverse and longitudinal proton magnetization decay for the nerve cord in Van Harreveld's bathing solution. Note the distinct multiexponentiality of the CPMG curve (·) and the apparent monoexponential behavior of the longitudinal magnetization (+).

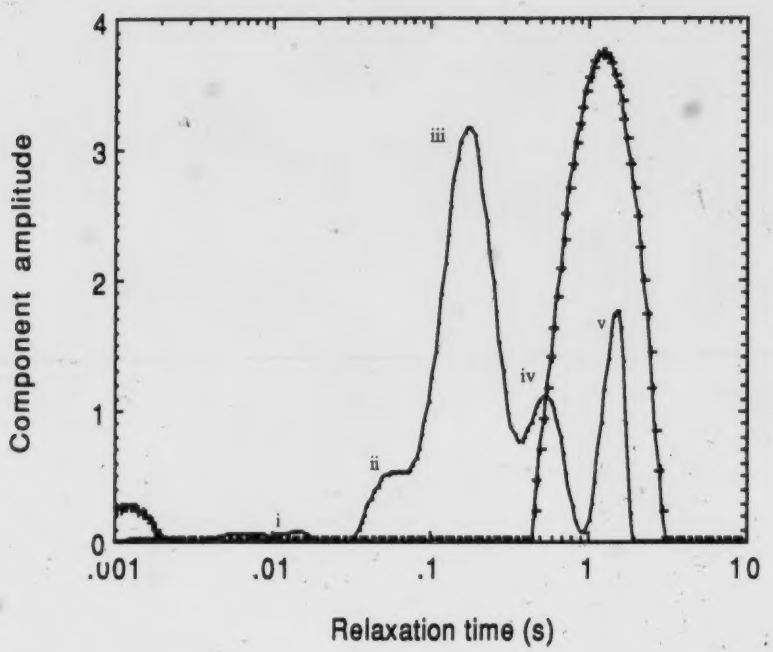


**Figure 5.5** Transverse and longitudinal relaxation time distributions. These are calculated using the non-negative least-squares technique on the data in Figure 5.4. The integrated area for both curves is 100 and corresponds to the notation of Figure 5.4 to match the initial intensity of the signal as illustrated in Figure 5.4. the $T_2$ distribution is shown as (·) and the $T_1$ distribution is shown as (+). The labels (i)-(v) are discussed in the text. Note that when a logarithmic abscissa is used, visual comparison of the areas of the components cannot be made.

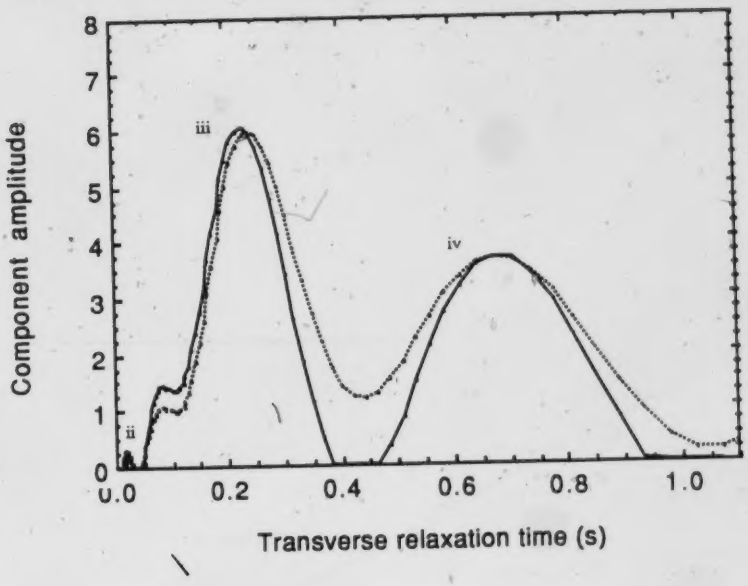


**Figure 5.6** Transverse relaxation time distribution before and after subperineural injection of the nerve cord with Van Harreveld's solution. The peak due to the bathing solution has been cut off for clarity. The solid line indicates the normal cord and the dotted line the injected cord. The volume fractions in the preinjected cord are, [peak (iv) 22.4 % @ $T_2$ of 680 ms)]; [peak (iii) 76.6 % @ $T_2$ of 197 ms)]. The volume fractions after injecting the cord are [peak (iv) 30.3 % @ $T_2$ of 806 ms)]; [peak (iii) 66.5 % @ $T_2$ of 228 ms)].

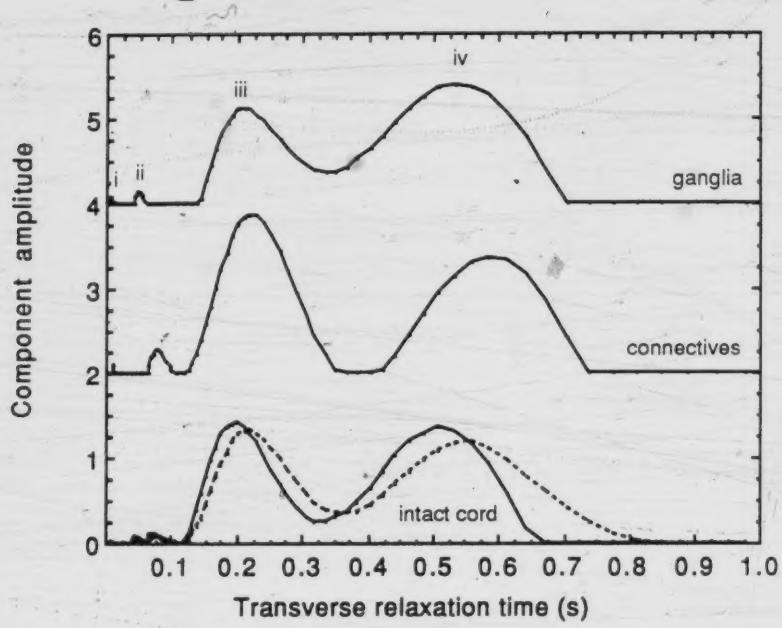


**Figure 5.7** Transverse relaxation time distribution of the whole and dissected nerve cord. The curves have been offset by units of 2 for clarity. The dashed line indicates a weighted sum of the $T_2$ distribution from the ganglia (60 %) and the connectives (40 %).

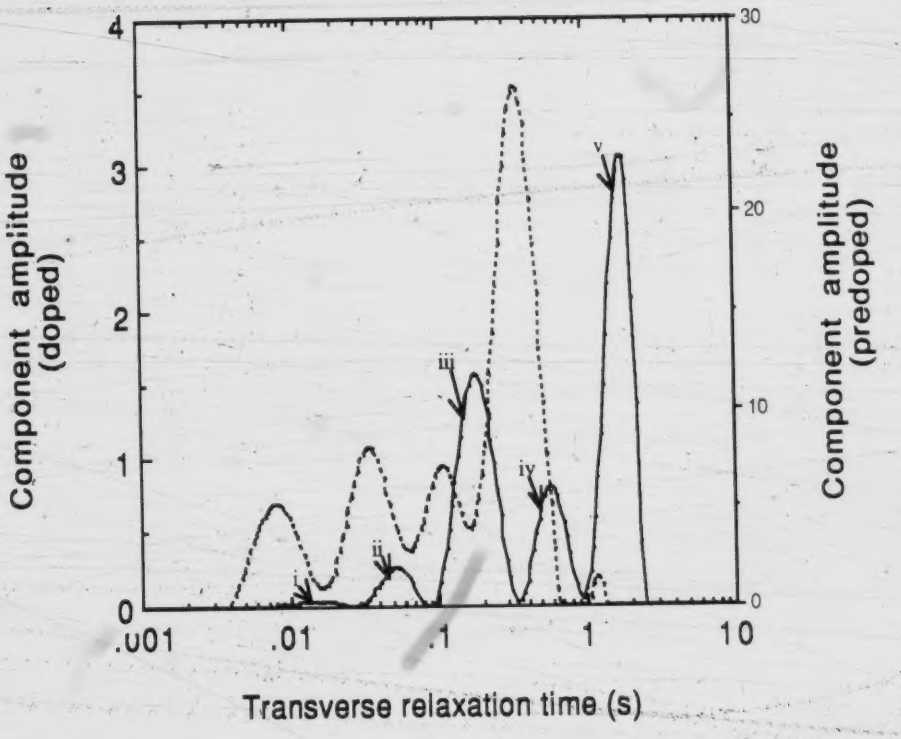


**Figure 5.8** Effects of paramagnetic doping (10 mM $CuSO_4$) of the bathing solution on the transverse relaxation time of the nerve cord. The curve for the same cord before doping is shown as a solid line and the doped cord is shown as a dashed line.

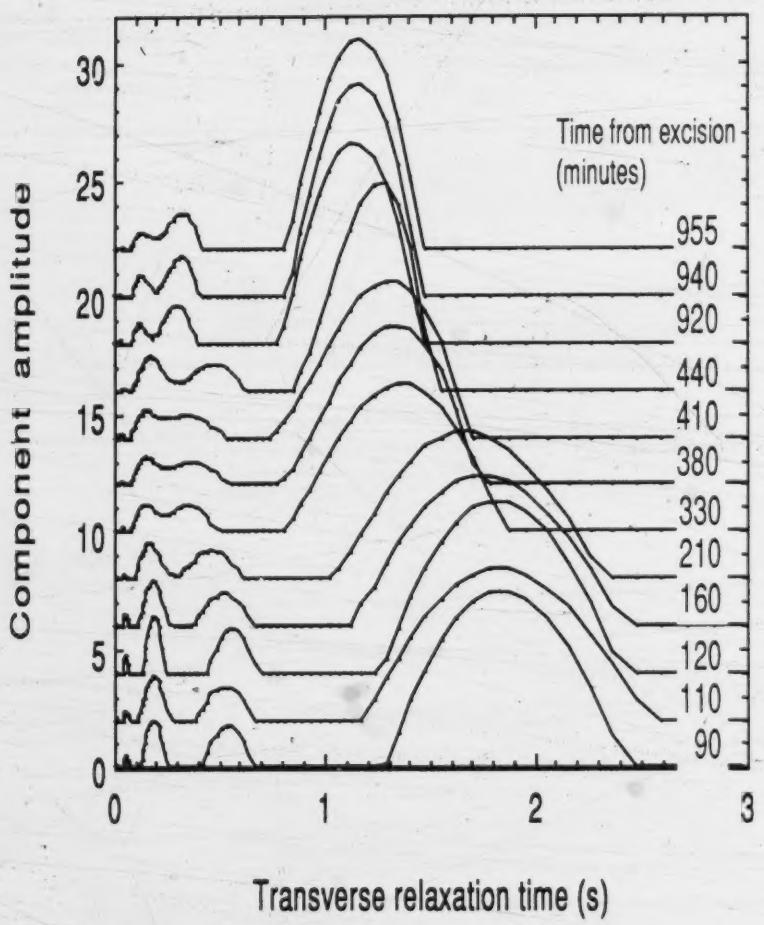


**Figure 5.9a** Change in the transverse relaxation time as a function of time after excision. The curves have been offset vertically by units of 2 for clarity. Note the linear abscissa.

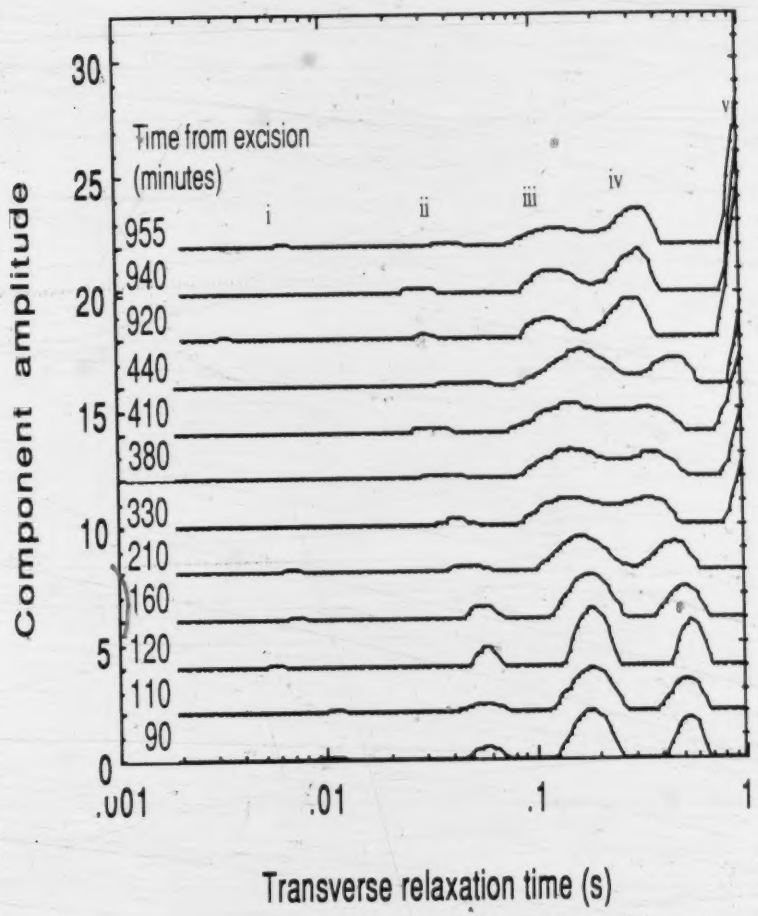


**Figure 5.9b** Change in the transverse relaxation time distribution as a function of time after excision. By using a logarithmic $T_2$ scale and cutting off the peak due to the bathing solution, the behavior of the smaller, shorter $T_2$ components (i)-(iv) can be followed.

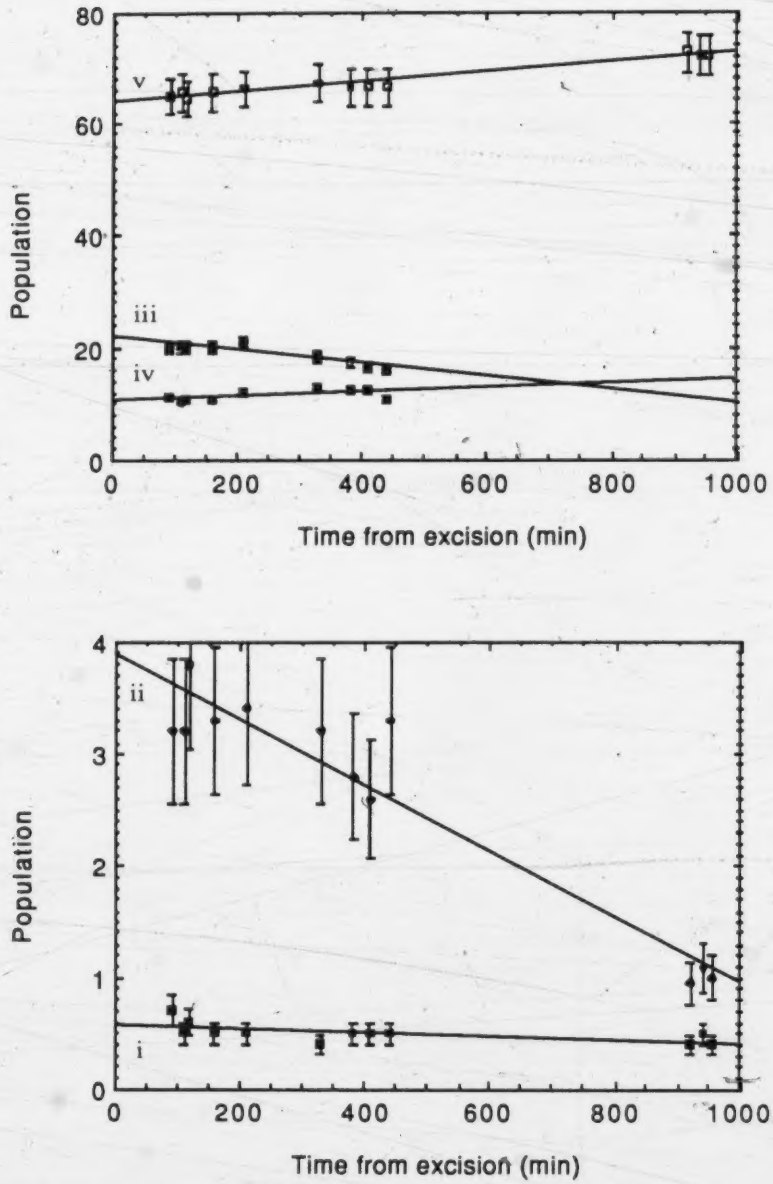


**Figure 5.9c** Behavior of the component populations over time after excision. The lines represent a least-squares fit to the data.

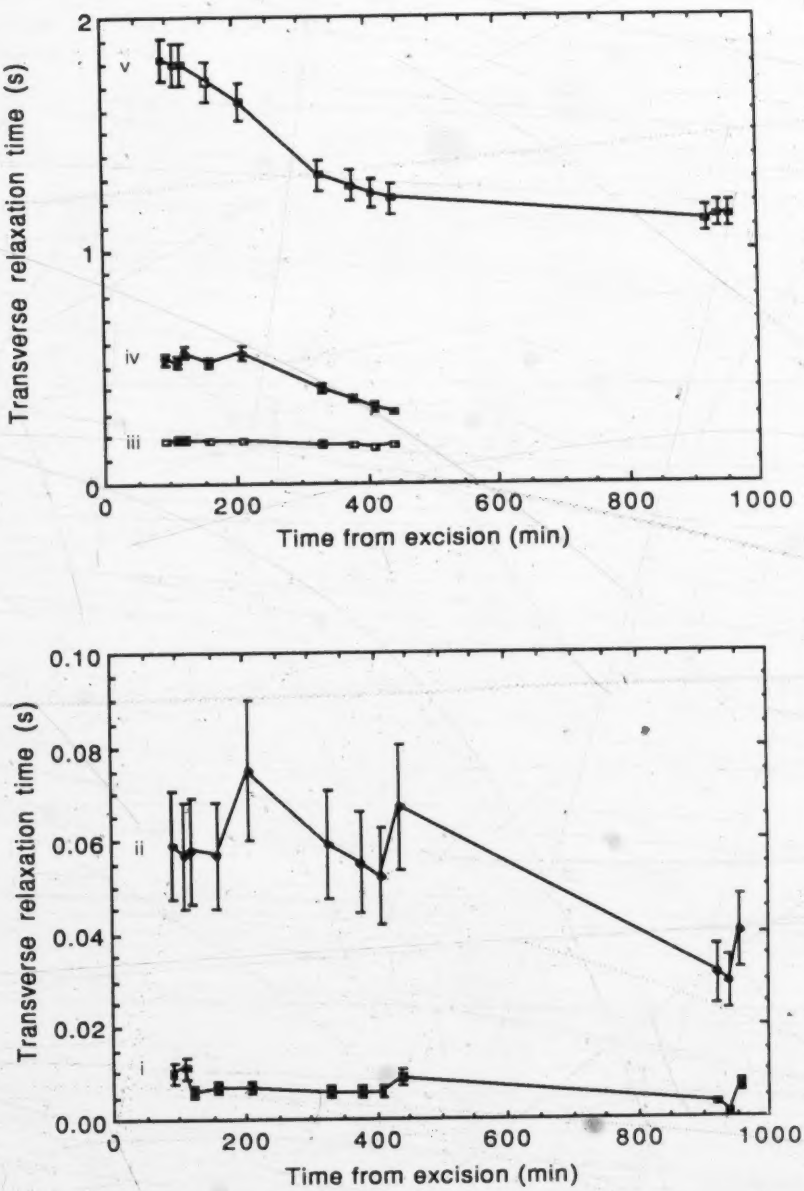


**Figure 5.9d** Behavior of the component transverse relaxation times as a function of time after excision. The lines are only to guide the eye.

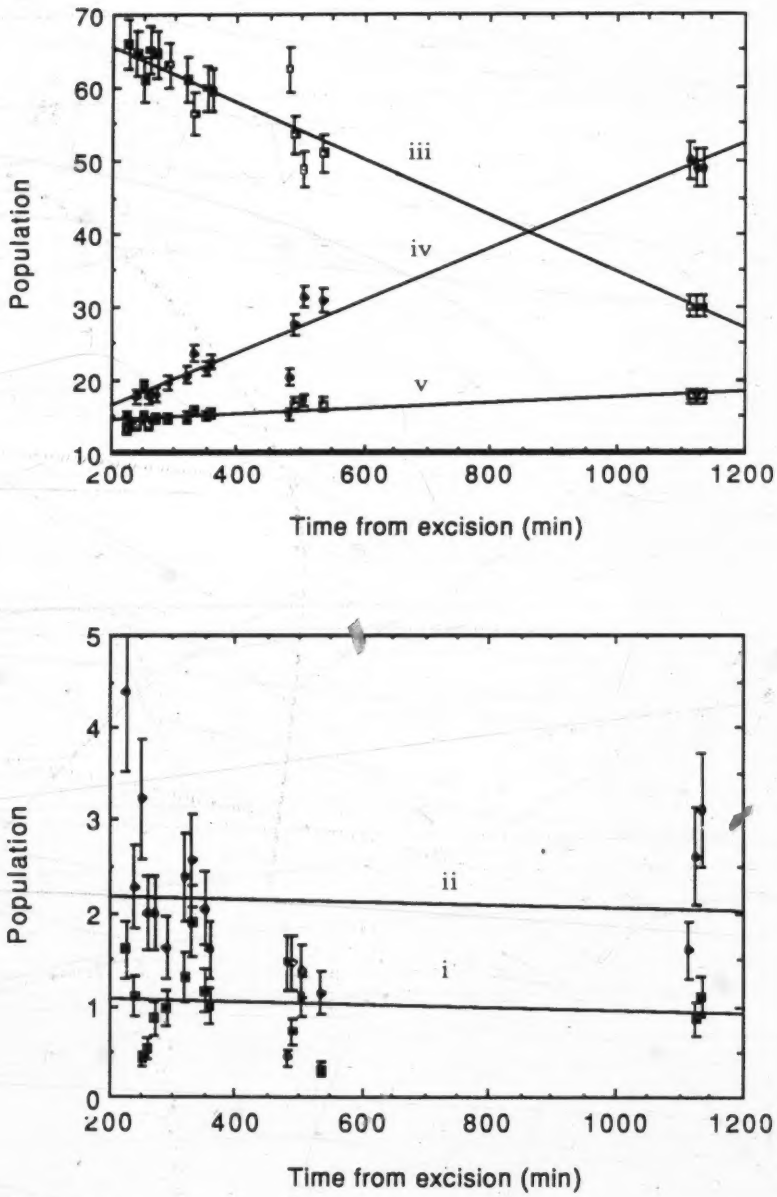


**Figure 5.10a** Behavior of the component populations over time after excision and storage at 4 °C for 3.75 hours. The lines represent a least-squares fit to the data.

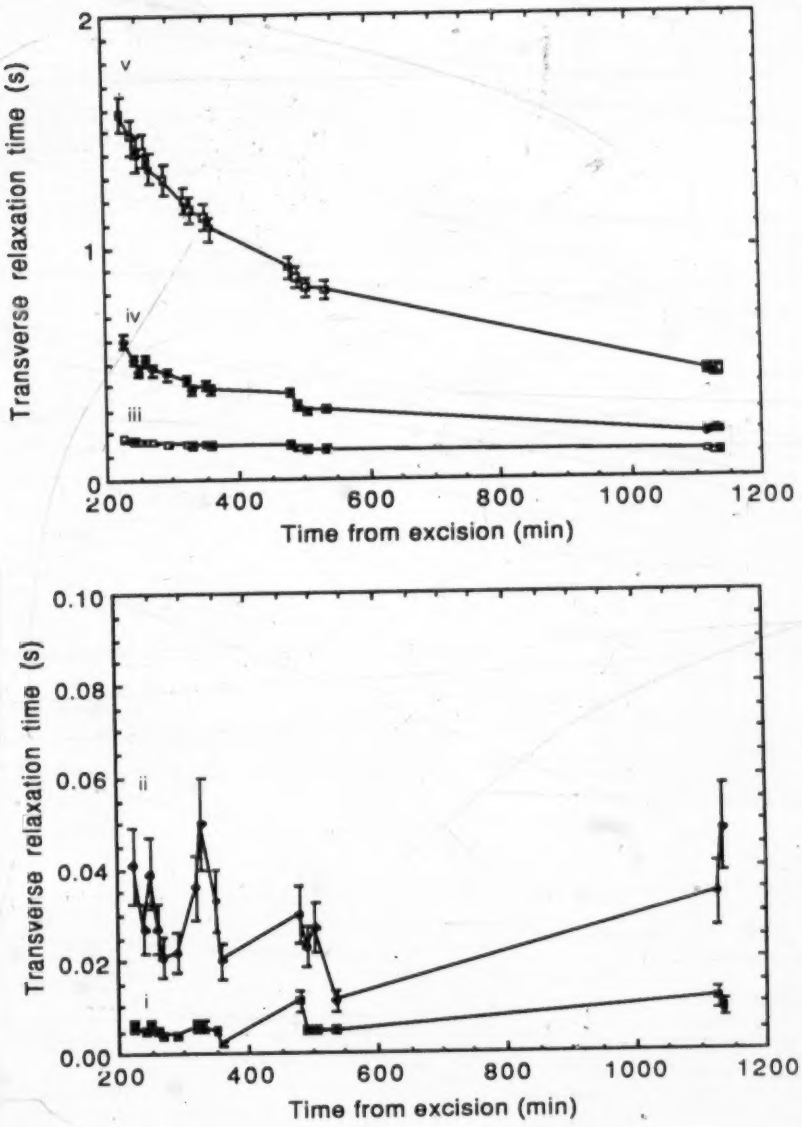


**Figure 5.10b** Behavior of the component transverse relaxation time after excision and storage at 4 °C for 3.75 hours. The lines are only to guide the eye.

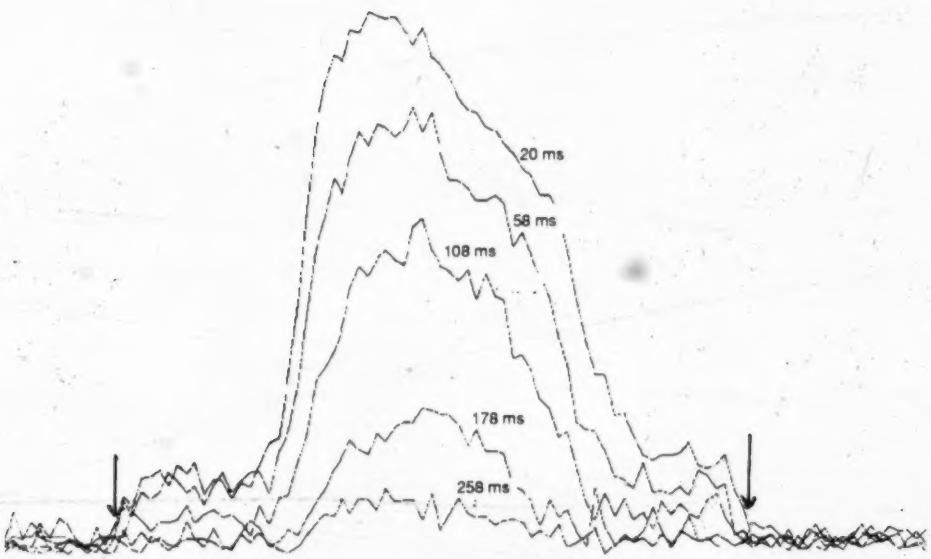


**Figure 5.11** Image projections throught the 3-4 connective of the crayfish nerve cord as a function of spin-echo time . These projections reflect the proton density of the crayfish nerve cord within the 150 μm slice. The arrows indicate the boundary of the teflon tube which is made visible by moisture on the inside rim. The projections were made with the microscopic imaging pulse sequence with no phase encoding gradients.

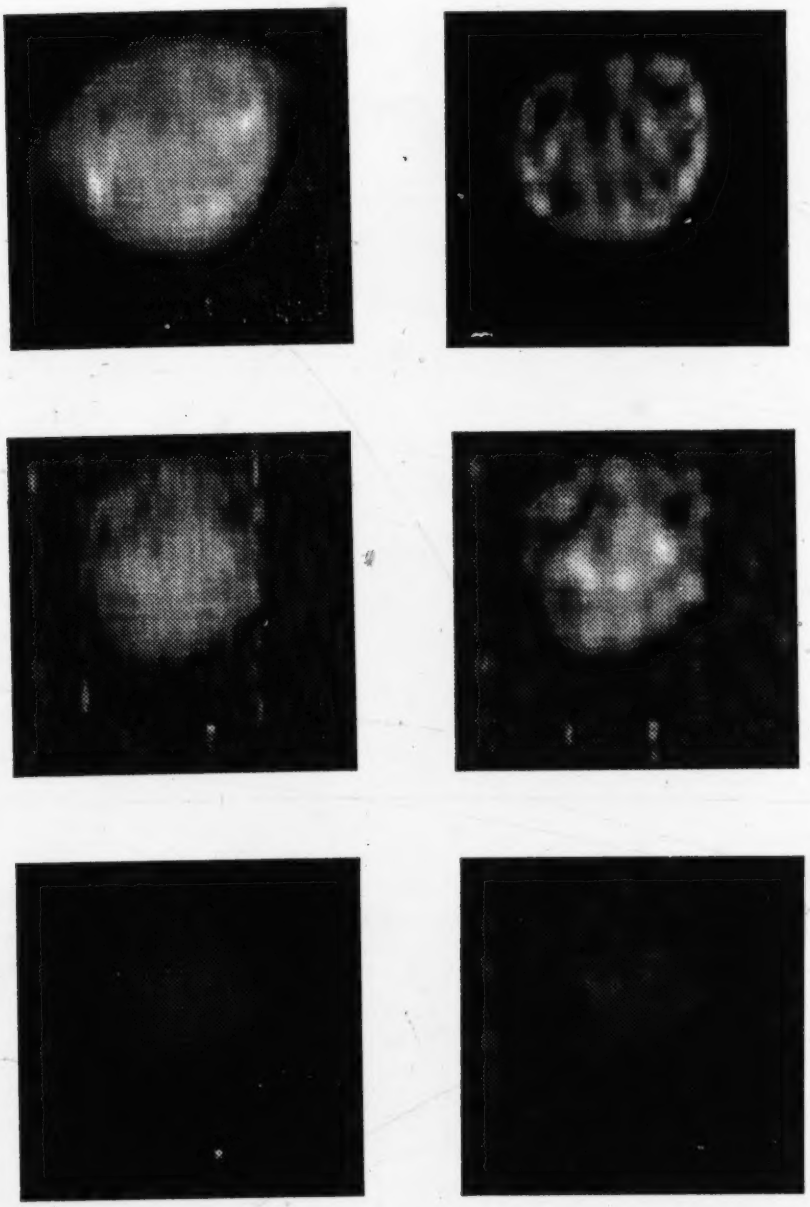

**Figure 5.12** Transverse proton NMR microscopic image of the crayfish 3-4 connective. The contrast enhanced image is shown on the right. The images were made with different spin-echo times to generate $T_2$ contrast. These echo times were 20 ms in (a), 178 ms in (b) and 258 ms in (c). The field of view is 2mm x 2mm.

5.8 References

1. T.H. Bullock and G.A. Horridge, "Structure and Function in the Nervous Sytem of Invertebrates, Freeman, San Francisco 1965.
2. D.C. Sandeman *in* "The Biology of Crustacea, Neurobiology: Structure and Function", Vol 3, p 1, Academic Press, New York , 1982.
3. R.M. Kroeker, C.A. Stewart, M.J. Bronskill and R.M. Henkelman, Continuous distributions of NMR relaxation times applied to tumors before and after therapy with x-rays and cyclophosphamide, *Magn. Reson. Med.* **6**, 24 (1988).
4. K.P. Whittall and A.L. Mackay, Quantitative interpretation of NMR relaxation data, *J.Magn. Reson.* **84**, 134 (1989).
5. R.S. Menon and P.S. Allen, Application of continuous relaxation time distributions to the fitting of data from model systems and excised tissue, *Magn. Reson. Med.* Submitted (1990).
6. C.A.G. Weirsma, Giant nerve fibre system of the crayfish. A contribution to comparative physiology of synapse. *J. Neurophsiol.* **10**, 23 (1947).
7. N.J. Lane and N. Abbott, The organization of the nervous system in the crayfish *Procambarus clarkii* with emphasis on the blood-brain interface, *Cell Tissue Res.* **156**, 173 (1975).
8. J.J. Kendig, Structure and function of the third abdominal ganglion of the crayfish *Procambarus clarkii* (Girard). *J. Exp. Zool.* **164**, 1 (1967).
9. N.J. Abbott, Y. Pichon and N.J. Lane, Primative forms of potassium homeostasis, Observations of crustacean central nervous system. *Exp. Eye Res.* **25**, 259 (1977).

10. H. Davson, *in* "Implications of the blood-brain barrier and its manipulation" (E.A. Neuwalt, Ed.), Vol. 1, p. 21, Plenum, New York, 1989.

11. J. Abbott and Y. Pichon, Ionic permeability of perineural sheath of the crayfish central nervous system, *J. Physiol.* **234**, 54P (1973).

12. A. Van Harreveld, A physiological solution for freshwater crustaceans, *Proc. Soc. Exp. Biol. (N.Y.)* **34**, 428 (1930).

13. H.Y. Carr and E.M. Purcell, Effects of diffusion on free precession in nuclear magnetic resonance experiments, *Phys. Rev.* **94**,630 (1954).

14. S. Meiboom and D. Gill, Modified spin-echo method for measuring nuclear relaxation times, *Rev. Sci. Instrum.* **29**, 688 (1958).

15. D.G. Hughes and L. Lindblom, Baseline drift in the Carr-Purcell-Meiboom-Gill pulsed NMR experiment, *J. Magn. Reson.* **26**, 469 (1977).

16. R. Freeman and D. Hill, Fourier transform study of NMR spin-spin relaxation, *J. Chem. Phys.* **55**, 1985 (1971).

17. F.A. Jolesz, J.F. Polak, D.F. Adams and P.W. Ruenzel, Myelinated and non-myelinated nerves, Comparison of Proton MR properties, *Radiology* **164**, 89 (1987).

18. N. Relkin, M. Eisenstadt, M. Spiller, R.D. Brown III and S. H. Koenig, Multiple proton relaxation components in nerve; The magnetic field dependence of $1/T_1$, *in* "Proc. VI$^{th}$ Annual Meeting of the Society of Magnetic Resonance in Medicine", p. 65, 1987.

19. V. Vasilescu, E. Katona, V. Simplaceanu and D. Demko, Water compartments in the myelinated nerve. III. Pulsed NMR results, *Experientia* **34**, 1444 (1978).

20. D.C. Chang and C.F. Hazlewood, An nuclear magnetic resonance study of squid giant axon, *Bioch. Biophys. Acta* **630**, 131 (1980).

21. T.J. Swift and O.G. Fritz, Jr., Proton spin-echo study of the state of water in frog sciatic nerve, *Biophys. J.* **9**, 54 (1969).

22. O.G. Fritz, Jr. and T.J Swift, The state of water in polarized and depolarized frog nerves. A proton magnetic resonance study, *Biophys. J.* **7**, 675 (1967).

23. C.L. Lawson and R.J. Hanson, Solving Least Squares Problems, Prentice-Hall, Englewood Cliffs N.J., 1974.

24. T.A. Viancour, K.R. Seshan, G.D. Bittner and P.A. Sheller, Organization of the axoplasm in crayfish giant axons, *J. Neurocyt.* **16**, 557 (1987).

25. B.G. Wallin, Water permeability in resting and stimulated crayfish nerve, *J. Gen. Physiol.* **54**, (1969).

26. R.S. Menon, M.S. Rusinko and P.S. Allen, Multiexponential proton relaxation in a model tissue system, *Magn. Reson. Med.* Submitted (1990).

27. P.T. Beal, C.F. Hazlewood and P.N. Rao, Nuclear magnetic resonance patterns of intracellular water as a function of HeLa cell cycle, *Science* **192**, 904 (1976).

28. G.P. Raaphorst, J. Kruuv and M.M. Pintar, Nuclear magnetic resonance study of mammalian cell water, *Biophys. J.* **15**, 391 (1975).

29. D.C. Chang, C.F. Hazlewood, B.L. Nichols and H.E. Rorschach, Spin echo studies of cellular water, *Nature* **235**, 170 (1972).

30. P.S. Belton and R.G. Ratcliffe, NMR and compartmentation in biological tissue, *Prog. NMR Spectrosc.* **17**, 241 (1985).

31. R. Mathur-De Vre, The NMR studies of water, *Prog. Biophys. Molec. Biol.* **35**, 103 (1979).

32. J. Abbott, Absence of blood-brain barrier in a crustacean, *Carcinus maenas L.*, *Nature* **225**, 291 (1970).

33. J. Brahm, Diffusional water permeability of human erythrocytes and their ghosts, *J. Gen. Physiol.* **79**, 791 (1982).

34. T. Conlon and R. Outhred, The temperature dependence of erythrocyte water diffusional permeability, *Biochim. Biophys. Acta* **511**, 408 (1978).

35. R.S. Menon, and P.S. Allen, Solvent proton relaxation of aqueous solutions of the serum proteins $\alpha_2$-macroglobulin, fibrinogen and albumin, *Biophys. J.* **57**, 389 (1990).

36. H.C. Powell and R.R. Myers, *in* "Implications of the blood-brain barrier and its manipulation" (E.A. Neuwalt, Ed.), Vol. 1, p. 199, Plenum, New York, 1989.

37. R.R. Myers, H.M. Heckman and H.C. Powell, Endoneurial fluid is hypertonic, *J. Neuropath. and Exp. Neurol.* **42**, 217 (1983).

38. H.C. Powell and M.L. Costello, Endoneurial fluid pressure in Wallerian degeneration, *Annals of Neurol.* **5**, 550 (1978).

39. E.D. Finch and A.S. Schneider, Mobility of water bound to biological membranes, A proton NMR study, *Bioch. Biophys. Acta* (1975).

# CHAPTER 6

## General Discussion and Conclusions

### 6.0 Towards quantifying cerebral edema

In the previous chapters, we have investigated water proton relaxation in a variety of increasingly complex model systems. These systems have been chosen specifically to improve our understanding of the factors governing water proton relaxation in edematous brain tissue. In order to judge the usefulness of these models in quantifying the degree and type of edema, a comparison of the results with *in-vivo* measurements will be made. While some of the comments in this chapter are undoubtedly speculative, they will hopefully serve to motivate further research into quantitative *in-vivo* relaxation measurements. First of all, one needs a common basis with which to analyse and discuss the different studies. Clinical and experimental *in-vivo* measurements have, in the past, been confined to $T_1$ and $T_2$, so it would be appropriate to use these as a basis to compare studies. Since the inverse of the quantities, namely the relaxation rates $R_1$ and $R_2$, are more meaningful when discussing relaxation changes due to difference in protein or water content, we chose to examine the ordered pair ($R_1$, $R_2$).

In Figure 6.1, $R_2$ versus $R_1$ is plotted for the three serum proteins studied in Chapter 2. It is clear that each protein follows a unique trajectory in the space ($R_1$, $R_2$) as the protein concentration increases. In general, these trajectories will depend on the relative sensitivity of $R_2$ and $R_1$ to unit changes in concentration as discussed in Chapter 2. Fibrinogen, the most anisotropic of the three proteins, and with the longest axis length, shows a much larger $R_2$ sensitivity due to its slower tumbling

motion than the smaller, more rapidly tumbling albumin. In all cases, the $R_2$ sensitivity is much larger than the $R_1$ sensitivity for proteins in solution and the graph in Figure 6.1 suggests that the ordered pair ($R_1$, $R_2$) could be used to distinguish uniquely between different sizes and shapes of protein in solution. This may indeed be true if there were only one type of protein in an edema fluid at any given time. In reality there are many different serum proteins and a measurement of $R_2$ and $R_1$ could not uniquely determine the types and concentrations of protein in the edema fluid. This is not necessarily a limitation because of the nature of the time course of edema as discussed in section 1.5. In vasogenic edema, the breakdown of the blood-brain barrier is usually gradual, the smaller serum proteins leaking into the brain parenchyma before the larger ones do. In cytotoxic or ischemic edema, one expects little initial change in tissue water content, only a shift in water from extra to intracellular spaces. Thus one might expect $R_1$ and $R_2$ to follow a specific pattern over time, which might be useful in staging the pathology.

As was demonstrated in Chapters 3 and 5, fast water exchange generally occurs between intra and extracellular regions when only a single plasma membrane separates the two. This is the assumption that we use to explain the monoexponential behavior of the transverse and longitudinal magnetization decays in grey matter in Chapter 4. If we consider a situation where vasogenic edema has developed at a site in grey matter, the voxel intensities of this site visualized by using a multi-echo clinical imaging sequence would have a simple monoexponential decay. The $R_2$ measured in a particular voxel would be the weighted average of the water proton relaxation rate in the neural cell bodies and glia and the relaxation rate of the water in the extracellular space (into which the edema fluid leaks). Such a situation can be modelled by the mixed RBC ghost solution results discussed in Chapter 3, if we

identify water inside the ghosts as intracellular water and the buffer on the outside as the edema fluid. By varying the protein content and volume fraction of extracellular fluid with respect to ghosts we can simulate the time course of the induction of edema in a tissue such as grey matter. This model is presented in Figure 6.2.

If the extracellular fluid is protein free, the ($R_1$, $R_2$) trajectory moves linearly from the ($R_1$, $R_2$) point for the packed ghosts to the point determined by the ($R_1$, $R_2$) of the buffer as the volume fraction of buffer increases. If however, there is protein in this extracellular fluid, the ($R_1$, $R_2$) trajectory heads toward the point that determines the ($R_1$, $R_2$) of the proteinaceous buffer. Clearly the ($R_1$, $R_2$) behavior of these two models as the extracellular fluid fraction increases is different over time. One can envisage a situation where the initial exudate contains mostly plasma ions and fluid, and then after further breakdown of the BBB, contains more fluid and larger proteins. Such a scenario could be described by the dashed line in the figure. If measurements of the timecourse of $R_1$ and $R_2$ could be made clinically, they may be useful in discerning the contents of the plasma exudate in grey matter as a function of time. Let us assume that the point marked "N" represents normal grey matter in our model (15 % extracellular space). We can envisage a situation where the initial breakdown of the BBB leads to increased plasma fluids in the extracellular space, leading to the point "I". At a later time, proteins leak into the extracellular space with (point "W") or without (point "WO") a further increase in extracellular space. Our model predicts an initial larger change in $R_2$ compared to $R_1$ and then increases in both $R_2$ and $R_1$ as the protein content and/or fluid content of the extracellular space increases. Note that the fractional changes in $R_2$ and $R_1$ are comparable, although the absolute magnitude of the changes in $R_2$ are larger. Furthermore, it should be clear that a measurement of only $R_2$ is not sufficient to distinguish the cases "N", "W" or

"WO", but that the addition of $R_1$ measurements improves the discrimination ability of the relaxation measurements. Another very satisfying point is the ability of our simple model to reproduce the often observed linear dependence of $R_1$ and $R_2$ on tissue water content. The tissue water content in our model is, to a very good approximation, simply related to the fraction of ghosts in the mixture.

In white matter, we have seen from Chapter 4, that the transverse relaxation is multiexponential in nature, due to the postulated slow exchange of water across the myelinated axolemma. Such a situation allows one to discriminate directly between intra and extracellular water using multiexponential analysis. However, the relaxation changes in these compartments are not simple functions of protein and water concentration as we discuss below. The longitudinal magnetization remains monoexponential in nature. During the development of vasogenic edema, pockets of edema can form in the white matter due to the high tissue compliance of the myelinated axon tracts. Such a system can be simulated by our layered RBC ghost models used in Chapter 3, where the transverse relaxation from two slowly exchanging fractions (ghosts and buffer) is found to be biexponential, while the longitudinal magnetization decay is still a simple exponential. We consider the following model. Let the layered buffer represent a pocket of edema fluid which has formed adjacent to a region with some axons (the packed RBC ghosts) and axon associated interstitial space (the trapped volume fraction in the packed RBC ghosts). As the volume fraction of the model edema fluid is increased, the interstitial space also increases as discussed in Chapter 3. This mimics the actual volume changes that occur in white matter quite well (3). Ideally, we would have liked slow exchange between the ghosts and the interstitial space to model the situation better in myelinated tissue.

The results for our model are shown in Figure 6.3 for the case where the model edema fluid is free of protein and the case where it contains 75 g/l of serum albumin. The points marked "N" might represent normal brain. If small edema pockets develop (points marked "E"), we can identify them from the fact that the transverse magnetization decay becomes biexponential. If the model edema fluid is protein free, the relaxation rate of the axon-interstitial-space compartment decreases as the volume of the interstitial space increases. However, if the protein is present in the edematous region, some of it becomes bound by the membranes in the enlarged axon-interstitial-space compartment, resulting in an enhancement of the relaxation rate of this compartment above what would be expected from simple equilibration of the protein in the edema fluid with the interstitial space. The model to explain this apparently anomalous finding was presented in Chapter 3. Thus the relaxation rates in our model, and presumably in tissue, are a function of both protein concentration and membrane-protein interactions in the tissue. The binding of proteins to the tissue membranes can result in considerable enhancement of the water proton relaxation rates over that expected for free proteins in solution, which means that the interpretation of relaxation changes in edematous tissue is considerably more complicated than initially thought.

An *in-vivo* study on the time course of edema can be used to demonstrate the applicability of some of the results in this thesis to the interpretation of relaxation changes in edematous tissue. Shioya and co-workers (1) have demonstrated two transverse relaxation components in rat lung as well as clearly identifying their origin. The faster of the two relaxation times is associated with cellular water while the longer one is associated with water in the interstitial space. Using his data from

oxygen-induced pulmonary edema (Figure 6.4), we can see very different behavior for the two components as edema develops. In the interstitial space, the $R_2$ and $R_1$ exhibit the same fractional change. In the cellular component, $R_2$ drops by almost a factor of two before it appears to level off, while the $R_1$ does not initially change, but then decreases. As indicated by our measurements on protein solutions and ghosts (Chapters 2 and 3), a drop in $R_2$ signifies a decrease in the macromolecular concentration in the compartment (as brought about by an influx of water), an increase in the mobility of the macromolecules (as brought about by cellular degeneration), or both. A decrease in $R_1$ generally signifies an increase in water content, since $R_1$ is not found to depend strongly on the slow motions of the hydration surfaces. Thus a concurrent decrease in $R_1$ and $R_2$ suggests changes in water content of the tissue, while a drop in $R_2$ with no change in $R_1$ suggests increases in the mobility of the cellular structures. Shioya's data show that the interstitial $R_2$ behaves much like a simple protein solution would upon dilution, but that the changes in the cellular compartment are more complex. We could interpret the initial rapid decrease in $R_2$ in the cellular compartment as being due to changes in the cellular structures, while the subsequent relaxation changes probably involve an influx of water, since $R_1$ begins to drop. This approach allows us to distinguish changes in rates due to (i) structural modifications and (ii) water content changes, in compartments. It is thus seen that even the simple protein solution data can aid in the interpretation of *in-vivo* models of edema.

## 6.1 Conclusions

NMR imaging has become a powerful and routine technique used in several thousand centres world wide. This is due mainly to the fact that the contrast

generated in an NMR image, especially for soft tissues, is an extremely sensitive function of the state of the water molecules in the tissues, primarily due to the water proton relaxation rates $R_1$ and $R_2$. The ability to quantify the water proton relaxation rates can provide extremely useful parameters (e.g., extracellular protein content or volume fraction) for use in the management of disease states such as edema in the brain provided that a fundamental understanding of the physical processes governing water proton relaxation in tissue can be obtained.

The original motivation for this project arose from the need to be able to differentiate between vasogenic and cytotoxic edematous states or tumor masses and peritumoral edema, using NMR imaging. Thus we chose to develop models that would help us study the water proton relaxation charateristics of edema fluids into which serum proteins have leaked because of a breakdown of the blood-brain barrier. However, the models developed in Chapters 2 to 5 are of general applicability to water proton relaxation in most tissues and have helped us develop a better understanding of water dynamics in tissue, including the interactions of water with membranes and proteins.

The simplest model of an edema fluid (or any biological tissue) consisted of serum proteins in aqueous solution as presented in Chapter 2. Working with human fibrinogen, serum albumin and $\alpha_2$-macroglobulin, we confirmed that $R_2$ is almost an order of magnitude more sensitive to protein concentration and shape than $R_1$ and is therefore the preferred parameter to use when trying to generate contrast in a NMR image. The field dependence of $R_{1\rho}$ was also studied and the low field values were found to be very close to $R_2$; in fact the ratio $R_2 / R_{1\rho}$ has allowed us to show clearly that it is the slow motions of proteins in solution that elevate the sensitivity of $R_2$ to

protein shape and concentration as compared to $R_1$. We adopted a model in which two motions are important in producing water proton relaxation in aqueous solutions of protein; a slow motion due to protein tumbling and a much faster motion due to water reorienting in the hydration layer of the protein. Figure 2.4 suggests the possibility that $R_{1\rho}$ weighted NMR images made at different spin-locking pulse amplitudes could be used to generate contrast between protein-rich and protein-poor fluid areas in a similar manner to conventional multi-echo images.

Having ascertained that protein motion can differentially affect the relaxation rates, it seemed appropriate to incorporate membranes into the model, to see how they would affect the protein motions, and hence the relaxation rates. We thus chose, in Chapter 3, to develop a model system which was pseudo-cellular in nature and in which external protein and ion concentrations could be varied. This was accomplished by designing a system using human red blood cell ghosts as the pseudo-cell. We directed our efforts at varying the concentration of proteins in the extracellular space as well as varying the membrane permeability of the RBC ghosts. Extensive electron-microscopy was done to show that the inside of the RBC ghosts is in fact clear of haemoglobin and that the membrane is intact. By varying the ratio of packed RBC ghosts to extracellular fluid as well as protein content in this fluid we have been able to mimic relaxation in protein-rich and protein-poor edema fluids. In well stirred samples of ghosts and fluid we have shown that for normal membrane permeabilities, $R_1$ ,$R_2$ and $R_{1\rho}$ are all monoexponential due to fast water exchange between the cells and their environment. By layering ghosts on top of the "edema" fluid, biexponentiality is observed in $R_{1\rho}$ and $R_2$. This clearly establishes the role of the slow exchange of water between the two different homogeneous tissue compartments in generating multi-exponential magnetization decays, which is

brought about in this case by the presence of multiple membrane barriers to water diffusion. Futhermore, in situations where the extracellular space is limited, protein binding to membranes in this space results in a dramatic enhancement of the extracellular compartment water proton relaxation rate. Thus simple models of tissue involving only aqueous protein solutions are of limited value in trying to interpret relaxation data from edematous tissue. Finally, we note that $R_{1\rho}$ measured at spin-locking fields of about 0.9 mT has a heightened sensitivity to the protein content and volume fraction of the model edema fluid. This can be seen in Figure 3.3, where the dependence of $R_{1\rho}$ (at 0.9 mT) on the protein content and fraction of extracellular fluid is stronger than the dependence of $R_2$, suggesting that the incorporation of spin-locking in a conventional imaging sequence could provide better discrimination between different types of edema.

In Chapter 4 we refined a linear non-negative least -squares technique which has previously been used to analyze magnetization decays in terms of a continuous distribution of relaxation times. This intuitively more reasonable approach to characterising the relaxation times in tissue also requires no *a priori* guess of the number of exponentially decaying components and is thus not prone to experimenter bias in the choice of components. We have shown that in order to be confident that the calculated distribution is a true reflection of the distribution of relaxation times in the sample, a large ($\geq 100$) number of time domain data with initial signal-to-noise ratio greater than $10^3$ are needed. In the situation that is currently realisable clinically, one can typically obtain 8 echos with a signal-to-noise around 60. This is sufficient to delineate multiple transverse components in cat lung edema (4), but the width of the calculated relaxation time distribution will be governed by the uncertainty in the measurements. Thus one loses the ability to correlate the width of the relaxation time

distribution with any underlying structure and distribution of compartments. However the ability to distinguish multiple relaxation time components is preserved when using NNLS, making separation of the relaxation times less ambiguous than with other less robust techniques. The magnetization decay or recovery should also be followed well into the noise in order to accurately quantify baseline offsets, and as well, a good model of the spectrometer noise is needed to produce meaningful estimates of the confidence in the solution. Using the continuous NNLS approach, we have analysed the transverse and longitudinal magnetization decays for excised cat grey and white matter and have found four cleanly separated $R_2$ components in white matter and one dominant $R_2$ component in grey matter. In both grey and white matter only one $R_1$ component is found, presumably because the water exchange between microenvironments is fast on the $T_1$ timescale. The major peak in the white matter $R_2$ was assigned to water in the myelinated axons, which was assumed to be in slow exchange with the extracellular water. The lack of myelin barriers in grey matter allows fast water exchange between intra and extracellular spaces, which are thus not differentiable using $R_2$. The arguments for slow and fast exchange are based on the results of Chapter 3.

As a further demonstration of the power of continuous NNLS, as well as in an effort to develop a more complex model of neurological tissue, we chose, as a final model, to study water proton relaxation in excised abdominal segments of the crayfish central nerve cord. In this model of human brain, presented in Chapter 5, we detected four $R_2$ components from the cord and one from the bathing solution, implying slow water exchange between the bathing solution and the nerve cord. However we found only one broad $R_1$ component as was the case in both the cat brain experiments and our simple model systems. The detectable water fractions in

the nerve cord were identified by correlating extensive electron and light microscopy sections of the samples with the NMR relaxation data. In particular, we associate a major volume fraction with water in the axons, assumed to relax as a single group, and another smaller fraction with water in both the extracellular space and the glial cells, also assumed to relax as a single group. These identifications are borne out by experiments designed to manipulate the populations and relaxation rates of various compartments, as well as by NMR microscopic imaging studies which clearly show that water in the axons relaxes with a different $R_2$ from water in the extraaxonal spaces. The axonal compartment is thought to be in slow exchange with the extraaxonal compartment because of the diffusion barrier created between these two spaces by the connective tissue sheaths surrounding most axons. We have been able to follow each of the five $R_2$ components over time, obtaining information about the changes that occur in the nerve cord during Wallerian degeneration. These studies can serve as a basis for the interpretation of relaxation changes seen in human nervous tissue as pathology develops. In our model we observe that water moves out of the nerve cord over time, and that this water appears to come predominantly from the axonal compartment. The gradual coalescence of the peaks due to the intraaxonal and extraaxonal water over time is thought not to be due to the convergence of their relaxation rates but more likely to an increase in the exchange rate between the two compartments due to increases in membrane water and ion permeability.

Several problems need to be circumvented before the information gathered from the experiments in this thesis can be applied to clinical practice. It would have to be determined whether the clinician was interested in simply obtaining the best contrast in a NMR image or if quantifying the underlying physical processes was

more diagnostically useful. In the first case, one could "edit" for certain $R_2$, $R_1$ and $R_{1\rho}$ relaxation time combinations using the pulse sequence to show the desired features, in a manner similar to NMR spectroscopic editing (2). If quantification is the desired goal, the problems are more difficult to surmount. The fundamental problem of biological variability in tissues means that relaxation rates measured on an individual on just one occasion are not necessarily sufficient for detecting pathology. In situations such as where edema develops, we advocate the study of the timecourse of the relaxation rates for aiding diagnosis. This places considerable demands on the accuracy of the measured relaxation rates.

All our measurements have been done on bulk samples in NMR tubes, which would thus be representative of the signal from individual voxels in a clinical NMR image acquisition sequence. Accurate multiexponential analysis of the transverse relaxation rate from multi-echo images requires very good refocussing pulses and large numbers of echos, both of which are technically feasible in modern NMR imagers. Using a method such as continuous NNLS on a 256 x 256 element image requires huge amounts of computer memory and time. To a certain extent, the advent of powerful array processors should make this problem more manageable, but methods to display the large amount of data produced (in this case, 65536 $R_2$ distributions) have to be developed. Secondly, accurate measurements of the longitudinal relaxation rate in NMR imaging are time consuming and not always practical in a clinical situation. Since we find that the longitudinal magnetization recovery can be characterised by a single time constant, a simple two point method could be used to measure $R_1$.

Continuing work is still needed in the area of model systems, since they allow tighter control of the experimental parameters, and isolation of particular contributions to the relaxation rates. Such studies promise to reap huge rewards in fundamental science where the state of water in biological systems is of great importance, as well vastly improving the specificity of the NMR imaging technique. We are fortunate because the NMR imaging technique can be exploited although the fundamental physical processes governing tissue relaxation and hence image contrast are not well understood.

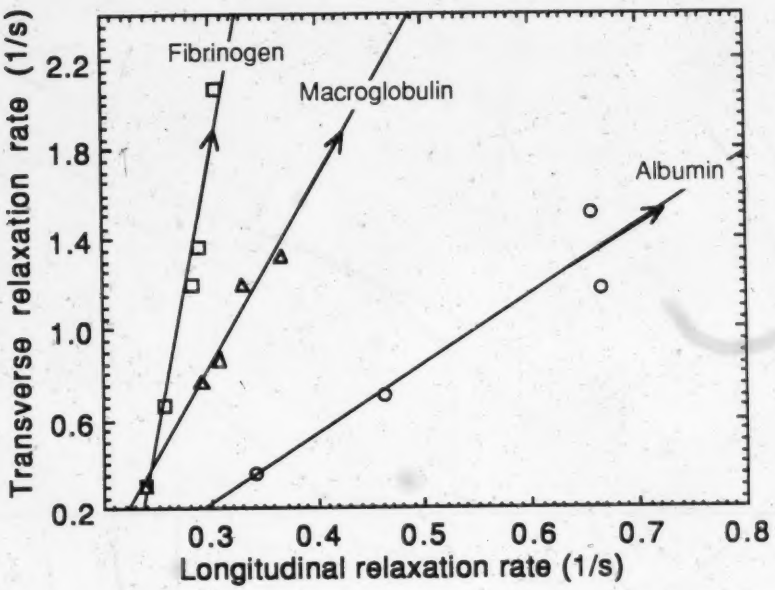


**Figure 6.1** $R_2$ vs. $R_1$ of three serum proteins in aqueous solution.The arrows indicate the direction of increasing protein concentration.

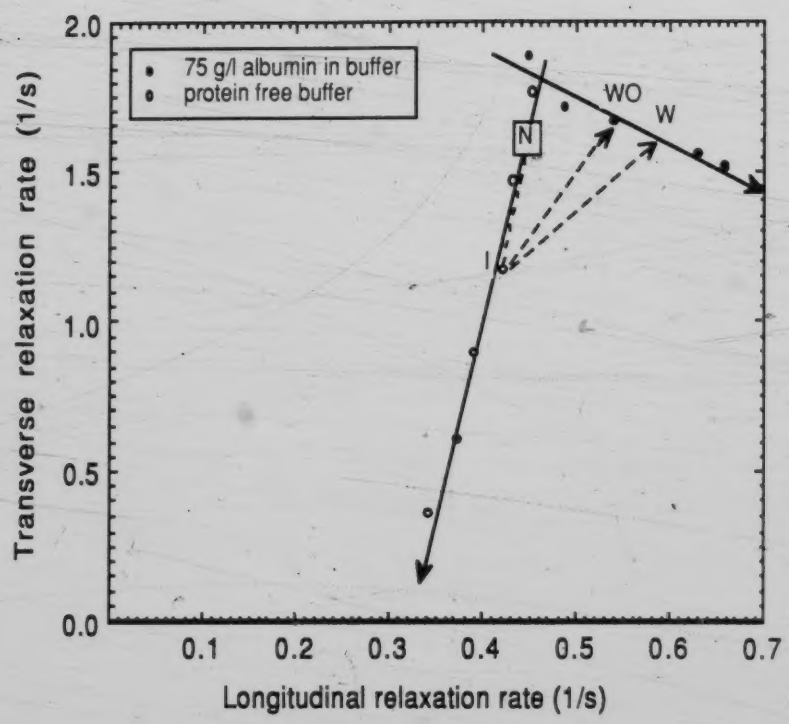


**Figure 6.2** $R_2$ vs. $R_1$ for a model of edematous grey matter. The arrows indicate the direction of increasing extracellular fluid fraction. The labels are discussed in the section 6.0.

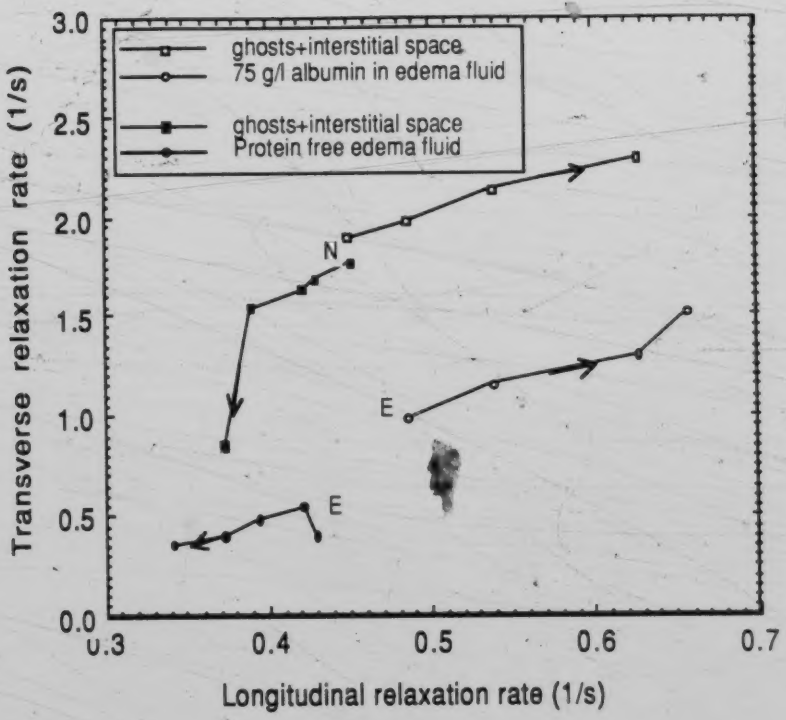


**Figure 6.3** $R_2$ vs. $R_1$ for a model of edematous white matter using different edema fluids. The arrows indicate the direction of increasing layered buffer fraction and interstitial space. The arrows go in opposite directions because the $R_1$ of the protein free buffer is smaller than that of the packed ghosts, while the $R_1$ of the proteinaceous buffer is larger than that of the packed ghosts. The labels are discussed in section 6.0.

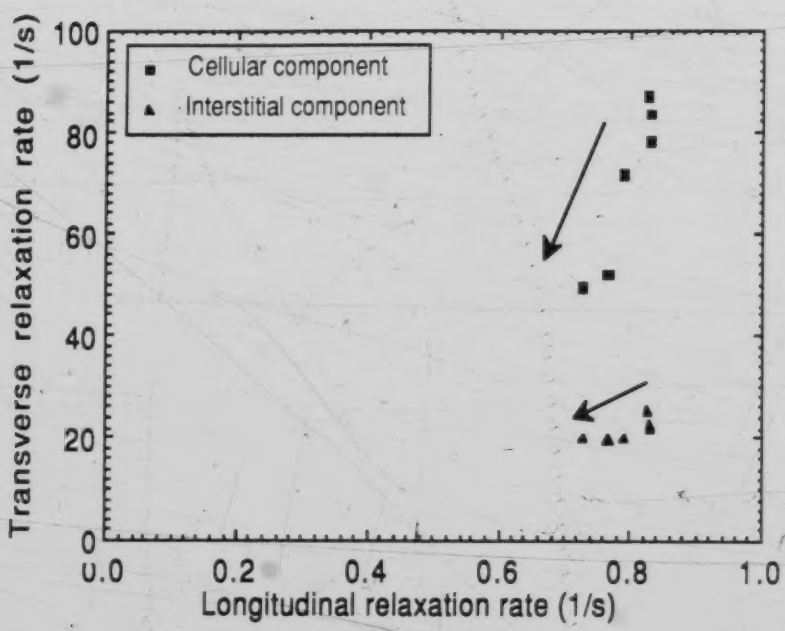


**Figure 6.4** Induction of edema in Shioya's model of pulmonary edema. The arrows indicate the time-course of the edema.

## 6.3 References

1. S. Shioya, M. Haida, C. Tsuji, Y. Ohta, H. Yamabayashi, M. Fukuzaki and Y. Kimula, Acute and repair stage characteristics of magnetic resonance relaxation times in oxygen-induced pulmonary edema, *Magn, Reson. Med.* **8**, 450 (1988).

2. P.S. Allen, In vivo nuclear magnetic resonance spectroscopy applied to medicine, *J. Can. Assoc. Radiol.* **41**, 39 (1990).

3. H.M. Pappius, *in* "Implications of the Blood-Brain Barrier and Its Manipulation" (E.A. Neuwelt, Ed.), Vol. 1, p. 293, Plenum, New York, 1989.

4. P.W. Stroman, *personal communication.*

## APPENDIX A

```
; PULSE PROGRAM FOR BRUKER CXP RMPCT2.PC
;
; T2 CPMG SEQUENCE INCORPORATING BASELINE CORRECTION
; FOR ERRORS DUE TO PHASE GLITCHES IN THE 180 PULSES.
;
; WRITTEN BY RAVI MENON
; LAST EDITED 05:02:90
;
; C2 IS THE NUMBER OF ECHOS
;
PROT NONE
RESET ALL
;
START,
    D0   [RGATE]                ; TR
    D1   [F1 @PLS1 RGATE]       ; 90 DEGREE PULSE
    D8   [RGATE]                ; DELAY
    LOOP C2 TIMES               ; ECHO COUNTER
     D1   [F1 @PLS2 RGATE]
     D1   [F1 @PLS2 RGATE]      ; 180 DEGREE PULSE
     D3   @PLS4                 ; CENTER AACQUISITION
     AQ   @PLS3                 ; ACQUIRE THE ECHO
     D3   @PLS4                 ; CENTER THE ECHO
    END LOOP                    ; END ECHO LOOP
;
++PLS1                          ; INCREMENT PHASES
++PLS2
++PLS3
++PLS4
;
GOTO START
;
BEGIN LISTS
;
PLS1, +X -X
PLS2, +Y -Y -Y +Y
PLS3, [STA DTRIG] [STA XAS DTRIG]
PLS4, [RGATE] [XAS RGATE]
;
END LISTS
```

THE FOLLOWING PROGRAM WILL CONDENSE THE DATA FROM THE CPMG PULSE PROGRAM TO 230 ECHOS, ROUGHLY LOG SAMPLED

```
C    PROGRAM T2PROC.FOR
C
C    THIS PROGRAM READS BRUKER DATA
C    PRODUCED BY RMT2.EXE AND RMPCT2.PC
C    AND PUTS IT IN A FORM THAT CURFIT OR T2LIN CAN READ.
C
C    WRITTEN BY RAVI MENON
C
C    LAST EDITED 13/05/89
C
C    TAKES INTO ACCOUNT THE ALTERNATE ECHO SAMPLING
C    OF THE WONDERFUL BRUKER SOFTWARE.
C
C    MODIFIED TO INCLUDE BOTH REAL AND IMAGINARY POINTS
C    IN THE MAGNITUDE CALCULATION TO COMPENSATE FOR PHASE
C    DRIFT IN THE SYSTEM
C
C    INCLUDES POINTS CUTOFF AT S/N OF 0.01
C
C    MODIFIED TO INCLUDE A LOG SAMPLING OF THE POINTS AND
C    TO TAKE ADVANTAGE OF CURFIT'S NEW POINT LIMIT OF 1024.
C
     INTEGER BLOCK,POINT,POINTS,FLAG
     INTEGER*4 FDATA(128)
     REAL NORMR,NORMI,T2RDATA(16),T2IDATA(16),T2DATAA(2048)
     REAL TDATAR(64),TDATAI(64),T2DATA(8192),TIME(8192),TIMEA(2048)
     REAL VAR,SUM,AVG,WAVG
     CHARACTER*60 FNAMEIN,FNAMEOUT
C
100  FORMAT(A)
101   FORMAT(1X,F20.8,5X,F20.8)
102  FORMAT('&INPUT DATA FILE')
103  FORMAT('&OUTPUT DATA FILE')
105  FORMAT(I10)
C
     WRITE(6,102)
     READ(5,100) FNAMEIN
     WRITE(6,103)
     READ(5,100) FNAMEOUT
C
      OPEN(UNIT=1, FILE=FNAMEIN, STATUS='OLD',
     +FORM='UNFORMATTED' )
     OPEN(UNIT=2, DEFAULTFILE='DISK$USER:[RAVI.DATA]',
     +FILE=FNAMEOUT, STATUS='NEW',
     +FORM='FORMATTED' )
C
     DO 110 J=1,2
110    READ (1) (FDATA(I),I=1,128,1)
     POINT=0
```

```
C
      DO 400 BLOCK=1,512
       READ (1) (FDATA(I),I=1,128,1)
C
       IF (BLOCK.EQ.1) THEN
       NORMR=FLOAT(FDATA(3)+FDATA(5)+FDATA(7))/3.0
       NORMR=NORMR+FLOAT(FDATA(9)+FDATA(11)+FDATA(13))/3.0
       NORMI=FLOAT(FDATA(4)+FDATA(6)+FDATA(8))/3.0
       NORMI=FLOAT(FDATA(10)+FDATA(12)+FDATA(14))/3.0
      TYPE*,'NORMALIZATION CONSTANT (REAL)=',NORMR
       TYPE*,'NORMALIZATION CONSTANT (IMAG)=',NORMI
       END IF
C
       DO 120 I=1,64,1
       TDATAR(I)=FLOAT(FDATA(2*I-1))
       TDATAI(I)=FLOAT(FDATA(2*I))
120     CONTINUE
C
       DO 130 IN=1,8
       POINT=POINT+1
       I=8*IN
       T2RDATA(IN)=TDATAR(I-6)+TDATAR(I-5)+TDATAR(I-4)
       T2RDATA(IN)=T2RDATA(IN)+TDATAR(I-3)+TDATAR(I-2)
     +  +TDATAR(I-1)
       T2IDATA(IN)=T2IDATA(IN)+TDATAI(I-6)+TDATAI(I-5)
     +  +TDATAI(I-4)
       T2IDATA(IN)=TDATAI(I-3)+TDATAI(I-2)+TDATAI(I-1)
      T2RDATA(IN)=T2RDATA(IN)*T2RDATA(IN)
      T2IDATA(IN)=T2IDATA(IN)*T2IDATA(IN)
      T2DATA(POINT)=100.0*(T2RDATA(IN)+T2IDATA(IN))**0.5/3.0/
     + (NORMR**2+NORMI**2)**0.5
      TIME(POINT)=1.60000*FLOAT(POINT)
130    CONTINUE
C
400   CONTINUE
C
     IND=0
     DO 420 I=1,25,1
      IND=IND+1
     TIMEA(IND)=TIME(I)
     T2DATAA(IND)=T2DATA(I)
420   CONTINUE
     DO 440 I=29,125,4
      IND=IND+1
     TIMEA(IND)=TIME(I)
     T2DATAA(IND)=T2DATA(I)
440   CONTINUE
     DO 460 I=133,309,8
      IND=IND+1
     TIMEA(IND)=TIME(I)
     T2DATAA(IND)=T2DATA(I)
```

```
460  CONTINUE
     DO 480 I=310,4070,24
     IND=IND+1
     TIMEA(IND)=TIME(I)
     T2DATAA(IND)=T2DATA(I)
480  CONTINUE
C
     FLAG=0
     POINTS=IND
C
     DO 600 IND=1,POINTS
      IF ((T2DATAA(IND)).LT.(0.01)) THEN
       IF (FLAG.EQ.0) THEN
        FLAG=1
        POINTS=IND-1
       END IF
      END IF
600  CONTINUE
C
     VAR=1.0
     WRITE(2,105) POINTS
     DO 700 IND=1,POINTS
700    WRITE(2,101) TIMEA(IND),T2DATAA(IND)
     WRITE(2,101) VAR
C
     END
```

## APPENDIX B

```
; PULSE PROGRAM FOR BRUKER CXP RMPCT1.PC
;
; T1 FREEMAN-HILL INVERSION RECOVERY SEQUENCE
;
; WRITTEN BY RAVI MENON
;
; LAST EDITED 09:01:88
;
; 0-TAU-90X-TR-180Y-TAU-90X-TR
;
; ********************  ADD SCAN
START,
PROT F1
    D0    [RGATE]
    D1                          ; 0 DEG PULSE
    D1                          ;
    D8                          ; INVERSION RECOVERY TIME
    D1    [F1 @PLS1 RGATE]      ; 90 DEG PULSE
    DW    [DTRIG]
    AQ    [STA]                 ; ACQUIRE M0
    D3
; ********************  SUBTRACT SCAN
    D0    [RGATE]
    D1    [F1 @PLS2 RGATE]
    D1    [F1 @PLS2 RGATE]      ; 180 DEG PULSE
    D8                          ; INV. REC. TIME TAU
    D1    [F1 @PLS1 RGATE]      ; 90 DEG PULSE
    DW    [DTRIG]
    AQ    [STA XAS]             ; ACQUIRE M
    D3    [XAS]
;
++PLS1                          ; INCREMENT PHASES
++PLS2
;
GOTO START
;
BEGIN LISTS

PLS1, +X +X
PLS2, +Y -Y

END LISTS

THE FOLLOWING PROGRAM WILL PRODUCE A FILE WITH
40 INVERSION RECOVERY OR SPIN-LOCKING POINTS'

C    PROGRAM T1PROC.FOR
C
C    THIS PROGRAM READS BRUKER DATA
```

```
C    AQUIRED USING RMT1.EXE, RMPCT1.PC
C    OR RMT1R.EXE, RMPCT1R.PC AND PUTS
C    IT IN A FORMAT THAT CURFIT OR T2LIN CAN USE
C
C    WRITTEN BY RAVI S. MENON
C
C    LAST EDITED 09/04/89
C
C    MODIFIED TO INCLUDE REAL AND IMAGINARY DATA IN THE
C    CALCULATION TO COMPENSATE FOR PHASE DRIFT
C
C    ALSO CUTS OFF DATA IF NORMALIZED SIGNAL DROPS BELOW 0.1
C
     INTEGER NPOINTS,FLAG,POINTS
     INTEGER*4 FDATA(128)
     INTEGER*4 Y(128)
     REAL TIME,AVG,AVGR,AVGI,NCONSTR,NCONSTI
     REAL NCONST,TIMEA(60),DATAA(60)
     CHARACTER*60 FNAMEIN,FNAMEOUT
C
100  FORMAT(A)
101   FORMAT(5X,F20.8,5X,F20.8)
102  FORMAT('&INPUT DATA FILE')
103  FORMAT('&OUTPUT DATA FILE')
105  FORMAT(I10)
C
     WRITE(6,102)
     READ(5,100) FNAMEIN
     WRITE(6,103)
     READ(5,100) FNAMEOUT
C
      OPEN(UNIT=1, FILE=FNAMEIN, STATUS='OLD',
    +FORM='UNFORMATTED' )
     OPEN(UNIT=2, DEFAULTFILE='DISK$USER:[RAVI.DATA]',
    +FILE=FNAMEOUT, STATUS='NEW',
    +FORM='FORMATTED' )
C
     IND=0
     NPOINTS=40
     DO 110 J=1,2
110   READ (1) (Y(I),I=1,128)
C
     NCONSTR=0
     NCONSTI=0
     DO 120 J=1,NPOINTS
      TIME=10.0**(-3.0+(FLOAT(J)-1.0)/10)
      TIME=TIME*1000
      AVG=0
      AVGR=0.0
      AVGI=0.0
      READ (1) (FDATA(I),I=1,128,1)
```

```
C
      DO 114 K=1,15,2
      AVGR=FDATA(K)+AVGR
      AVGI=FDATA(K+1)+AVGI
114    CONTINUE
      AVGR=AVGR/8.0
      AVGI=AVGI/8.0
      AVG=(AVGR**2.0+AVGI**2.0)**0.5
      IF (J.EQ.1) THEN
      NCONSTR=AVGR
      NCONSTI=AVGI
         TYPE*,'THE REAL CHANNEL NORMALIZATION IS ',NCONSTR
         TYPE*,'THE IMAGINARY CHANNEL NORMALIZATION IS
',NCONSTI
      END IF
C
C
     IND=IND+1
     IF (J.EQ.0) GO TO 115
      NCONST=(NCONSTR**2.0+NCONSTI**2.0)**0.5
     TIMEA(IND)=TIME
     DATAA(IND)=100.0*AVG/NCONST
115   CONTINUE
C
      DO 116 K=1,7
116     READ (1) (FDATA(I),I=1,128,1)
C
120   CONTINUE
C
    FLAG=0
    POINTS=NPOINTS
    DO 150 IND=1,NPOINTS
     IF (DATAA(IND).LT.0.1) THEN
      IF (FLAG.EQ.0) THEN
      FLAG=1
      POINTS=IND-1
     END IF
    END IF
150   CONTINUE
C
    VAR=1.0
    WRITE(2,105) POINTS
    DO 200 IND=1,NPOINTS
200    WRITE(2,101) TIMEA(IND),DATAA(IND)
    WRITE(2,101) VAR
C
    END
```

## APPENDIX C

```
; PULSE PROGRAM FOR BRUKER CXP RMPCT1R.PC
;
; T1-RHO SEQUENCE
;
; WRITTEN BY RAVI MENON
; LAST EDITED 10:01:88
;
; 90(X)-LOCK-ACQ-TR-90(-X)-LOCK-ACQ-TR
;
; ************************ ADD/SUBTRACT SCAN
START,
PROT NONE
     D0   [RGATE]                          ; TR
     D1   [F1 @PLS1 RGATE]                 ; 90 DEGREE PULSE
     D8   [F1 @PLS2 PRE RGATE]             ; SPIN-LOCK PULSE
     DW   [RGATE]
     AQ   @PLS3                            ; ACQUIRE FID
     D3   @PLS4
;
++PLS1                                     ; INCREMENT PHASES
++PLS2
++PLS3
++PLS4
;
GOTO START

BEGIN LISTS

PLS1,  +X -X
PLS2,  +Y -Y
PLS3, [STA DTRIG] [STA XAS DTRIG]
PLS4, [RGATE] [XAS RGATE]

END LISTS
```

THE SAME PROCESSING PROGRAM USED FOR THE 40 INVERSION RECOVERY POINTS IS USED TO PROCESS THE $T_{1\rho}$ DATA.

## APPENDIX D

```
; PULSE SEQUENCE FOR BRUKER CXP MICE.PC
;
; MICROSCOPIC IMAGING PULSE PROGRAM @ T1RHO SLICE SELECTION
; WRITTEN BY RAVI S. MENON
; LAST EDITED 2 NOV 1988
;
RESET ALL
PROT NONE
START,
    AD1  [RGATE]                          ; TR
    LOOP AC1 TIMES                        ; SLICE COUNTER (NOT USED)
     AD3  [RGATE]                         ; TIME BETWEEN SLICES
     10M  [F2+X RGATE] <CNG NO1>          ; SLICE SELECTION GRAD ON
     AD2  @P1LST                          ; 90 DEGREE PULSE
     AD4  @P2LST                          ; SPIN LOCK SLICE SELECTION
     2M   [F2+X RGATE] <CNG NO1>          ; SLICE COMP, PHASE ON
     AD6  [RGATE]                         ; AND READ COMP ON
     AD7  [F2+X RGATE] <CNG>              ; ALL GRADS OFF
     AD8  [RGATE]                         ; ECHO TIME VARIABLE
     LOOP AC2 TIMES                       ; ECHO COUNTER
      AD2  @P3LST
      AD2  @P3LST                         ; 180 DEGREE PULSE
      AD8  [RGATE]                        ; ECHO TIME VARIABLE
      AD7  [RGATE]                        ; CENTRE THE ECHO
      2M   [F2+X RGATE] <CNG NO1>
      AQ   @P4LST                         ; AQUIRE ECHO
      2M   [F2+X XAS RGATE] <CNG>         ; READ OFF, CENTER ON
      2U   [RGATE]                        ; SEPARATE GRAD TRIG PULSES
      AD7  [F2+X RGATE] <CNG>             ; CENTERING GRAD OFF
     END LOOP                             ; END ECHO LOOP
     10M  [F2+X RGATE] <CNG>              ; ALL GRADS OFF
    END LOOP                              ; END SLICE LOOP

    ++P1LST                               ; INCREMENT PHASES
    ++P2LST
    ++P3LST
    ++P4LST

GOTO START

BEGIN LISTS

P1LST, [F1+X RGATE] [F1-X RGATE]
P2LST, [F1+Y PRE RGATE] [F1-Y PRE RGATE]
P3LST, [F1+Y RGATE] [F1-Y RGATE] [F1-Y RGATE] [F1+Y RGATE]
P4LST, [STA] [STA XAS]
P5LST, [F1+Y RGATE] [F1-Y RGATE]

END LISTS
```

# APPENDIX F

## Design of a Gradient Coil Set for Microscopic Imaging

General System Design Philosophy.

The gradient coils used for microscopic imaging are designed to be driven by the Bruker hardware. The cables leading to the coil are designed to mate directly with the connectors for the normal gradient coils. To ensure that the gradient driver unit can efficiently drive the new coils, the resistance of each coil was chosen to match the nominal source impedance of the driver. This places limitations on the number of turns used for the gradient coils and the gauge of wire used.

The only modification made to the standard Bruker electronics involves replacement of the pre-emphasis unit with a simple three channel amplifier with a gain of two. This decision was made on the basis that the coil set produces no eddy currents in the cryostat walls by virtue of the distance of the coil unit from the magnet bore walls and the inductance of the coils is sufficiently low that no gradient pulse shaping is required. The amplifiers are of a low drift/low noise design, which is essential because the x, y and z shim currents are also fed into the coils via this circuit path.

The x and y coils are Golay pairs wound on the coil former by first drafting the pattern onto a large sheet of paper and wrapping this template around the coil former. Holes were tapped at the corners of each coil pattern and nylon screws threaded into the former. The wire was wrapped flat on the former around the screw posts and taped down with fibreglass tape with a tension of about 100 pounds. The z Maxwell pair was wound in two layers and strapped down with fibreglass tape. The coils were strapped down instead of potting in epoxy in order to make air cooling the gradient coils straightforward. Air cooling is required at steady state currents over 10 amps or at higher currents and correspondingly lower duty cycles, but is not required for normal multiple-echo imaging duty cycles.

System Specifications

i) Bruker Gradient Drivers.

Nominal output impedance is 0.6 Ohms per channel.
Lead resistance from Drivers to gradient coils is 0.21 Ohms per channel including the filter box.
Lead length is approximately 6m.
Maximum current drive is 60 Amps per channel.

ii) 3 Channel Amplifier.

Gain of 2.0.
Drift in resonance frequency due to shim current drift,
<5 Hz. per hour
<10 Hz. per day.

iii) Amphenol connectors.

Amphenol 97 series 7 pin cable connectors for 12 gauge which in the standard finish are non-magnetic.
Cable receptacle 97-3101-A-24-2 P
Cable plug 97-3106-A-24-2 S
Cable clamps MS3057-16A
Cable bushings AN3420-16A

iv) Gradient Coil Protection Circuit.

Consists of 3 Potter and Brumfield thermal circuit breakers, Model W58XB1A4A-10, rated at 10 Amps, but which trip in less than 3 seconds at 30 Amps.

v) Gradient Coil Unit.

Golay pairs for x and y are used.
A Maxwell pair is used for the z direction ie. along the bore.
The template was made up as per the article by Romeo and Hoult, Mag. Res. in Med. 1 ,44-65 (1984).

The coil former is made of 4 inch ABS plastic sewer pipe.
outer radius of 10.2 cm.
inner radius of 9.4 cm.
length of 41cm.

x coil: 8 flat turns, 0.747 Ohms.
y coil: 9 flat turns, 0.649 Ohms.
z coil: 9 flat turns stacked on 10 flat turns, 0.534 Ohms.
(Resistances measured from Amphenol connector at protection circuit box..All coils are made from 20 gauge magnet wire.)

Coil inductance is approximately 80 microHenries.at 2 kHz.

Isolation between x and y coils is 46 dB (1 part in 200).
Isolation between x and z coils or y and z is 40 dB (1 part in 100).
(Isolation measured by putting a 10 Amp square wave in one coil and measuring the induced current in the other.)

Gradient Linearity
x: strength down 17% from isocentre value at r=4cm.
y: strength down 17% from isocentre value at r=4cm.
z: strength down 20% from isocentre value at r=4cm.
x: down 5% at r=1.5cm.
y: down 5% at r=1.5cm.
z: down 5% at r=3.0cm.

Gradient Strength
x: 0.369 Gauss/cm/Amp. Maximum of 22 Gauss/cm.
y: 0.482 Gauss/cm/Amp. Maximum of 29 Gauss/cm.
z: 0.536 Gauss/cm/Amp. Maximum of 32 Gauss/cm.

vi) RF Coil Assembly.

The RF coil is a 6 turn solenoid, 2cm in length and 1cm in diameter, mounted with the tune and match capacitors in a copper shielded box. The shielded box is designed to prevent eddy currents, but act as anRF shield. It has ports for temperature control of the entire box contents. The box sits in a ABS plastic cradle which slides tightly into the bore of the gradient coil unit for easy sample mounting , centering and changing.

LAYOUT FOR MICROSCOPIC IMAGING ON THE UNIVERSITY OF ALBERTA
*IN-VIVO* NMR GROUP's MEDIUM BORE UNIT.

SYSTEM BLOCK DIAGRAM

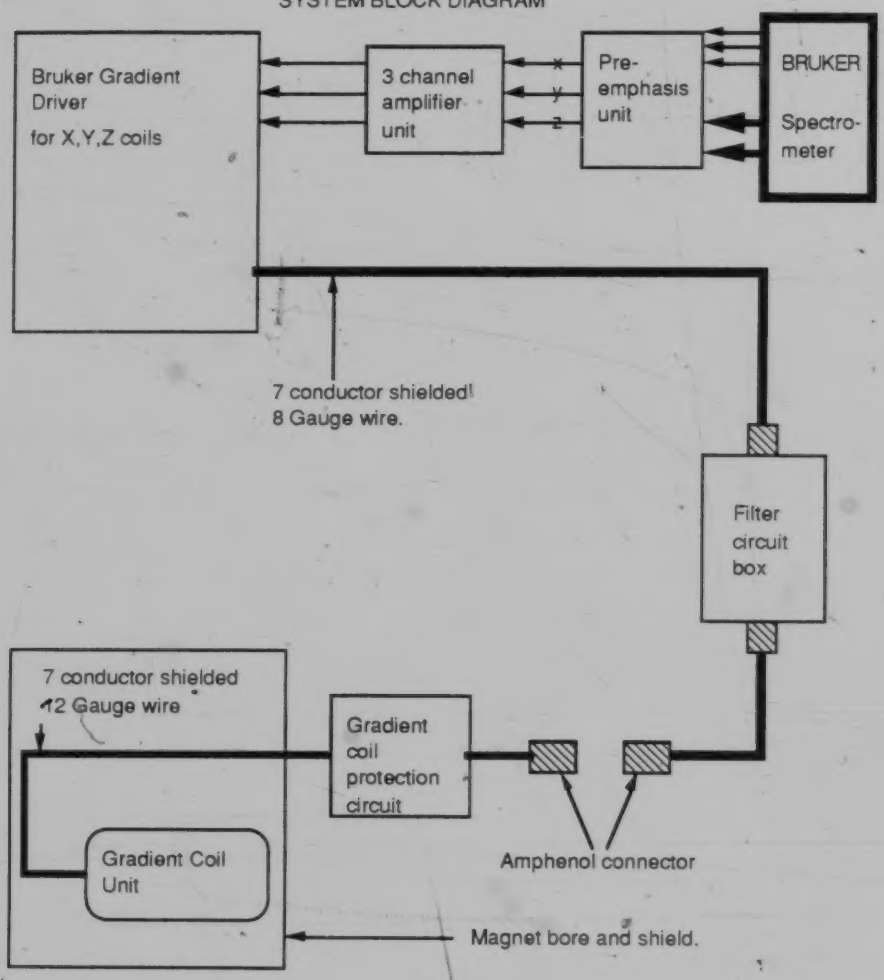

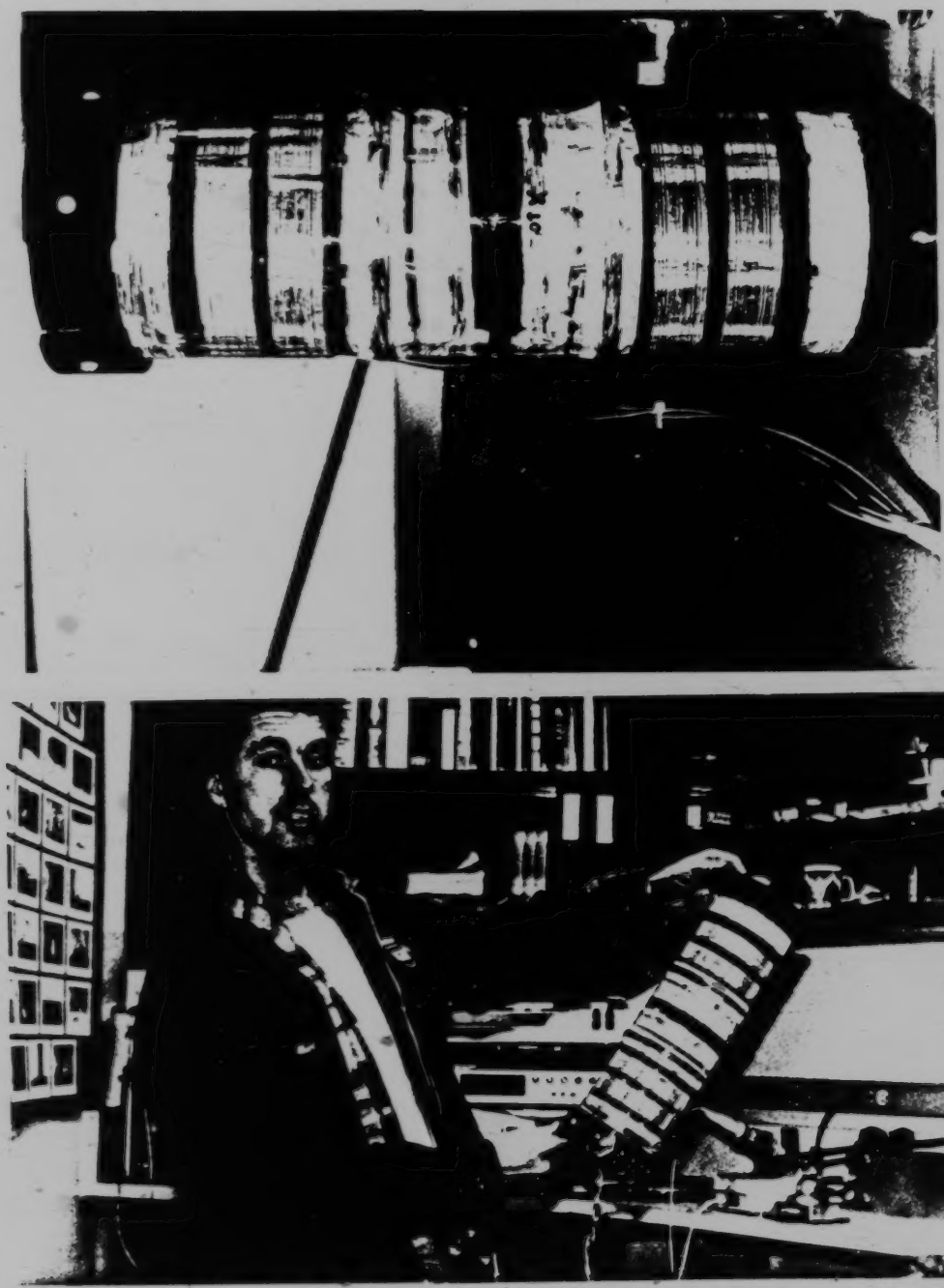

Details of gradient coil construction

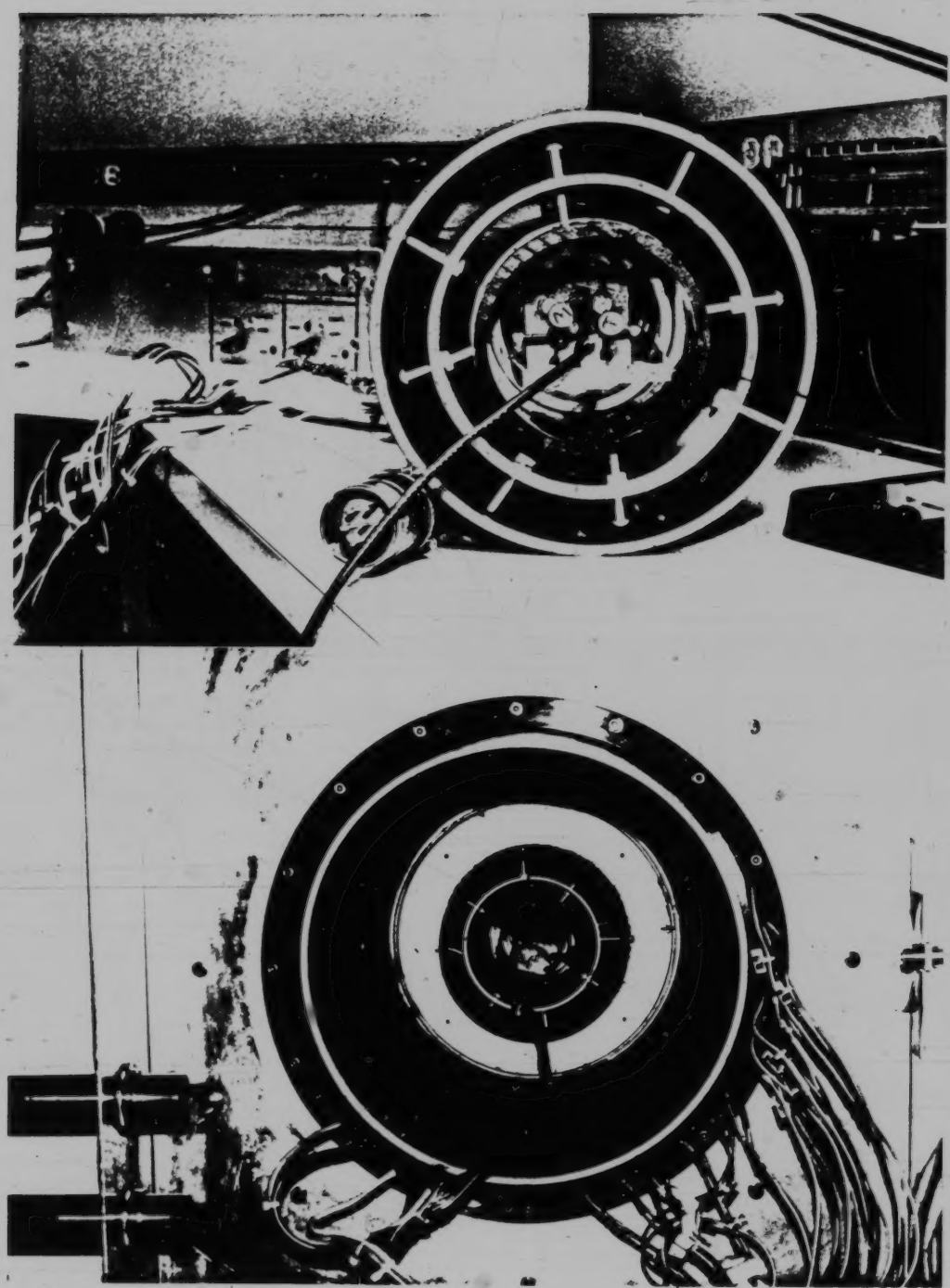

Details of gradient coil mounting